frontiers | Research Topics

A year in review: Discussions in molecular and structural endocrinology, 2nd edition

Edited by
Alain Couvineau and Ernestina Marianna De Francesco

Published in
Frontiers in Endocrinology

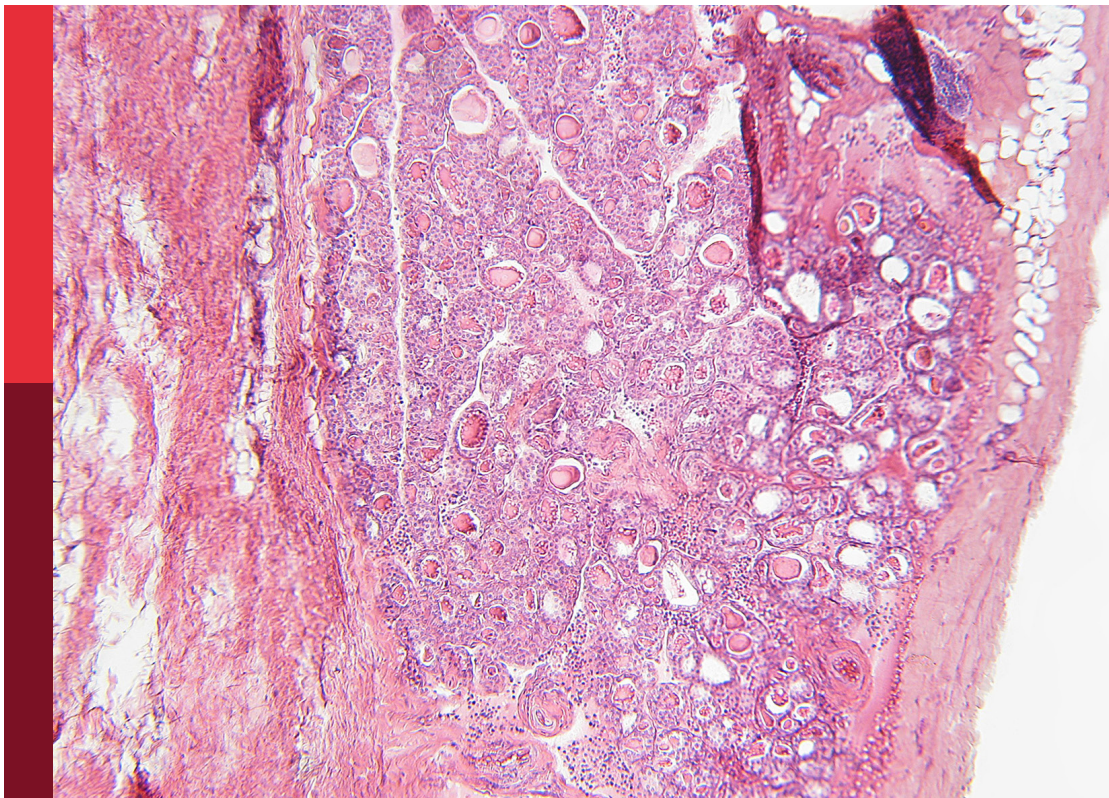

ISSN 1664-8714
ISBN 978-2-8325-6226-0
DOI 10.3389/978-2-8325-6226-0

About Frontiers

Frontiers is more than just an open access publisher of scholarly articles: it is a pioneering approach to the world of academia, radically improving the way scholarly research is managed. The grand vision of Frontiers is a world where all people have an equal opportunity to seek, share and generate knowledge. Frontiers provides immediate and permanent online open access to all its publications, but this alone is not enough to realize our grand goals.

Frontiers journal series

The Frontiers journal series is a multi-tier and interdisciplinary set of open-access, online journals, promising a paradigm shift from the current review, selection and dissemination processes in academic publishing. All Frontiers journals are driven by researchers for researchers; therefore, they constitute a service to the scholarly community. At the same time, the *Frontiers journal series* operates on a revolutionary invention, the tiered publishing system, initially addressing specific communities of scholars, and gradually climbing up to broader public understanding, thus serving the interests of the lay society, too.

Dedication to quality

Each Frontiers article is a landmark of the highest quality, thanks to genuinely collaborative interactions between authors and review editors, who include some of the world's best academicians. Research must be certified by peers before entering a stream of knowledge that may eventually reach the public - and shape society; therefore, Frontiers only applies the most rigorous and unbiased reviews. Frontiers revolutionizes research publishing by freely delivering the most outstanding research, evaluated with no bias from both the academic and social point of view. By applying the most advanced information technologies, Frontiers is catapulting scholarly publishing into a new generation.

What are Frontiers Research Topics?

Frontiers Research Topics are very popular trademarks of the *Frontiers journals series*: they are collections of at least ten articles, all centered on a particular subject. With their unique mix of varied contributions from Original Research to Review Articles, Frontiers Research Topics unify the most influential researchers, the latest key findings and historical advances in a hot research area.

Find out more on how to host your own Frontiers Research Topic or contribute to one as an author by contacting the Frontiers editorial office: frontiersin.org/about/contact

A year in review: Discussions in molecular and structural endocrinology, 2nd edition

Topic editors

Alain Couvineau — Institut National de la Santé et de la Recherche Médicale (INSERM), France

Ernestina Marianna De Francesco — University of Catania, Italy

Citation

Couvineau, A., De Francesco, E. M., eds. (2025). *A year in review: Discussions in molecular and structural endocrinology, 2nd edition*. Lausanne: Frontiers Media SA. doi: 10.3389/978-2-8325-6226-0

Publisher's note: This is a 2nd edition due to an article retraction.

Table of contents

frontiers | Frontiers in Endocrinology

TYPE Editorial
PUBLISHED 12 June 2023
DOI 10.3389/fendo.2023.1231470

OPEN ACCESS

EDITED AND REVIEWED BY
Pierre De Meyts,
Université catholique de Louvain, Belgium

*CORRESPONDENCE
Alain Couvineau
alain.couvineau@inserm.fr
Ernestina Marianna De Francesco
ernestinamarianna@yahoo.it

RECEIVED 30 May 2023
ACCEPTED 02 June 2023
PUBLISHED 12 June 2023

CITATION
Couvineau A and De Francesco EM (2023) Editorial: A year in review: discussions in molecular and structural endocrinology. *Front. Endocrinol.* 14:1231470. doi: 10.3389/fendo.2023.1231470

Editorial: A year in review: discussions in molecular and structural endocrinology

Alain Couvineau[1]* and Ernestina Marianna De Francesco[2]*

[1]Institut National de la Santé et de la Recherche Médicale (INSERM) UMR1149/Inflammation Research Center (CRI), Université Paris Cité, Departement Hospitalo-Universitaire (DHU) UNITY, Faculty of Medicine X, Bichat, Paris, France, [2]Endocrinology Unit, Department of Clinical and Experimental Medicine, University of Catania, Garibaldi-Nesima Hospital, Catania, Italy

KEYWORDS

endocrinology, obesity, diabetes, cancer, development

Editorial on the Research Topic
A year in review: discussions in molecular and structural endocrinology

A year in review is a research theme on molecular and structural endocrinology from 2021 onwards. Molecular and structural endocrinology focuses on the molecular processes regulating many functions related to endocrine signalling, hormone synthesis/secretion and interactions between hormones, their receptors and interaction with other signaling molecules. This broad spectrum of action involves molecular mechanisms, structural biology, hormonal regulation, genetic, epigenetic and cell signalling, in both physiological and/or pathological contexts such as metabolic diseases encompassing diabetes and obesity, developmental diseases and cancer. Here, contributions by researchers/clinicians offer us a very comprehensive overview of recent findings that extend the current knowledge on several aspects of molecular and structural endocrinology, providing novel challenges and future perspectives in this field.

In an attempt to better clarify how structural changes may affect receptor function and facilitate the establishment of a pathological phenotype, Purba et al. analysed the structure of Epidermal Growth Factor Receptor (EGFR) to determine its ability to auto-activate. In various human cancers, mutations of EGFR promote its aberrant activation, leading to cell proliferation in the absence of ligand. Here, the authors purify full-length EGFR which adopts a homodimeric form in the presence or in the absence of ligand. The ligand was able to stabilize the extracellular domain of the receptor which is very flexible in its absence. This flexibility was associated to the dissociation of the intracellular kinase dimer. Moreover, mutations of residues of the inactive kinase dimer induced auto-activation of EGFR. This structural study of EGFR shows that mutations are able to spontaneously activate the receptor.

Proto-oncogene amplification is a common pathogenetic trait in several cancers. In this regard, Liverani et al. investigated the impact of HRAS proto-oncogene overexpression on lenvatinib treatment in gastroenteropancreatic neuroendocrine tumors (GEP-NET). Lenvatinib, a multi-tyrosine kinase inhibitor, has demonstrated efficacy in GEP-NET

patients. In 55% of primary cultures from patients with GEP-NET, lenvatinib showed antitumor activity. This antitumor effect was associated with HRAS overexpression. The Authors show that lenvatinib is highly effective in the treatment of NETs, and that HRAS overexpression could be a reliable marker of its success.

Beyond amplification, genomic alterations such as mutations may strongly contribute to tumorigenesis, therefore their identification in normal vs cancer tissue may pave the way to the identification of better diagnostic and therapeutic tools. In this context, Chorti et al. performed an updated review of the molecular genetics of sporadic parathyroid adenoma, a neoplastic condition affecting 1% of the global population. By analyzing 78 articles, the Authors retrieved several mutated genes and/or proteins differentially expressed or localized in neoplastic vs normal tissue, including CaSR, MEN1, CCND1/PRAD, 41 CDKI, VEGF, FGF, TGFβ and IGF1. Such an effort could have relevant implications in the identification of novel biomarkers for endocrine tumors.

A similar approach has been used for endocrinological diseases other than tumors. For instance, Ahmad et al. analyzed individuals affected by Isolated Growth Hormone Deficiency (IGHD), a disorder associated with reduced circulating levels of GH which causes short stature and skeletal anomalies. In consanguineous family members of patients affected by IGHD, a p.Glu72 mutation in the gene codifying for the growth-hormone-releasing hormone receptor (GHRHR) was identified by whole-exome sequencing (WES) and Sanger sequencing. The pathogenicity of such mutation was further confirmed by performing computational analyses such as structural modeling and docking studies, together with molecular simulation analyses.

Gau et al. studied a novel variant of NR5A1 named R350W in its ability to potentiate NR5A1 functions. NR5A1 is a gene family that encodes transcription factors belonging to the nuclear receptor superfamily. These transcription factors are involved in various biological processes such as gonad development. The authors demonstrated that R350 impaired the transcriptional activities of various genes (hTES, CYP17) which have a strong impact on Sertoli and Leydig cell differentiation. Moreover, R350W could interact with a putative endogenous ligand or co-factor, potentiating NR5A1 activities but not NR5A2. This study demonstrated that orphan factors may play a significant role in human pathophysiology.

Research efforts are directed toward the identification of novel players in obesity and diabetes, due to the growing incidence of these metabolic conditions. In this context, Brustolin et al. studied the impact of TREM-1 (Triggering Receptor of Expressed Myeloid Cells-1) on low-grade inflammation associated with obesity. TREM-1 is involved in many acute inflammation (Septic shock and IBD) and is overexpressed in adipose tissue and liver in obese and diabetic patients. TREM-1 is functionally expressed in subcutaneous and omental adipocytes. A *trem1* KO mouse model associated with a high-fat diet showed limited gain of weight, insulin resistance, and liver inflammation. These results demonstrated that TREM-1 could play a crucial role in obesity development and complications.

Hurley et al. examined the role of ORMDL3 (one of three isoforms of orosomucoid-like proteins), which is identified as a key factor in sphingolipid homeostasis, in pancreatic β-cell functions. A β-cell failure was observed during chronic sphingolipid elevation. The development of a mouse model invalidated for the *ormdl3* gene in pancreatic β-cells showed the absence of alteration in glucose tolerance, insulin sensitivity and secretion, islet morphology, and high fat diet *ormdl3*$\beta^{-/-}$ mice did not display metabolic alterations. ORMDL3 is not essential for β-cells survival and function on normal and fatty diets. Considering that diabetes may trigger severe clinical issues as observed during pregnancy, Li et al. investigated certain mechanisms through which hyperglycemia leads to obstetrical complications. The authors found that high glucose levels decrease myometrium contractility in patients affected by gestational diabetes mellitus (GDM). Reduced cell contractility was observed also in hypoxic conditions and was paralleled by the up-regulation of HIF-1a (Hypoxia inducible Factor-1a) and TREK1 (TWIK-1-related potassium channel). These findings may provide a mechanistic explanation of the higher rate of obstetrical complications related with GDM.

Other approaches are focused on major diabetes complications; in this regard, Zhao et al. studied the role of growth differentiation factor (GD-10) in wound healing of diabetic foot ulcer (DFU) (a major complication of diabetes mellitus), involving TGF-β1 (Transforming growth factor-beta 1/Smad3 signaling pathway). The use of weighted gene co-expression network analysis (WGCNA) combined with an animal model reproducing DFU, allowed to demonstrate that GD-10 promotes angiogenesis via TGF-β1/Smad3 signaling pathway, leading to a beneficial effect on DFU.

Using high-throughput tools, You et al. mimicked glaucoma *in vitro* by subjecting R28 retinal cells to a pressurized stress model. RNA-seq analyses performed on this model revealed several long-non-coding RNAs (lncRNAs) and microRNAs (mRNAs) differentially regulated and possibly associated with glaucoma. Validation of the cellular data was obtained using clinical samples and confirmed the lncRNAs AC120246.2 and XLOC_006247 as the most strongly increased in glaucoma patients *vs* patients affected by cataracts. These findings set the stage for broadening the diagnostic and therapeutic perspectives of glaucoma patients.

The cross-talk between hormone and growth-factor receptors is known to play a key regulatory role in signaling transduction, potentially affecting endocrine homeostasis in normal and pathological conditions. Mistry et al. demonstrated that Fibroblast Growth 21 (FGF21) is directly implicated in the resistance to Growth Hormone (GH) and in the failure of linear growth in very pre-term (VPT) infants. By using rare and unique human growth plates obtained from children, the Authors found that FGF21 decreases GHR half-life and inhibits downstream GHR signaling events (i.e. IGF-1 release). In VPT infants, FGF21 levels were higher in the stage of deflected linear growth, whereas in the phase of catch-up growth a reduction of FGF21 levels was observed, together with an increase of IGF1 levels. These findings suggest that FGF21 may dampen GH/GHR signaling toward growth failure.

Author contributions

All authors listed have made a substantial, direct and intellectual contribution to the work, and approved it for publication.

Funding

The research leading to these results has received funding from AIRC under Start-Up 2018—ID. 21651—EMDF.

Acknowledgments

The topic editors want to kindly thank all authors for their articles presented in this Research Topic.

Conflict of interest

The authors declare that the research was conducted in the absence of any commercial or financial relationships that could be construed as a potential conflict of interest.

Publisher's note

frontiers | Frontiers in Endocrinology

TYPE Original Research
PUBLISHED 30 November 2022
DOI 10.3389/fendo.2022.1042787

OPEN ACCESS

EDITED BY
Alain Couvineau,
Institut National de la Santé et de la Recherche Médicale (INSERM), France

REVIEWED BY
Birgit Leitinger,
Imperial College London, United Kingdom
Costin N Antonescu,
Toronto Metropolitan University, Canada

*CORRESPONDENCE
Ichiro N. Maruyama
ichi@oist.jp

†These authors have contributed equally to this work and share first authorship

SPECIALTY SECTION
This article was submitted to Molecular and Structural Endocrinology, a section of the journal Frontiers in Endocrinology

RECEIVED 13 September 2022
ACCEPTED 14 November 2022
PUBLISHED 30 November 2022

CITATION
Purba ER, Saita E-i, Akhouri RR, Öfverstedt L-G, Wilken G, Skoglund U and Maruyama IN (2022) Allosteric activation of preformed EGF receptor dimers by a single ligand binding event.
Front. Endocrinol. 13:1042787.
doi: 10.3389/fendo.2022.1042787

Allosteric activation of preformed EGF receptor dimers by a single ligand binding event

Endang R. Purba[1†], Ei-ichiro Saita[1†], Reetesh R. Akhouri[2], Lars-Goran Öfverstedt[2], Gunnar Wilken[2], Ulf Skoglund[2] and Ichiro N. Maruyama[1*]

[1]Information Processing Biology Unit, Okinawa Institute of Science and Technology Graduate University, Okinawa, Japan, [2]Cellular Structural Biology Unit, Okinawa Institute of Science and Technology Graduate University, Okinawa, Japan

Aberrant activation of the epidermal growth factor receptor (EGFR) by mutations has been implicated in a variety of human cancers. Elucidation of the structure of the full-length receptor is essential to understand the molecular mechanisms underlying its activation. Unlike previously anticipated, here, we report that purified full-length EGFR adopts a homodimeric form *in vitro* before and after ligand binding. Cryo-electron tomography analysis of the purified receptor also showed that the extracellular domains of the receptor dimer, which are conformationally flexible before activation, are stabilized by ligand binding. This conformational flexibility stabilization most likely accompanies rotation of the entire extracellular domain and the transmembrane domain, resulting in dissociation of the intracellular kinase dimer and, thus, rearranging it into an active form. Consistently, mutations of amino acid residues at the interface of the symmetric inactive kinase dimer spontaneously activate the receptor *in vivo*. Optical observation also indicated that binding of only one ligand activates the receptor dimer on the cell surface. Our results suggest how oncogenic mutations spontaneously activate the receptor and shed light on the development of novel cancer therapies.

KEYWORDS

cancer biology, conformational change, cooperativity, cryo-electron tomography, receptor tyrosine kinase, signal transduction, single-molecule biophysics, transmembrane signaling

Introduction

The human epidermal growth factor receptor (EGFR) family, a member of the receptor tyrosine kinase (RTK) superfamily, plays vital roles in various cellular processes, including cell survival, proliferation, differentiation, motility, and metabolism (1, 2). The EGFR signaling pathway is one of the most dysregulated pathways in many human cancers (3, 4). The EGFR family members, EGFR (also known as ErbB1 and HER1),

ErbB2/HER2/Neu, ErbB3/HER3 and ErbB4/HER4, are all synthesized as type-1 single-pass transmembrane proteins. Seven known ligands, such as epidermal growth factor (EGF) and transforming growth factor-α, activate EGFR, while neuregulins (NRGs) bind to ErbB3 and ErbB4 (5). ErbB2 is an orphan receptor, for which a peptide ligand has not been found, although it can be activated by mildly alkaline pH (6) or by forming heterodimers with other family members (7).

The EGFR protein, ~170 kDa in mass, consists of an extracellular ligand-binding domain, single transmembrane domain (TMD), intracellular juxtamembrane (JM) region, cytoplasmic tyrosine kinase domain (TKD), and C-terminal tail (Figure 1A) (8). Crystallographic studies of the isolated extracellular domain (ECD) and intracellular domain (ICD) of EGFR have provided insight into liganded and unliganded forms of the receptor. The ECD contains four subdomains (9–11). Subdomains I (also known as L1) and III (L2) have a β-helix solenoid structure and are responsible for ligand binding by simultaneously contacting the same ligand bound. Subdomains II (CR1) and IV (CR2) are cysteine-rich and interact with each other in the unliganded, tethered form. Ligand binding to subdomains I and III breaks this intramolecular contact for intermolecular association of two β-hairpins of subdomain II in its liganded, extended form. Crystal structures of symmetric and asymmetric TKD dimers have also been determined as the inactive and active forms of the receptor, respectively (12–16).

The traditional model of RTK activation is that a ligand binds to the monomeric receptor and induces receptor dimerization. This brings the intracellular TKDs into close proximity, resulting in kinase activation and phosphorylation of the receptor and its substrate tyrosine residues (17). This model was first proposed for the EGFR (18), and phosphotyrosines of the receptor interact with effector molecules, including the Src homology 2 domain-containing transforming protein-1 (Shc1) and growth factor receptor-bound protein-2 (Grb2) adapters, for downstream signaling (19–21). Consistent with this model, loose linkage between ligand binding and kinase activation of the receptor has been proposed (22). Furthermore, a nearly full-length EGFR protein was purified as a monomer, which upon ligand binding, became a dimer *in vitro* (23). When full-length EGFR was ectopically expressed at low levels in *Xenopus* oocytes, the receptor was predominantly monomeric in the absence of

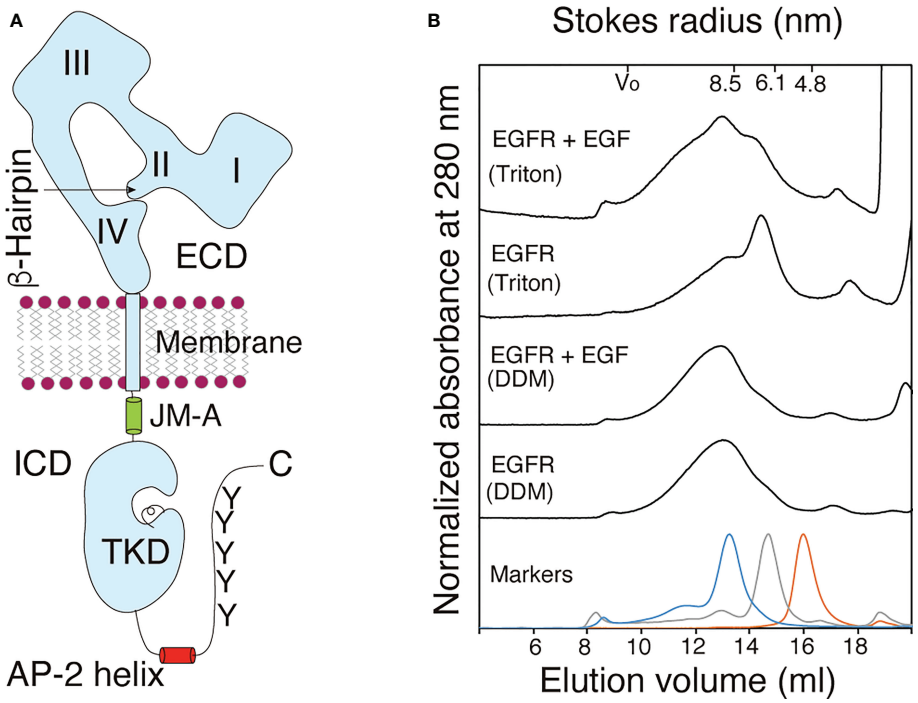

FIGURE 1
Purified EGFR adopts a dimeric structure before and after ligand binding. **(A)** Schematic representation of an EGFR monomer. The extracellular domain (ECD) of EGFR consists of the four subdomains I-IV. The β-hairpin of the subdomain II interact with the tethering arm of the subdomain IV for the receptor's closed (tethered) form. The intracellular domain (ICD) of the receptor comprises intracellular juxtamembrane (JM), the tyrosine kinase domain (TKD), AP-2 helix and tyrosine (Y) residues as major phosphorylation sites among others. Not drawn to scale. **(B)** Gel filtration chromatograms of purified full-length EGFR solubilized from the membrane by using 1.0% DDM (DDM) or 1.0% Triton X-100 (Triton) before (EGFR) and after (EGFR+EGF) ligand binding. Elution patterns of molecular mass markers are shown at the bottom. A representative of three chromatograms independently carried out.

ligand, and the addition of EGF generated dimers and oligomers (24).

Concave-up curvilinear Scatchard plots were first described for the interaction between EGF and its cell surface receptor (25, 26), and has traditionally been interpreted as heterologous, high-affinity and low-affinity, sites on the cell surface, which correspond to dimeric and monomeric receptors, respectively (27). However, Macdonald and Pike (28) have recently argued that the concave-up Scatchard plots arise from negative cooperative EGF binding to the preformed EGFR dimer, as previously predicted (29). Indeed, numerous biochemical and optical imaging studies have demonstrated that in the absence of bound ligand, EGFR adopts a dimeric, yet inactive, form at various levels on the cell surface, depending on methods and cell lines used for the analysis (30–37).

There are a number of oncogenic mutations that spontaneously activate EGFR in the absence of bound ligands (38–40). Among such mutations, deletion mutations in the receptor's ICD were found. EGFRvIVa lacks three exons 25-27, resulting in a C-terminal deletion of residues 959-1066 (41–43). EGFRvIVb lacks two exons 25 and 26, resulting in a C-terminal deletion of residues 959-1030 (41–43). These tumorigenic mutations suggest that EGFR is actively inhibited prior to ligand binding (44, 45). However, the ligand-induced dimerization model does not explain the tumorigenic activity of these EGFR mutants.

In the present study, we analyzed the structures of full-length EGFR in the absence and presence of a bound ligand. When purified EGFR was analyzed by gel filtration chromatography, it behaved as a dimer before and after activation upon ligand binding. Cryo-electron tomography (Cryo-ET) analysis of the purified, full-length receptor also showed dimeric unliganded and liganded receptors, the latter of which showed a relatively stable ECD structure with a bound ligand. Consistent with these *in vitro* results, artificial mutations of amino acid residues at the interface of the symmetric inactive kinase dimer spontaneously activate the receptor *in vivo*. Optical observation also showed that binding of only one ligand activates the receptor dimer on the cell surface. Furthermore, ligand-induced phosphorylation was essential for dimerization and oligomerization of the receptor dimers.

Results

EGFR adopts a dimeric structure *in vitro*

Full-length human EGFR tagged with eight histidine residues (His tag) at its C-terminus was expressed in human embryonic kidney HEK293T cells and was purified by nickel chelating Sepharose column chromatography after solubilization with 1.0% (w/v) n-dodecyl-β-D-maltoside (DDM) (Supplementary Figure S1). The purified full-length EGFR was observed to be phosphorylated at the basal level when analyzed by immunostaining with an anti-phosphotyrosine antibody. Upon stimulation with its ligand, epidermal growth factor (EGF), autophosphorylation of full-length EGFR was enhanced markedly *in vitro* in the presence of ATP (Supplementary Figure S2), indicating that the purified receptor molecules are functional.

When analyzed by gel filtration chromatography, the full-length receptor molecules solubilized with DDM were eluted as a symmetric peak with an average Stokes radius (± SD) of 9.05 ± 0.34 nm or 9.01 ± 0.46 nm before or after incubation with EGF, respectively (Figure 1B). In contrast, full-length EGFR receptor molecules solubilized with 1.0% Triton X-100 were eluted as two peaks with the Stokes radii of 6.96 ± 1.03 nm and 8.95 ± 0.73 nm (Figure 1B). The lower molecular mass peak shifted to the position of the higher peak after incubation with EGF, indicating that monomeric EGFR became a dimer upon ligand binding. These results indicated that the full-length EGFR molecules with and without bound EGF adopt homodimeric structures when solubilized with 1.0% DDM. When solubilized with 1.0% Triton X-100, in contrast, a large fraction of the full-length EGFR adopted a monomeric structure, which upon EGF binding, became dimeric. When an EGFR mutant that lacks its C-terminal tail was solubilized with 0.2% Triton X-100, the mutant receptor was completely monomeric (46), indicating that the C-terminal tail stabilizes its dimeric structure. The longer hydrophobic tail and/or smaller hydrophilic headgroup of Triton X-100 than DDM may destabilize the receptor's dimeric structure. To exclude the possibility that the His tag contributes to the formation of the dimeric structure, the tag was cleaved from the full-length EGFR by digestion with tobacco etch virus (TEV) endopeptidase (Supplementary Figure S3). The Stokes radius of the cleaved EGFR was similar to that of the full-length EGFR with the His tag, indicating that the tag does not contribute to dimer formation. These results show that prior to ligand binding, full-length EGFR has a homodimeric structure and that the receptor dimer can be activated by ligand binding without changing its dimeric form.

3D density maps of purified EGFR

We collected 18 and 15 tomograms by cryo-electron tomography (Cryo-ET) of the purified full-length EGFR without and with bound EGF, respectively (Supplementary Table S1). Cryo-ET is more sensitive than single particle cryo-electron microscopy to detect various conformers of EGFR before and after ligand binding. After refinement using the constrained maximum entropy tomography (COMET) software package (47), final three-dimensional (3D) "density maps" of the proteins were calculated from forward-scattered electrons at 300 kV. Within these tomograms (Supplementary Figure S4), the MINER program of the package was used to extract subtomograms. We reconstructed 474 molecules of full-

length unliganded EGFR from the 18 tomograms. The CORRPAIR program was applied to produce correlation matrices between pairs of all the subtomograms and to classify the 474 subtomograms into 25 clusters (Supplementary Figure S5). Using the CORRAVE program, subtomograms of each cluster were averaged to represent the respective cluster (Figure 2A). From the 15 tomograms, we also reconstructed 557 liganded EGFR molecules activated by EGF binding, which were classified into 25 clusters (Supplementary Figure S6). Subtomograms of each cluster were averaged, as shown in Figure 2B.

The 25 averaged density maps of unliganded or liganded EGFRs were analyzed by determining the principal axis of minimum moment of inertia and the molecular center of mass. The mean volumes of slices of both the unliganded and liganded receptors along the principal axis showed two peaks, one of which was larger than the other (Figure 2C). Based on the crystal structures of EGFR ECD and ICD, the results indicated

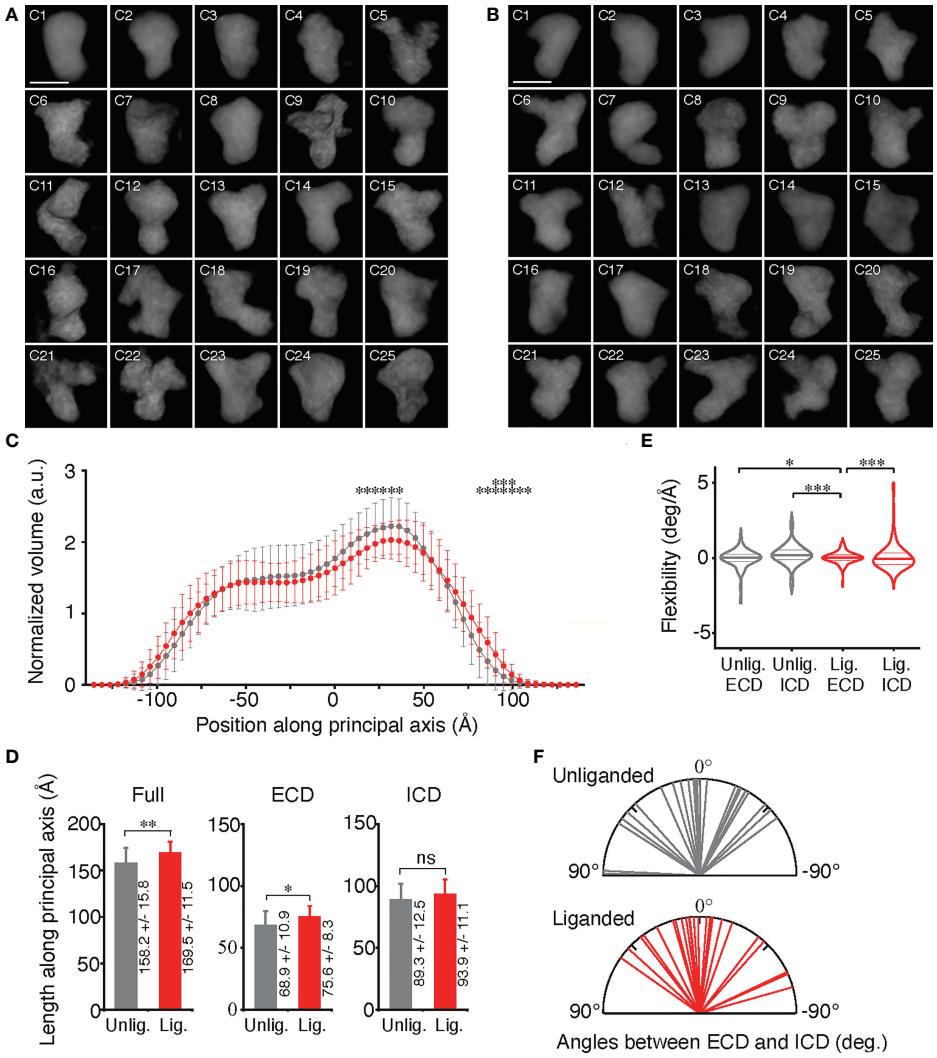

FIGURE 2
Conformational variables of EGFR before and after activation. **(A, B)** Averaged electron density maps of 25 subtomogram clusters of unliganded and liganded EGFRs, respectively. **(C)** Plots of averaged volumes of unliganded (gray) and liganded (red) EGFRs along the principal axis with distances from the molecular center of mass. Data points are mean ± SD. Two-sided Student's *t*-test in the range between -140Å and 75Å or Mann-Whitney U test in the range over 80Å along the principal axis (*$p < 0.05$, **$p < 0.01$). **(D)** Long-axis lenghts of ECD and ICD of unliganded and liganded EGFRs were measured as shown in Supplementary Figure S8A. Data points are mean ± SD. Two-sided Student's *t*-test. ns, not significant. **(E)** Flexibility of ECD and ICD of unliganded and liganded EGFRs, which was measured as shown in Supplementary Figure S8B. Lines in the violin plots show 25th, 50th and 75th percentile values. Asterisks indicate that variances are significantly different (Levene's test; *$p < 0.05$, ***$p < 0.001$). **(F)** Angles between long axes of ECD and ICD of unliganded and liganded EGFRs, which were measured as described in Supplementary Figure S8A.

that the large and small peaks correspond to ECD and ICD dimers, respectively, which are separated by the TMDs (Supplementary Figure S7). Furthermore, full lengths and ECD lengths of the liganded receptors were significantly longer than those of the unliganded receptors (Figure 2D), suggesting that a fraction of the unliganded ECD may take a tethered structure through the interaction of the subdomains II and IV, whereas liganded EGFR ECD may have an extended structure (9–11).

When the flexibility of ECD and ICD of unliganded and liganded EGFRs was examined (Supplementary Figures S8A, B), it was observed that the ECD dimer was significantly stabilized by ligand binding and had the most rigid structure (Figure 2E). Angles between the long axes, which are perpendicular to the principal axis of minimum moment of inertia, of ICD and ECD of the unliganded EGFRs were variable and ranged from 89° (clockwise) to −54° (counterclockwise) when observing the molecules extracellularly (Figure 2F; Supplementary Figures S9D, E). Similarly, angles between the long axes of ICD and ECD of the liganded EGFRs also ranged from 55° to −74°. These rotation angle variabilities were not significantly different between the unliganded and liganded receptors, indicating that the receptor dimers twist flexibly perpendicular to the principal axis before and after ligand binding.

Conformational flexibility transition

Density maps from the 3D reconstruction were sufficient for defining ECD and ICD and their conformational changes, as described above. Using CHIMERA software (48), crystal structures of EGFR domains were manually docked into the envelope of each averaged subtomogram of 25 unliganded and 25 liganded receptor clusters (Figure 3). Crystal structures of the tethered (PDB ID: 1NQL) or extended (half of 3NJP) ECD monomer were docked into the envelope of unliganded receptors. The ECD dimer (3NJP) was docked into the envelope of liganded EGFRs. The crystal structure (3GT8) of a symmetric inactive TKD dimer and the NMR structure (2M0B) of inactive TMDs were docked into the envelope of unliganded EGFRs (Figure 3A), whereas the crystal structure (2GS6) of the asymmetric active TKD dimer and the NMR structure (2M20) of active TMDs were docked into the envelopes of liganded receptors (Figure 3B).

Then, the 25 docked crystal structures of unliganded or liganded receptors were manually aligned to each other along two principal axes of minimum and maximum moments of inertia and the molecular center of mass (Figures 3C, D). These alignments show that both ECD and ICD dimers of unliganded and liganded EGFR dimers have flexible structures, which are likely to correspond to large rotation angles between ECD and ICD of the averaged density maps, as shown in Figure 2F. The spontaneous structural transition of unliganded receptor ECD from tethered to extended is also likely to contribute to the flexibility of the domain (49, 50). Such a spontaneous transition was predicted in the wild-type receptor by molecular dynamics analysis (51). Furthermore, an NMR study of EGFR in native membranes has also shown that ECD of the unliganded receptor is highly dynamic, while ICD is rigid (52). This relative stability of ICD is consistent with its role in the formation of the unliganded receptor dimer, as described below. In contrast, ECD dimers of the liganded receptor showed the most rigid structures among other domains of unliganded and liganded receptors (Figure 2E), consistent with the previous small angle X-ray scattering study of the ECD (50). Although our flexibility analysis (Figure 2E) did not detect statistically significant flexibility transition in the ICDs of the EGFR dimer, it may also be true that the ICDs become flexible upon ligand binding (compare Figures 3C, D). Upon ligand binding, therefore, conformational flexibility transition occurs in ECDs of the EGFR dimer from a flexible to rigid structure, and flexibility transition may also occur in ICDs of the receptor dimer from a rigid to flexible structure.

Role of ICD in preformed dimers *in vivo*

As described above, our structural analysis of the solubilized EGFR with DDM showed that the receptor is dimeric *in vitro*. Therefore, we also examined whether EGFR adopts a homodimeric form *in vivo*. Full-length EGFR was expressed in modified HeLa cells that did not express any of the four EGFR family members on the cell surface to prevent heterodimerization with endogenous receptors (Supplementary Figures S10A-C). A structural study indicates that a symmetric inactive TKD dimer is stabilized by the AP-2 helices, which interact with the interfaces of two protomers of the dimer (16) (Figures 1A and 4A). The "electrostatic hook", which consists of acidic residues in the turn after the AP-2 helix, also forms ion pairs with residues in the other subunit. When we mutated Phe-973 and Leu-977 of the AP-2 helix, which forms hydrophobic interactions with residues of the other protomer, to hydrophilic arginine residues, the mutant receptor was spontaneously autophosphorylated in the absence of bound ligand (Figures 4B, C). When negatively charged Glu-981 and Asp-982 of the "electrostatic hook" were mutated to positively charged arginine and lysine residues, respectively, the mutant receptor was also spontaneously activated. Consistently, a substitution of four negatively charged amino acid residues in the "electrostatic hook" makes the mutant receptor spontaneously active (53). These results indicate that the mutations destabilize the kinase dimer for spontaneous activation, suggesting that the C-terminal tail encompassing the AP-2 helix and "electrostatic hook" plays a major role in the formation of unliganded dimers (32, 37).

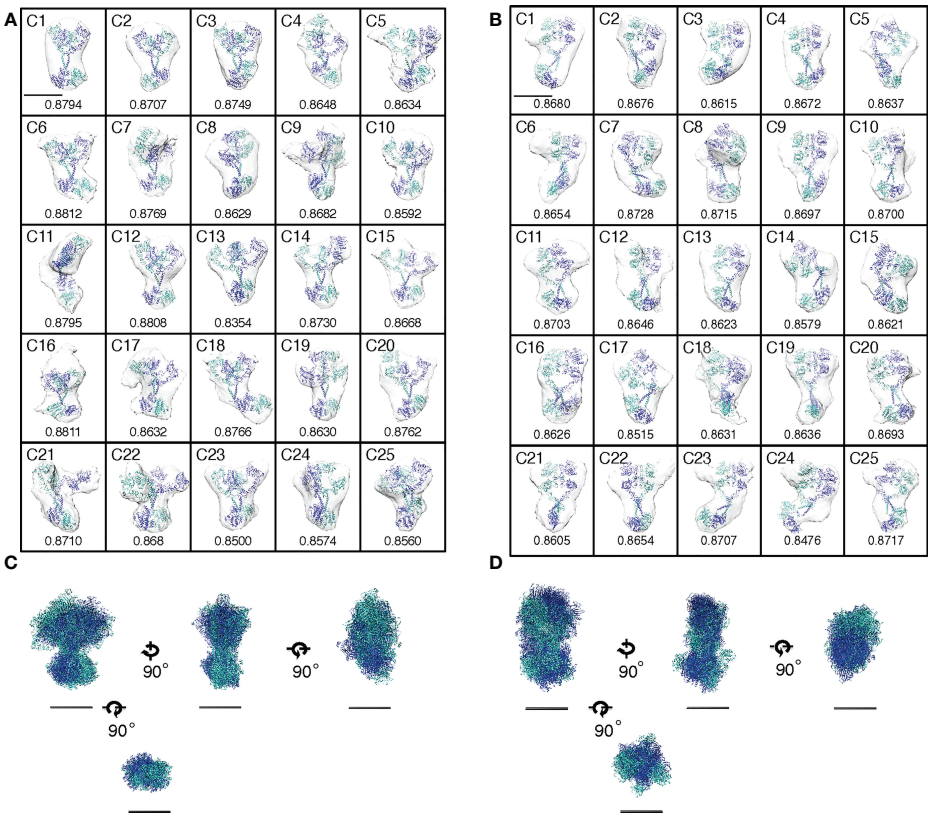

FIGURE 3
Activation of EGFR dimers by conformational flexibility transition or by mutations. **(A, B)** Envelopes of averaged density maps of unliganded and liganded EGFRs, respectively, were docked with crystal and NMR structures. Cross-correlation coefficients between the averaged density maps and the crystal/NMR structures are shown below each map. Scale bar, 10 nm. **(C, D)** Alignments of crystal and NMR structures docked into the averaged density maps of unliganded or liganded EGFR, respectively, along two principal axes of minimum and maximum moments of inertia and the molecular center of mass. Four orthogonal views are shown, but ECDs are removed from bottom views for clarity. Scale bar, 10 nm.

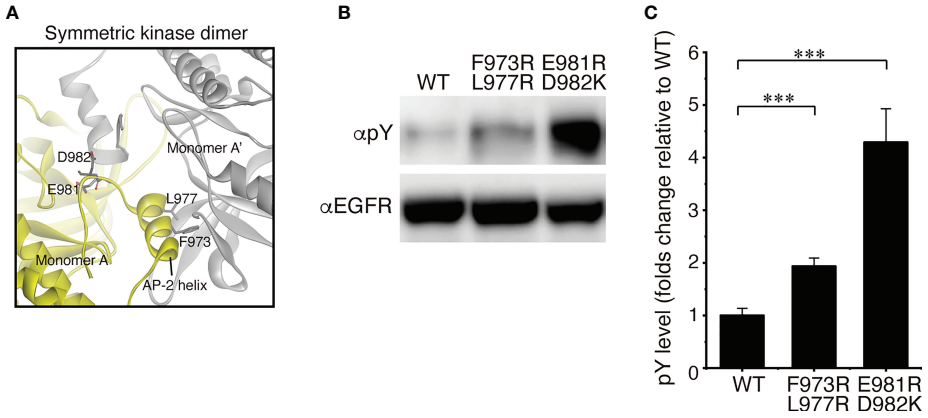

FIGURE 4
EGFR mutations that spontaneously activate the receptor. **(A)** Crystal interface between protomers of symmetricTKD dimer, each of which is shown in gray or yellow. **(B)** Western blots of wild-type EGFR and two mutants with two amino acid substitutions. **(C)** Summary of five independent Western blots. Data points are means ± SEM. Two-sided Student's *t*-test (***$p < 0.001$).

Single ligand activates EGFR *in vivo*

The homodimeric structure of EGFR described above is contradict with the ligand-induced dimerization model proposed for the activation of EGFR. The model predicts that a ligand binds to the monomeric receptor and induces receptor dimerization (18). Using the highly inclined and laminated optical sheet (HILO) illumination (54), therefore, we tried to optically observe the EGFR activation on the top surface of living cells in real time. Full-length human EGFR was expressed exogenously in the modified HeLa cells (Supplementary Figure S10) that do not express any of the four EGFR family members on the cell surface to prevent spontaneous heterodimerization (37). To monitor the activation of the receptor by ligand binding *in vivo*, we also expressed the Shc1 adaptor protein fused with GFP (GFP-Shc1) in the modified HeLa cell, which upon the receptor phosphorylation, is recruited to the cell surface by interacting with the receptor's phosphortyrosine residues. When two fluorescently labeled EGF molecules, 0.1 nM (~0.6 ng/ml) each of Alexa555-EGF and Alexa647-EGF at a final concentration, were simultaneously incubated with the cell culture, the number of EGF fluorescence spots (red or purple) was gradually increased during the incubation time (Figures 5A, B). Each spot seems to initially represent a single EGF molecule since the spot appeared in a single step within a few video frames (Supplementary Video S1). To support this, furthermore, colocalization of Alexa555-EGF (red) and Alexa647-EGF (purple) spots could not be detected at the beginning of the incubation (Figures 5A, B).

The number of EGF fluorescence spots was more than twice of that of GFP-Shc1. This suggests the following two possibilities: (1) EGF binding does not always activate the EGFR molecule. (2) A significant amount of endogenous, unlabeled Shc1 interacts with activated EGFR and prevent GFP-Shc1 binding to the activated receptor. The number of GFP-Shc1 (green) was always larger than that of colocalization (light blue) of GFP-Shc1 and either Alexa555- or Alexa647-EGF, suggesting that the fluorescently labeled EGF solution contains unlabeled and/or photo-bleached EGF molecules. Colocalization of GFP-Shc1 and Alexa555- or Alexa647-EGF spots (light blue in Figures 5A, B) was much faster than that of Alexa555- and Alexa647-EGF spots (pink) or of GFP-Shc1 and Alexa555- and Alexa647-EGF spots (gray) (Figures 5A, B). Similar results were obtained by expressing Grb2 fused with GFP (Grb2-GFP) in the modified HeLa cell (Supplementary Figures S11B, C). When colocalization of GFP-Shc1 (green) and either Alexa555- or Alexa647-EGF (light blue) or of Alexa555- and Alexa647-EGF (gray) was analyzed (Figure 5C), only Alexa555- or Alexa647-EGF initially colocalized with GFP-Shc1, followed by colocalization of GFP-Shc1 and Alexa555- and Alexa647-EGF at later stages. Furthermore, the majority of activated EGFR molecules interacts with single EGF molecules (Figure 5C).

Interestingly, colocalization of Alexa555- and Alexa647-EGF spots and of GFP-Shc1 and Alexa555- and Alexa647-EGF spots was not observed when kinase-dead EGFR was expressed on the cell surface (Figure 5D), or the kinase was inhibited by a specific inhibitor (Supplementary Figures S11D, E). These results indicate that singly liganded EGFR autophosphorylates the receptor without interacting with another singly liganded receptor. This is inconsistent with the ligand-induced dimerization model, where two liganded monomers interact with each other to autophosphorylate in *trans*. Therefore, the simplest explanation of the results is that the colocalization of Alexa555- and Alexa647-EGF or of GFP-Shc1 and Alexa555- and Alexa647-EGF spots is due to dimerization and oligomerization of a single-ligand-bound EGFR dimer after single ligand-induced autophosphorylation of the receptor dimer (37, 55). This is consistent with the homodimeric structure of DDM-solubilized EGFR *in vitro* as described above. These results indicate that binding of only one EGF molecule induces autophosphorylation of the receptor dimer and recruits Shc1 to the phosphorylated receptor on the cell surface.

Discussion

The present study shows that, unlike previously observed (18), detergent-solubilized full-length EGFR adopts a dimeric form before and after the receptor activation *in vitro*, when analyzed by gel filtration chromatography and cryo-ET. The dimeric form of the receptor *in vivo* is also supported by site-directed mutagenesis of amino acid residues involved in interaction between two protomers and by optical observation of ligand binding to its cell surface receptor. Like other RTKs (56, 57), these results indicate that most, if not all, of EGFR molecules adopt a dimeric form. Indeed, single-wave fluorescence cross-correlation spectroscopy analysis of fluorescent protein-labeled EGFR and ErbB2 expressed in Chinese hamster ovary cells shows that most, if not all, EGFR and ErbB2 adopt preformed homodimers and heterodimers *in vivo*, irrespective of the expression levels (35). Recent structural studies on the EGFR family members using cryo-electron microscopy demonstrate that the receptor complexes with its ligand in detergent micelles or lipid nanodiscs look very similar (58, 59), although unliganded receptor molecules have not been analyzed.

Based on analyses of the crystal structure and disulfide cross-linking of EGFR, in contrast, loose linkage between ligand binding and the activation of the receptor kinase has been proposed (22). When EGFR mutants with cysteine substitutions in the extracellular JM and TMD were studied, disulfide cross-linking of the receptor was observed only in the presence of EGF (22). In the absence of EGF, however, the spontaneously cross-linked

10.3389/fendo.2022.1042787

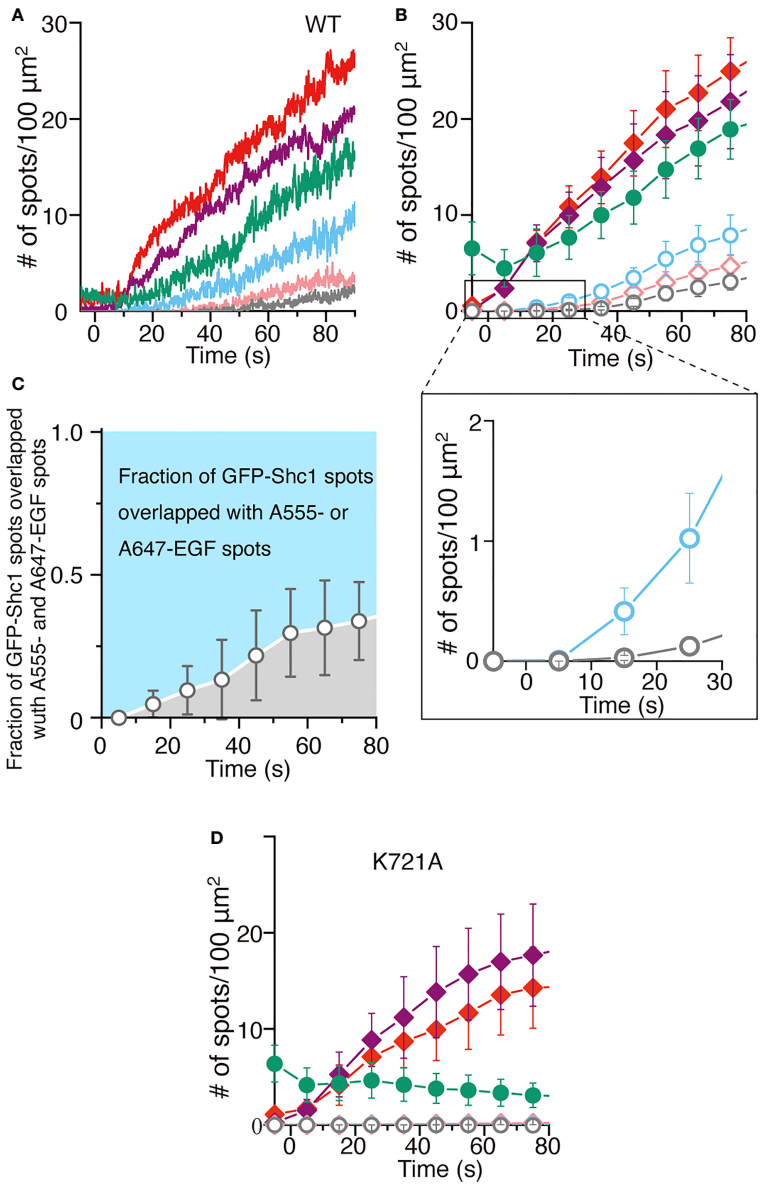

FIGURE 5
Single ligand binding activates EGFR dimers. **(A)** Time courses of the number of spots of Alexa555-labeled EGF (red), Alexa647-labeled EGF (purple) or GFP-Shc1 (green) appeared on the surface of modified HeLa cells exogenously expressing EGFR. Colocalization of GFP-Shc1 and either Alexa555-EGF or Alexa647-EGF, of Alexa555-EGF and Alexa647-EGF, or of all the three is shown in light blue, pink and gray, respectively. The fluorescently labeled EGF molecules, 0.1 nM each at a final concentration, were incubated with cells expressing EGFR. **(B)** Same as in **(A)**. Data points are means ± SEM (n=4). **(C)** The fraction of GFP-Shc1 spots overlapped with both Alexa555- and Alexa647- or Alexa-647-EGF spots. **(D)** Time courses of the number of fluorescent spots as in **(A)**, which appeared on the surface of cells exogenously expressing kinase-dead (k721A) EGFR. Data points are means ± SEM (*n*=4).

receptors through a cysteine disulfide bridge could be autophosphorylated to some extents, endocytosed and degraded. To observe cross-linking of the receptors in the absence of bound ligand, therefore, endocytosis of the receptor should be prevented as previously demonstrated (30). Furthermore, the insertion of 20-40 amino acid residues into the extracellular linker region abolished the receptor capacity to bind ligand and caused autophosphorylation of the receptor in the absence of ligand (60, 61). These results indicate a significant functional linkage between the ECD and ICD through TMD in the wild-type receptor.

When EGFR was expressed at low levels,< 5 molecules per μm^2, in *Xenopus* oocytes, the receptor was predominantly monomeric in the absence of ligand (24). This claim was

based on photobleaching of stable EGFR spots in position and counted the number of steps until fluorescence intensities disappear. After incubation with 2 μM EGF for 1-2 min, however, more than 25% of spots were still photobleached with a single step. This result indicates that a significant fraction of the spots with single-step photobleaching contains dark spots due to incomplete maturation of the fluorophore. This incomplete maturation is particularly true at low temperatures, such as 18°C required for the cultivation of *Xenopus* oocytes (62). The number of dark spots is likely to be underestimated, and dimers and even oligomers might be counted as monomers.

Numerous studies have demonstrated that in the absence of bound ligand, ~40-100% EGFR molecules adopt a preformed dimeric structure, depending upon methods and cell lines used for the analyses (30, 32–37, 63). Considering inefficient fluorescent protein folding and chemical crosslinking (64, 65), the fraction of the receptor dimer is likely to be, if at all, underestimated. The inactive dimer or predimer fraction, ~40%, of total EGFR molecules expressed in NIH 3T3 cells (66) is also underestimated since the EGFR molecules form heterodimers with ErbB2 endogenously expressed in NIH 3T3 cells (37, 67). Reversible firefly luciferase enzyme fragment complementation assays show that prior to ligand binding, most, if not all, EGFR molecules adopt a preformed dimeric form (68). While EGF binding augmented luciferase activity due to dimerization of an ICD-deleted EGFR, the luciferase activity of the full-length EGFR decreased presumably due to a conformational change of the preformed dimer of the receptor (68). Reversible luciferase complementation assay also indicates that other RTKs, such as TrkA and TrkB (56, 57), adopt a preformed dimeric structure.

Prior to ligand binding, therefore, it now appears that most, if not all, of EGFR molecules adopt a preformed dimeric structure *in vitro* and *in vivo* through the interaction of the receptor ICDs, in which the AP-2 helix and "electrostatic hook" play crucial roles, as shown in the present study. The TKD (12, 14, 16), TMD (69) and extracellular subdomains II and IV (11) also seem to contribute to the formation of the unliganded dimer. All the EGFR family members spontaneously form homodimers and heterodimers in endoplasmic reticulum (ER) before reaching the cell surface (37), as observed in other RTKs (56, 57, 70, 71). The dimer spontaneously formed in ER, which is not dependent on the expression levels of the receptor (35, 55), is stable and does not dissociate. The preformed dimeric structure of EGFR may also ensure its inactive form prior to ligand binding. Random collision of monomeric EGFR molecules on the cell surface could spontaneously activate the receptor and would be harmful to the cell. EGFR activation modeling predicts that the activation of the preformed dimers would be 100-fold faster than that of the monomers (34).

The present study indicates that dimerization (tetramerization) and oligomerization of the receptor dimer occur after phosphorylation of the receptor upon ligand binding (Figure 5C; Supplementary Figures S11D, E), as previously observed (37). Consistently, homo-FRET analysis by Hofman et al. (55) also demonstrated that EGF binding did not cause dimerization or oligomerization of the receptor at detectable levels *in vivo*, when a kinase-dead (K721A) EGFR mutant or an EGFR mutant where nine tyrosine residues as major phosphorylation sites were replaced with phenylalanine. Therefore, tetramerization and oligomerization of EGFR previously observed (33) occurs after phosphorylation of the receptor upon ligand binding.

The present study also shows that only a single ligand binding event activates EGFR *in vivo*. Liu et al. (72) also reported the similar result based on Western blot analysis of co-expressed mutant EGFRs, kinase-deficient receptor and ligand-binding-deficient one that functioned as a receiver/acceptor kinase. These results are consistent with the preformed dimeric structure of EGFR and negative cooperative binding of ligand to EGFR, which is seen when the binding of a ligand to the first site on a dimer reduces ligand affinity for the second site on the dimer. Indeed, Alvarado et al. (73) determined two crystal structures of *Drosophila* EGFR extracellular domain dimers without bound ligand and with a single bound ligand as a symmetric unliganded dimer and an asymmetric, single-liganded dimer, respectively. The authors propose that a single ligand binding event to the unliganded symmetric dimer with two identical binding sites induces conformational changes that promote asymmetry in the dimer and constrains the second binding site to reduce its affinity for ligand. The receptor dimer with negative cooperative ligand binding is more sensitive to ligand at low concentrations than the monomeric receptor.

It has been shown that the C-terminal tail inhibits self-autophosphorylation by the TKD, suggesting that self-autophosphorylation of the C-terminal tail is likely a mechanism for removing inhibitory constrains on enzyme activity (74, 75). Indeed, the mutations in the AP-2 helix and the "electrostatic hook" in the present study are likely to dissociate the symmetric inactive ICD dimer, resulting in spontaneous activation of the receptor (Figures 4B, C). EGFR mutants with C-terminal deletions, EGFRvIVa and EGFRvVIb, have been found in human glioblastoma multiforme (41–43). These two mutants have transforming and tumorigenic properties and show ligand-independent constitutive activation. EGFRvV has the C-terminal truncation from Gly-959 and exhibits increased ligand-dependent kinase activity (41, 42). The oncogenic function of these mutants depends on their intrinsic kinase activity, and the proximal region of the C-terminal tail (residues 959 to 1030) participates in autoinhibitory interactions (45, 76). This proximal region contains the AP-2 helix and the "electrostatic hook", which play roles in the formation of symmetric inactive TKD dimer.

Therefore, the autoinhibitory function of the C-terminal tail is likely to stabilize the symmetric inactive TKD dimer. It has also been proposed that residues Tyr-992 to Leu-1014 make specific docking interactions in *cis* with the C-lobe of the activator/doner TKD and thus contribute to autoinhibition (76).

It has recently been proposed that ligand binding to the ECD of EGFR induces the conformational change of the ICD in monomeric EGFR (77). Unfortunately, however, the authors did not experimentally analyze whether the EGFR synthesized *in vitro* is monomeric or dimeric. The receptor seems to be dimeric since it was phosphorylated in the absence of bound ligand.

Materials and methods

Plasmid construction

A DNA fragment coding for full-length human EGFR was amplified from the plasmid pNUT/EGFR (30) as a template by PCR using a forward primer, 5'-GGGCTAGCATGCGACCCTCCGGGACG, in which the *Nhe* I site is underlined, and a reverse primer, 5'-GGCTCGAGTCATGCTCCAATAAATTCACTGCTTTG with the *Xho* I site underlined. The resulting PCR product was cloned between the *Nhe* I and *Xho* I sites of a pIRES2-ZsGreen1-Thr-His8 expression vector, a derivate of pIRES2-ZsGreen1 (Clontech) with a thrombin digestion site, LVPRGS, before the His tag. The thrombin digestion site was then replaced with a TEV protease digestion site, ENLYFQG, by inserting an In-Fusion fragment prepared with two pairs of PCR primers, 5'-CGTCAGATCCGCTAGCATGCGACCCTCCGGGA/3'-CTGGAAATAGAGGTTCTCTCCGTTTGTTGCTCCAATAAATTCACT and 5'- GAGAACCTCTATTTCCAGGGATCGGATCCGCACCATCACCACCATCACCATCAC/3'-GTTAACAACAACAATTGCATTCATTTTATGTTTCAGGTTCAGGGGGAGGTGTGGG, where the *Nhe* I and *Mfe* I restriction enzyme sites are underlined and In-Fusion sites are underlined with dots in bold, using an In-Fusion cloning kit (Takara Bio, Shiga, Japan). After digesting with *Nhe* I and *Mfe* I, the resulting fragment was replaced with the *Nhe* I-*Mfe* I fragment of pIRES2-ZsGreen1-Thr-His8, resulting in pIRES2-ZsGreen1-EGFR-TEV-His8.

cDNA encoding human Shc1was amplified by PCR from pcDNA3.1His p66Shc1 (Plasmid #32574; addgene), with a pair of oligonucleotide primers, 5'- CACCAAGCTTATGAACAAGCTGAGTGGAGGCG and 5'- AACCGCGGCAGTTTCCGCTCCACAGGTTGC, wherein the *Hin*dIII and *Sac* II sites are underlined, respectively. The resulting PCR product was cloned into a pAcGFP1-N1 vector (#632469; Clontech) digested with restriction enzymes *Hin*dIII and *Sac* II to make pAC-N1-GFP-Shc1, in which Shc1 was fused to the C-terminus of AcGFP1. To generate pAc-Grb2-GFP, human *GRB2* cDNA was amplified by PCR using a pair of oligonucleotide primers, 5'-CACCAAGCTTATGGAAGCCATCGCCAAATATG (forward) and 5'- AACCGCGGGACGTTCCGGTTCACGGGGGTG (reverse), from a cDNA library of HEK293T cells and then cloned into pAcGFP1-N1 in which human GRB2 was fused to the N-terminus of AcGFP1. To construct pIRES2-EGFR-GFP-Shc1, a cDNA fragment encoding full-length *EGFR* was amplified from pNUT-EGFR (30), and AcGFP1 fused Shc1 fragment was amplified from pAC-N1-GFP-Shc1. The amplified cDNAs encoding *EGFR* and *AcGFP1-Shc1* were transferred to upstream and downstream of the internal ribosome entry site (IRES) sequence of pIRES2-ZsGreen (Clontech), respectively. To construct pIRES2-EGFR-Grb2-AcGFP1, a DNA fragment encoding *Grb2-AcGFP1* was amplified from pAc-Grb2-AcGFP1 and then replaced the AcGFP1-Shc1fragment of IRES of pIRES2-EGFR-AcGFP1-Shc1. Similarly, full-length ErbB4 was amplified by PCR from pBiFC-ErbB4-JMa-VN (37), using a pair of oligonucleotide primers, 5'-CGTCAGATCCGCTAGCATGAAGCCGGCGACAGGACTTTG and 5'-GAAGCTTGAGCTCGAGTCACACCACAGTATTCCGG. Using In-Fusion, the resulting PCR product was inserted into pIRES2-EGFR-Grb2-AcGFP1 after removing its EGFR fragment by digesting with *Nhe* I and *Xho* I.

To construct pcDNA3.1-EGFR, full-length *EGFR* was amplified from pIRES2-EGFR-AcGFP1-Shc1 and transferred to pcDNA3.1 (Invitrogen). Two double mutations, F973R/L977R and E981R/D982K, were introduced to pcDNA3.1-EGFR by In-Fusion using oligonucleotide primers encoding the mutations, 5'-CCAACCGGTACCGTGCCCGGATGGATGAAG/5'-CACGGTACCGGTTGGAGTCTGTAG and 5'-GATGAACGAAAGATGGACGACGTGGTGGATGCCGAC/5'-CATCTTTCGTTCATCCATCAGGGCACGGTAGAAGTT, wherein the mutation sites are underlined, respectively. To construct pIRES2-EGFR(K721A)-AcGFP1-Shc1, a mutation, K721A, was introduced to pIRES2-EGFR-AcGFP1-Shc1 by In-Fusion using oligonucleotide primers, 5'-CGCTATCGCAGAATTAAGAGAAGCAAC and 5'-AATTCTGCGATAGCGACGGGAATTTTAAC, in which the mutation sites are underlined.

Protein expression and purification

Full-length EGFR was expressed by transforming HEK293T cells (American Type Culture Collection) in a 15-cm Petri dish with a mixture of 20 μg pIRES2-ZsGreen1-EGFR-TEV-His8 and polyethylenimine (PEI; Polysciences, Warrington, PA) at a 1:3 (w/w) ratio of DNA to PEI. HEK293T cells were cultured in Dulbecco's modified Eagle medium (DMEM; Gibco) supplemented with 10% (v/v) fetal bovine serum (FBS; Invitrogen) and 2 mM glutamine. This culture medium was replaced with FBS-free DMEM, 5 h prior to transformation. Cells derived from 24 dishes (15 cm in diameter) were harvested 48 h after the transformation and washed once with PBS (pH 7.4). Approximately 9×10^8 cells freshly harvested, or cells

stored at -80°C were incubated for 3 h in 20 ml of bursting buffer, consisting of 20 mM HEPES (pH 7.4), 0.1 mM EDTA, 0.1 mM EGTA, 5.0 mM $MnCl_2$, and an EDTA-free protease inhibitor cocktail (1.0×; Nacalai Tesque, Kyoto, Japan). Cells were disrupted with a Dounce homogenizer on ice and centrifuged at 50,000 ×*g* in a micro ultracentrifuge (model CS150GXL; Hitachi Koki, Tokyo, Japan) for 30 min at 4°C. Pellets were suspended in 20 ml of solubilization buffer, consisting of bursting buffer supplemented with 1.0% (w/v) DDM (Thermo Fisher Scientific) or 1.0% (w/v) Triton X-100 (Nacalai Tesque) for 3 h and were cleared by centrifugation at 150,000 ×*g* for 30 min at 4°C. The supernatant was then mixed with 1.0 ml of Ni Sepharose resin (GE Healthcare), which was equilibrated with solubilization buffer, on an orbital shaker for 1.0 h in a cold room. The suspension was then collected in a Poly-Prep affinity chromatography column (9 cm in height, 10 ml reservoir volume, and 2 ml bed volume; Bio-Rad) by gravity and washed with 20-times bed volume of washing buffer (20 mM Tris-HCl, pH 8.0; 400 mM NaCl; and 0.01% DDM) supplemented with 20 mM imidazole. The column was then washed with the same volume of washing buffer supplemented with 30 mM imidazole, followed by washing with the same volume of washing buffer supplemented with 40 mM imidazole. EGFR was eluted with five-times the bed volume of washing buffer supplemented with 250 mM imidazole, and the eluate was fractionated into five fractions of 1.0 ml each. To determine fractions containing EGFR, 15 µl of each fraction was analyzed by PAGE using precast 10% Extra PAGE gels (Nacalai Tesque). Collected fractions, which contained 2-4 µM EGFR (~1.5 ml in total), were dialyzed overnight against 1.0 liter of dialysis buffer (20 mM Tris-HCl, pH 8.0; 200 mM NaCl; and 0.01% DDM).

Purified full-length EGFR, 15 µl, was mixed with the same volume of 2 x Laemmli sample buffer (Bio-Rad) containing 5% (v/v) β-mercaptoethanol and then heated at 95°C for 5 min. The samples were separated by using precast 10% Extra PAGE gel with running buffer (25 mM Tris-HCl, pH 8.6; 192 mM glycine; 0.1% (w/v) SDS) at room temperature. Proteins on the gel were fixed in solution [40% (v/v) methanol and 10% (v/v) acetic acid in water] for 15 min at room temperature and then stained with 0.25% (w/v) Coomassie Brilliant Blue G-250 (Nacalai Tesque) in acidic methanol [45% (v/v) methanol and 10% (v/v) acetic acid in water] for 30 min at room temperature. The gel was destained with aqueous 10% (v/v) acetic acid until visible bands appeared.

Gel electrophoresis and phosphorylation assay

In PAGE analysis (Supplementary Figure S1), purified EGFR (10 µg in 15 µl of dialysis buffer) was subjected to SDS-PAGE analysis as described above. For Western blotting after gel electrophoresis, proteins on the gel were transferred to polyvinylidene difluoride (PVDF) membrane (pore size, 0.45 µm; GE Healthcare) using a TurboBlot dry blotting system (Bio-Rad) and were then immunostained with antibodies, D-8 (sc-365829, Santa Cruz Biotechnology) for EGFR and pY-20 (sc-508, Santa Cruz Biotechnology) for phosphorylated EGFR. Horse radish peroxidase (HRP)-conjugated anti-mouse IgG antibody (GE Healthcare) was used as a secondary antibody for the detection of EGFR bound with the first antibody.

For the phosphorylation assay (Supplementary Figure S2), an aliquot (15 µl of 20 µg/ml) of purified EGFR was reacted at 30°C for 15 min with or without 100 ng EGF in the presence of 1.0 mM ATP in phosphorylation buffer containing 25 mM HEPES (pH 7.4), 20 mM $MgCl_2$, 5 mM β-glycerophosphate, 0.5 mM DTT, and 0.1 mM $NaVO_3$. The reaction was stopped by adding the same volume of two-fold concentrated Laemmli sample buffer and was analyzed by SDS-PAGE and Western blotting as described above.

For the autophosphorylation analysis (Figures 4B, C) of doubly mutated EGFRs, F973R/L977R and E981R/D982K, plasmid constructs, pcDNA3.1-EGFR, pcDNA3.1-EGFR (F973R/L977R) and pcDNA3.1-EGFR(E981R/D982K), were transfected to the modified HeLa cells, which were seeded in a Coster® 6-well plate (Corning, NY) at a density of 1 x 10^5 cells/well in growth media (DMEM supplemented with 10% (v/v) FBS) one day before transfection. Next day, the media in the wells were replaced with 2 ml of fresh media. A transfection mixture, containing 1.5 µg plasmid DNA and 3 µg PEI in 200 µl Opti-MEM (Gibco), was incubated at room temperature for 10 min and was then added to each well. The plate was incubated for 4 h at 37°C in a 5% CO_2 atmosphere. After the incubation, media in wells were replaced with 2 ml of fresh growth media, and the plate was incubated at 37°C in a 5% CO_2 atmosphere. After incubation for 26 h, wells were washed three times with 2 ml of fresh growth media and were covered with 2 ml of Dulbecco's MEM without FBS for serum starvation, followed by incubation at 37°C for 14 h in a 5% CO_2 atmosphere. After starvation, the plate was placed on ice for 10 min, and washed twice with 2 ml of ice-cold Dulbecco's PBS. Cells in each well were lysed by adding 70 µl Laemmli buffer containing 5% (v/v) β-mercaptoethanol, 1.0 mM Na_3VO_4, a phosphatase inhibitor cocktail (PhosSTOP; Sigma) and a protease inhibitor cocktail (cOmplete EDTA free; Sigma). An aliquot, 15 µg of total proteins, of the lysed cells was incubated at 95°C for 7 min and was subjected to SDS-PAGE analysis, which was performed using 7% (w/v) acrylamide gels in running buffer [25 mM Tris-HCl (pH 8.6), 192 mM glycine, 0.1% (w/v) SDS]. Proteins on the gel were transferred to PVDF by electrophoresis using a Mini Trans-Blot cell (Bio-Rad) at 30 V for 16 h in a cold room. The membrane was probed with a primary antibody, mouse anti-phosphotyrosine monoclonal (pY-20, 1/500 dilution; Santa Cruz Biotechnology), rabbit anti-EGFR monoclonal (D38B1, 1/3000 dilution; Cell Signaling Technology), or rabbit anti-phosphotyrosine (pY1173) monoclonal (53A5; 1/1000 dilution; Cell Signaling Technology), and then with secondary antibodies,

HRP-conjugated anti-mouse IgG (dilution, 1/3000; GE Healthcare) and HRP-conjugated anti-rabbit IgG (dilution, 1/3000; GE Healthcare), respectively. Phosphorylation signals were detected using ECL prime (Amersham Biosciences) and recorded by LAS-3000 imager (FujiFilm, Tokyo, Japan). Phosphorylation intensity was quantified using ImageJ. This autophosphorylation analysis was repeated five times and a representative result is shown in Figure 4B.

Gel filtration chromatography

Full-length EGFR, 2 μM at a final concentration, in dialysis buffer was reacted with or without 20 μM EGF (recombinant human; Abbiotec, Escondido, CA) for 30 min on ice in the presence of 1.0 mM ATP in 1.0 ml of total reaction volume, and an aliquot (500 μl) was analyzed by gel filtration column chromatography at a flow rate of 0.4 ml/min (24 ml bed volume, 10 mm inner diameter, 300 mm in height; prepacked with Superose 6 Increase; GE Healthcare), which was equilibrated with running buffer (20 mM Tris-HCl, pH 8.0; 200 mM NaCl; and 0.01% DDM), by fast protein liquid chromatography (FPLC) using an AKTA-Explorer (GE Healthcare) in a cold room.

Purified EGFR-TEV-His8 (0.15 mg) was digested with 0.05 mg (250 unit) of TEV protease (Accelagen, San Diego, CA) in 0.6 ml of buffer, which contains 20 mM Tris-HCl (pH 8.0), 200 mM NaCl, and 0.01% DDM, for 18 h at 4°C. An aliquot (500 μl) was subjected to analysis by gel filtration chromatography using a column prepacked with Superose 6 Increase 10/300 GL as described above. A representative result from three independent experiments is shown in Figure 1B.

Apparent Stokes radii of full-length EGFR in the presence or absence of bound EGF were determined using the following proteins as standard markers in gel filtration chromatography: bovine thyroid thyroglobulin (Mw, 669 kDa; Stokes radius, 8.5 nm; GE Healthcare), horse spleen ferritin (440 kDa, 6.1 nm; GE Healthcare), and rabbit muscle aldolase (158 kDa, 4.8 nm; GE Healthcare).

Cryo-ET

Colloidal gold particles (10 nm; Amersham Biosciences), 2 μl of a "1.0 OD" solution, were equilibrated with purification buffer (20 mM Tris-HCl, pH 8.0; 200 mM NaCl; and 0.01% DDM). Purified EGFR (20 μl, 0.2 mg/ml) before or after incubation with 20 μM EGF at a final concentration on ice for 30 min was mixed with the equilibrated colloidal gold particles at 3:1 ratio for alignment purposes. A Quantifoil holey carbon copper grid (R 1.2/1.3; Electron Microscopy Sciences, Hatfield, PA) was glow-discharged for 60 s, and the EGFR and colloidal gold mixture (3 μl) was spotted on the grid. The grid was blotted with filter paper (grade 595; Ted Pella, Redding, CA) for 3 s and was vitrified at 4°C with 80%-90% humidity (78) using a Vitrobot Mark IV plunge-freezing device (FEI). An FEI Titan Krios equipped with a Falcon II direct electron detector was operated at 300 kV (accelerating voltage) and at a magnification of 37,000 with the defocus value of -2.0 μm for data collection (resulting in a pixel size of 2.258 on the specimen scale). Specimens were tilted from 0° to –70° and 0° to +70° with an increment of 1° tilt/image. The total dose for each tilt series did not exceed 90 $e^-/Å^2$ to minimize radiation damage. Tomography software (version 4.0; Thermo Fisher Scientific) was used for data acquisition.

Image processing and docking

Unliganded and liganded EGFR tilt-series were aligned using 10-nm gold particles as fiducial markers with mean errors of 3.5 Å (1.55 pixels) and 3.7 Å (1.6 pixels), respectively. A series of 2D slices perpendicular to the tilt axis were reconstructed by using a radius-weighted back-projection algorithm from a stack of extracted areas from the tilt images. This stack of 2D slices constituted the initial 3D map and was also called a back-projection map or a tomogram. The back-projections were run on multiple selected areas, generating volumes of 800 × 800 × 800 voxels. The tomograms were further improved *via* a regularizing process by COMET (47, 79, 80), version 6.4.2, which enhances the contrast of density to increase the signal-to-noise in the final tomograms. The MINER program of the package was used to identify coordinates for desired maps in the regularized tomograms using either a 3D voxel or a molecular mass range as a parameter. From the list of coordinates, an automated extraction of subtomograms was performed in a volume of 110 × 110 × 110 voxels that were already low-pass filtered to 15 Å. Individual snapshots of the extracted subtomograms were generated using BOB software (81) with a volume-rendering option. The CORRPAIR program of the package was applied to the individual 3D subtomograms to create a correlation matrix pairing all the subtomograms. The correlation matrix contained clusters of subtomograms that had similar correlations. The CORRAVE program of the package was then run to maximize the correlations within each cluster and to generate an averaged subtomogram from each cluster. CHIMERA (48), version 1.14.0 (http://www.cgl.ucsf.edu/chimera/), was subsequently used for docking the model of EGFR domains from PDB entries to the averaged subtomograms of the clusters. The crystal structures of EGFR domains were aligned to the individual subtomogram maps by using CHIMERA with the manual option. The PDB entries used for docking were 1NQL (11), 3NJP (22), 2M0B (82), 2M20 (62), 3GT8 (16), and 2GS6 (14). These representative clusters were cross-correlated with the 20 Å-resolution low-pass filtered crystal structures of EGFR domains. We used all the crystal and NMR structures available for docking and the structures

docked to the envelopes with the highest correlation coefficient were chosen. In Figures 3A, B, 1NQL was docked to C1, C2, C3, C6, C8, C10, C12, C13, C15, C16, C18, C19, C22, C23, C24, C25; half of 3NJP to C4, C5, C7, C9, C11, C14, C17, C20, C21; 2M0B to all TMD of unliganded EGFR; 3GT8 to all TKD of unliganded EGFR; 3NJP to all ECD of liganded EGFR; 2M20 to all TMD of liganded EGFR; and 2GS6 to all TKD of liganded EGFR.

Electron density distribution along the axis of minimum moment of inertia

Electron density maps were represented by a set of vectors (x_i, y_i, z_i, and d_i) ($1 \le i \le N$), where x_i, y_i, and z_i are the coordinates of each voxel, and d_i is the density of each voxel. N is the number of voxels in each density map. The coordinates (x_i, y_i, z_i) of each density map were transformed to fit the center of mass of the density map to the origin of the coordinate system (x'_i, y'_i, z'_i), using equation (1).

$$\left(x_i^{'},\ y_i,\ z_i^{'}\right) = \left(x_i - \frac{\sum_i x_i d_i}{\sum_i d_i},\ y_i - \frac{\sum_i y_i d_i}{\sum_i d_i},\ z_i - \frac{\sum_i z_i d_i}{\sum_i d_i}\right) \quad (1)$$

The inertia tensor I of the electron density map was calculated using equation (2).

$$I = \begin{bmatrix} \Sigma_i\, d_i(y_i'2 + z_i'2) & -\Sigma_i\, d_i x_i' y_i' & -\Sigma_i\, d_i x_i' z_i' \\ -\Sigma_i\, d_i y_i' x_i' & \Sigma_i\, d_i(z_i'2 + x_i'2) & -\Sigma_i\, d_i y_i' z_i' \\ -\Sigma_i\, d_i z_i' x_i' & -\Sigma_i\, d_i z_i' y_i' & \Sigma_i\, d_i(x_i'2 + y_i'2) \end{bmatrix} \quad (2)$$

The axis of minimum or maximum moment of inertia was determined from an eigenvector that give a minimum or maximum eigenvalue, λ, respectively, in the following equation:

$$I \cdot n = \lambda n$$

where n is a 3D unit vector. The coordinates of each density map, (x'_i, y'_i, z'_i), were rotated around the center of mass so that the eigenvectors of the minimum and maximum moments of inertia can be aligned to the z- and x-axes, respectively. Among the two possible opposite alignments along the z-axis, one of the two alignments was chosen based on the docked models of crystal structures (Figures 3A, B). The data processing above was performed on R (https://www.r-project.org/) with custom scripts.

Each aligned density map was sectioned into two voxels (~4.5 Å) each along the z-axis, and the electron density within each section was plotted against the z-axis. The mean values of the plots of 25 unliganded or 25 liganded EGFR density maps are shown in Figure 2C, after normalized by total volumes. Error bars indicate standard deviation (SD). Asterisks indicate significant differences (*p< 0.05, **p< 0.01) of the two groups with two-sided Student's t-test (in the range between -140 Å and 75 Å), or Mann-Whitney U-test (in the range over 80 Å) using R.

HeLa cells lacking EGFR family members

HeLa cells (RIKEN BRC, Saitama, Japan) were cultured in DMEM supplemented with 10% (v/v) FBS and incubated in a humidified incubator containing 5% CO_2 at 37°C. To knockout EGFR family members in HeLa cells, a Cas9-RNA complex transfection system (Alt-R CRISPR-Cas9; Integrated DNA Technologies, Coralville, IA) was used. A custom-made guide RNA was complexed with Cas9 protein, and the resulting RNA and protein complex was transfected to HeLa cells with Lipofectamine RNAiMAX (Thermo Fisher Scientific) according to the manufacturer's instructions. After three days, the transfected cells were transferred to 96-well plates for the isolation of single cells. The isolated cells were further cultured for 1–2 weeks, and their genomes were analyzed by PCR for deletion, which was then confirmed by DNA sequencing. To knockout of multiple EGFR family members, the above knockout procedure was repeated three times to create a triple-knockout cell line, "*124* KO HeLa", which lacks EGFR, ErbB2, and ErbB4. The target 20-nucleotide genome sequences of guide RNA for EGFR, ErbB2, and ErbB4 are 5'-AGGGTTGTTGCTGAACCGCA in exon #4, 5'-TGAGTCCATGCCCAATCCCG in exon #7, and 5'-TGCTGCCATCGAGAATGTGC in exon #6, respectively. All genome deletions introduced to the cell line created stop codons within the extracellular domain regions of each receptor. As ErbB3 is not expressed on the HeLa cell surface (95), we used a HeLa cell line lacking EGFR, ErbB2, and ErbB4, which was confirmed by Western blot analysis and ligand binding optically observed described below (Supplementary Figure S3).

Optical observation

To label EGF with fluorescent dyes, 1.0 mg/ml EGF (PeproTech, Cranbury, NJ) solution in water was mixed with the same volume of 100 mM potassium phosphate buffer, pH 7.0. Alexa Fluor 555 NHS (Thermo Fisher Scientific) or Alexa Fluor 647 NHS in dimethyl sulfoxide was added to the EGF solution to a final concentration of 400 μM. The reaction mixture was incubated at room temperature for 70 min and then loaded onto a PD-10 desalting column (GE Healthcare) to remove unbound dye molecules. Eluates from the column were concentrated with a centrifugal filter device (Amicon Ultra 3K; Millipore). Concentrations of EGF and fluorescent dyes in the concentrated samples were determined using a spectrophotometer (NanoDrop; Thermo Fisher Scientific) based on molecular extinction coefficients, 18000 $M^{-1}cm^{-1}$ at 280 nm for EGF, 150000 $M^{-1}cm^{-1}$ at 550 nm for Alexa555, and 239000 $M^{-1}cm^{-1}$ at 650 nm for Alexa647. We used only EGF samples with higher labelling efficiency than 95%.

To prepare a trolox and troloxquinone mixture (TXTQ), 2.5 mg/ml trolox (Cayman Chemical, Ann Arbor, MI) was dissolved in 10 mM potassium phosphate, pH 7.2. After dissolving, the pH of the solution was adjusted to pH 7.0 using 1.0 M NaOH. Approximately 10% of trolox (~0.25 mg/ml) was converted to troloxquinone by oxidization under illumination using a mercury lump (Olympus) on a stereo microscope (SZX16; Olympus). Generation of troloxquinone was monitored by measuring the absorbance at 255 nm using a spectrophotometer. Oxidization was continued until the absorbance at 255 nm reached ~1.2 in 0.1 mm path length (83).

To construct cell lines co-expressing EGFR and GFP-tagged Shc1 or EGFR and GFP-tagged Grb2, a plasmid construct, pIRES2-EGFR-AcGFP1-Shc1, pIRES2-EGFR-Grb2-AcGFP1, or pIRES2-EGFR(K721A)-AcGFP1-Shc1, was transfected into the modified HeLa cell line that did not express EGFR, ErbB2, ErbB3, or ErbB4 on the cell surface. Cells (0.5×10^3) were seeded in a glass-bottom dish (35 mm in diameter; Iwaki, Shizuoka, Japan) one day before transfection, and the next day, medium was replaced with 0.3 ml of fresh growth medium, DMEM supplemented with 10% (v/v) FBS. Transfection mixture, which contained 0.3 µg plasmid DNA and 0.6 µg of PEI in 30 µl of Opti-MEM (Gibco), was incubated at room temperature for 10 min and was then added to each dish. The dish was incubated at 37°C for 4 h under a 5% CO_2 atmosphere. After incubation, growth media in the wells were replaced with fresh media, and the plates were further incubated at 37°C for 40 h in a 5% CO_2 atmosphere. Then, the dish was washed three times with 0.3 ml of DMEM without FBS and filled with 0.3 ml of DMEM without FBS for serum starvation. The dish was further incubated at 37°C for more than 3 h in a 5% CO_2 atmosphere.

Optical observation of EGF binding to the cell surface of the modified HeLa cell was performed using an inverted microscope (Eclipse Ti; Nikon) with an oil-immersion objective (SR APO TIRF ×100/1.49; Nikon) at room temperature. GFP, Alexa555, and Alexa647 were excited by a laser unit (LU-N4; Nikon) with 488 nm, 561 nm, and 640 nm, respectively. The fluorescent signal was split into three EM CCD cameras (DU-897; Andor Technology, Belfast, UK) using dichroic mirrors (FF580-FDi01 and FF662-FDi01; Semrock, Rochester, NY) and bandpass filters (FF01-525/45, FF01-600/37, and FF01-692/40; Semrock). Before observation, cells were washed twice with Hank's balanced salt solution (HBSS; Gibco) and covered with 200 µl HBSS containing 1.0 mM TXTQ. The apical surface of the cell was observed under oblique illumination (54). At 10 s after video recording started, 200 µl HBSS containing 1.0 mM TXTQ, 0.5 mg/ml glucose oxidase, 0.04 mg/ml catalase, 1.0 mg/ml glucose, and fluorescently labeled EGF was applied to the dish. As shown in Supplementary Figure S12, the fluorescently labeled EGF activated EGFR at the similar level to that by unlabeled ligand. Movements of fluorescent spots derived from fluorescently labeled EGF, GFP-Shc1 or Grb2-GFP on the cell surface were recorded at 10 frames/s for 90 s after EGF stimulation of the cell.

The images of three-color channels were shifted and distorted, primarily due to chromatic aberration. We used an ImageJ plugin (DoM_Utrecht, Netherlands) to correct the aberration. The GFP and Alexa647 channels were corrected to fit the Alexa555 channel. Fluorescent bead images of a calibration slide (Tool for calibration Multi Spec #1783-455; Zeiss) were used as references for correction. After correction, fluorescent spots in each channel were detected by an ImageJ plugin (MosaicSuite; MOSAIC Group, Towson, MD) and analyzed using a custom R script. We defined colocalization of spots in different channels when the distance between the spots was less than $\sqrt{2}$ pixel (0.21 µm). The fluorescent spots in different channels sometimes approached each other within the threshold distance by chance without actual colocalization. The number of this "pseudo-colocalization" in different channels was estimated by the colocalization analysis, where one of two images was flipped vertically and horizontally. The mean of two numbers of colocalization with vertically and horizontally flipped images was used as the number of the pseudo-colocalization for every frame and subtracted from the number of colocalization of the original unmodified two images to obtain the corrected numbers of colocalization shown in Figure 5 and Supplementary Figure S11, for every pair of different channel images. In case of the number of colocalizations of all three channels, a colocalized image of Alexa555–EGF and Alexa647–EGF was used for the colocalization analysis with the remaining Shc1 (or Grb2) channel image in the same way.

Statistical analysis

Statistical analysis of data was performed using R (version 3.6.3) or SigmaPlot (version 13.0). All data were checked for normality of distribution and homogeneity of variance using χ<σπ>2</σπ> goodness of fit test ($p< 0.05$) and were evaluated using two-sided Student's *t*-test for comparisons between pairs of groups. If normality did not hold, Mann-Whitney U test or Levine's test was used. Results are reported as mean ± SD or standard error of the mean (SEM). Asterisks in figures indicate significant differences ($^*p < 0.05$, $^{**}p < 0.01$, $^{***}p < 0.001$) of two groups.

Data availability statement

The datasets presented in this study can be found in online repositories. The names of the repository/repositories and accession number(s) can be found below: https://www.ebi.ac.uk/pdbe/emdb/, 30714-30721 https://www.ebi.ac.uk/pdbe/emdb/, 30723-30734 https://www.ebi.ac.uk/pdbe/emdb/,

30736-30765 https://www.ebi.ac.uk/pdbe/emdb/, 30862 https://www.ebi.ac.uk/pdbe/emdb/, 30864.

Author contributions

Conceptualization, IM.; methodology, EP, E-IS, RA, and L-GÖ.; software, GW and L-GÖ; investigation, EP, E-IS, and L-GÖ; formal analysis, EP, E-IS, L-GÖ, and IM; writing - original draft, EP, E-IS, and IM; writing – review & editing, EP, E-IS, IM, and US; funding acquisition, IM and US; supervision, IM and US. All authors contributed to the article and approved the submitted version.

Funding

This work was supported by Okinawa Institute of Science and Technology Graduate University.

Acknowledgments

We are grateful to T. Sassa for his construction of pAC-N1-GFP-Shc1 and pAc-Grb2-GFP, A. Mugo for his advice on purification of the full-length EGFR, and T. Murayama and H. Iha for comments on the manuscript.

Conflict of interest

The authors declare that the research was conducted in the absence of any commercial or financial relationships that could be construed as a potential conflict of interest.

Publisher's note

Supplementary material

The Supplementary Material for this article can be found online at: https://www.frontiersin.org/articles/10.3389/fendo.2022.1042787/full#supplementary-material

References

1. Chen J, Zeng F, Forrester SJ, Eguchi S, Zhang MZ, Harris RC. Expression and function of the epidermal growth factor receptor in physiology and disease. *Physiol Rev* (2016) 96:1025–69. doi: 10.1152/physrev.00030.2015

2. Miettinen PJ, Berger JE, Meneses J, Phung Y, Pedersen RA, Werb Z, et al. Epithelial immaturity and multiorgan failure in mice lacking epidermal growth factor receptor. *Nature* (1995) 376:337–41. doi: 10.1038/376337a0

3. An Z, Aksoy O, Zheng T, Fan QW, Weiss WA. Epidermal growth factor receptor and EGFRvIII in glioblastoma: signaling pathways and targeted therapies. *Oncogene* (2018) 37:1561–75. doi: 10.1038/s41388-017-0045-7

4. London M, Gallo E. Epidermal growth factor receptor (EGFR) involvement in epithelial-derived cancers and its current antibody-based immunotherapies. *Cell Biol Int* (2020) 44:1267–82. doi: 10.1002/cbin.11340

5. Mitchell RA, Luwor RB, Burgess AW. Epidermal growth factor receptor: structure-function informing the design of anticancer therapeutics. *Exp Cell Res* (2018) 371:1–19. doi: 10.1016/j.yexcr.2018.08.009

6. Serova OV, Chachina NA, Gantsova EA, Popova NV, Petrenko AG, Deyev IE. Autophosphorylation of orphan receptor ErbB2 can be induced by extracellular treatment with mildly alkaline media. *Int J Mol Sci* (2019) 20:1515. doi: 10.3390/ijms20061515

7. Tzahar E, Waterman H, Chen X, Levkowitz G, Karunagaran D, Lavi S, et al. A hierarchical network of interreceptor interactions determines signal transduction by neu differentiation factor/neuregulin and epidermal growth factor. *Mol Cell Biol* (1996) 16:5276–87. doi: 10.1128/mcb.16.10.5276

8. Ferguson KM. Structure-based view of epidermal growth factor receptor regulation. *Annu Rev Biophys* (2008) 37:353–73. doi: 10.1146/annurev.biophys.37.032807.125829

9. Garrett TP, McKern NM, Lou M, Elleman TC, Adams TE, Lovrecz GO, et al. Crystal structure of a truncated epidermal growth factor receptor extracellular domain bound to transforming growth factor alpha. *Cell* (2002) 110:763–73. doi: 10.1016/s0092-8674(02)00940-6

10. Ogiso H, Ishitani R, Nureki O, Fukai S, Yamanaka M, Kim JH, et al. Crystal structure of the complex of human epidermal growth factor and receptor extracellular domains. *Cell* (2002) 110:775–87. doi: 10.1016/s0092-8674(02)00963-7

11. Ferguson KM, Berger MB, Mendrola JM, Cho HS, Leahy DJ, Lemmon MA. EGF activates its receptor by removing interactions that autoinhibit ectodomain dimerization. *Mol Cell* (2003) 11:507–17. doi: 10.1016/s1097-2765(03)00047-9

12. Stamos J, Sliwkowski MX, Eigenbrot C. Structure of the epidermal growth factor receptor kinase domain alone and in complex with a 4-anilinoquinazoline inhibitor. *J Biol Chem* (2002) 277:46265–72. doi: 10.1074/jbc.M207135200

13. Wood ER, Truesdale AT, McDonald OB, Yuan D, Hassell A, Dickerson SH, et al. A unique structure for epidermal growth factor receptor bound to GG572016 (Lapatinib): relationships among protein conformation, inhibitor off-rate, and receptor activity in tumor cells. *Cancer Res* (2004) 64:6652–9. doi: 10.1158/0008-5472.Can-04-1168

14. Zhang X, Gureasko J, Shen K, Cole PA, Kuriyan J. An allosteric mechanism for activation of the kinase domain of epidermal growth factor receptor. *Cell* (2006) 125:1137–49. doi: 10.1016/j.cell.2006.05.013

15. Yun CH, Boggon TJ, Li Y, Woo MS, Greulich H, Meyerson M, et al. Structures of lung cancer-derived EGFR mutants and inhibitor complexes: mechanism of activation and insights into differential inhibitor sensitivity. *Cancer Cell* (2007) 11:217–27. doi: 10.1016/j.ccr.2006.12.017

16. Jura N, Endres NF, Engel K, Deindl S, Das R, Lamers MH, et al. Mechanism for activation of the EGF receptor catalytic domain by the juxtamembrane segment. *Cell* (2009) 137:1293–307. doi: 10.1016/j.cell.2009.04.025

17. Lemmon MA, Schlessinger J. Cell signaling by receptor tyrosine kinases. *Cell* (2010) 141:1117–34. doi: 10.1016/j.cell.2010.06.011

18. Yarden Y, Schlessinger J. Self-phosphorylation of epidermal growth factor receptor: evidence for a model of intermolecular allosteric activation. *Biochemistry* (1987) 26:1434–42. doi: 10.1021/bi00379a034

19. Downward J, Parker P, Waterfield MD. Autophosphorylation sites on the epidermal growth factor receptor. *Nature* (1984) 311:483–5. doi: 10.1038/311483a0

20. Honegger AM, Kris RM, Ullrich A, Schlessinger J. Evidence that autophosphorylation of solubilized receptors for epidermal growth factor is mediated by intermolecular cross-phosphorylation. *Proc Natl Acad Sci USA* (1989) 86:925–9. doi: 10.1073/pnas.86.3.925

21. Wilson KJ, Gilmore JL, Foley J, Lemmon MA, Riese DJ2nd. Functional selectivity of EGF family peptide growth factors: implications for cancer. *Pharmacol Ther* (2009) 122:1–8. doi: 10.1016/j.pharmthera.2008.11.008

22. Lu C, Mi LZ, Grey MJ, Zhu J, Graef E, Yokoyama S, et al. Structural evidence for loose linkage between ligand binding and kinase activation in the epidermal growth factor receptor. *Mol Cell Biol* (2010) 30:5432–43. doi: 10.1128/mcb.00742-10

23. Mi LZ, Lu C, Li Z, Nishida N, Walz T, Springer TA. Simultaneous visualization of the extracellular and cytoplasmic domains of the epidermal growth factor receptor. *Nat Struct Mol Biol* (2011) 18:984–9. doi: 10.1038/nsmb.2092

24. Huang Y, Bharill S, Karandur D, Peterson SM, Marita M, Shi X, et al. Molecular basis for multimerization in the activation of the epidermal growth factor receptor. *eLife* (2016) 5:e14107. doi: 10.7554/eLife.14107

25. Shoyab M, De Larco JE, Todaro GJ. Biologically active phorbol esters specifically alter affinity of epidermal growth factor membrane receptors. *Nature* (1979) 279:387–91. doi: 10.1038/279387a0

26. Magun BE, Matrisian LM, Bowden GT. Epidermal growth factor. ability of tumor promoter to alter its degradation, receptor affinity and receptor number. *J Biol Chem* (1980) 255:6373–81. doi: 10.1016/S0021-9258(18)43747-7

27. Schlessinger J. Allosteric regulation of the epidermal growth factor receptor kinase. *J Cell Biol* (1986) 103:2067–72. doi: 10.1083/jcb.103.6.2067

28. Macdonald JL, Pike LJ. Heterogeneity in EGF-binding affinities arises from negative cooperativity in an aggregating system. *Proc Natl Acad Sci USA* (2008) 105:112–7. doi: 10.1073/pnas.0707080105

29. Wofsy C, Goldstein B, Lund K, Wiley HS. Implications of epidermal growth factor (EGF) induced EGF receptor aggregation. *Biophys J* (1992) 63:98–110. doi: 10.1016/s0006-3495(92)81572-2

30. Moriki T, Maruyama H, Maruyama IN. Activation of preformed EGF receptor dimers by ligand-induced rotation of the transmembrane domain. *J Mol Biol* (2001) 311:1011–26. doi: 10.1006/jmbi.2001.4923

31. Martin-Fernandez M, Clarke DT, Tobin MJ, Jones SV, Jones GR. Preformed oligomeric epidermal growth factor receptors undergo an ectodomain structure change during signaling. *Biophys J* (2002) 82:2415–27. doi: 10.1016/s0006-3495(02)75585-9

32. Yu X, Sharma KD, Takahashi T, Iwamoto R, Mekada E. Ligand-independent dimer formation of epidermal growth factor receptor (EGFR) is a step separable from ligand-induced EGFR signaling. *Mol Biol Cell* (2002) 13:2547–57. doi: 10.1091/mbc.01-08-0411

33. Clayton AHA, Walker F, Orchard SG, Henderson C, Fuchs D, Rothacker J, et al. Ligand-induced dimer-tetramer transition during the activation of the cell surface epidermal growth factor receptor-a multidimensional microscopy analysis. *J Biol Chem* (2005) 280:30392–9. doi: 10.1074/jbc.M504770200

34. Teramura Y, Ichinose J, Takagi H, Nishida K, Yanagida T, Sako Y. Single-molecule analysis of epidermal growth factor binding on the surface of living cells. *EMBO J* (2006) 25:4215–22. doi: 10.1038/sj.emboj.7601308

35. Liu P, Sudhaharan T, Koh RML, Hwang LC, Ahmed S, Maruyama IN, et al. Investigation of the dimerization of proteins from the epidermal growth factor receptor family by single wavelength fluorescence cross-correlation spectroscopy. *Biophys J* (2007) 93:684–98. doi: 10.1529/biophysj.106.102087

36. Saffarian S, Li Y, Elson EL, Pike LJ. Oligomerization of the EGF receptor investigated by live cell fluorescence intensity distribution analysis. *Biophys J* (2007) 93:1021–31. doi: 10.1529/biophysj.107.105494

37. Tao RH, Maruyama IN. All EGF(ErbB) receptors have preformed homo- and heterodimeric structures in living cells. *J Cell Sci* (2008) 121:3207–17. doi: 10.1242/jcs.033399

38. Lynch TJ, Bell DW, Sordella R, Gurubhagavatula S, Okimoto RA, Brannigan BW, et al. Activating mutations in the epidermal growth factor receptor underlying responsiveness of non-small-cell lung cancer to gefitinib. *N Engl J Med* (2004) 350:2129–39. doi: 10.1056/NEJMoa040938

39. Imielinski M, Berger AH, Hammerman PS, Hernandez B, Pugh TJ, Hodis E, et al. Mapping the hallmarks of lung adenocarcinoma with massively parallel sequencing. *Cell* (2012) 150:1107–20. doi: 10.1016/j.cell.2012.08.029

40. Binder ZA, Thorne AH, Bakas S, Wileyto EP, Bilello M, Akbari H, et al. Epidermal growth factor receptor extracellular domain mutations in glioblastoma present opportunities for clinical imaging and therapeutic development. *Cancer Cell* (2018) 34:163–77. doi: 10.1016/j.ccell.2018.06.006

41. Ekstrand AJ, Sugawa N, James CD, Collins VP. Amplified and rearranged epidermal growth factor receptor genes in human glioblastomas reveal deletions of sequences encoding portions of the n- and/or c-terminal tails. *Proc Natl Acad Sci USA* (1992) 89:4309–13. doi: 10.1073/pnas.89.10.4309

42. Frederick L, Wang XY, Eley G, James CD. Diversity and frequency of epidermal growth factor receptor mutations in human glioblastomas. *Cancer Res* (2000) 60:1383–7.

43. Kuan CT, Wikstrand CJ, Bigner DD. EGF mutant receptor vIII as a molecular target in cancer therapy. *Endocr Relat Cancer* (2001) 8:83–96. doi: 10.1677/erc.0.0080083

44. Zhu HJ, Iaria J, Orchard S, Walker F, Burgess AW. Epidermal growth factor receptor: association of extracellular domain negatively regulates intracellular kinase activation in the absence of ligand. *Growth Factors* (2003) 21:15–30. doi: 10.1080/0897719031000096424

45. Pines G, Huang PH, Zwang Y, White FM, Yarden Y. EGFRvIV: a previously uncharacterized oncogenic mutant reveals a kinase autoinhibitory mechanism. *Oncogene* (2010) 29:5850–60. doi: 10.1038/onc.2010.313

46. Mi LZ, Grey MJ, Nishida N, Walz T, Lu C, Springer TA. Functional and structural stability of the epidermal growth factor receptor in detergent micelles and phospholipid nanodiscs. *Biochemistry* (2008) 47:10314–23. doi: 10.1021/bi801006s

47. Skoglund U, Öfverstedt L-G, Burnett RM, Bricogne G. Maximum-entropy three-dimensional reconstruction with deconvolution of the contrast transfer function: a test application with adenovirus. *J Struct Biol* (1996) 117:173–88. doi: 10.1006/jsbi.1996.0081

48. Pettersen EF, Goddard TD, Huang CC, Couch GS, Greenblatt DM, Meng EC, et al. UCSF chimera–a visualization system for exploratory research and analysis. *J Comput Chem* (2004) 25:1605–12. doi: 10.1002/jcc.20084

49. Kozer N, Henderson C, Jackson JT, Nice EC, Burgess AW, Clayton AHA. Evidence for extended YFP-EGFR dimers in the absence of ligand on the surface of living cells. *Phys Biol* (2011) 8:66002. doi: 10.1088/1478-3975/8/6/066002

50. Bessman NJ, Bagchi A, Ferguson KM, Lemmon MA. Complex relationship between ligand binding and dimerization in the epidermal growth factor receptor. *Cell Rep* (2014) 9:1306–17. doi: 10.1016/j.celrep.2014.10.010

51. Orellana L, Thorne AH, Lema R, Gustavsson J, Parisian AD, Hospital A, et al. Oncogenic mutations at the EGFR ectodomain structurally converge to remove a steric hindrance on a kinase-coupled cryptic epitope. *Proc Natl Acad Sci USA* (2019) 116:10009–18. doi: 10.1073/pnas.1821442116

52. Kaplan M, Narasimhan S, de Heus C, Mance D, van Doorn S, Houben K, et al. EGFR dynamics change during activation in native membranes as revealed by NMR. *Cell* (2016) 167:1241–51. doi: 10.1016/j.cell.2016.10.038

53. Chang CM, Shu HK, Ravi L, Pelley RJ, Shu H, Kung HJ. A minor tyrosine phosphorylation site located within the CAIN domain plays a critical role in regulating tissue-specific transformation by ErbB kinase. *J Virol* (1995) 69:1172–80. doi: 10.1128/jvi.69.2.1172-1180.1995

54. Tokunaga M, Imamoto N, Sakata-Sogawa K. Highly inclined thin illumination enables clear single-molecule imaging in cells. *Nat Methods* (2008) 5:159–61. doi: 10.1038/nmeth1171

55. Hofman EG, Bader AN, Voortman J, van den Heuvel DJ, Sigismund S, Verkleij AJ, et al. Ligand-induced EGF receptor oligomerization is kinase-dependent and enhances internalization. *J Biol Chem* (2010) 285:39481–9. doi: 10.1074/jbc.M110.164731

56. Shen J, Maruyama IN. Nerve growth factor receptor TrkA exists as a preformed, yet inactive, dimer in living cells. *FEBS Lett* (2011) 585:295–9. doi: 10.1016/j.febslet.2010.12.031

57. Shen J, Maruyama IN. Brain-derived neurotrophic factor receptor TrkB exists as a preformed dimer in living cells. *J Mol Signal* (2012) 7:2. doi: 10.1186/1750-2187-7-2

58. Huang Y, Ognjenovic J, Karandur D, Miller K, Merk A, Subramaniam S, et al. A molecular mechanism for the generation of ligand-dependent differential outputs by the epidermal growth factor receptor. *eLife* (2021) 10:e73218. doi: 10.7554/eLife.73218

59. Diwanji D, Trenker R, Thaker TM, Wang F, Agard DA, Verba KA, et al. Structures of the HER2-HER3-NRG1beta complex reveal a dynamic dimer interface. *Nature* (2021) 600:339–43. doi: 10.1038/s41586-021-04084-z

60. Endres NF, Das R, Smith AW, Arkhipov A, Kovacs E, Huang Y, et al. Conformational coupling across the plasma membrane in activation of the EGF receptor. *Cell* (2013) 152:543–56. doi: 10.1016/j.cell.2012.12.032

61. Sorokin A. Activation of the EGF receptor by insertional mutations in its juxtamembrane regions. *Oncogene* (1995) 11:1531–40.

62. Balleza E, Kim JM, Cluzel P. Systematic characterization of maturation time of fluorescent proteins in living cells. *Nat Methods* (2018) 15:47–51. doi: 10.1038/nmeth.4509

63. van Belzen N, Rijken PJ, Hage WJ, de Laat SW, Verkleij AJ, Boonstra J. Direct visualization and quantitative analysis of epidermal growth factor-induced receptor clustering. *J Cell Physiol* (1988) 134:413–20. doi: 10.1002/jcp.1041340312

64. Canals F. Signal transmission by epidermal growth factor receptor: coincidence of activation and dimerization. *Biochemistry* (1992) 31:4493–501. doi: 10.1021/bi00133a016

65. Nagai T, Ibata K, Park ES, Kubota M, Mikoshiba K, Miyawaki A. A variant of yellow fluorescent protein with fast and efficient maturation for cell-biological applications. *Nat Biotechnol* (2002) 20:87–90. doi: 10.1038/nbt0102-87

66. Bader AN, Hofman EG, Voortman J, van Bergen en Henegouwen PMP, Gerritsen HC. Homo-FRET imaging enables quantification of protein cluster sizes with subcellular resolution. *Biophys J* (2009) 97:2613–22. doi: 10.1016/j.bpj.2009.07.059

67. Vijapurkar U, Cheng K, Koland JG. Mutation of a shc binding site tyrosine residue in ErbB3/HER3 blocks heregulin-dependent activation of mitogen-activated protein kinase. *J Biol Chem* (1998) 273:20996–1002. doi: 10.1074/jbc.273.33.20996

68. Yang KS, Ilagan MXG, Piwnica-Worms D, Pike LJ. Luciferase fragment complementation imaging of conformational changes in the epidermal growth factor receptor. *J Biol Chem* (2009) 284:7474–82. doi: 10.1074/jbc.M808041200

69. Fleishman SJ, Schlessinger J, Ben-Tal N. A putative molecular-activation switch in the transmembrane domain of ErbB2. *Proc Natl Acad Sci USA* (2002) 99:15937–40. doi: 10.1073/pnas.252640799

70. Maruyama IN. Activation of transmembrane cell-surface receptors *via* a common mechanism? the "rotation model". *Bioessays* (2015) 37:959–67. doi: 10.1002/bies.201500041

71. Purba ER, Saita EI, Maruyama IN. Activation of the EGF receptor by ligand binding and oncogenic mutations: the "rotation model". *Cells* (2017) 6. doi: 10.3390/cells6020013

72. Liu P, Cleveland TE,4, Bouyain S, Byrne PO, Longo PA, Leahy DJ. A single ligand is sufficient to activate EGFR dimers. *Proc Natl Acad Sci USA* (2012) 109:10861–6. doi: 10.1073/pnas.1201114109

73. Alvarado D, Klein DE, Lemmon MA. Structural basis for negative cooperativity in growth factor binding to an EGF receptor. *Cell* (2010) 142:568–79. doi: 10.1016/j.cell.2010.07.015

74. Walton GM, Chen WS, Rosenfeld MG, Gill GN. Analysis of deletions of the carboxyl terminus of the epidermal growth factor receptor reveals self-phosphorylation at tyrosine 992 and enhanced *in vivo* tyrosine phosphorylation of cell substrates. *J Biol Chem* (1990) 265:1750–4. doi: 10.1016/S0021-9258(19)40080-X

75. Bublil EM, Pines G, Patel G, Fruhwirth G, Ng T, Yarden Y. Kinase-mediated quasi-dimers of EGFR. *FASEB J* (2010) 24:4744–55. doi: 10.1096/fj.10-166199

76. Kovacs E, Das R, Wang Q, Collier TS, Cantor A, Huang Y, et al. Analysis of the role of the c-terminal tail in the regulation of the epidermal growth factor receptor. *Mol Cell Biol* (2015) 35:3083–102. doi: 10.1128/mcb.00248-15

77. Srinivasan S, Regmi R, Lin X, Dreyer CA, Chen X, Quinn SD, et al. Ligand-induced transmembrane conformational coupling in monomeric EGFR. *Nat Commun* (2022) 13:3709. doi: 10.1038/s41467-022-31299-z

78. Adrian M, Dubochet J, Lepault J, McDowall AW. Cryo-electron microscopy of viruses. *Nature* (1984) 308:32–6. doi: 10.1038/308032a0

79. Skoglund U, Andersson K, Strandberg B, Daneholt B. Three-dimensional structure of a specific pre-messenger RNP particle established by electron microscope tomography. *Nature* (1986) 319:560–4. doi: 10.1038/319560a0

80. Öfverstedt L-G, Zhang K, Isaksson LA, Bricogne G, Skoglund U. Automated correlation and averaging of three-dimensional reconstructions obtained by electron tomography. *J Struct Biol* (1997) 120:329–42. doi: 10.1006/jsbi.1997.3915

81. Chin-Purcell K. *Bob-brick of bytes (motif edition).* Minnesota Supercomputer Center, University of Minnesota (1993).

82. Bocharov EV, Lesovoy DM, Pavlov KV, Pustovalova YE, Bocharova OV, Arseniev AS. Alternative packing of EGFR transmembrane domain suggests that protein-lipid interactions underlie signal conduction across membrane. *Biochim Biophys Acta* (2016) 1858:1254–61. doi: 10.1016/j.bbamem.2016.02.023

83. Cordes T, Vogelsang J, Tinnefeld P. On the mechanism of trolox as antiblinking and antibleaching reagent. *J Am Chem Soc* (2009) 131:5018–9. doi: 10.1021/ja809117z

frontiers | Frontiers in Endocrinology

TYPE Original Research
PUBLISHED 09 January 2023
DOI 10.3389/fendo.2022.983827

OPEN ACCESS

EDITED BY
Ahmad Al-Mrabeh,
University of Edinburgh,
United Kingdom

REVIEWED BY
Tatiana Rodrigues de Moura,
Federal University of Sergipe, Brazil
Xavier Prieur,
INSERM U1087 Institut du Thorax,
France

*CORRESPONDENCE
Benjamin Brustolin
benjamin.brustolin@gmail.com

SPECIALTY SECTION
This article was submitted to Obesity,
a section of the journal
Frontiers in Endocrinology

RECEIVED 01 July 2022
ACCEPTED 05 December 2022
PUBLISHED 09 January 2023

CITATION
Brustolin B, Touly N, Maillefer M, Parisot L, Di Pillo E, Derive M and Gibot S (2023) Triggering receptor expressed on myeloid cells-1 deletion in mice attenuates high-fat diet-induced obesity. *Front. Endocrinol.* 13:983827. doi: 10.3389/fendo.2022.983827

Triggering receptor expressed on myeloid cells-1 deletion in mice attenuates high-fat diet-induced obesity

Benjamin Brustolin[1]*, Nina Touly[1], Marine Maillefer[2], Lola Parisot[2], Elisa Di Pillo[1], Marc Derive[2] and Sébastien Gibot[1,3]

[1]Inserm Unité Mixte de Recherche (UMR) S1116, Faculté de Médecine de Nancy, Université de Lorraine, Vandœuvre-lès-Nancy, France, [2]INOTREM, University of Lorraine, Nancy, France, [3]Service de Médecine Intensive Réanimation, Hôpital Central, Nancy, France

Introduction: The low-grade inflammatory state present in obesity leads to the development and perpetuation of comorbidities associated with obesity. Our laboratory has been working for several years on an amplification loop of the inflammatory response mediated by TREM-1 (Triggering Receptor of Expressed on Myeloid Cells-1). It is implicated in many acute (septic shock) and chronic (IBD) inflammatory diseases. Previously, TREM-1 has been shown to be overexpressed in adipose and liver tissue in obese and diabetic patients, but its impact has never been characterized in these pathologies.

Methods: Our hypothesis is that TREM-1 plays a major role in the generation and perpetuation of inflammation during obesity and its associated complication (Insulin resistance and cardiac dysfunction). We assessed TREM-1 protein expression by western blot and immunofluorescence in omental and subcutaneous (pre-)adipocyte. Moreover, we submitted mice to a high-fat diet and investigated the effects of the genetic *Trem1* deletion (*trem1* KO mice).

Results: We showed, for the first time, that TREM-1 is expressed and is functional in subcutaneous and omental (pre-)adipocytes. In the mouse model of high-fat diet-induced obesity, we found that *Trem1* suppression limited weight gain, insulin resistance and inflammation in white adipose tissue and liver.

Discussion/conclusion: Our results reveal the *trem1* KO model can be viewed as a preventive model and that TREM-1 seems to play an important role in the development of obesity and its associated complication. It could therefore be a new therapeutic target in this context.

KEYWORDS

Obesity, TREM-1, adipocyte, inflammation, insulin resistance

1 Introduction

Obesity is a complex and heterogeneous disease in which the interplay between adipocytes and adipose tissue macrophages or other surrounding immune cells (CD4, CD8, NKT, mastocytes…) drives the development of a chronic inflammatory state (1). This inflammation is considered to be responsible for insulin resistance that causes or exacerbates obesity-associated complications such as type 2 diabetes mellitus, atherosclerosis, hypertension, liver, kidney, or heart dysfunction (2). In this context, numerous agents have been tested in pre-clinical models of obesity, from curcumin to inhibitors of Interleukin-1 beta (3, 4). However, none of these successfully applied to humans. Indeed, as of today, only 6 anti-obesity medications have been approved by the FDA, all of them promoting weight loss through appetite suppression or decreased fat absorption (5).

The Triggering Receptor Expressed on Myeloid cells-1 (TREM-1) is an immune receptor mostly expressed at the membrane of neutrophils, mature monocytes, and macrophages (6). Following activation of Toll-Like Receptors (TLRs), the expression of TREM-1 is up-regulated and dimerization occurs, allowing the binding of its still unknown ligand that triggers the association of TREM-1 with the adaptor protein DAP-12, leading to intracellular signaling (6–8). The engagement of TREM-1 yields to an amplification of the inflammatory response (6, 9). The role of TREM-1 in mounting a dysregulated and deleterious inflammation has been proven in acute diseases or syndromes such as septic shock (9), myocardial infarction (10), or stroke (11), but also in chronic disorders: inflammatory bowel diseases, atherosclerosis, arthritis, lupus, and cancer (12–16).

Vasquez et al. showed that serum concentrations of the soluble form of TREM-1 (sTREM-1), which is known to be a marker of the TREM-1 pathway activation (17), were elevated in non-obese young healthy adults with cardiometabolic risk factors (abdominal obesity, fasting hyperglycemia, hypertriglyceridemia, high blood pressure) (18).

To get more insights into the role of TREM-1 in obesity, we submitted mice to a high-fat diet and investigated the effects of the genetic *Trem1* deletion on obesity development and its consequences.

2 Material and methods

2.1 Cells maintenance, differentiation, and stimulation

Cryopreserved, subcutaneous and omental preadipocytes from male donors with normal body mass index (22.5 +/- 1.5 kg/m^2) were purchased from Zen-Bio Inc (Durham, USA). Cells were maintained at 5% CO_2 in preadipocyte DMEM/Ham's F-12 medium from Zen-Bio with 3.15 g/L D-glucose (17.5 mmol/L), HEPES, Fetal Bovine Serum (FBS), Penicillin, Streptomycin, Amphotericin B. Cells were seeded into T75 flasks and expanded once before differentiating using accutase (Sigma-Aldrich, France). The medium was replaced every 2 days.

For differentiation, the preadipocyte medium was replaced with DMEM-Ham's F-12 medium supplemented with HEPES, FBS, biotin, pantothenate, human Insulin, dexamethasone, IBMX, PPARγ agonist, penicillin, streptomycin, and amphotericin B during 7 days. Cells were then fed by removing some of the media and replacing it with fresh adipocyte DMEM/Ham's F-12 medium containing HEPES, FBS, biotin, pantothenate, human insulin, dexamethasone, penicillin, streptomycin and amphotericin B (Zen-Bio, USA). 2 weeks after the initiation of differentiation, cells appear with large lipid droplets and are considered mature adipocytes.

Each *in vitro* experiment was conducted using preadipocytes from at least three individual donors. Human preadipocytes or adipocytes were incubated under resting conditions or with LPS from Escherichia coli 0127:B8 at 100 ng/ml (Sigma-Aldrich, France) with or without TREM-1 agonists at 5 µg/ml (MAB1278, Biotechne, R&D Systems, USA) or IgG control (Biotechne, R&D Systems, USA) at 2, 4, 6 and 24h. Cells supernatants and protein lysates were recovered to perform cytokine and protein assays respectively.

2.2 Confocal microscopy

Cells were seeded and differentiated or not on LabTek chambers (Thermo Fisher Scientific, USA). Cells were washed using PBS and tween 20 (0.05%) and fixed with paraformaldehyde (4%) for 20 min and permeabilized with Triton 0.1% for 30 min before incubation with 1/200 anti-TREM-1-AF488 and 1/200 anti-DAP12-AF555 antibodies (Bioss, USA) at 4°C overnight. Nuclei were stained with TO-PRO-3 at 1 µg/ml (Invitrogen, USA) for 1h at 37°C. After washing, coverslips were mounted using a Vectashield solution (Vector Laboratories, USA). Confocal images were obtained using a Leica SP5 confocal laser-scanning microscope system (Leica, Germany) fitted with appropriated filter sets and acquired in sequential scan mode.

2.3 TREM-1 protein analysis

Pre-adipocytes and adipocytes proteins were extracted using RIPA extraction buffer containing (1% NP-40, 1% sodium deoxycholate, 0.1% SDS, 0.15 M NaCl, 0.01 M sodium phosphate pH 7.2, 2mM EDTA, 50mM sodium fluoride, 0.2 mM orthovanate sodium, 100 U/ml protease inhibitor) (Abcam, U.K). Mouse liver proteins were extracted using PhosphoSafe buffer (Novagen, Merck Biosciences, Nottingham, U.K). Total

protein concentration was measured by Pierce BCA Protein Assay Kit (Thermo Fisher Scientific, USA) and used for protein normalization. Lysates were then analyzed by western blot. Electrophoresis was performed with 10 µg of proteins per well using a polyacrylamide Criterion XT Bis-Tris Gel, 4-12%, and XTMES buffer (Bio-Rad, USA). Migration was carried out at 170V, 3A, and 300W for 30 minutes. Then, proteins were transferred on a 0.2 µm nitrocellulose membrane (Transblot Turbo Transfer Pack, Bio-Rad, USA) with a Transblot Turbo system set to 2.5A, 25V for 7 minutes (Bio-Rad, USA). Coomassie blue (Thermo Fisher Scientific, USA) and ponceau (Sigma-Aldrich, France) stains were performed on the membrane and the gel respectively to control the transfer. TREM-1 (Bio-Rad, USA) antibody with its corresponding secondary antibody conjugated to horseradish peroxidase (Bio-Rad, USA) and Super-Signal West Femto Substrate (Thermo Fisher Scientific, USA) were used for protein detection. GAPDH antibody (Cell Signalling Technology, USA) was used for normalization on the same membranes after stripping for 20 minutes in stripping buffer (1% tween, 1.5% glycine, and 0.1% SDS, pH 2.2). For mouse liver analysis mouse p-ERK/ERK, p-mTOR/mTOR, p-GSK3αβ/GSK3αβ, Glut1, Glut2, p-AKT/AKT, IRα, IRβ, and GAPDH with their corresponding secondary antibodies were used. The acquisition was performed with LAS-4000 imager (Fujifilm, Japan) and Multi-Gauge software (LifeScience Fujifilm, Japan).

2.4 Cytokines measurements

Supernatants from stimulated cells were recovered after 2, 4, 6, and 24h LPS (100 ng/ml) stimulation. MCP-1, IL-6, and IL-8 were assessed by multiplex assay using the ELLA microfluidic system (Ella Automated Immunoassay Systems, R&D Systems, U.K) according to the supplier's recommendation.

2.5 Animals

The homozygous knock-out animals were produced at Charles River (Saint Germain sur l'Arbresle, France), AALAC-accredited mouse breeder. Mating duos or trios are established for maintaining and producing animals. Animals remain undisturbed during pregnancy; newborns are genotyped by PCR screening on tail biopsies taken at 2 weeks' of age. Colony maintenance is done in compliance with the 3-R guidelines. Animal health and welfare are verified during bedding changes. All experimentations involving animals have been carried out according to the French and European institutional legislation concerning the care and use of laboratory animals and have been approved by the French ethics committee (Number 23273) for animal experimentation. 20 six-week-old male *Trem1* knockout (KO) and 20 C57Bl/6 wild-type littermate (WT) mice were used. Mice were housed in ventilated racks placed in an EOPS-Type environment maintained at a temperature of 21 +/- 1°C, an humidity of 55% +/- 10%, and exposed to a cycle of 12 hours of light for 12 hours of darkness. The animal had free access to water and food. Four groups were constituted: 10 littermate C57Bl/6 wild-type mice with a standard diet (LFD Low Fat Diet), 10 littermate C57Bl/6 wild-type mice with a high- fat diet (HFD), 10 *Trem1* ko mice with a standard diet, and 10 *Trem1* ko mice with a high- fat diet. High-fat diet was composed of 60.6% of the calories from lipids, 17% from proteins, and 22.5% from carbohydrates (Safe-Lab, France). 10 grams of food per day and per mouse were distributed in the feeders and at the bottom of the cages to facilitate access to food. The food was weighed and extended 3 times per week in to monitor calorie consumption. Mice were weighed weekly to monitor weight gain. The diet started after two weeks of acclimatization, for 12 weeks.

2.6 Oral glucose tolerance test

The procedure used to perform glucose tolerance tests is based on the work of Andrikopoulos et al. (19) taking into account the influence of the glucose administration route, dosage, fasting time, and the influence of anesthesia. The oral glucose tolerance tests were performed following 10 weeks of diet feeding. Mice were fasted for 6 hours before the test and transferred to a procedure room. Blood was obtained by removing the distal 2 mm of the tail and was assessed for baseline glucose levels using the Accutrend® Plus glucometer (Roche, Switzerland). Mice then received 2g/kg body weight of a 100 mg/ml glucose solution in sterile water. 20 µl of blood was collected at each time and glucose concentration was measured at 15, 30, 60, and 120 min after the administration of glucose by oral gavage. Plasma samples were collected and stored at -80°C for measuring insulin levels. Plasma insulin concentrations were determined in the same mice by a commercially available mouse insulin ELISA kit (Merck, Germany).

2.7 Real-time quantitative PCR

Frozen liver, subcutaneous, mesenteric, and perigonadal white adipose tissue were cut into small pieces, kept frozen, and ground in a homogenizer (FastPrep-24, MP biomedicals SARL, France) using ceramic balls 1.4 mm in diameter in the presence of Trizol reagent (Thermo Fisher Scientific, USA) to extract total RNA. RNA purification was performed using RNAeasy Plus Mini Kit (Qiagen, Netherlands) according to the manufacturer's instructions and quantified with MicroDrop (Thermo Fisher Scientific, USA) to determine RNA purity and concentration. Samples were diluted to the same concentration before being reverse transcribed using the iScript cDNA synthesis kit (Bio-Rad,

USA) and quantified by quantitative polymerase chain reaction (PCR) using Qiagen probes (Quantitect Primers) for murine *Tnfa*, *Il6*, and *Ccl2*. Murine *Gapdh*, *ActinB*, *Rna18S* probes served as housekeeping genes.

2.8 Statistical analyses

Unless otherwise stated, data were normally distributed and are presented as mean +/- SEM. The normality of the data distribution was determined by the Shapiro-Wilk test. Between-group differences were tested using Student's t-test or ANOVA or with Mann-Whitney or Kruskal Wallis tests when appropriate. Statistical analysis was performed using Prism Version 8.0.1 software (GraphPad, USA). P-value < 0.05 was deemed significant.

3 Results

3.1 TREM-1 is expressed by (pre-) adipocytes and is functional

Although TREM-1 is known to be mostly expressed by myeloid cells, it has been found on the surface of some epithelial and endothelial cells.

Confocal microscopy analysis revealed the presence of TREM-1 along with its adaptive protein DAP-12 in unstimulated subcutaneous and omental pre-adipocytes and adipocytes (Figure 1A). We confirmed this finding by Western blot (Figure 1B). Moreover, we observed that TREM-1 was more expressed by omental than subcutaneous cells and that lipopolysaccharide (LPS) increased its expression.

To decipher whether TREM-1 was functional, we stimulated cells with LPS along with a TREM-1 agonist antibody (MAB1278, Bio-Techne, clone 193015) or a control IgG and measured IL-8, IL-6, and MCP-1 concentrations in the supernatants (Figure 2). LPS stimulation time-dependently increased the concentrations of these proteins. Co-stimulation with MAB1278 potentiated this elevation, more in omental than subcutaneous (pre-) adipocytes following the higher expression of TREM-1 on the former.

Thus, TREM-1 is expressed by (pre-)adipocytes and is functional.

3.2 *Trem1* deletion limits weight gain in mice fed with a high-fat diet

TREM-1 KO mice and wild-type (WT) littermates were fed with a low (LFD) or high fat diet (HFD) and followed up for 12 weeks. As expected, weight gain was modest in LFD mice, whatever the genotype (Figures 3A–D). By contrast, HFD animals became obese but weight gain was lower in TREM-1 KO than in WT mice (47% +/- 4,11% vs. 60% +/- 3,73%, $p<0.05$) (Figures 3A–D). Of note, food and calorie intake were similar in TREM-1 KO and WT animals all along the experiment (Figures 3E, F). Subcutaneous, perigonadal, and mesenteric adipose tissue, as well as liver, were less heavy in KO than in WT mice (Figures 3G–J).

Trem-1 genetic ablation reduces weight gain, and adipose tissue and liver enlargement during HFD.

3.3 Inflammation is reduced in TREM-1 KO mice

To investigate the inflammatory response induced by HFD, we quantified *Tnfa*, *Il6*, and *Ccl2* mRNA by qRT-PCR in adipose and liver tissues (Figure 4). Expression of these genes remained at a low level after an LFD, with no difference between genotypes except for a mild reduction of *Tnfa* in mesenteric adipose tissue from KO mice (Figure 4G). By contrast, *Tnfa*, *Il6*, and *Ccl2* mRNA increased in most tissues following HFD. With the noticeable exception of subcutaneous adipose tissue (Figures 4A–C), *Trem1* deletion was associated with a decrease in these cytokines expression as compared to WT littermates (Figures 4D–L), but importantly, inflammation was not totally abrogated.

Adipose tissue macrophages have an important role in generating or perpetuating inflammation. We, therefore, quantified macrophage infiltration in adipose tissues by qRT-PCR. HFD increased the macrophage population as assessed by higher *Adgre1* gene expression (encoding for the macrophage marker F4/80) in subcutaneous, perigonadal, and mesenteric adipose tissues (Supplementary Figure 1). In these tissues, *Itagx* (CD11c) may be considered a marker of type 1 (M1) and *Mrc1* (CD206) a marker for type 2 (M2) macrophages. We observed that HFD mostly induced an increase of M1 macrophages with few effects on M2 (except in perigonadal tissue). This was reduced in TREM-1 KO mice.

Therefore, *Trem1* deletion dampens HFD-induced inflammation in several adipose tissues and the liver.

3.4 Trem1 deletion protects against insulin resistance

One of the major consequences of obesity is insulin resistance which may lead to type 2 diabetes and its related complications. We performed an oral glucose tolerance test in LFD and HFD mice. As expected, HFD animals displayed higher blood glucose concentrations than LFD (Figure 5A). However, hyperglycemia was reduced and shortened in TREM-1 KO mice

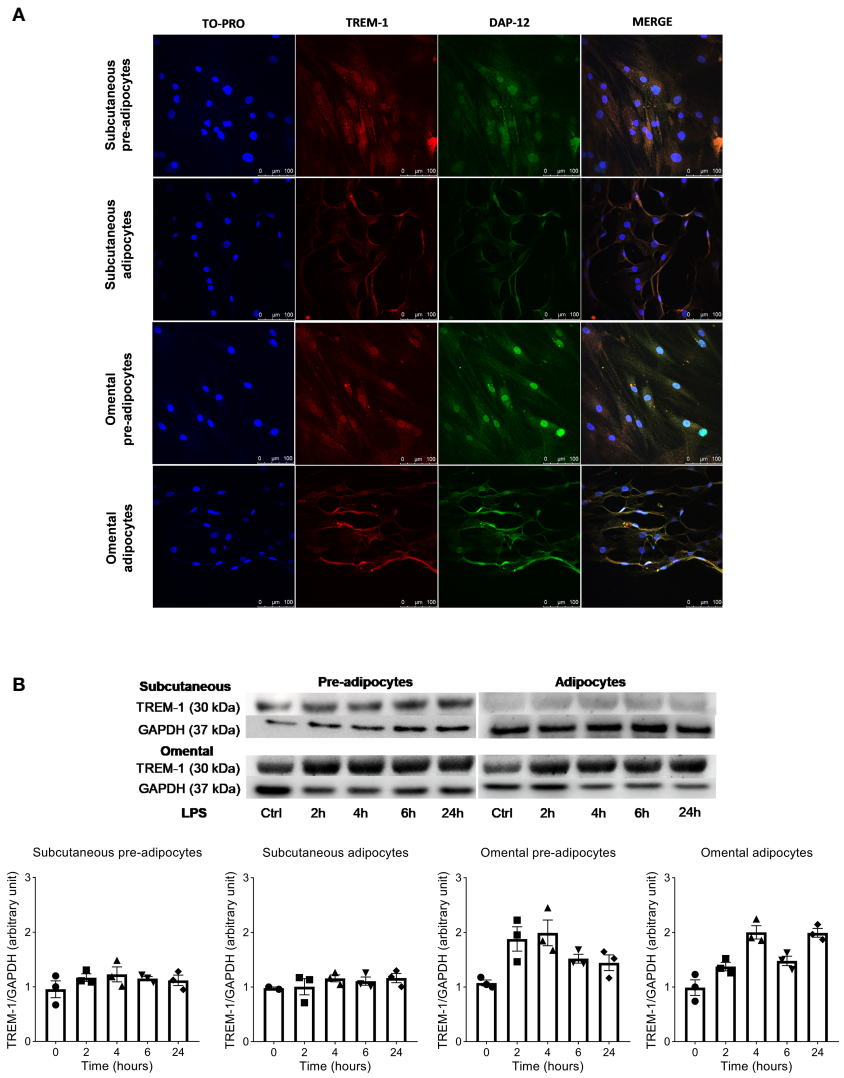

FIGURE 1
Triggering Receptor Expressed on Myeloid cells-1 (TREM-1) is expressed by human subcutaneous and omental pre-adipocyte and adipocytes. **(A)** Confocal fluorescent images of human subcutaneous (top panels) and omental (bottom panels) pre-adipocytes and adipocytes. Cells were stained with anti-human TREM-1 (red), DAP-12 (green), and TO-PRO3 (blue) mAbs, Scale bars: 100 µm. **(B)** Western blot of lysates of human subcutaneous and omental pre-adipocytes and adipocytes treated for 2, 4, 6, and 24 hours with LPS (100 ng/ml). Images are representatives from 3 different experiments each performed on three different donors.

as compared to WT littermates. In parallel, hyperinsulinemia was more pronounced in WT than in TREM-1 KO HFD mice, witnessing the presence of insulin resistance (Figure 5B).

To get insights into the mechanisms of insulin resistance, we performed a western blot analysis of crucial proteins involved in this phenomenon (Figure 5C). Glucose transporters GLUT1 and insulin receptor (IR-α and IR-β) expression did not differ regarding the genotype. By contrast, activation of mTOR, known to down-regulate insulin signaling (20), was reduced in TREM-1 KO. On another side, glucose transporter GLUT2 and AKT, GSK3, and ERK phosphorylation was increased in TREM-1 KO animals: these pathways have been shown to promote cell survival and growth through their action on insulin-stimulated glucose uptake, glycogen, and protein synthesis (21). These data show that *Trem1* deletion prevents HFD-induced insulin resistance.

As part of the deleterious consequences of obesity, heart dysfunction may occur. We thus evaluated cardiac function at the end of the 12 weeks of HFD. Echocardiography revealed a decrease in left ventricular fractional shortening in HFD WT but not in TREM-1 KO mice (Supplementary Figure 2).

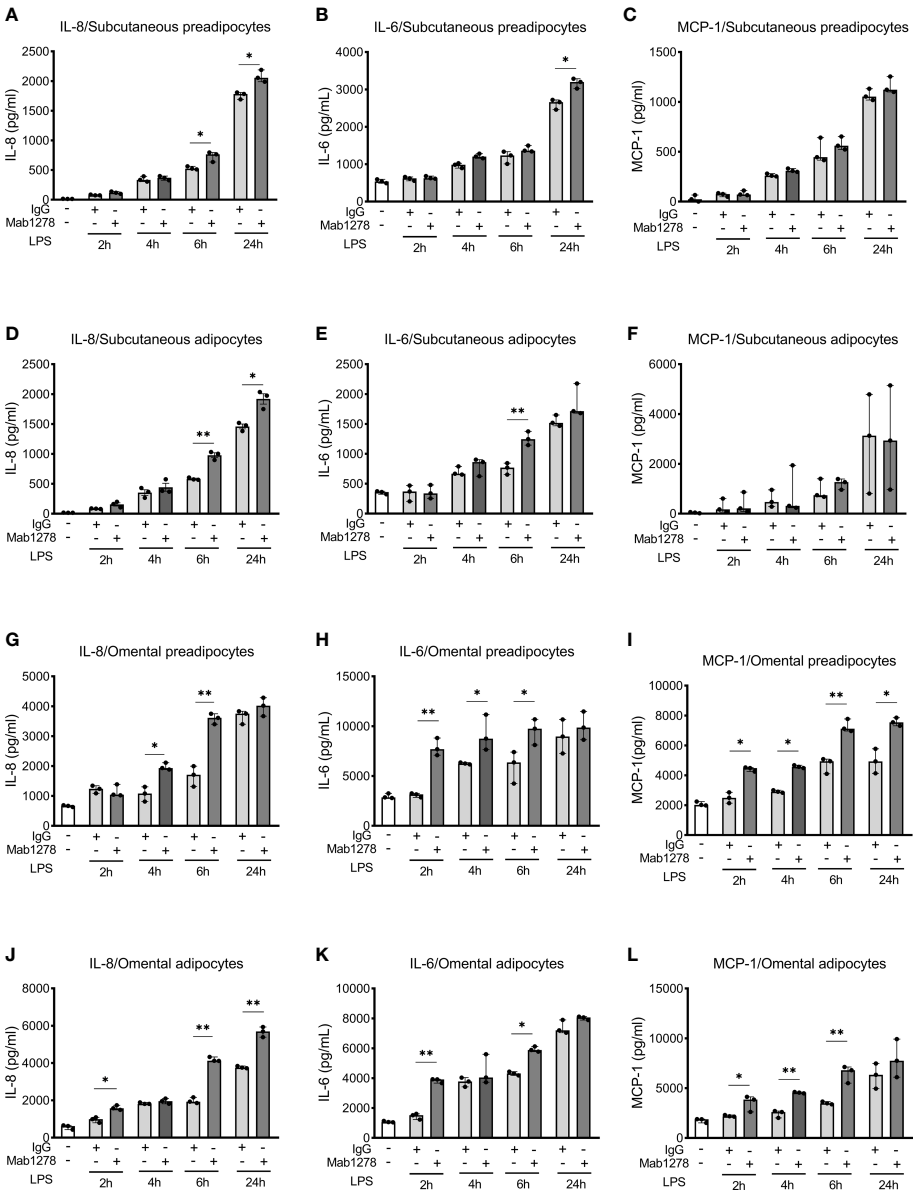

FIGURE 2
Activation of TREM-1 increases LPS-induced inflammation in human subcutaneous and omental pre-adipocyte and adipocytes. Automated multiplex ELISA quantification of IL-8, IL-6, and MCP-1 in cell supernatants from subcutaneous pre-adipocytes **(A–C)**, adipocytes **(D–F)**, and omental pre-adipocytes **(G–I)**, adipocytes **(J–L)**. Cells were incubated under resting conditions or stimulated with LPS (100 ng/ml) with or without TREM-1 agonist (MAB1278 at 5µg/ml) or control immunoglobulin G (IgG) for indicated times. Data are representative of 3 independent experiments each performed on three different donors. The significance between the IgG and MAB1278 conditions was determined using the Mann-Whitney test *p < 0.05, **p < 0.01. Data are presented as median and 95% confidence interval.

4 Discussion

Here we show that TREM-1 is expressed and functional in (pre-) adipocytes and that its genetic ablation confers favorable effects in HFD mice including reduction of weight gain, inflammation, and insulin resistance.

Although TREM-1 was initially considered to be only expressed by myeloid cells (neutrophils, monocytes/macrophages), it has been observed in many other cell types including epithelial or endothelial cells (22, 23). Whatever its cellular localization, TREM-1 activation leads to an amplification of the inflammatory response triggered by the

10.3389/fendo.2022.983827

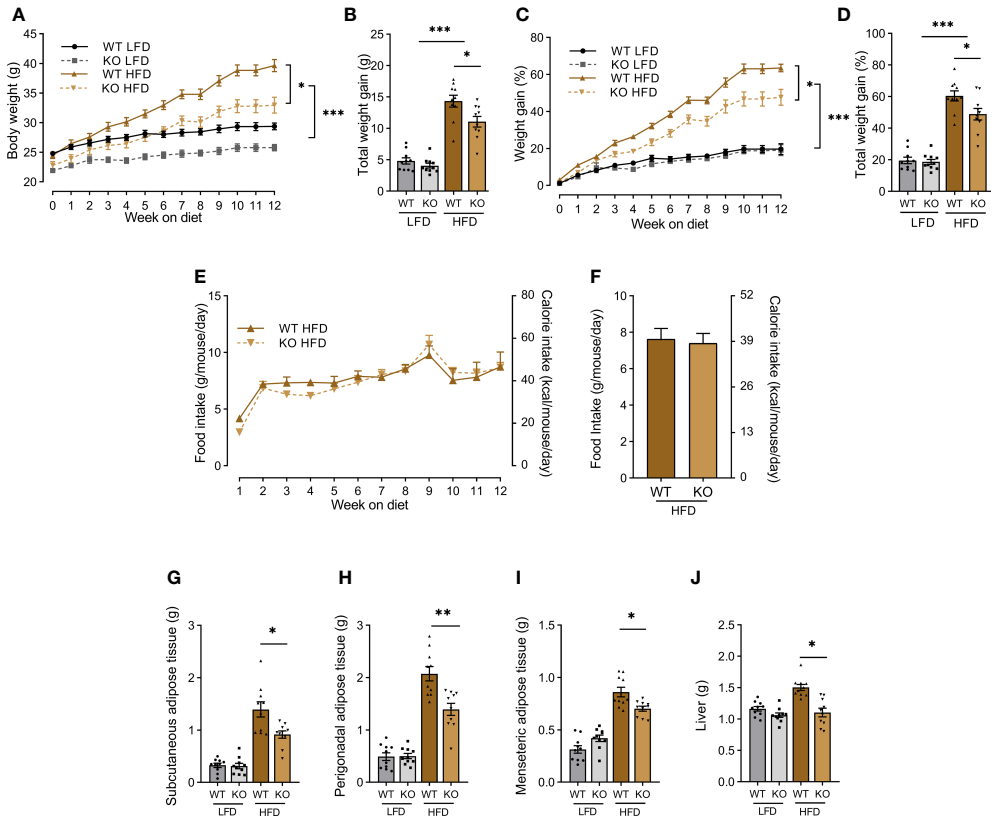

FIGURE 3
Trem1 deletion limits weight gain in HFD mice. **(A)** Body weights of Wild-Type (WT) or TREM-1 Knock-Out (KO) mice fed with control Low Fat Diet (LFD) or High Fat Diet (HFD) during 12 weeks. **(B)** Total body weight gain (g), **(C)** body weight gain (%), **(D)** total body weight gain (%), **(E)** food and calorie intake over 12 weeks, **(F)** mean of food and calorie intake over 12 weeks in WT and KO mice fed with LFD or HFD (n=10 mice per groups One-way ANOVA analysis). **(G)** subcutaneous, **(H)** perigonadal, **(I)** mesenteric adipose tissue, and **(J)** liver weight after 12 weeks of feeding of WT and KO LFD and HFD mice. (n=10 mice per group Student's *t*-test analysis). Data are presented as mean ± SEM (*p < 0.05, **p < 0.01, ***p < 0.001).

previous engagement of TLRs. The deleterious role of TREM-1 over-activation is established in acute diseases such as septic shock (9) or myocardial infarction (10), as well as during chronic disorders such as atherosclerosis (13).

In 187 young, healthy, non-obese adults, Vasquez et al. showed that those with several cardiometabolic risk factors (hypertension, hypertriglyceridemia, low HDL, or abdominal obesity) had higher serum concentrations of sTREM-1 (18), a biomarker of the TREM-1 pathway activation (24), and suggested that the follow-up of this marker may alert on the development of a future metabolic syndrome.

In a small population (n=22) of obese patients, Subramanian et al. observed the presence of TREM-1 in tissue biopsies (liver, omental, and subcutaneous tissues), as well as elevated plasma sTREM-1 concentrations as compared to non-obese control subjects (25). Interestingly, TREM-1 expression was higher in diabetic obese as compared to non-diabetic obese patients, suggesting an association between insulin resistance and TREM-1 activation.

As adipose tissue is made of many different cell types (adipocytes, myeloid cells, stromal cells…), we first confirmed the presence of TREM-1 in pre-, and adipocytes and observed that its expression seems to be higher in omental than in subcutaneous adipose cells. Moreover, TREM-1 expression was upregulated following LPS stimulation in omental (pre-) adipocytes. In line with its role in amplifying the inflammatory response, we observed that TREM-1 activation increased the production of some cytokines and chemokines by adipose cells, especially the omental ones.

Having demonstrated the expression and functionality of TREM-1 in adipose cells, we moved to the classical diet-induced obesity model in mice. Although the difference is not statistically significant, the body weight of TREM-1 KO mice is slightly lower than wild mice of the same age. To study the evolution of weight gain, we expressed the results in percentages. We observed that the genetic ablation of *Trem1* dampened HFD-induced weight gain, inflammation, and insulin resistance, hallmarks of obesity. Although the

10.3389/fendo.2022.983827

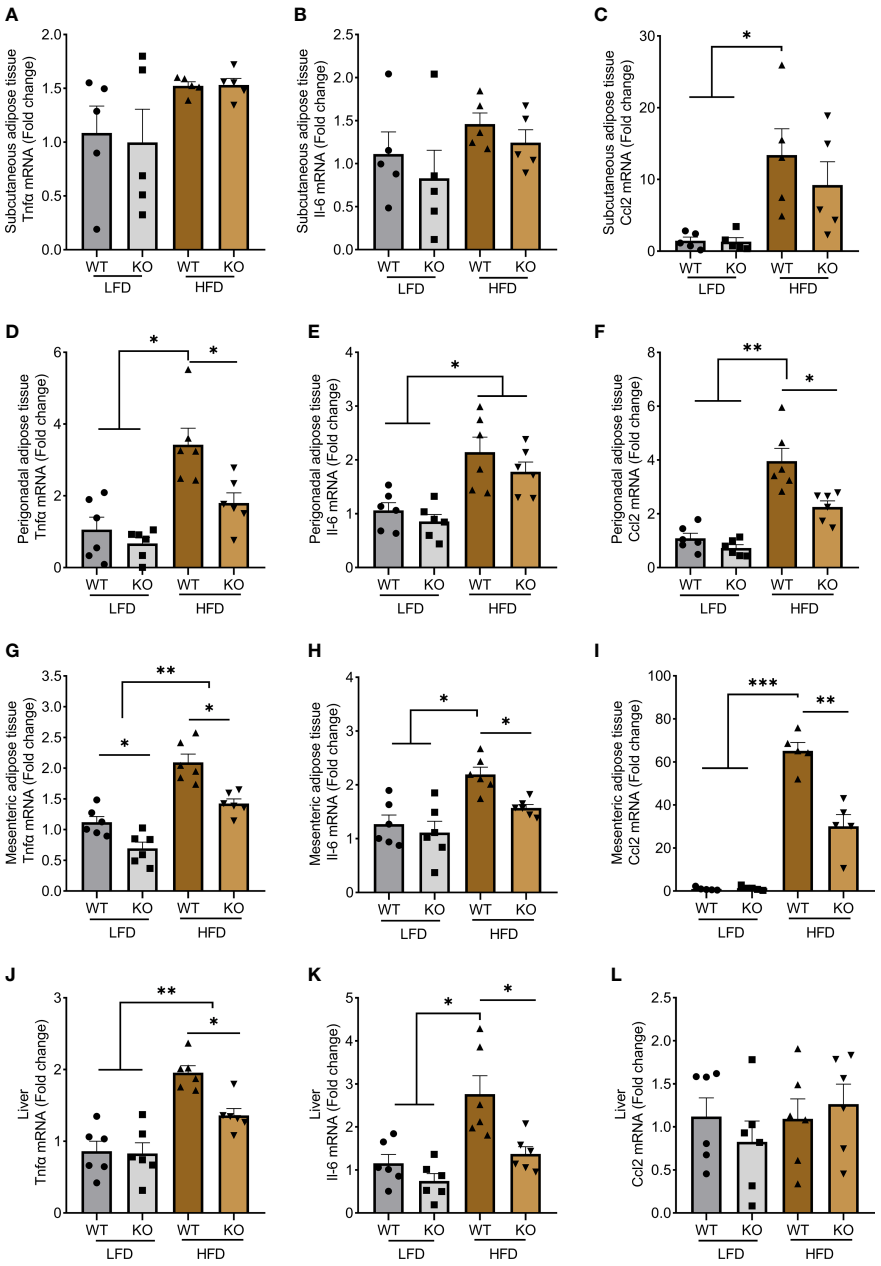

FIGURE 4
Trem1 deletion decreases inflammation in obese mice. Quantification of *Tnfα*, *Il6*, and *Ccl2* mRNA expression by RT-qPCR in **(A–C)** subcutaneous, **(D–F)** perigonadal, **(G–I)** mesenteric adipose tissue, and **(J–L)** liver from WT or TREM-1 KO mice fed with control LFD or HFD. Data are presented as mean ± SEM, n=5-6 mice per group (Kruskal Wallis test *p < 0.05, **p < 0.01, ***p < 0.001).

precise mechanisms by which TREM-1 inhibition confers protection remain to be elucidated, we hypothesized that the reduction of the HFD-induced inflammation may be the *primum movens* preventing the development of insulin resistance and thus breaking the vicious circle (HFD induces inflammation that leads to insulin resistance that alters energy use and fat deposition and perpetuates inflammation). Indeed, Li et al. (26) showed that oxidized low-density lipoprotein (oxLDL), whose production is increased during HFD, can activate TREM-1 that in turn contributes to atherogenesis and foam cell formation by enhancing proinflammatory cytokine production. The link between oxLDL and TREM-1-induced inflammation has recently been confirmed by Wang et al. (27).

10.3389/fendo.2022.983827

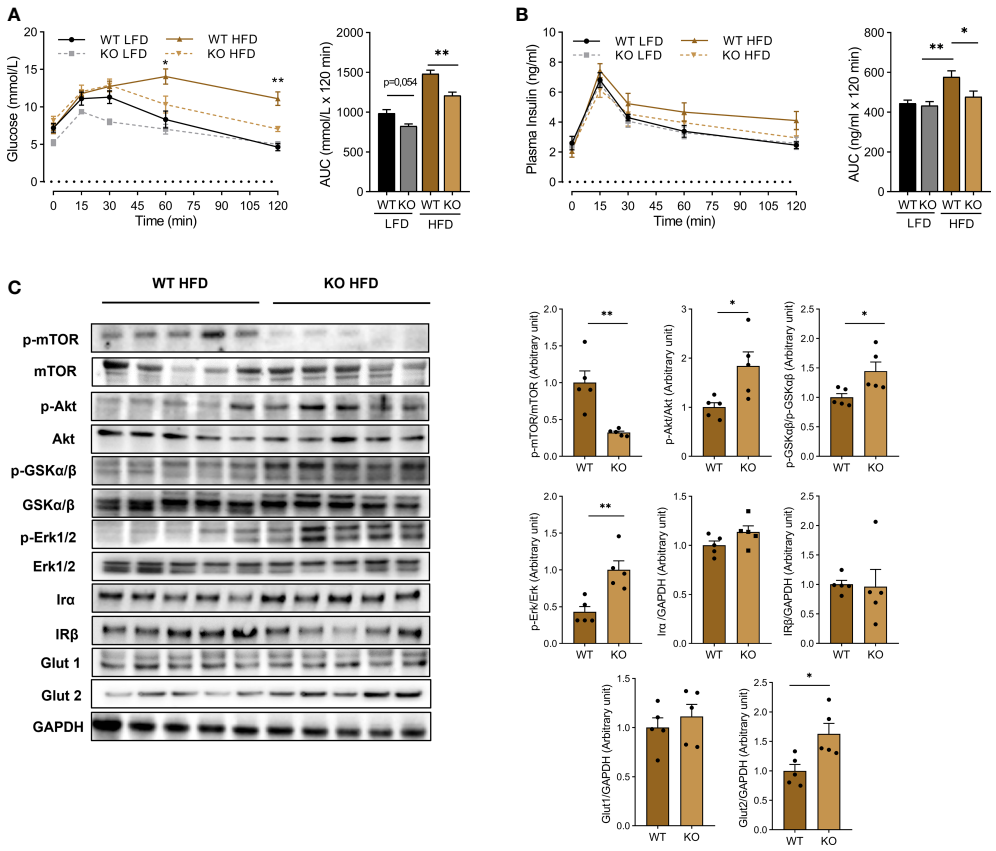

FIGURE 5
Trem1 deletion dampens HFD-induced insulin resistance liver. **(A)** Blood glucose and **(B)** insulin were measured during an oral glucose tolerance test on WT or TREM-1 KO mice fed with control LFD or HFD after 10 weeks of diet. Mice were fasted for 6 hours before the test. (AUC: Area Under the Curve). Data were presented mean ± SEM, n=5 mice per group. Brown-Forsythe and Welch ANOVA were used for Glucose and insulin measurement to compare WT HFD vs KO HFD (*p < 0.05, **p < 0.01). **(C)** Western blot of liver lysates and their densitometric quantification. Data were presented as mean ± SEM, n=5 mice per group (Mann-Whitney test *p < 0.05, **p < 0.01).

However, as we used TREM-1 KO animals, we are left with the question of the cell type(s) involved in this protective genotype: is it the deletion of *Trem1* on adipocytes, myeloid cells, or both that confers beneficial effects? Further studies are needed using adipocyte-specific *Trem1* deletion, or irradiated TREM-1 KO mice reconstituted with bone marrow from WT littermates.

The TREM-1 KO model can be viewed as a 'preventive' model, and then another important question arises: is the modulation of TREM-1 able to reverse an established phenotype? To address this we could use the TREM-1 inhibitory peptide Nangibotide (under clinical study in septic shock patients) but this would require repeated injection as its half-life is very short (28). The administration of an antagonist antibody would be more practical but it does not exist yet.

Several questions remain unanswered. We were able to determine the mechanisms involved in weight gain differences. Food intake monitoring indicated it was not due to fluctuation in calorie intake and that *Trem1* ablation didn't modify leptin secretion. TREM-1 could have affected food assimilation by influencing the intestinal microbiota or energy expenditure through variation in the population of beige adipocytes. Moreover, it is necessary to determine whether *Trem1* deletion could provide long-term protection for mice from the development of obesity-related comorbidities. Finally, we could not determine whether the reduction in insulin resistance was due to weight differences or to a more direct protective effect of the *Trem1* deletion. Anyway, TREM-1 activation seems to have a role in diet-induced obesity in mice by reducing weight gain, liver inflammation and protecting

against associated comorbidities such as insulin resistance and cardiac dysfunction. Its pharmacological modulation deserves further investigation with the aim to break the vicious circle of insulin resistance and inflammation.

Data availability statement

The original contributions presented in the study are included in the article/Supplementary Material. Further inquiries can be directed to the corresponding author.

Ethics statement

The animal study was reviewed and approved by French ethics committee (Number 23273).

Author contributions

BB and SG conceived the study. BB, NT, MM, LP, and ED performed experiments. MD reviewed the data. BB and SG wrote the first draft of the manuscript. All authors read and approved the final version of the manuscript. All authors contributed to the article and approved the submitted version.

Funding

This work was supported by a grant from the French ministry of Higher Education and Research.

Acknowledgments

The authors thank Kevin Carrasco, Lucie Jolly, Amir Boufenzer for their expertise, and Julie Voison Christophe, Nelly Colne, Marc-Damien Lourenco-Rodrigues, and Pauline Renard for their technical assistance.

Conflict of interest

Authors MD and MM are employees of Inotrem SA, a French company that develops TREM-1 inhibitors. Authors SG and MD are the co-founders of Inotrem SA.

The authors declare that this study received funding from Inotrem SA. The funder was involved in data recovery.

Publisher's note

Supplementary material

The Supplementary Material for this article can be found online at: https://www.frontiersin.org/articles/10.3389/fendo.2022.983827/full#supplementary-material

References

1. Liu R, Nikolajczyk BS. Tissue immune cells fuel obesity-associated inflammation in adipose tissue and beyond. *Front Immunol* (2019) 10:1587. doi: 10.3389/fimmu.2019.01587

2. Piché M-E, Tchernof A, Després J-P. Obesity phenotypes, diabetes, and cardiovascular diseases. *Circ Res* (2020) 126:1477–500. doi: 10.1161/CIRCRESAHA.120.316101

3. Akbari M, Lankarani KB, Tabrizi R, Ghayour-Mobarhan M, Peymani P, Ferns G, et al. The effects of curcumin on weight loss among patients with metabolic syndrome and related disorders: A systematic review and meta-analysis of randomized controlled trials. *Front Pharmacol* (2019) 10:649. doi: 10.3389/fphar.2019.00649

4. Osborn O, Brownell SE, Sanchez-Alavez M, Salomon D, Gram H, Bartfai T. Treatment with an interleukin 1 beta antibody improves glycemic control in diet-induced obesity. *Cytokine* (2008) 44:141–8. doi: 10.1016/j.cyto.2008.07.004

5. Tak YJ, Lee SY. Long-term efficacy and safety of anti-obesity treatment: Where do we stand? *Curr Obes Rep* (2021) 10:14–30. doi: 10.1007/s13679-020-00422-w

6. Bouchon A, Dietrich J, Colonna M. Cutting edge: Inflammatory responses can be triggered by TREM-1, a novel receptor expressed on neutrophils and monocytes. *J Immunol* (2000) 164:4991–5. doi: 10.4049/jimmunol.164.10.4991

7. Carrasco K, Boufenzer A, Jolly L, Le Cordier H, Wang G, Heck AJ, et al. TREM-1 multimerization is essential for its activation on monocytes and neutrophils. *Cell Mol Immunol* (2019) 16:460–72. doi: 10.1038/s41423-018-0003-5

8. Klesney-Tait J, Turnbull IR, Colonna M. The TREM receptor family and signal integration. *Nat Immunol* (2006) 7:1266–73. doi: 10.1038/ni1411

9. Bouchon A, Facchetti F, Weigand MA, Colonna M. TREM-1 amplifies inflammation and is a crucial mediator of septic shock. *Nature* (2001) 410:1103–7. doi: 10.1038/35074114

10. Boufenzer A, Lemarié J, Simon T, Derive M, Bouazza Y, Tran N, et al. TREM-1 mediates inflammatory injury and cardiac remodeling following myocardial infarction. *Circ Res* (2015) 116:1772–82. doi: 10.1161/CIRCRESAHA.116.305628

11. Xu P, Zhang X, Liu Q, Xie Y, Shi X, Chen J, et al. Microglial TREM-1 receptor mediates neuroinflammatory injury *via* interaction with SYK in experimental ischemic stroke. *Cell Death Dis* (2019) 10:555. doi: 10.1038/s41419-019-1777-9

12. Kökten T, Gibot S, Lepage P, D'Alessio S, Hablot J, Ndiaye N-C, et al. TREM-1 inhibition restores impaired autophagy activity and reduces colitis in mice. *J Crohns Colitis* (2018) 12:230–44. doi: 10.1093/ecco-jcc/jjx129

13. Joffre J, Potteaux S, Zeboudj L, Loyer X, Boufenzer A, Laurans L, et al. Genetic and pharmacological inhibition of TREM-1 limits the development of

experimental atherosclerosis. *J Am Coll Cardiol* (2016) 68:2776–93. doi: 10.1016/j.jacc.2016.10.015

14. Collins CE, La DT, Yang H-T, Massin F, Gibot S, Faure G, et al. Elevated synovial expression of triggering receptor expressed on myeloid cells 1 in patients with septic arthritis or rheumatoid arthritis. *Ann Rheum Dis* (2009) 68:1768–74. doi: 10.1136/ard.2008.089557

15. Gao S, Yuan L, Wang Y, Hua C. Enhanced expression of TREM-1 in splenic cDCs in lupus prone mice and it was modulated by miRNA-150. *Mol Immunol* (2017) 81:127–34. doi: 10.1016/j.molimm.2016.12.006

16. Ho C-C, Liao W-Y, Wang C-Y, Lu Y-H, Huang H-Y, Chen H-Y, et al. TREM-1 expression in tumor-associated macrophages and clinical outcome in lung cancer. *Am J Respir Crit Care Med* (2008) 177:763–70. doi: 10.1164/rccm.200704-641OC

17. Gibot S, Kolopp-Sarda M-N, Béné M-C, Bollaert P-E, Lozniewski A, Mory F, et al. A soluble form of the triggering receptor expressed on myeloid cells-1 modulates the inflammatory response in murine sepsis. *J Exp Med* (2004) 200:1419–26. doi: 10.1084/jem.20040708

18. Vázquez CMP, Costa JO, Bomfim LGS, Pires LV, da Silva DG, Fukutani KF, et al. Oxidized low-density lipoprotein (Ox-LDL) and triggering receptor-expressed myeloid cell (TREM-1) levels are associated with cardiometabolic risk in nonobese, clinically healthy, and young adults. *Oxid Med Cell Longev* (2019) 2019:7306867. doi: 10.1155/2019/7306867

19. Andrikopoulos S, Blair AR, Deluca N, Fam BC, Proietto J. Evaluating the glucose tolerance test in mice. *Am J Physiol Endocrinol Metab* (2008) 295:E1323–1332. doi: 10.1152/ajpendo.90617.2008

20. Saxton RA, Sabatini DM. mTOR signaling in growth, metabolism, and disease. *Cell* (2017) 168:960–76. doi: 10.1016/j.cell.2017.02.004

21. Khalid M, Alkaabi J, Khan MAB, Adem A. Insulin signal transduction perturbations in insulin resistance. *Int J Mol Sci* (2021) 22:8590. doi: 10.3390/ijms22168590

22. Schmaußer B, Endrich S, Beier D, Moran AP, Burek CJ, Rosenwald A, et al. Triggering receptor expressed on myeloid cells-1 (TREM-1) expression on gastric epithelium: Implication for a role of TREM-1 in helicobacter pylori infection. *Clin Exp Immunol* (2008) 152:88–94. doi: 10.1111/j.1365-2249.2008.03608.x

23. Jolly L, Carrasco K, Derive M, Lemarié J, Boufenzer A, Gibot S. Targeted endothelial gene deletion of triggering receptor expressed on myeloid cells-1 protects mice during septic shock. *Cardiovasc Res* (2018) 114:907–18. doi: 10.1093/cvr/cvy018

24. Jolly L, Carrasco K, Salcedo-Magguilli M, Garaud J-J, Lambden S, van der Poll T, et al. sTREM-1 is a specific biomarker of TREM-1 pathway activation. *Cell Mol Immunol* (2021) 18:2054–6. doi: 10.1038/s41423-021-00733-5

25. Subramanian S, Pallati PK, Sharma P, Agrawal DK, Nandipati KC. Significant association of TREM-1 with HMGB1, TLRs and RAGE in the pathogenesis of insulin resistance in obese diabetic populations. *Am J Transl Res* (2017) 9:3224–44.

26. Li H, Hong F, Pan S, Lei L, Yan F. Silencing triggering receptors expressed on myeloid cells-1 impaired the inflammatory response to oxidized low-density lipoprotein in macrophages. *Inflammation* (2016) 39:199–208. doi: 10.1007/s10753-015-0239-5

27. Wang YK, Wang J, Hua F, Shen YL, Han L, You JY, et al. TREM-1 modulates dendritic cells maturation and dendritic cell-mediated T-cell activation induced by ox-LDL. *Oxid Med Cell Longevity* (2022) 2022:e3951686. doi: 10.1155/2022/3951686

28. Parent M, Boudier A, Maincent P, Gibot S, Ait-Oufella H, Boufenzer A, et al. LR12-peptide quantitation in whole blood by RP-HPLC and intrinsic fluorescence detection: Validation and pharmacokinetic study. *Biomed Chromatogr* (2017) 31: e3877. doi: 10.1002/bmc.3877

frontiers | Frontiers in Endocrinology

TYPE Original Research
PUBLISHED 13 January 2023
DOI 10.3389/fendo.2022.1013018

OPEN ACCESS

EDITED BY
Undurti Narasimha Das,
UND Life Sciences LLC, United States

REVIEWED BY
Mh Busra Fauzi,
Independent Researcher, Kuala Lumpur, Malaysia
Qian Lin,
University of Louisville, United States

*CORRESPONDENCE
Zhifeng Cheng
002537@hrbmu.edu.cn

†These authors have contributed equally to this work

SPECIALTY SECTION
This article was submitted to Diabetes: Molecular Mechanisms, a section of the journal Frontiers in Endocrinology

RECEIVED 06 August 2022
ACCEPTED 23 November 2022
PUBLISHED 13 January 2023

CITATION
Zhao Q, Xu J, Han X, Zhang Z, Qu J and Cheng Z (2023) Growth differentiation factor 10 induces angiogenesis to promote wound healing in rats with diabetic foot ulcers by activating TGF-β1/Smad3 signaling pathway. *Front. Endocrinol.* 13:1013018. doi: 10.3389/fendo.2022.1013018

Growth differentiation factor 10 induces angiogenesis to promote wound healing in rats with diabetic foot ulcers by activating TGF-β1/Smad3 signaling pathway

Qingsong Zhao†, Jinmei Xu†, Xu Han, Zheqi Zhang, Jiahui Qu and Zhifeng Cheng*

Department of Endocrinology, The Fourth Affiliated Hospital of Harbin Medical University, Harbin, China

Background: Diabetic foot ulcer (DFU) represents a highly-prevalent complication of diabetes mellitus (DM). Herein, the current study sought to identify the role of growth differentiation factor 10 (GDF-10) in wound healing in DFU *via* regulation of the transforming growth factor-beta 1 (TGF-β1)/Smad3 pathway.

Methods: DM- and DFU-related microarray datasets GSE29221 and GSE134431 were firstly retrieved, and weighted gene co-expression network analysis (WGCNA) was carried out to construct a co-expression network affecting wound healing in DFU, followed by differential analysis. A protein-protein interaction (PPI) network of the DFU-related genes was subsequently constructed, and the core genes and signaling pathways in DFU were screened with the Gene Ontology and Kyoto Encyclopedia of Genes and Genomes functional analyses. A DFU rat model was constructed for mechanism verification of the effect of GDF-10 on wound healing in DFU.

Results: WGCNA screened five co-expression modules, and the brown module was most closely-related to DM. Clustering analysis screened 4417 candidate genes, of which 175 differential genes were associated with wound healing, further involved in TGF-β1/Smad3 signaling pathway regulation of wound healing in DFU. The PPI network analysis predicted that GDF-10 might regulate the TGF-β1/Smad3 signaling pathway to participate in DFU development. Results of animal experimentation showed that the wound healing rates of NFU, DFU, DFU + GDF and GDF + SIS3 groups on the 22nd day were (87.66 ± 6.80)%, (56.31 ± 7.29)%, (71.64 ± 9.43)% and (55.09 ± 7.13)%, respectively. Besides, the expression of TGF-β1 in NFU, DFU, DFU + GDF and GDF + SIS3 groups was 0.988 ± 0.086, 0.297 ± 0.036, 0.447 ± 0.044, and 0.240 ± 0.050, respectively, and that of Smad3 was 1.009 ± 0.137, 0.145 ± 0.017, 0.368 ± 0.048, and 0.200 ± 0.028, respectively. Specifically, GDF-10 exerted a significant diminishing effect on fasting blood

glucose level, and promoted wound healing in DFU rats, in addition to up-regulation of VEGF, FGF, Ang-1, TGF-β1, Smad3 and enhancement of IL-1b, IL-6, TNF-a and MMP-9, thereby promoting fibroblast proliferation, collagen deposition and angiogenesis.

Conclusions: Our findings highlight that GDF-10 may promote angiogenesis by activating TGF-β1/Smad3 signaling, thereby promoting wound healing in DFU rats.

KEYWORDS

GDF-10, TGF-β1/Smad3 signaling, diabetic foot ulcer, wound healing, angiogenesis, GEO database

Introduction

Diabetic foot ulcer (DFU) is understood as a consequence of peripheral neuropathy and peripheral arterial disorder in patients afflicted by diabetes mellitus (DM) (1). As a refractory complication of diabetes, DFU is featured by disturbed inflammatory, as well as impaired proliferative stages of wound healing (formation of granulation tissue, collagen deposition, proliferation of fibroblast cells and angiogenesis as hallmarks) (2). DFU accounts for significant morbidity and mortality, and can result in hospitalization and lower limb amputation if not treated in a timely-manner (3). In light of the same, it is prudent to promote diabetic wound healing for prevention of ulcer infections as well as subsequent amputations (4). Interestingly, a number of growth factors are closely-correlated with the repair cells, and further possess great potentials in wound repair, among which fibroblast growth factor is one of them (5). Meanwhile, activation of the PI3K/Akt/mTOR pathway can lead to the up-regulation of VEGF, FGF and EGF expressions, facilitating cell growth and migration, angiogenesis and collagen synthesis, inducing EMT and accelerating wound healing (6).

Growth differentiation factor 10 (GDF-10), also known as bone morphogenic protein-3b (Bmp3b), is a member of the transforming growth factor (TGF)-β superfamily (7), and intriguingly, possess the ability to promote wound healing in diabetic patients (8). In addition, GDF-10 is well-known for its important roles in maintaining homeostasis and glucose metabolism, and even diminishing cardiovascular risk (9). What's more, GDF-10 has been shown to protect against islet graft rejection in recipient diabetic mice (10). Herein, initial analysis using the Gene Expression Omnibus (GEO) database predicted that GDF-10 and TGF-β1/Smad3 signaling pathway might participate in wound healing in DFU. As previously reported, the up-regulation of GDF-10 contributes to the selective activation of Smad3 phosphorylation, which is dependent on the TGF-β receptor (11). Inherently, TGF-β1 is regarded as a multifunctional gene with regulatory functions in scar formation for wound healing and angiogenesis (12). Importantly, the secretion of TGF-β1 is crucial for angiogenesis in the process of wound healing in DFU (13). Meanwhile, Smad proteins serve as key downstream regulators of the signaling activities regulated by TGF-β family, including TGF-βs and GDF members (14). Furthermore, a prior study indicated that up-regulation of TGF-β1 and Smad3 expression by lncRNA H19 can aid the promotion of wound healing of DFU by regulating the biological behaviors of fibroblasts (15). Taking the aforementioned reports into consideration, we proposed a hypothesis that GDF-10 might play a regulatory role in wound healing in DFU with the involvement of the TGF-β1/Smad3 signaling pathway, and thus performed a series of experiments for verification.

Materials and methods

Ethical approval

The current study was performed with the approval of the Ethics Committee of The Fourth Affiliated Hospital of Harbin Medical University. All animal experimentation was conducted in strict accordance with the guidelines for the care and use of laboratory animals.

GEO microarray dataset acquisition

Firstly, the DM expression profile dataset GSE29221 was retrieved from the GEO database, which included 12 non-DM tissue samples and 12 DM tissue samples. This database was

based on the platform information GPL6947. Additionally, the DFU dataset GSE134431 was obtained, comprising of 8 normal samples and 6 DFU samples, and was based on the platform information GPL18573.

Weighted gene co-expression network analysis

A co-expression network of DM samples was constructed using the WGCNA algorithm. Gene co-expression network was established with the R software "WGCNA" package, and differentially expressed genes (DEGs) were screened and utilized to construct a weighted co-expression network. Hierarchical clustering analysis was subsequently performed using the Hclust function, then appropriate soft threshold was selected using the "pickSoftThreshold" function, and adjacent matrix was converted into topological overlap matrix. Hierarchical clustering dendrogram was constructed, and the genes with similar expression were divided into different modules and 50 genes were selected as the minimum number of genes in the module. To merge possibly similar modules, 0.25 was defined as the threshold of cutting height. Finally, the expression profile of each gene was summarized by the module genes, the correlation between the module genes and traits was calculated, and the most relevant modules were selected for further analysis.

Differential analysis

Differential analyses were carried out using the R software "limma" package. DEGs in GSE29221 and GSE134431 microarray datasets were screened with logFC > 1 and $p < 0.05$ serving as the screening condition. Volcano maps and expression heatmaps of DEGs were drawn simultaneously employing the "ggplot2" and "pheatmap" packages.

Intersection gene screening and functional enrichment analysis

Candidate genes were obtained through the intersection of the key genes in the weighted gene co-expression network and the DEGs in the GSE29221 and GSE134431 microarray datasets using the R software "venn" package. Protein-protein interaction (PPI) analysis based on the intersection genes was performed with "species" set as "human". The PPI results were subsequently ranked by gene correlation with the R software. Functional enrichment analysis was performed on the selected DEGs using the SangerBox website.

DM model establishment

A total of 48 Wistar rats (aged 6-weeks-old, weighing 200-220 g) were purchased from Beijing Vital River (Beijing, China), and reared in a specific-pathogen-free animal room (temperature: 22-25°C, humidity: 60-65%) under 12-h light/dark cycles. The included rats were allowed to acclimatize for one week prior to experimentation.

The rats were randomly divided into the two following groups: the control group (n = 12, rats were fed with standard diet) and the DM group (n = 36, rats were fed with high fat and high glucose diet). Prior to model establishment, the rats were fasted for 12 h with *ad libitum* access to water. The rats were weighed on the day of model establishment, blood samples were collected from the tail vein, and basal blood glucose levels were assessed with a glucose meter (Omnitest plus, Melsungen, Germany). Next, streptozocin (STZ; V900890, Merck, New Jersey, USA) was dissolved in a pH4.2 0.1 mol/L citric acid-sodium citrate solution (Aladdin, Shanghai, China) to prepare 1% solution. A single intraperitoneal injection of STZ solution at a dosage of 55 mg/kg body weight was administered to induce DM, while an intraperitoneal injection of an equal volume of citric acid-sodium citrate solution was performed for rats in the control group. After 72 h of STZ injection, the fasting blood glucose levels were measured with blood from the tail vein. Rats presenting with blood glucose level higher than 16.7 mmol/L, and typical symptoms of polydipsia, increased appetite, polyuria and wasting were regarded as DM rats. Rat body weight and blood glucose were measured weekly, and insulin was injected to achieve blood glucose control at 20 – 25 mmol/L.

DFU model establishment and grouping

After maintenance of hyperglycemia in DM rats (n = 40) for 8 weeks, the rats were treated with ketamine (dosage of 75 mg/kg, i.p.) and toluene thiazide (dosage of 10 mg/kg, i.p.) (X1251, Merck, New Jersey, USA) for anesthesia. A rectangular-shaped wound was created on each rat's instep using a soft clear plastic template, and a layer of skin with a standard area of 2 mm × 5 mm was then removed. The DM rats were randomly divided into the following different experimental groups (n = 10): the DFU group (DM rats injected with same volume of double-distilled water), the DFU + GDF-10 group (DM rats injected with 0.1 mg/kg of GDF-10 recombinant protein [1543-BP-025/CF, R&D Systems, Minneapolis, MN] *via* rat femoral artery and intermuscular of ischemic tissue around the wound), and the DFU + GDF-10 + SIS3 group (DM rats injected with 0.1 mg/kg of GDF-10 recombinant protein and 2 μM Smad inhibitor SIS3 (S3552, Selleck, Houston, Texas, USA) *via* rat femoral artery and intermuscular of ischemic tissue around the wound). Another

group of rats without DM induction was also subjected to wound injury to serve as control rats.

All rats were administered their respective concoctions at 1, 3, 5, 7, 10, 14, and 21 days, and the wound area was photographed using a camera. After 22 days, the rats were anesthetized with ether to obtain blood samples, followed by euthanasia, and the wound tissue was quickly removed and placed at -80°C for preservation.

Measurement of the wound area

The wound area was recorded with a camera at 1, 4, 6, 8, 11, 15, and 22 days, and calculated using the ImageJ analysis software. Calculation of wound healing percentage: wound healing percentage = [(initial wound area - wound area at calculation day)/initial wound area] * 100.

Hematoxylin and eosin staining

Fresh wound tissues of rats were collected, fixed with 4% paraformaldehyde, fixed with xylene, embedded with paraffin, and sliced. Following hydration, the slices were stained with hematoxylin (C0105, Beyotime, Shanghai, China) for 5-10 min and with eosin for 30 s - 2 min, followed by immersion in 70% ethanol for 10 s, 80% ethanol for 10 s, 90% ethanol for 10 s, absolute ethanol for 10 s. Afterwards, the slices were cleared twice with xylene, each for 5 min, sealed with neutral gum, and visualized under a microscope.

Masson trichrome staining

Fresh wound tissue of rats was collected, fixed with 4% formaldehyde solution, dehydrated, embedded, and sectioned. The paraffin-embedded sections were dewaxed with xylene and stained with Weigert hematoxylin for 10 min. After washing, the sections were soaked in Lichunred for 8 min, 2% glacial acetic acid for 1 min, 1% molybdate acid for 4 min, aniline blue for 5 min, then 0.2% glacial acetic acid-acid solution for 2 min, and treated with 95% alcohol. Later, the sections were cleared with xylene and finally sealed with neutral gum. The Masson-stained sections were visualized using a microscope.

Immunofluorescence

Fresh wound tissue of rats was fixed with 4% paraformaldehyde solution, dehydrated, embedded, and sectioned. Next, the sections were incubated with CD31 antibody (ab24590, Abcam, Cambridge, MA, USA) and SMA (ab128107, 1:100, Abcam, Cambridge, MA, USA) at 4°C overnight, and then treated with goat anti-mouse IgG H&L secondary antibody (ab150116, 1:200, Abcam, Cambridge, MA, USA) or goat anti-rabbit IgG H&L (Alexa Fluor® 488, ab150077, 1:200, Abcam, Cambridge, MA, USA) for 90 min at room temperature. Subsequently, the nuclei were stained with DAPI (D9542, Merck, New Jersey, USA), and the tissue sections were visualized under a fluorescence microscope (ApoTome 2, Carl Zeiss MicroImaging, Inc., Thornwood, NY, USA). Vascular number was determined by counting three random regions around the wound using the ImageJ analysis software.

Reverse transcription-quantitative polymerase chain reaction

Total RNA content was isolated from fresh wound granulation tissue of rats, homogenized using the TRIzol reagent (10296010, Thermo Fisher Scientific, Rockford, IL, USA) (1 mL per 100 mg tissue), and then mixed with chloroform (200 μL) and centrifuged at 4°C and 12000 g for 10 min. Next, the upper aqueous phase was collected, and mixed with isopropanol (500 μL) to precipitate RNA. Subsequently, the RNA was dissolved in RNA enzyme-free water (10-30 μL) and quantified by Nanodrop (Nanodrop 3300, Thermo Fisher Scientific, Rockford, IL, USA). One μg of total RNA was reverse-transcribed with the TaqMan reverse transcription reagent (N8080234, Thermo Fisher Scientific, Rockford, IL, USA). PCR analysis was performed using the PowerUp SYBR Green premix kit (A25741, Thermo Fisher Scientific, Rockford, IL, USA). Primer sequences are illustrated in Supplementary Table 1.

Enzyme-linked immunosorbent assay

Granulation tissue from fresh wounds of rats was collected, homogenized with pre-cooled PBS, centrifuged at 4°C at 1000 rpm for 20 min, followed by collection of supernatant. The levels of tumor necrosis factor-α (TNF-α) (H052-1, NanJing JianCheng Bioengineering Institute, Nanjing, China), interleukin-6 (IL-6) (H007-1-1, NanJing JianCheng Bioengineering Institute, Nanjing, China), interleukin- (IL)-1β (H002, NanJing JianCheng Bioengineering Institute, Nanjing, China), matrix metalloproteinase-9 (MMP-9) (E-EL-R3021, 7.81-500 ng/mL, Elabscience, TX, USA), TGF-β1 (70-EK981-96, 31.25-2000 pg/mL, Multi sciences (Lianke Biotech, Co., LTD., Hangzhou, China), vascular endothelial growth factor (VEGF) (ab100786, 0.82-200 pg/mL, Abcam, Cambridge, MA, USA), angiopoietin-1 (Ang1) (E-EL-R0626c, 0.16-10 ng/mL, Elabscience, TX, USA) were determined as per kit instructions.

Statistical analysis

All data were analyzed using the SPSS 21.0 statistical software (IBM Corp. Armonk, NY). Measurement data were expressed as mean ± standard deviation. Data comparisons between two groups were performed using *t*-tests. Data comparisons among multiple groups were conducted by one-way analysis of variance. A value of $p < 0.05$ was regarded statistically significant.

Results

WGCNA screened five co-expression modules of genes associated with DM

DM is a highly-prevalent metabolic disease characterized by hyperglycemia, with poor control inducing severe complications, of which DFU represents one of the most common chronic complications in patients with DM (16). Herein, we adopted the WGCNA algorithm to analyze the DFU-related genes, and functional enrichment analysis was further performed to clarify the biological functions of core genes. An online database was utilized to construct a PPI network to further investigate the mechanism of core genes in DFU.

Firstly, marker genes associated with DM were identified with the construction of a scale-free co-expression network with the R software package "WGCNA". The DM related GSE29221 microarray was selected for cluster evaluation, which comprised of 12 control samples and 12 DM samples. To test sample outliers, the samples were hierarchically clustered according to the distribution of sample expression values (Figure 1A), and the samples included in the analysis were slightly different. $\beta = 20$ (scale-free $R^2 = 0.9$) was regarded as the soft threshold to establish a scale-free network and establish a gene expression network (Figure 1B). Five co-expression modules were identified in the DM expression profile, with each color representing a different module (Figure 1C).

Clustering analysis identified 4417 candidate genes related to DFU

All genes were assessed and clustered by their correlation to obtain an expression cluster analysis map between the individual modules (Figure 2A). Pearson correlation analysis was carried out for each module gene with different groups. Five co-expression modules were obtained for subsequent analysis (Figure 2B), including the Meblue module (containing 621 genes), Mebrown module (containing 4417 genes), Megreen module (containing 156 genes), Meyellow module (containing 215 genes) and Megrey module (containing 877 genes) (Figure 2C; Supplementary Figures 1A–D). Module feature correlation analysis showed that the Mebrown module (containing 4417 genes) was most associated with the disease, and the correlation coefficient was 0.47. Therefore, the 4417 genes in the brown module were regarded as DM related genes.

Differential analysis selected 175 DEGs associated with wound healing in DFU

To further screen the key genes implicated in DFU, differential analyses were performed on the GSE29221 dataset and a total of 5338 DEGs were selected, of which 2286 were up-regulated and 3052 were down-regulated (Figure 3A; Supplementary Figure 2A).

Following differential analyses of the DFU-related microarray dataset GSE134431, a total of 5522 DEGs were obtained, of which 2961 genes were up-regulated and 2561 genes were down-regulated (Figure 3B; Supplementary Figure 2B).

To further screen the key genes involved in DFU, the DEGs of the GSE134431 microarray dataset, the DEGs of the GSE29221 microarray dataset and the brown module genes were intersected, which reared 175 intersection genes for subsequent functional analysis (Figure 3C).

The TGF-β1/Smad3 signaling pathway might be involved in wound healing in DFU

Decreased angiogenesis in damaged skin is regarded as a key reason for the impaired wound healing in DM complications (17). Accordingly, angiogenesis-related genes were screened using the GSEA database, and a total of 132 genes were obtained. The STRING analysis was adopted to construct a PPI network map of the angiogenesis and DFU-related genes (Figure 4A). In regard to previous studies, the molecular functions of the candidate gene regulation were deeply explored, and the GO function analysis and KEGG pathway analysis of the candidate genes were carried out.

Results of GO function illustrated that candidate genes in biological process (BP) were primarily enriched in the negative regulation of immune system process, regulation of immune effector process, antigen processing, presentation of endogenous antigen and cellular response to interferon-gamma in biological processes. Moreover, candidate genes in cellular component (CC) were primarily enriched in the MHC protein complex, collagen-containing extracellular matrix, endocytic vesicle membrane, integral component of lumenal side of endoplasmic reticulum membrane in cellular components. Additionally, candidate genes in molecular function (MF) were largely enriched in the glycosaminoglycan binding, extracellular

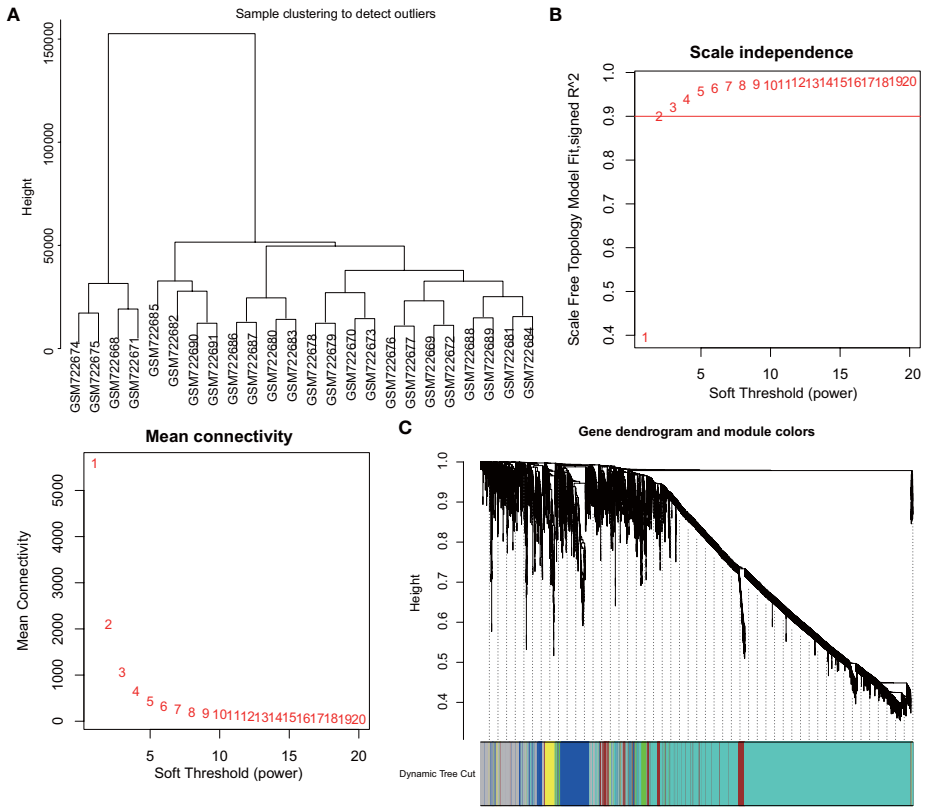

FIGURE 1
WGCNA identifies DM-related gene co-expression modules. **(A)**, Clustering dendrogram of GSE29221 gene expression profile. **(B)**, Scale-free fit index (top) of various soft threshold β and average connectivity (below); correlation coefficient (0.9) is represented by red line. **(C)**, Clustering dendrogram of gene expression network constructed by WGCNA; each color represents a module in the gene co-expression network.

matrix structural constituent, peptide antigen binding and peptide binding in molecular function (Figure 4B).

Furthermore, results of KEGG pathway analysis showed that the candidate genes were primarily enriched in RNA transport, type 1 DM, TFG-β signaling pathway, bladder cancer, endometrial cancer, longevity regulating pathway, TNF signaling pathway and inflammatory bowel disease, progesterone-mediated oocyte maturation, NF-kappa B signaling pathway, cholesterol metabolism and inostiol phosphate metabolism (Figure 4C). Among the aforementioned, type 1 DM and TGF-β signaling pathway were predominated.

Together, the above mentioned findings indicated that the candidate genes largely exerted roles in biological processes including angiogenesis regulation, extracellular matrix organization, extracellular structural organization, and the candidate genes were enriched in the endoplasmic reticulum cavity, collagen trimers, and collagen-containing extracellular matrix.

Moreover, the KEGG analysis results demonstrated that the candidate genes were involved in RNA transport, type 1 DM, TFG-β signaling pathway, TNF signaling pathway, and NF-κB signaling pathway, among which the TFG-β signaling pathway was predominated.

GDF-10 might be involved in wound healing in DFU *via* regulation of the TGF-β1/Smad3 signaling pathway

The interaction network between DEGs and angiogenesis-related proteins was constructed using a PPI network, and TGFBR3 was interacted with more proteins (Figure 5A). TGFBR3 represents a type III TGF-β superfamily receptor transmembrane, which influences angiogenesis and migration by regulating the TGF-β1/Smad3 signaling pathway (18). Further PPI analysis of the TGFBR3-related genes showed that TGFBR3 interacted with GDF-10 (Figure 5B), and these two genes were markedly poorly-expressed in DFU (Figure 5C, D). Meanwhile, BMP3B is a member of the TGF-β superfamily, and also known as GDF-10. Existing evidence suggests that GDF-10 can promote the differentiation and growth of osteoblasts (19).

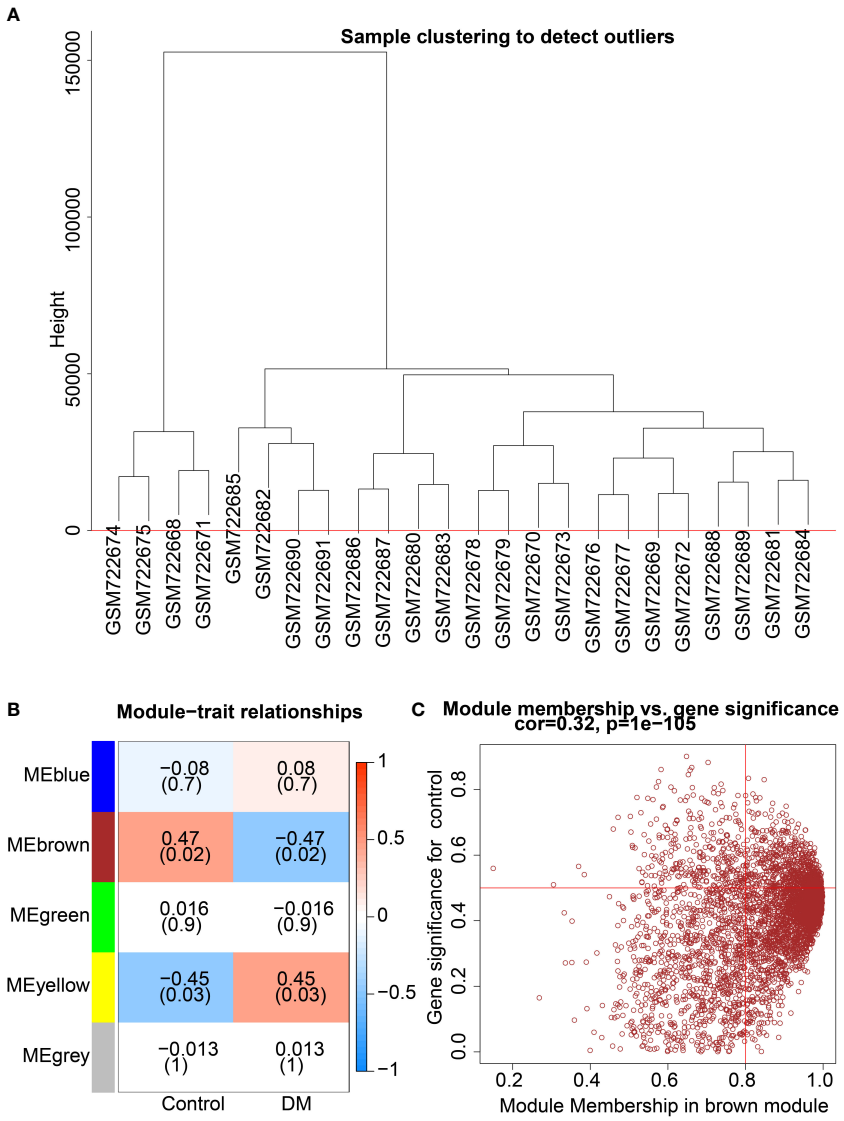

FIGURE 2
Screening of key co-expression module for DM-related genes. **(A)**, Clustering analysis according to correlation between modules to obtain expression cluster analysis diagram between modules. **(B)**, Correlation heat map between modules and traits in DM; each cell contains corresponding correlation and *p* value. **(C)**, Module correlation diagram of the brown module.

Meanwhile, GDF-10 can activate the TGFBR1/Smad3/ERK pathway to promote the growth and migration of tumor cells (20), and further regulate the recruitment and activation of Smad family transcription factors (21).

The transforming factor TGF-β1 is well-characterized for its role in DM (22), and further activates two key downstream mediators including Smad2 and Smad3 (23). Meanwhile, TGF-β is also implicated in the regulation of proliferation, differentiation, migration and survival of various different cell types (including blood endothelial cells) (24). Given the fact that GDF-10 is a member of the TGF-β family, we speculated that GDF-10 could activate the TGF-β1/Smad3 signaling pathway to stimulate angiogenesis, and thus promote wound healing in DFU.

GDF-10 stimulated angiogenesis and promoted wound healing in DFU rats

DFU rat models were established to further investigate the effect of GDF-10 on wound healing in DFU rats. The weight of DM rats showed a gradual decline, while GDF-10 treatment led to the opposing trends. Compared with the DM rats treated with GDF-10, the weight of DM rats treated with GDF-10 and Smad

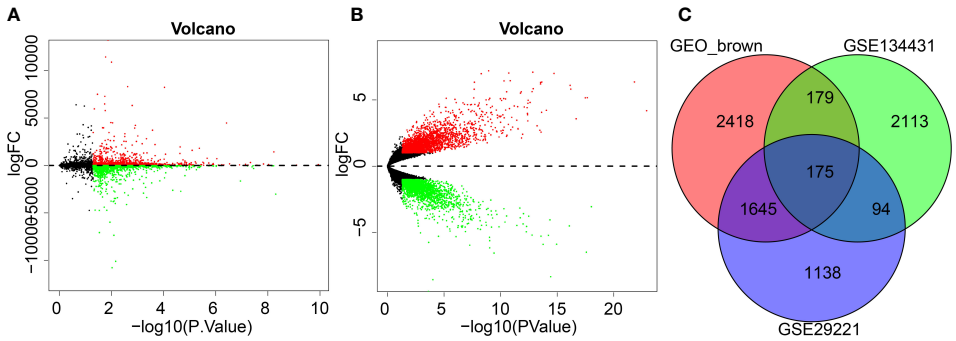

FIGURE 3
GEO differential analysis for screening DFU-related DEGs. **(A)**, Volcano map of GSE29221 dataset (Black color represents genes not differently expressed, red color represents up-regulated genes and green color represents downregulated genes). **(B)**, Volcano map of GSE134431 dataset (Black color represents genes not differently expressed, red color represents up-regulated genes and green color represents downregulated genes). **(C)**, Venn diagram shows brown modules obtained from intersection of DEGs in GSE134431 and GSE29221 datasets.

inhibitor SIS3 was decreased (Figure 6A). Meanwhile, fasting glucose results showed that blood glucose was increased in DFU rats, while DFU rats treated with GDF-10 presented with decreased blood glucose. Compared with the DFU rats treated with GDF-10, the DFU rats treated with GDF-10 and SIS3 presented with increased blood glucose levels (Figure 6B). Moreover, the wound healing area results showed that the control rats showed faster healing, and the redness and swelling around the wound subsided 15 days later. In contrast to the control rats, poor wound healing was noted in the DFU rats, and granulation tissue grew more slowly, in dark red color; there were more inflammatory exudates around the wound, and reduced healing area. Compared to the DFU rats, the DFU rats treated with GDF-10 exhibited minimal redness around the wound and no significant exudate, accompanied by rapidly growing granulation tissue and increased healing area, and the

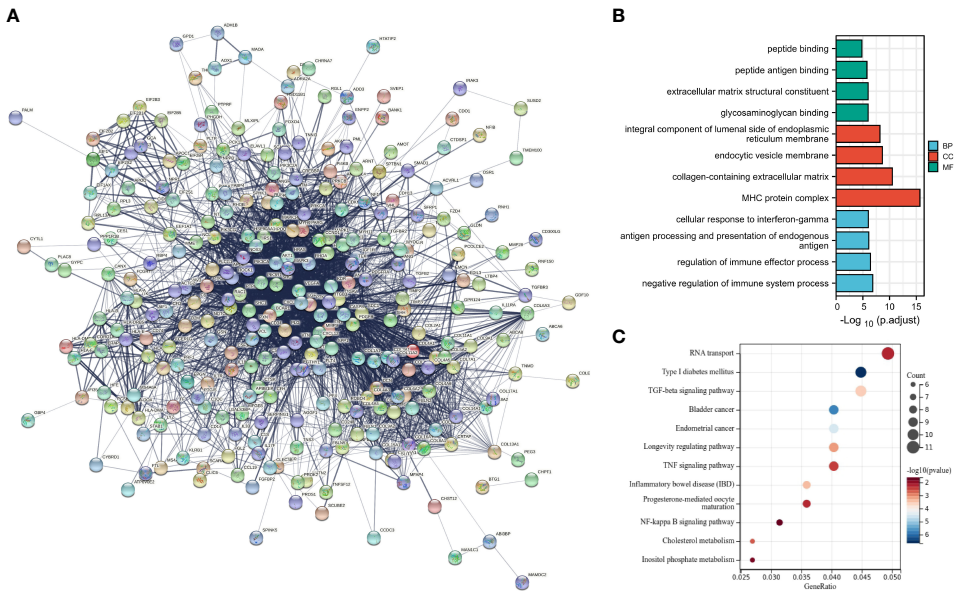

FIGURE 4
Construction of DFU-related gene network and screening of key pathway. **(A)**, PPI network of DFU related genes. **(B)**, GO function analysis of candidate genes at the biological process, cellular component and molecular function levels. **(C)**, KEGG pathway enrichment analysis of candidate genes.

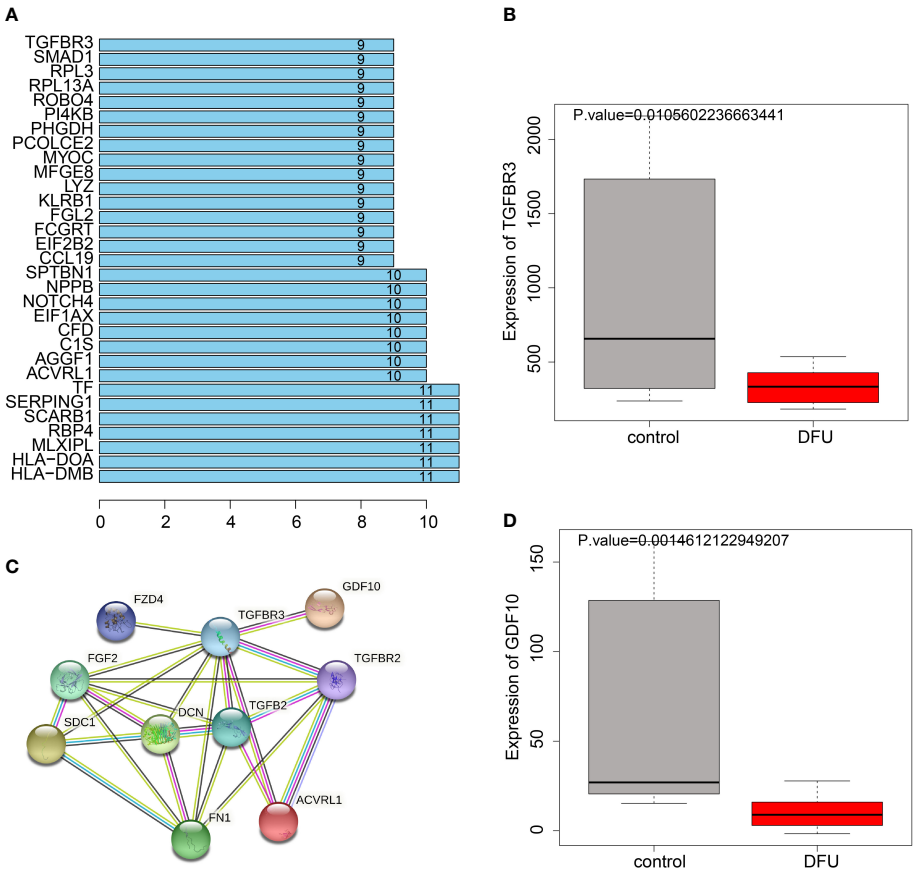

FIGURE 5
PPI relationship between TGFBR3 and GDF10. **(A)**, Degree values of the genes. **(B)**, PPI diagram showing interaction of genes with TGFBR3. **(C)**, Expression of TGFBR3 in DFU in GSE134431 dataset. **(D)**, GDF10 expression in DFU in GSE134431 dataset.

trends of which could be reversed by further treatment of SIS3 (Figure 6C).

Granulation tissue formation, collagen deposition, fibroblast proliferation and vascularization are widely-adopted as markers for wound healing (2). HE staining results illustrated that control rats exhibited less inflammatory cells and few new capillaries. Meanwhile, the DFU rats presented with more neutrophils and lymphocytes and rarely new capillaries. Compared with the DFU rats treated with GDF-10, the DFU rats co-treated with GDF-10 and SIS3 exhibited reduced fibroblasts and neonatal capillaries, and increased infiltration of inflammatory cells (Figure 6D). Masson trichrome staining was further performed to visualize collagen deposition in tissues, the results of which demonstrated fewer collagen fibers in DFU rats. Compared with DFU rats treated with GDF-10, those treated with GDF-10 and SIS3 in combination exhibited fewer collagen fibers (Figure 6E). Immunofluorescence detected wound neovascularization, and the results illustrated that total and mature vessels were decreased in DUF rats relative to control rats. Compared with the DFU rats treated with GDF-10, the DFU rats treated with GDF-10 and SIS3 presented with decreased total and mature vessels (Figure 6F).

Furthermore, RT-qPCR results demonstrated that the expression levels of Smad3, VEGF, Ang-1, TGF-β1, collagen I, and collagen III were decreased and the expression levels of IL-1β, IL-6, TNF-α, and MMP-9 were enhanced in DFU rats, while the opposing trends were noted following GDF-10 treatment; relative to GDF-10 treatment alone, both GDF-10 and SIS3 treatment brought about reductions in the expressions of Smad3, VEGF, Ang-1, TGF-β1, collagen I, and collagen III, but elevated those of IL-1β, IL-6, TNF-α, and MMP-9 (Figure 7A). ELISA results further depicted that expression levels of VEGF, Ang-1 and TGF-β1 were decreased, but expression levels of IL-1β, IL-6, TNF-α and MMP-9 were elevated in DFU rats, while the opposing trends were documented following GDF-10 treatment. Relative to the DFU rats treated with GDF-10, the DFU rats treated with GDF-10 and SIS3 presented with

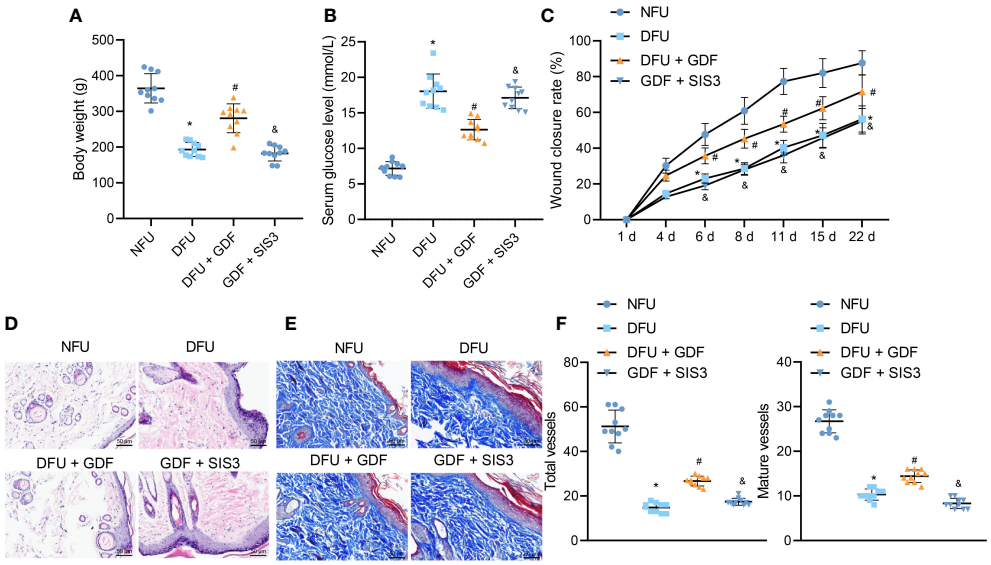

FIGURE 6
Effects of GDF10-stimulated angiogenesis on the wound healing in DFU rats. **(A)**, Rat weight. **(B)**, Blood glucose of rats after fasting. **(C)**, Representative picture of DFU rats after GDF10 treatment. **(D)**, HE staining of pathological changes in control rats and DFU rats of different treatment. **(E)**, Masson trichrome staining of collagen deposition in control rats and DFU rats of different treatment. **(F)** Immunofluorescence detection of angiogenesis in wounds: red fluorescent marks α-SMA, green fluorescent marks CD31, and blue fluorescent marks nucleus. Measurement data were expressed in the form of mean ± standard deviation. One-way ANOVA was used for comparison between multiple groups, and repeated measures ANOVA was used to compare data between groups at different times. $^{*}p < 0.05$ vs. the NFU group. $^{\#}p < 0.05$ vs. the DFU group. $^{\&}p < 0.05$ vs. the DFU + GDF group. Ten rats were used in each group.

decreased expression levels of VEGF, Ang-1, and TGF-β1 and increased expression levels of IL-1β, IL-6, TNF-α and MMP-9 (Figure 7B).

The above findings highlighted that GDF-10 could reduce blood glucose, TNF-α, IL-1β and IL-6 in DM rats and promote the expression of VEGF, TGF-β1 and Ang-1 to accelerate wound healing in DFU *via* activation of the TGF-β1/Smad3 signaling pathway; the therapeutic effect could be reversed after treatment with the Smad inhibitor SIS3.

Discussion

DFU is one of the most prevalent complications of DM, exerting a burden on not only the patients, but also on overall health, nursing practice, as well as the social environment (25). Herein, the current study sought to identify the role of GDF-10 in wound healing in DFU, and the obtained findings indicated that GDF-10 could facilitate wound healing in DFU *via* the activation of the TGF-β1/Smad3 signaling pathway, underlining a novel modality for DFU treatment.

Firstly, GEO-based analyses were widely-adopted in our study. The WGCNA algorithm screened five co-expression modules, wherein the brown module was most closely-associated with DM. Subsequent clustering analysis screened 4417 candidate genes, such that a total of 175 DEGs were found to be associated with wound healing. What's more, the TGF-β1/Smad3 signaling pathway was predicted as a key pathway for wound healing in DFU. In line with our findings, an ever-increasing number of studies have documented the roles of the TGF-β1/Smad3 signaling pathway in DFU and wound healing. For instance, the up-regulation of TGF-β and Smad2/3 by baicalin led to the suppression of wound healing in STZ-induced rat models of DFU (26). On the other hand, silencing of TGF-β1 and Smad3 *via* down-regulation of lncRNA H19 results in attenuated wound healing in DFU (15). Moreover, activation of TGF-β/Smad3 signaling pathway by fatty acid extracts can aid in facilitating cutaneous wound healing through promotion of angiogenesis (27). Further in accordance with our discovery, Zhang F et al. indicated that TGF-β1 is highly-expressed in the serum and the dorsalis pedis arteries of DFU patients, while being markedly lower in the muscles with ulcers relative to controls (28). Additionally, the activity of Smad3 has been suggested to serve as the requisite for wound healing functions of Periplaneta americana extracts (29).

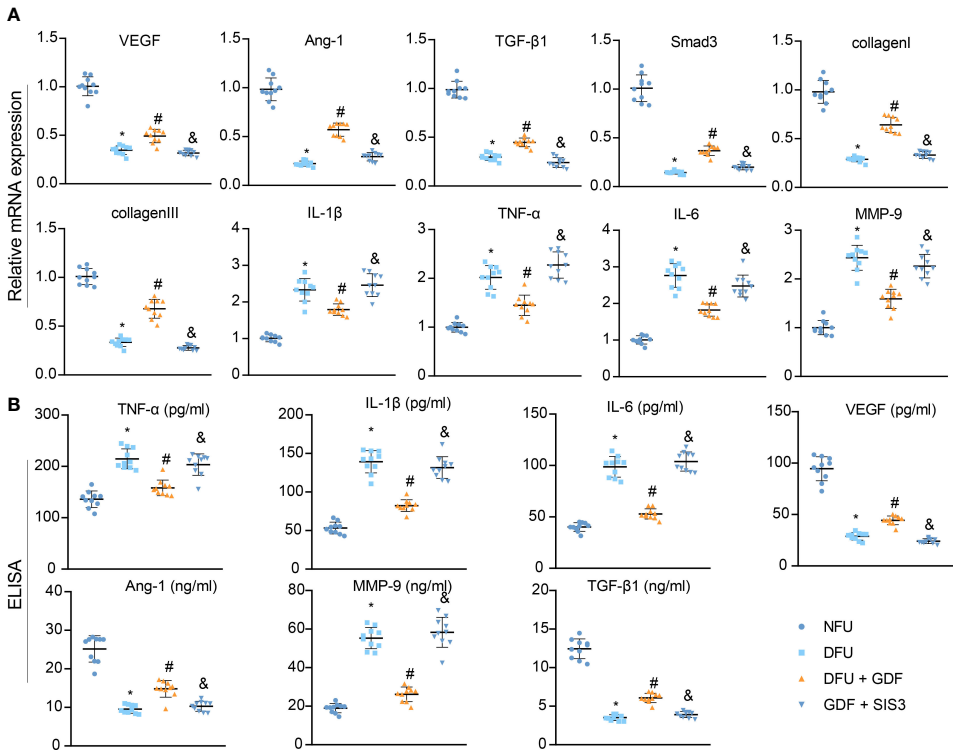

FIGURE 7
Effects of GDF10-stimulated angiogenesis on the wound healing-related factors in DFU rats. **(A)**, RT-qPCR for detecting mRNA expression of Smad3, VEGF, Ang-1, TGF-β1, collagenI, collagenIII, IL-1β, IL-6, TNF-α, and MMP-9. **(B)**, ELISA for determining expression of VEGF, Ang-1, TGF-β1, IL-1β, IL-6, TNF-α, and MMP-9. Measurement data were expressed in the form of mean ± standard deviation. One-way ANOVA was used for comparison between multiple groups, and repeated measures ANOVA was used to compare data between groups at different times. $^{*}p < 0.05$ vs. the NFU group. $^{\#}p < 0.05$ vs. the DFU group. $^{\&}p < 0.05$ vs. the DFU + GDF group. Ten rats were used in each group.

Additional mechanistic experimentation in our study based on the prediction from PPI network analysis revealed that GDF-10 might promote wound healing in DFU by activating the TGF-β1/Smad3 signaling pathway to induce angiogenesis. The same was further confirmed by means of *in vivo* animal experimentation. Despite the role of GDF-10 in DFU being rarely reported, prior studies have unfolded its role in various other types of diseases. Existing evidence indicates that GDF-10 is implicated in the anti-inflammatory activity of certain cytokines, and can further relieve relieving nerve injury-induced neuropathic pain in rats (30). Moreover, another prior study reported that silencing of GDF-10 leads to neuropathic pain by activation of the N-methyl-D-aspartate receptor (31). However, up-regulation of GDF-10 by erythropoieti has previously shown to promote axonal sprouting for neurological recovery after brain injury (32). Interestingly, GDF-10 has also been demonstrated to be capable of reducing islet graft rejection in mice models of DM (10). Further in accordance with our findings, a number of authors have explored the interaction between GDF-10, Smad and TGF-β. For example, Kraunz KS et al. suggested that GDFs transduce their signals *via* the Smad protein family in a direct manner (33). Besides, another study reported that up-regulation of GDF-10 can selectively activate Smad3 phosphorylation relying on the TGF-β receptor (11). Similary, the study performed by Zhou et al. reported that specifically over-expressed GDF-10 can up-regulate SMAD7 and down-regulate p-SMAD2 expression, thereby promoting tumor cell apoptosis and inhibiting tumor cell proliferation (34). Furthermore, over-expression of GDF-10 brings about the up-regulation of p-SMAD3, consequently promoting the activation of stromal fibroblasts and the proliferation and migration of tumor cells (20). Similarly, the interaction between GDF10 and TGFBR3 regulates epithelial mesenchymal transition and tumor cell resistance through SMAD2/3 pathway in oral squamous cell carcinoma (35). A prior study has unveiled that GDF-10 through interaction with the transcription factor RUNX family transcription factor 2 can activate the TGFβRI/Smad3/ERK

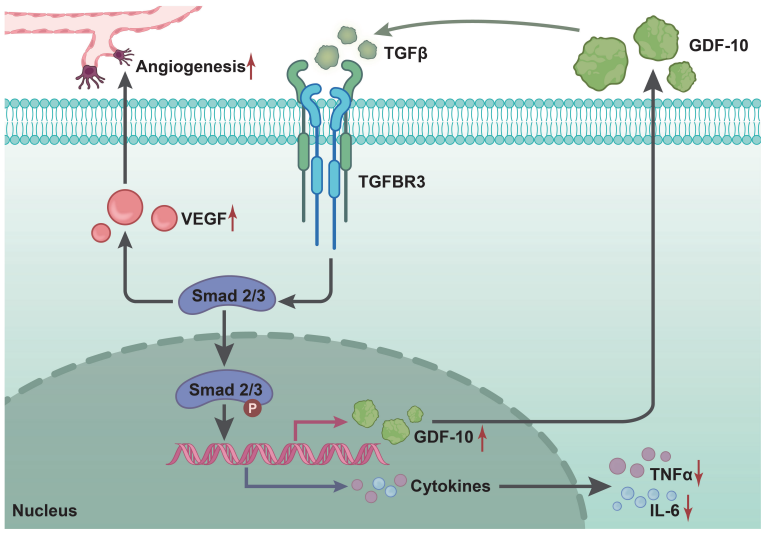

FIGURE 8
Molecular mechanism diagram of GDF10 regulating TGF-β1/smad3 signaling pathway to affect wound healing in rats with DFU. GDF10 reduces STZ-induced blood glucose levels in rats, inhibits the expression of inflammatory factors (TNF-a, IL-1β, IL-L 6) and promotes growth factors (VEGF, TGF-β1), thus activating TGF-β1/smad3 signaling to regulate the expression of Ang-1 and collagen I/collagen III to induce angiogenesis, which promotes wound healing in DFU.

pathway in oral squamous cell carcinoma cells (20). In addition, fibrocytes can release TGF-β1 to diminish the accumulation of collagens while maintaining tissue integrity for cornea wound healing, and TGF-β1 activates Smad3 to down-regulate the levels of α-SMA (36). Together, the above mentioned findings and evidence highlight the promoting role of GDF-10-mediated TGF-β1/Smad3 signaling pathway in wound healing in DFU.

Conclusions

To sum up, findings uncovered in the current study indicate that GDF-10 can reduce blood glucose levels in STZ-induced rats, inhibit the expression of inflammatory factors and promote that of the growth factors (VEGF, TGF-β1) to activate the TGF-β1/Smad3 signaling pathway, which induces angiogenesis, thereby promoting wound healing in DFU (Figure 8). Our findings may provide a novel direction in the search for diagnostic and therapeutic targets of DFU, but the results still needs further validation due to limited information regarding the role of GDF-10 in DFU.

Data availability statement

The original contributions presented in the study are included in the article/Supplementary Material. Further inquiries can be directed to the corresponding author.

Ethics statement

The animal study was reviewed and approved by the Ethics Committee of The Fourth Affiliated Hospital of Harbin Medical University.

Author contributions

Conception and design: QZ, JX; Administrative support: QZ, ZC; Provide research materials or patients: JQ; Data collection and aggregation: ZZ; Data analysis and interpretation: XH; Manuscript writing: All Authors; Final Approval of Manuscripts: All Authors. All authors contributed to the article and approved the submitted version.

Funding

This work is supported by The President's Fund of the Fourth Affiliated Hospital of Harbin Medical University (HYDSYYZ201502); Natural Science Foundation of Heilongjiang Province (LH2020H063); Outstanding Youth Fund of the Fourth Hospital of Harbin Medical University (HYDSYYXQN202008); Heilongjiang Provincial Academy of Science and Technology Cooperation Project (YS18C06); Heilongjiang Province Postdoctoral Fund (LBH-Z21170); Sichuan Provincial Western Psychiatric Association's CSPC LEADING Scientific Research Project.

Conflict of interest

The authors declare that the research was conducted in the absence of any commercial or financial relationships that could be construed as a potential conflict of interest.

Publisher's note

All claims expressed in this article are solely those of the authors and do not necessarily represent those of their affiliated organizations, or those of the publisher, the editors and the reviewers. Any product that may be evaluated in this article, or claim that may be made by its manufacturer, is not guaranteed or endorsed by the publisher.

Supplementary material

The Supplementary Material for this article can be found online at: https://www.frontiersin.org/articles/10.3389/fendo.2022.1013018/full#supplementary-material.

References

1. Subrata SA, Phuphaibul R, Kanogsunthornrat N, Siripitayakunkit A. ADIE - nursing interventions of diabetic foot ulcer: An integrative review of the literature. *Curr Diabetes Rev* (2019) 16:40–51. doi: 10.2174/1573399815666190307164119

2. Gourishetti K, Keni R, Nayak PG, Jitta SR, Bhaskaran NA, Kumar L, et al. Sesamol-loaded PLGA nanosuspension for accelerating wound healing in diabetic foot ulcer in rats. *Int J Nanomed* (2020) 15:9265–82. doi: 10.2147/IJN.S268941

3. Reardon R, Simring D, Kim B, Mortensen J, Williams D, Leslie A. The diabetic foot ulcer. *Aust J Gen Pract* (2020) 49:250–5. doi: 10.31128/AJGP-11-19-5161

4. Anastasiou IA, Eleftheriadou I, Tentolouris A, Samakidou G, Papanas N, Tentolouris N. Therapeutic properties of honey for the management of wounds; is there a role in the armamentarium of diabetic foot ulcer treatment? Results from *In vitro* and *In vivo* studies. *Int J Low Extrem Wounds* (2021) 20:291–9. doi: 10.1177/15347346211026819

5. Liu Y, Liu Y, Deng J, Li W, Nie X. Fibroblast growth factor in diabetic foot ulcer: Progress and therapeutic prospects. *Front Endocrinol (Lausanne)* (2021) 12:744868. doi: 10.3389/fendo.2021.744868

6. Jere SW, Houreld NN, Abrahamse H. Role of the PI3K/AKT (mTOR and GSK3beta) signalling pathway and photobiomodulation in diabetic wound healing. *Cytokine Growth Factor Rev* (2019) 50:52–9. doi: 10.1016/j.cytogfr.2019.03.001

7. Mecklenburg N, Martinez-Lopez JE, Moreno-Bravo JA, Perez-Balaguer A, Puelles E, Martinez S. Growth and differentiation factor 10 (Gdf10) is involved in bergmann glial cell development under shh regulation. *Glia* (2014) 62:1713–23. doi: 10.1002/glia.22710

8. Qi M, Zhou Q, Zeng W, Wu L, Zhao S, Chen W, et al. Growth factors in the pathogenesis of diabetic foot ulcers. *Front Biosci (Landmark Ed)* (2018) 23:310–7. doi: 10.2741/4593

9. Marti-Pamies I, Thoonen R, Seale P, Vite A, Caplan A, Tamez J, et al. Deficiency of bone morphogenetic protein-3b induces metabolic syndrome and increases adipogenesis. *Am J Physiol Endocrinol Metab* (2020) 319:E363–E75. doi: 10.1152/ajpendo.00362.2019

10. Choi SE, Noh JR, Seo J, Yang KJ, Kook MC, Lee CH. Gene expression profiling of allogeneic islet grafts in an experimental mouse model before rejection or tolerance phenotypes arise. *Transplant Proc* (2013) 45:597–604. doi: 10.1016/j.transproceed.2012.09.122

11. Upadhyay G, Yin Y, Yuan H, Li X, Derynck R, Glazer RI. Stem cell antigen-1 enhances tumorigenicity by disruption of growth differentiation factor-10 (GDF10)-dependent TGF-beta signaling. *Proc Natl Acad Sci USA* (2011) 108:7820–5. doi: 10.1073/pnas.1103441108

12. Kajdaniuk D, Marek B, Borgiel-Marek H, Kos-Kudla B. Transforming growth factor beta1 (TGFbeta1) in physiology and pathology. *Endokrynol Pol* (2013) 64:384–96. doi: 10.5603/EP.2013.0022

13. Chang M, Nguyen TT. Strategy for treatment of infected diabetic foot ulcers. *Acc Chem Res* (2021) 54:1080–93. doi: 10.1021/acs.accounts.0c00864

14. Luo K. Signaling cross talk between TGF-beta/Smad and other signaling pathways. *Cold Spring Harb Perspect Biol* (2017) 9:a022137. doi: 10.1101/cshperspect.a022137

15. Li B, Zhou Y, Chen J, Wang T, Li Z, Fu Y, et al. Long noncoding RNA H19 acts as a miR-29b sponge to promote wound healing in diabetic foot ulcer. *FASEB J* (2021) 35:e20526. doi: 10.1096/fj.201900076RRRRR

16. Liu H, Li Z, Zhao Y, Feng Y, Zvyagin AV, Wang J, et al. Novel diabetic foot wound dressing based on multifunctional hydrogels with extensive temperature-tolerant, durable, adhesive, and intrinsic antibacterial properties. *ACS Appl Mater Interfaces* (2021) 13:26770–81. doi: 10.1021/acsami.1c05514

17. De Gregorio C, Contador D, Diaz D, Carcamo C, Santapau D, Lobos-Gonzalez L, et al. Human adipose-derived mesenchymal stem cell-conditioned medium ameliorates polyneuropathy and foot ulceration in diabetic BKS db/db mice. *Stem Cell Res Ther* (2020) 11:168. doi: 10.1186/s13287-020-01680-0

18. Wang S, Zhou H, Wu D, Ni H, Chen Z, Chen C, et al. MicroRNA let-7a regulates angiogenesis by targeting TGFBR3 mRNA. *J Cell Mol Med* (2019) 23:556–67. doi: 10.1111/jcmm.13960

19. Gigante A, Bruge F, Cecconi S, Manzotti S, Littarru GP, Tiano L. Vitamin MK-7 enhances vitamin D3-induced osteogenesis in hMSCs: Modulation of key effectors in mineralization and vascularization. *J Tissue Eng Regener Med* (2015) 9:691–701. doi: 10.1002/term.1627

20. Zhang D, Song Y, Li D, Liu X, Pan Y, Ding L, et al. Cancer-associated fibroblasts promote tumor progression by lncRNA-mediated RUNX2/GDF10 signaling in oral squamous cell carcinoma. *Mol Oncol* (2022) 16:780–94. doi: 10.1002/1878-0261.12935

21. He H, Wang Y, Ye P, Yi D, Cheng Y, Tang H, et al. Long noncoding RNA ZFPM2-AS1 acts as a miRNA sponge and promotes cell invasion through regulation of miR-139/GDF10 in hepatocellular carcinoma. *J Exp Clin Cancer Res* (2020) 39:159. doi: 10.1186/s13046-020-01664-1

22. Belghith M, Bluestone JA, Barriot S, Megret J, Bach JF, Chatenoud L. TGF-beta-dependent mechanisms mediate restoration of self-tolerance induced by antibodies to CD3 in overt autoimmune diabetes. *Nat Med* (2003) 9:1202–8. doi: 10.1038/nm924

23. Fang T, Lv H, Lv G, Li T, Wang C, Han Q, et al. Tumor-derived exosomal miR-1247-3p induces cancer-associated fibroblast activation to foster lung metastasis of liver cancer. *Nat Commun* (2018) 9:191. doi: 10.1038/s41467-017-02583-0

24. Han J, Alvarez-Breckenridge CA, Wang QE, Yu J. TGF-beta signaling and its targeting for glioma treatment. *Am J Cancer Res* (2015) 5:945–55.

25. Subrata SA, Phuphaibul R. A nursing metaparadigm perspective of diabetic foot ulcer care. *Br J Nurs* (2019) 28:S38–50. doi: 10.12968/bjon.2019.28.6.S38

26. Mao X, Li Z, Li B, Wang H. Baicalin regulates mRNA expression of VEGF-c, ang-1/Tie2, TGF-beta and Smad2/3 to inhibit wound healing in streptozotocin-induced diabetic foot ulcer rats. *J Biochem Mol Toxicol* (2021) 35:e22893. doi: 10.1002/jbt.22893

27. Zong J, Jiang J, Shi P, Liu J, Wang W, Li B, et al. Fatty acid extracts facilitate cutaneous wound healing through activating AKT, ERK, and TGF-beta/Smad3 signaling and promoting angiogenesis. *Am J Transl Res* (2020) 12:478–92.

28. Zhang F, Ren Y, Liu P, Ren Y, Wang D. Expression of TGF-beta1 and miRNA-145 in patients with diabetic foot ulcers. *Exp Ther Med* (2016) 11:2011–4. doi: 10.3892/etm.2016.3123

29. Song Q, Xie Y, Gou Q, Guo X, Yao Q, Gou X. JAK/STAT3 and Smad3 activities are required for the wound healing properties of periplaneta americana extracts. *Int J Mol Med* (2017) 40:465–73. doi: 10.3892/ijmm.2017.3040

30. Echeverry S, Shi XQ, Haw A, Liu H, Zhang ZW, Zhang J. Transforming growth factor-beta1 impairs neuropathic pain through pleiotropic effects. *Mol Pain* (2009) 5:16. doi: 10.1186/1744-8069-5-16

31. Jiang L, Tan B, Li S, Wang L, Zheng L, Liu Y, et al. Decrease of growth and differentiation factor 10 contributes to neuropathic pain through n-methyl-D-aspartate receptor activation. *Neuroreport* (2017) 28:444–50. doi: 10.1097/WNR.0000000000000785

32. Li SJ, Cui KF, Fu JJ, Fu XJ, Gao YF, Zhang D, et al. EPO promotes axonal sprouting *via* upregulating GDF10. *Neurosci Lett* (2019) 711:134412. doi: 10.1016/j.neulet.2019.134412

33. Kraunz KS, Nelson HH, Liu M, Wiencke JK, Kelsey KT. Interaction between the bone morphogenetic proteins and Ras/MAP-kinase signalling pathways in lung cancer. *Br J Cancer* (2005) 93:949–52. doi: 10.1038/sj.bjc.6602790

34. Zhou T, Yu L, Huang J, Zhao X, Li Y, Hu Y, et al. GDF10 inhibits proliferation and epithelial-mesenchymal transition in triple-negative breast cancer *via* upregulation of Smad7. *Aging (Albany NY)* (2019) 11:3298–314. doi: 10.18632/aging.101983

35. Cheng CW, Hsiao JR, Fan CC, Lo YK, Tzen CY, Wu LW, et al. Loss of GDF10/BMP3b as a prognostic marker collaborates with TGFBR3 to enhance chemotherapy resistance and epithelial-mesenchymal transition in oral squamous cell carcinoma. *Mol Carcinog* (2016) 55:499–513. doi: 10.1002/mc.22297

36. de Oliveira RC, Wilson SE. Fibrocytes, wound healing, and corneal fibrosis. *Invest Ophthalmol Vis Sci* (2020) 61:28. doi: 10.1167/iovs.61.2.28

frontiers | Frontiers in Endocrinology

TYPE Original Research
PUBLISHED 20 January 2023
DOI 10.3389/fendo.2022.1033074

OPEN ACCESS

EDITED BY
Amit V. Pandey,
University of Bern, Switzerland

REVIEWED BY
Núria Camats,
Vall d'Hebron Research Institute (VHIR), Spain
Kenji Kurosawa,
Kanagawa Children's Medical Center, Japan
Noriyuki Namba,
Tottori University, Japan

*CORRESPONDENCE
Kenichi Kashimada
kkashimada.ped@tmd.ac.jp

SPECIALTY SECTION
This article was submitted to Pediatric Endocrinology, a section of the journal Frontiers in Endocrinology

RECEIVED 31 August 2022
ACCEPTED 29 December 2022
PUBLISHED 20 January 2023

CITATION
Gau M, Suga R, Hijikata A, Kashimada A, Takagi M, Nakagawa R, Takasawa K, Shirai T, Kashimada K and Morio T (2023) A novel variant of NR5A1, p.R350W implicates potential interactions with unknown co-factors or ligands. *Front. Endocrinol.* 13:1033074. doi: 10.3389/fendo.2022.1033074

A novel variant of NR5A1, p.R350W implicates potential interactions with unknown co-factors or ligands

Maki Gau[1], Ryota Suga[2], Atsushi Hijikata[3], Ayako Kashimada[1], Masatoshi Takagi[1], Ryuichi Nakagawa[1], Kei Takasawa[1], Tsuyoshi Shirai[3], Kenichi Kashimada[1]* and Tomohiro Morio[1]

[1]Department of Pediatrics and Developmental Biology, Tokyo Medical and Dental University, Tokyo, Japan, [2]School of Medicine, Tokyo Medical and Dental University, Tokyo, Japan, [3]Faculty of Bioscience, Nagahama Institute of Bio-Science and Technology, Nagahama, Shiga, Japan

Introduction: NR5A1 and NR5A2 belong to an orphan nuclear receptor group, and approximately 60% of their amino acid sequences are conserved. Transcriptional regulation of NR5A receptors depends on interactions with co-factors or unidentified ligands.

Purpose and methods: We employed in vitro and in silico analysis for elucidating the pathophysiology of a novel variant in the ligand-binding domain of NR5A1, p.R350W which was identified from a 46,XY patient with atypical genitalia.

Results: In the study, [1] reporter assays demonstrated that R350 is essential for NR5A1; [2] 3D model analysis predicted that R350 interacted with endogenous ligands or unknown cofactors rather than stabilizing the structure; [3] R350 is not conserved in NR5A2 but is specifically required for NR5A1; and [4] none of the 22 known missense variants of the ligand binding domain satisfied all the previous conditions [1]-[3], suggesting the unique role of R350 in NR5A1.

Conclusion: Our data suggest that NR5A1 has unidentified endogenous ligands or co-activators that selectively potentiate the transcriptional function of NR5A1 *in vivo*.

KEYWORDS

NR5A1, NR5A2, orphan nuclear receptor, 46,XY DSD, co-factors, ligands

Introduction

NR5A1 and NR5A2, also known as SF-1 and LRH-1, respectively, belong to the orphan nuclear receptor group, which is characterized by a lack of identified endogenous ligands (1, 2). NR5A1 and NR5A2 share a substantially conserved sequence (approximately 60% amino acid sequence), forming the Ftz-F1 subfamily of nuclear receptors (3). Both receptors

modulate cholesterol homeostasis, steroidogenesis, tissue-specific cell proliferation, and stem cell pluripotency (4, 5). Although their binding sequences are identical, both molecules exhibit different and non-overlapping effects on target organs due to their distinctive expression profiles (6). *NR5A1* (HGNC:7983) and *NR5A2* (HGNC:7984) are expressed primarily in steroidogenic tissues and in tissues of endodermal origin and gonads, respectively (7, 8). Due to its critical role in gonadal development and testicular differentiation, loss-of-function mutations in NR5A1 cause 46,XY disorders of sex development (DSD) (4, 9). While NR5A2 deletion in mice is embryonically lethal (10, 11), consequences of NR5A2 mutation in humans are still unknown (3).

The regulation of NR5A receptor transcriptional activity has been suggested to be dependent on interactions with co-factors. SHP (NR0B2) (12), DAX1 (NR0B1) (13, 14), NCOR1, NCOR2 (15), and β-catenin (16, 17) are major cofactors that can interact with NR5A1 and NR5A2. Regulation by cofactors can be either positive (co-activation) or negative (co-repression). The interactive domains in NR5A1 and NR5A2 vary depending on the type of cofactor (3).

Recent *in vitro* studies have suggested that, in addition to co-factors, unidentified ligands for NR5A receptors could regulate its activity (18, 19). Crystallography and mass spectrophotometry analyses revealed large hydrophobic pockets that were occupied by phospholipids, especially phosphatidylinositol- (3–5)-trisphosphate in both NR5As. Introducing point mutations in the ligand-binding domains such as A269, G341, L344, V348, A433, Y436, and K440 of *hNR5A1* failed to recruit co-activators and induce transcription (20, 21). Several pharmacological ligands have been developed for NR5A1 and NR5A2 (22–24), yet no reports demonstrating ligand function in mouse models or human diseases exist. Therefore, their biological relevance remains unknown.

Recently, we encountered a patient with 46,XY disorder of sex development (DSD) with a novel missense variant p.R350W in the ligand-binding domain (LBD) of NR5A1. *In vitro* analysis suggested that this variant deteriorated the transcriptional activity. Interestingly, the amino acid was not conserved between NR5A1 and NR5A2, and 3D analysis predicted that the variant would not cause a conformational change in the protein. These results suggest that arginine, the 350th amino acid of NR5A1 plays a crucial role in its interaction with co-factors or ligands, thereby providing a valuable insight into the regulation of the transcriptional activity.

Case presentation

The patient was born full-term with a normal birth weight (40W1D, 3226 g). Although clitromegaly was noted at birth, the patient was raised as female. At 3 years of age, the patient developed a bilateral inguinal hernia that was surgically treated, but no further examination for disorder of sex development was performed. At 12 years of age, the patient exhibited pubertal development with virilization such as an increased size of the clitoris and was referred to our hospital. Chromosomal analysis revealed that the patient carried 46,XY genotype with *SRY*, and endocrinological tests suggested that the gonads had testicular function (Testosterone: 4.96 ng/mL, Estradiol: <5 pg/mL), although gonadotropin levels were elevated (LH:14.7 mIU/mL, FSH:70.7 mIU/mL). The patient showed no signs or symptoms of adrenal insufficiency. The patient was diagnosed with 46,XY DSD, and genetic analysis revealed a missense variant (NM_004959.4 c.1048 C>T, NP_004950.2 p.Arg350Trp [RefSeq version5], rs754336683) in the NR5A1 gene. We did not perform genetic analysis of the parents, but they did not show any signs or symptoms of the disorder of sex development. The frequency of the variant is low, 0 in gnomAD (https://gnomad.broadinstitute.org/gene/ENSG00000136931?dataset=gnomad_r3), and according to the American College of Medical Genetics guidelines, the variant was classified as highly pathogenic. Registration of the variant in our case resulted in a MAF (minor allele frequency) of 0.00005665 in the East Asian population (https://gnomad.broadinstitute.org/variant/9-127253450-G-A?dataset=gnomad_r2_1).

Materials and methods

The study was approved by the Institutional Review Board Committee at Tokyo Medical and Dental University and written informed consent was obtained from the parents (G2000-103). We confirmed that all methods were performed in accordance with the relevant guidelines and regulations.

Mutation analysis

Genomic DNA was obtained from the lymphocytes of the patient, and DNA analysis was conducted using the TruSightTM One sequencing panel, #FC-141-1006 (Illumina, CA, USA). The known causative genes for 46,XY DSD, such as *AR* (HGNC:644), *HSD17B3* (HGNC:5212), *HSD3B2* (HGNC:5218), *NR5A1*, *SRD5A2* (HGNC:11285), *WT1* (HGNC:12796), *ANOS1* (HGNC:6211), *CHD7* (HGNC:20626), *FGF8* (HGNC:3686), *FGFR1* (HGNC:3688), *and SRY* (HGNC:11311), were screened, and a missense variant c.1048 C>T was identified in the NR5A1 gene, which was further confirmed by Sanger sequencing.

Plasmids

The expression vector for wild-type human *NR5A1* was purchased from the Kazusa DNA Research Institute (Kisarazu, Chiba, Japan). The expression vectors for mutant *NR5A1*, R350W, R350L, R350H, A260V, C283R, and Q460R, were generated by mutagenesis using a QuikChange II Site-Directed Mutagenesis Kit (Agilent, CA, USA). Reporter vectors containing the *SOX9* (HGNC:11204) testis enhancer sequence (hTES) and the promoter of *CYP17* (HGNC:2593) were kindly gifted by V. Harley (Hudson Institute of Medical Research) (25) and JS. Richards (Baylor College of Medicine), respectively.

Luciferase assay

The transcriptional activities of the wild-type and the missense variants of NR5A1 on hTES and the *CYP17* promoter were

determined by dual luciferase reporter assays. CHO cells were prepared in 24-well plates (1.0×10^5 cells/well). *NR5A1* (100 ng) of the wild-type or the missense variant expression plasmids or the pcDNA3 empty plasmids were transiently introduced with 200 ng of the reporter plasmids (hTES or the *CYP17* promoter). Relative luciferase activity was measured 48 h after transfection using the Dual-Luciferase Reporter Assay System (Promega, MD, USA). Samples were measured in triplicates in each assay, and all the assays were independently repeated three to four times.

Western blotting

The *NR5A1* expression plasmids of the wild-type or the missense variants were introduced into CHO cells, and whole-cell lysates were collected using lysis buffer containing 50 mM Tris-HCl (pH 8.0), 50 mM NaCl, 1 mM EDTA, and 1% SDS (26). After SDS-PAGE, immunoblotting was performed with anti-Ad4BP/SF-1 antiserum (1:1000, a kind gift from K. Morohashi Lab) and anti-β-actin antibody (1:10000, A1978, Sigma-Aldrich, St. Louis, MO, USA). Anti-rabbit IgG (1:5000, GE Healthcare, UK) and anti-mouse IgG (1:10000, GE Healthcare, UK) were used as secondary antibodies.

In silico analysis of missense mutations on a three-dimensional structure model

Mutated residues were mapped to the crystal structure of human NR5A1 (PDB code: 4qjr). The effects of each missense variant on thermal stability were evaluated using FoldX 5.0 software (26). Putative interfaces of molecular interactions were predicted using the SPPIDER web server(http://sppider.cchmc.org/) (27). Supramolecular structural modeling of NR5A1 and its interacting molecules was performed by superimposing the structure of NR5A1 in complex structures according to previously described methods (28). Prediction analysis was performed according to the guidelines of Vihinen M (29). REVEL scores for the predicted pathogenicity of missense variants were estimated using a computational method (30).

Immunofluorescence analysis

We transiently introduced expression vector of wild type or R350W NR5A1 into CHO cells and performed immunofluorescence analysis as previously described (15, 31). The rabbit anti-NR5A1 (Ad4BP) antibody (kindly provided by K Morohashi) was used at a 1:500 dilution, and the goat Texas-Red dye-conjugated anti-rabbit antibody (#111-076-047, Jackson ImmunoResearch, PA, USA) was used as the secondary antibody at 1:100 dilution. The slides were mounted with Vectashield mounting medium (H-1200; Vector Laboratories, Burlingame, CA, USA), allowing for nuclear 4,6-diamidino-2-phenylindole (DAPI) staining. Images were obtained using a confocal microscope, TCS-SP8 (Leica microsystems, Germany).

Results

R350 was essential for NR5A1 function *in vitro*

The clinical phenotypes of the patient suggested that R350 is essential for NR5A1 function *in vivo*. Reporter analysis revealed that p.R350W significantly impaired the transcriptional activities of hTES and the *CYP17* promoter, which are thought to play major roles in Sertoli and Leydig cell differentiation (Figure 1A). This assay confirmed the essential role of R350 in NR5A1 *in vitro*.

The predicted role of R350 was interacting with other molecules

In silico 3D analysis revealed that R350 was on helix7, which is a major component of the ligand-binding pocket (Figure 1B), and R350 was located external of the predicted potential molecular interface (Figures 1C, D, 2). REVEL scores were elevated in p.R350W and its surrounding areas suggesting the importance of R350 and its neighboring amino acids for NR5A1 function (Figure 1E). The computational software FoldX predicted that p.R350W would increase the thermal stability of NR5A1, suggesting that p.R350W would not destabilize the LBD structure. These results indicate that p.R350W is a unique missense mutation, as most of the previously reported missense pathological variants in the LBD decreased stability (Figure 2). Further analysis of the known complex structures of the NR5A1-LBD and its co-factors, β-catenin and DAX1, showed that R350 was not in direct contact, although it was in close proximity to these molecules (Figure 1F). Taken together, the predicted role of R350 would be a part of the interaction sites for other molecules, that is, an endogenous ligand or an unknown co-factor, rather than being a stabilizing factor for the LBD structure.

Function of the 350th amino acid residue in NR5A1 was distinctive from that in NR5A2

Despite the conservation of R350 in NR5A1 among species, the equivalent amino acid residue was altered to leucine or histidine in NR5A2 (Figure 3A), suggesting that an unknown molecule would exclusively interact with NR5A1 through R350. To verify the exclusivity of the potential interaction, we assessed whether the function of R350 could be replaced with the corresponding amino acid residues in NR5A2, leucine or histidine, and carried out a reporter assay for NR5A1 whose R350 was substituted with leucine (p.R350L) or histidine (p.R350H). Although the protein expression of p.R350L and p.R350H (Figure 3B) was not affected, the transcriptional activities of p.R350L and p.R350H were significantly impaired (Figures 3C, D). Thus, NR5A1 specifically requires arginine as the 350th amino acid residue, and the function of the 350th amino acid residue in NR5A1 is distinct from the corresponding amino acid residue in NR5A2. However, nuclear localization of R350W was not affected (Figure 3G).

10.3389/fendo.2022.1033074

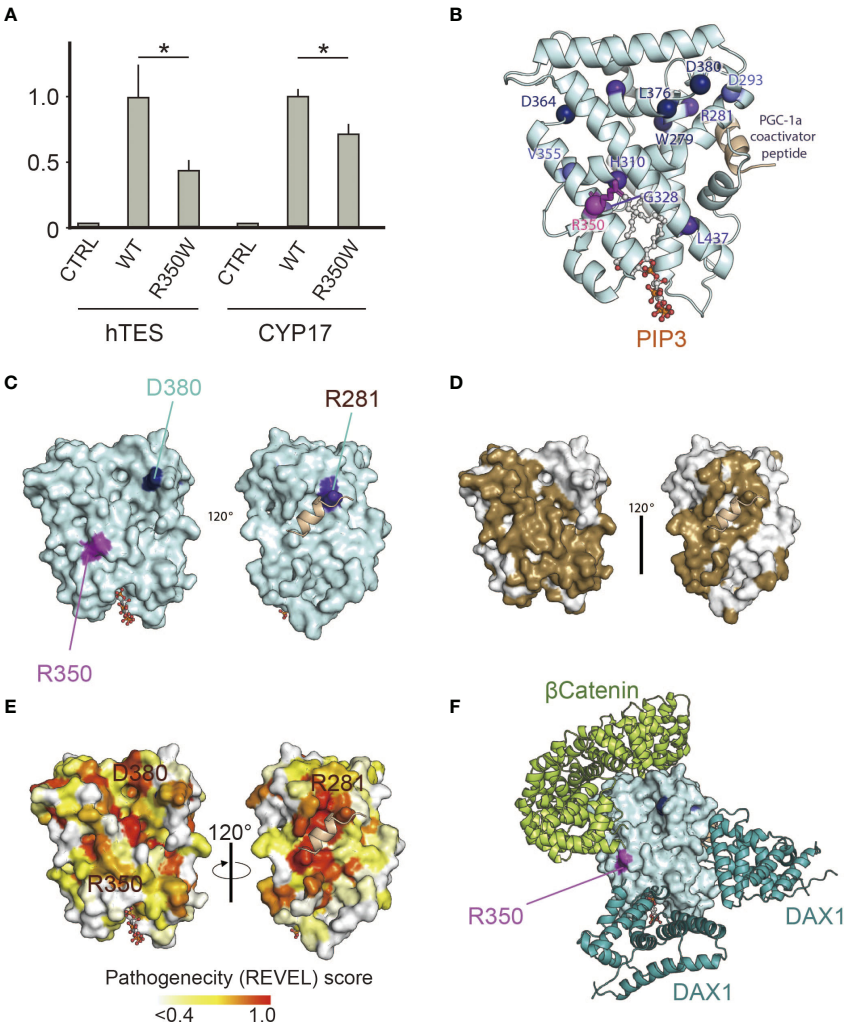

FIGURE 1
(A) p.R350W variant of NR5A1 revealed significantly impaired translational activities. Reporter assay of the wild type and R350W for hTES, the human testicular enhancer for *Sox9*, and the promoter of *CYP17*. Data sets represent activation of the reporters relative to wild type, whose value was adjusted to 1.0. The mean and SD of three to five biological replicates measured was calculated. Asterisks indicate statistical significance (*, P <0.05). Unpaired Student's t test was used to demonstrate statistically significant difference between the given sample and the wild type. **(B)** 3D model analysis of LBD in NR5A1, indicating that R350W was on the helix7. **(C)** R350 (purple) was located on the surface of LBD in NR5A1. **(D)** The 3D model analysis by SPPIDER server (http://sppider.cchmc.org/) predicted the surface area of the LBD to interact with other molecules (Brown). The location of R350 indicated in Fig. 1C is covered by the brown area. **(E)** The REVEL pathogenicity score was elevated in R350 and its surrounding area. **(F)** Known co-factors that bind to the LBD of NR5A1, β-catenin and DAX1(NR0B1) were not predicted to interact with R350 directly in the 3D model of the predicted protein complexes.

Comparison to the other missense pathogenic variants on the LBD revealed the unique function of the R350 role in NR5A1

In the LBD of NR5A1 of patients with 46,XY DSD, 22 missense variants have been identified, suggesting that these 22 amino acids play essential roles in the LBD of NR5A1 *in vivo*. Of these 22 amino acid residues, 19 were conserved between NR5A1 and NR5A2 while three, p.A260V, p.C283R, and p.Q460R, were not conserved (Figure 2). The reporter assay revealed that the trans-activating activity was impaired in the variant p. C283R, but not in p. A260V or p. Q460R (Figures 3E, F), indicating that p. A260V and p.Q460R are not pathological variants. Thus, in addition to p.R350W, p. C283R is the only pathological missense variant whose substituted amino acid residue is not conserved in NR5A2. During thermal stability analysis, the LBD with the p. C283R variant was destabilized (Figure 2), and the major role of C283 was to stabilize the structure of the LBD rather than to interact with other molecules, co-factors, or ligands.

Discussion/Conclusion

R350 has an essential role in NR5A1, as we have proven *in vivo* (46,XY DSD) and *in vitro* (reporter assays). Our present study suggests that there is an endogenous ligand or a co-activator that selectively potentiates the transcriptional function of NR5A1, but not that of NR5A2, *in vivo*. The profoundly impaired testicular function in our case with severely under-virilized external genitalia indicated that R350 in the LBD of NR5A1 plays an essential role in testicular development in humans, which was confirmed by our *in vitro* reporter assay. *In silico* 3D analysis predicted that the major

	# A.A.	Variant	Phenotype	Solvent accessiblity	Total Energy (FoldX)	Conservated in *NR5A2*	Impaired transactivity *in vitro* assay	REVEL score	AF in gnomAD(vol.3)
Present study	350	p.Arg350Trp	46, XY DSD	0.31	-0.57	-	+	0.84	0
1	260	p.Ala260Val	DSD, severe hypospadias	0.53	0.25	-	-	0.30	6.97e-6(1/143370)
2	283	p.Cys283Arg	DSD, severe hypospadias	0.00	10.60	-	+	0.96	0
3	460	p.Gln460Arg	DSD, severe hypospadias	0.91	-0.66	-	-	0.29	7.94e-6(1/125938)
4	279	p.Trp279Arg	DSD, severe hypospadias	0.01	3.28	+	NA	0.97	0
5	281	p.Arg281Pro	DSD, severe hypospadias	0.60	6.29	+	NA	0.95	0
6	310	p.His310Asp	DSD, severe hypospadias	0.20	0.68	+	NA	0.93	0
7	313	p.Arg313Cys	DSD, severe hypospadias	0.14	2.25	+	NA	0.92	0
8	328	p.Gly328Val	DSD, severe hypospadias	0.31	7.52	+	NA	0.98	0
9	347	p.Leu347Gln	DSD, severe hypospadias	0.09	2.42	+	NA	0.97	0
10	364	p.Asp364Tyr	DSD, severe hypospadias	0.22	2.8	+	NA	0.97	0
11	370	p.Cys370Tyr	DSD, severe hypospadias	0.00	21.57	+	NA	098	0
12	376	p.Leu376Phe	DSD, severe hypospadias	0.01	3.81	+	NA	0.97	0
13	380	p.Asp380Tyr	DSD, severe hypospadias	0.47	0.57	+	NA	0.94	0
14	293	p.Asp293Asn	Anorchia micro penis	0.02	1.54	+	NA	0.94	2.79e-5(4/143338)
15	355	p.Val355Met	Anorchia micro penis	0.05	0.00	+	NA	0.81	5.5e-5(8/143340)
16	257	p.Asp257Asn	Male infertility	0.66	0.27	+	NA	0.41	2.79e-5(4/143338)
17	323	p.Ile323Thr	Male infertility	0.07	2.24	+	NA	0.77	0
18	255	p.Arg255Leu	Adrenal Failure	0.37	0.24	+	NA	0.68	6.98e-6(1/143344)
19	223	p.Val223Met	SNP in gnomAD	0.20	0.70	+	NA	0.26	8.37e-5(12/143316)
20	238	p.Asp238Asn	SNP in gnomAD	0.66	0.02	+	NA	0.10	6.98e-5(10/143336)
21	259	p.Pro259Leu	SNP in gnomAD	0.65	0.81	+	NA	0.25	9.07e-5(13/143370)
22	460	p.Gln460Pro	SNP in gnomAD	0.91	-0.41	+	NA	0.46	1.03e-4(13/125938)

FIGURE 2
Summary of the reported missense variants on the NR5A1 LBD. Yellow colored amino acids are predicted to be located outside surface. In the LBD of NR5A1, 22 missense variants have been identified in patients with 46,XY DSD to date. Of these 22 amino acid residues, 19 were conserved in NR5A2, and only three, p.A260V, p.C283R, and p.Q460R, were not conserved. The functional analyses showed that p.A260V and p.Q460R were not deleterious variants. The thermal stability analysis (FoldX), indicated that p.R350W would not destabilize LBD structure while p. C283R variant would. The specificity of the REVEL score at 0.5 and 0.75 for pathogenic are 89.1% and 95%, respectively (31). DSD, Disorder of Sex Development; NA, not available.

function of R350 was interacting with other molecules, such as co-factors and endogenous ligands, rather than maintaining the structure of NR5A1. However, R350 was not conserved in NR5A2. Furthermore, NR5A1 exclusively requires arginine as the 350th amino acid residue, as substitution of R350 with the corresponding histidine/leucine residues in NR5A2 did not compensate for the transcriptional activity of NR5A1.

Although identifying the molecule interacting with R350 is beyond the scope of this study, we presume that known co-factors are not likely to be involved in the interaction with NR5A1 through R350. The only known co-factor that activates NR5A1 trans-activity is β-catenin (3), which is unlikely to be involved in the pathophysiology of severely impaired testicular development. During gonadal development, β-catenin acts in favor of ovarian development by suppressing key molecules for testicular development, such as FGF9 (32). In this biological context, β-catenin presumably counteracts NR5A1 function rather than activating it. Indeed, supramolecular complex models of NR5A1 predicted that R350 did not mediate the interaction with β-catenin. Furthermore, all known cofactors have been suggested to interact with both NR5A1 and NR5A2 or NR5A2 alone (3). In other words, co-activators whose association is limited to NR5A1 have not yet been reported. Identifying novel co-factors of NR5A1 will advance our understanding of its function.

Another implication of our data is the possible presence of an endogenous ligand *in vivo*. Although the unaffected nuclear localization of R350W suggests that its binding ability was maintained, R350 may have essential roles in ligand-dependent conformational changes of NR5A1. To the best of our knowledge, no data using mouse models or human diseases have revealed that NR5A1 requires an endogenous ligand for its transcriptional activity. Furthermore, our data suggest the existence of an endogenous ligand selective for NR5A1, as the equivalent amino acid residue of NR5A2 did not restore NR5A1 function. Recently, artificial ligands that can bind to either NR5A1 or NR5A2 have been developed. Low molecular weight compounds containing cis-bicyclo [3.3.0]oct-2-ene in their core structure selectively increases NR5A1 activity (23), whereas dilauryol-phosphatidyl-choline (DLPC) activates NR5A2 (22). These findings indicate that NR5A1 and NR5A2 have similar structures but require different ligands; however, it is not clear whether there are active endogenous ligands for either NR5A receptor *in vivo* (33). Our observations support the *in vitro* observation of artificial ligands, thereby shedding new light on the unidentified ligands of NR5A1.

It is intriguing that the trans-activity of p.R350H varied depending on the reporters; the trans-activity was maintained on the *CYP17* promoter, but not on the hTES promoter. The interaction between cofactors and NR5A1/NR5A2 is presumed to be controlled by ligands, and cofactors of NR5A1/NR5A2 are known to regulate its transcriptional activity in a context-specific manner (3). Our data would be an example to show the complexity of the interaction between NR5A1/NR5A2 and co-factors/ligands.

10.3389/fendo.2022.1033074

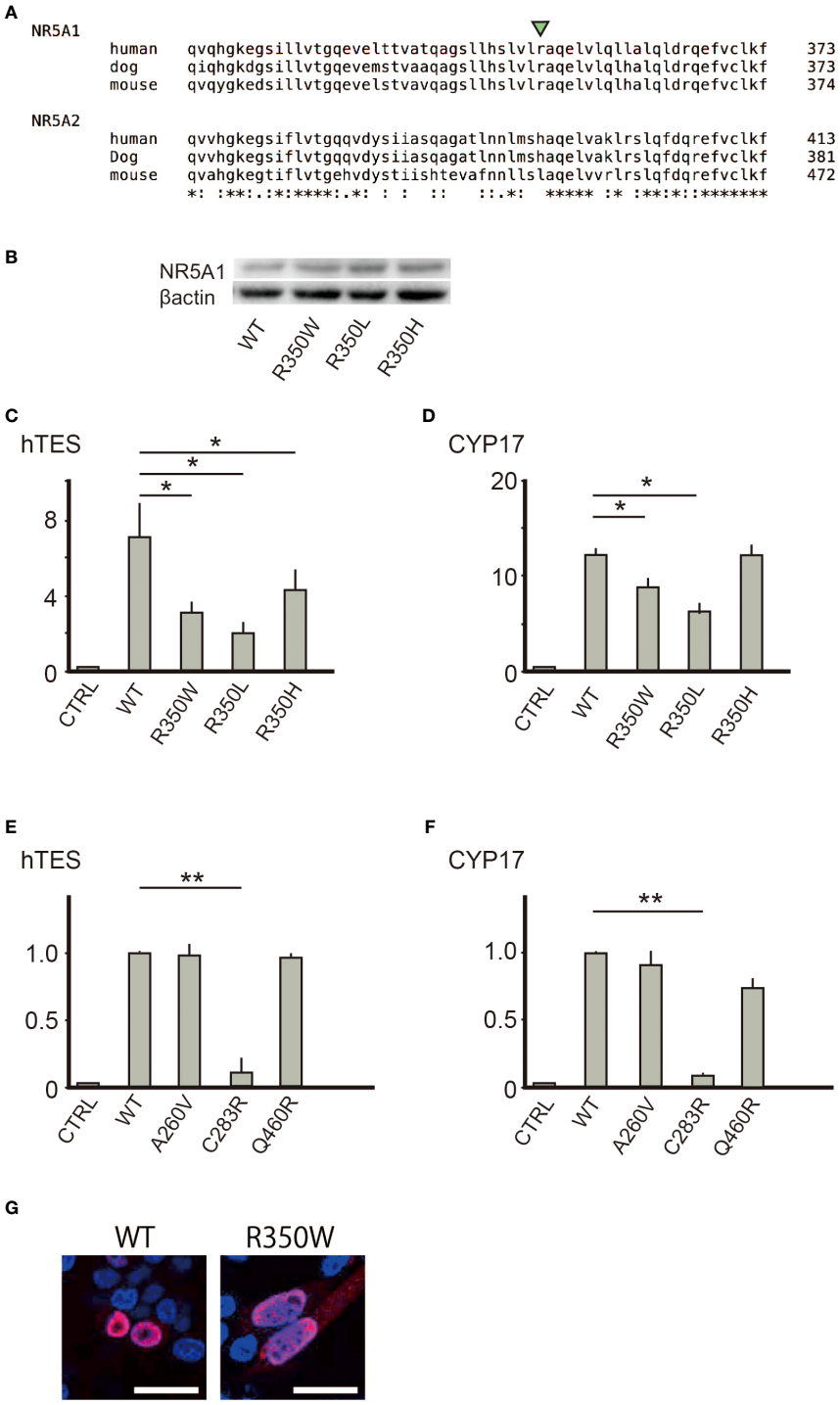

FIGURE 3
(A) R350 is conserved among NR5A1 of various species, but not in NR5A2. **(B)** Substitution of the 350th arginine with tryptophan, leucine, or histidine did not affect the protein expression levels. **(C, D)** Substitution of the 350th arginine with leucine or histidine reduced the trans-activating ability in hTES and the *CYP17* promoter. Asterisks indicate statistical significance (*, P <0.05). **(E, F)** Of the three missense variants (p.A260V, p. C283R, and p.Q460R) suggested to cause 46,XY DSD, only p.C283R reduced the trans-activating ability in hTES and the *CYP17* promoter. Data sets represent activation of the reporters relative to wild-type whose value was adjusted to 1.0. The mean and SD values of three to five biological replicates measured were calculated. Asterisks indicate statistical significance (**, P <0.001). Unpaired Student's t-test was used to demonstrate statistically significant difference between the given sample and the control. **(G)** Immunofluorescence of transiently transfected CHO cells with the wild type or R350W NR5A1 expression vectors. The nuclear localization was identical between wild type and R350W (red) White bar indicate 25μm.

The present study has some limitations. The parents of the patient did not allow us to perform a familial analysis, which could have provided further insights. Using our 3D model analysis, it was difficult to completely exclude the possibility that p.R350W would indirectly interfere with the allosteric regulation of the known co-factors for ligand binding. Our analysis is based on a single-case study, and further case studies are required to elucidate the precise function of LBD, especially regarding its interaction with other molecules. Nevertheless, the 46,XY DSD case with p.R350W provided intriguing insights into possible molecules, co-factors, or endogenous ligands interacting with NR5A1.

NR5A1 has been reported to play a role in organ development and oncogenesis (3, 34). We envisage that, in addition to identifying the pathophysiology of DSD, an improved understanding of the molecules interacting with NR5A1 may provide novel insights, leading to the development of valuable therapeutic options for malignant diseases.

Data availability statement

The data presented in the study are deposited in the ClinVar repository, accession number SCV002099761.

Ethics statement

The studies involving human participants were reviewed and approved by the Institutional Review Board Committee at Tokyo Medical and Dental University. Written informed consent to participate in this study was provided by the participants' legal guardian/next of kin.

Author contributions

KK, MG, and KT contributed to the conception and design of this study, acquisition of data, and analysis and interpretation of the data. All experiments were performed by MG, RS, AH, AK, MT, RN, KT, and TS. The manuscript was drafted by KK and MG and critically revised by AH and TM. All authors have read and approved the final manuscript. All authors contributed to the article and approved the submitted version.

Funding

This study was partially supported by a grant from KAKENHI, Kiban (C) (15K09615) funded by the Japan Society for the Promotion of Science (JSPS), to KK. This research was partially supported by the Platform Project for Supporting Drug Discovery and Life Science Research (Basis for Supporting Innovative Drug Discovery and Life Science Research (BINDS)) from AMED under Grant Number JP20am0101111 (support number 2103).

Acknowledgments

We thank K Morohashi for providing the NR5A1 antibody, VR Harley for providing the hTES promoter plasmid, and JS. Richards for providing the CYP17 promoter plasmid.

Conflict of interest

The authors declare that the research was conducted in the absence of any commercial or financial relationships that could be construed as a potential conflict of interest.

Publisher's note

References

1. S.Melmed RJA, Goldfine AB. *Williams textbook of endocrinology. 14th ed* Vol. 11:31–41. ELSEVIER (2020).

2. Zhang Z, Burch PE, Cooney AJ, Lanz RB, Pereira FA, Wu J, et al. Genomic analysis of the nuclear receptor family: New insights into structure, regulation, and evolution from the rat genome. *Genome Res* (2004) 14(4):580–90. doi: 10.1101/gr.2160004

3. Meinsohn MC, Smith OE, Bertolin K, Murphy BD. The orphan nuclear receptors steroidogenic factor-1 and liver receptor homolog-1: Structure, regulation, and essential roles in mammalian reproduction. *Physiol Rev* (2019) 99(2):1249–79. doi: 10.1152/physrev.00019.2018

4. Lin L, Achermann JC. Steroidogenic factor-1 (Sf-1, Ad4bp, Nr5a1) and disorders of testis development. *Sex Dev* (2008) 2(4-5):200–9. doi: 10.1159/000152036

5. Luo X, Ikeda Y, Parker KL. A cell-specific nuclear receptor is essential for adrenal and gonadal development and sexual differentiation. *Cell* (1994) 77(4):481–90. doi: 10.1016/0092-8674(94)90211-9

6. Fayard E, Auwerx J, Schoonjans K. Lrh-1: An orphan nuclear receptor involved in development, metabolism and steroidogenesis. *Trends Cell Biol* (2004) 14(5):250–60. doi: 10.1016/j.tcb.2004.03.008

7. Falender AE, Lanz R, Malenfant D, Belanger L, Richards JS. Differential expression of steroidogenic factor-1 and Ftf/Lrh-1 in the rodent ovary. *Endocrinology* (2003) 144 (8):3598–610. doi: 10.1210/en.2002-0137

8. Hinshelwood MM, Shelton JM, Richardson JA, Mendelson CR. Temporal and spatial expression of liver receptor homologue-1 (Lrh-1) during embryogenesis suggests a potential role in gonadal development. *Dev Dyn* (2005) 234(1):159–68. doi: 10.1002/dvdy.20490

9. Achermann JC, Ito M, Ito M, Hindmarsh PC, Jameson JL. A mutation in the gene encoding steroidogenic factor-1 causes xy sex reversal and adrenal failure in humans. *Nat Genet* (1999) 22(2):125–6. doi: 10.1038/9629

10. Duggavathi R, Volle DH, Mataki C, Antal MC, Messaddeq N, Auwerx J, et al. Liver receptor homolog 1 is essential for ovulation. *Genes Dev* (2008) 22(14):1871–6. doi: 10.1101/gad.472008

11. Pare JF, Malenfant D, Courtemanche C, Jacob-Wagner M, Roy S, Allard D, et al. The fetoprotein transcription factor (Ftf) gene is essential to embryogenesis and cholesterol homeostasis and is regulated by a Dr4 element. *J Biol Chem* (2004) 279 (20):21206–16. doi: 10.1074/jbc.M401523200

12. Goodwin B, Jones SA, Price RR, Watson MA, McKee DD, Moore LB, et al. A regulatory cascade of the nuclear receptors fxr, shp-1, and lrh-1 represses bile acid biosynthesis. *Mol Cell* (2000) 6(3):517–26. doi: 10.1016/s1097-2765(00)00051-4

13. Babu PS, Bavers DL, Beuschlein F, Shah S, Jeffs B, Jameson JL, et al. Interaction between dax-1 and steroidogenic factor-1 in vivo: Increased adrenal responsiveness to acth in the absence of dax-1. *Endocrinology* (2002) 143(2):665–73. doi: 10.1210/endo.143.2.8658

14. Suzuki T, Kasahara M, Yoshioka H, Morohashi K, Umesono K. Lxxll-related motifs in dax-1 have target specificity for the orphan nuclear receptors Ad4bp/Sf-1 and lrh-1. *Mol Cell Biol* (2003) 23(1):238–49. doi: 10.1128/mcb.23.1.238-249.2003

15. Steffensen KR, Holter E, Bavner A, Nilsson M, Pelto-Huikko M, Tomarev S, et al. Functional conservation of interactions between a homeodomain cofactor and a mammalian ftz-F1 homologue. *EMBO Rep* (2004) 5(6):613–9. doi: 10.1038/sj.embor.7400147

16. Botrugno OA, Fayard E, Annicotte JS, Haby C, Brennan T, Wendling O, et al. Synergy between lrh-1 and beta-catenin induces G1 cyclin-mediated cell proliferation. *Mol Cell* (2004) 15(4):499–509. doi: 10.1016/j.molcel.2004.07.009

17. Jordan BK, Shen JH, Olaso R, Ingraham HA, Vilain E. Wnt4 overexpression disrupts normal testicular vasculature and inhibits testosterone synthesis by repressing steroidogenic factor 1/Beta-catenin synergy. *Proc Natl Acad Sci U.S.A.* (2003) 100(19):10866–71. doi: 10.1073/pnas.1834480100

18. Li Y, Choi M, Cavey G, Daugherty J, Suino K, Kovach A, et al. Crystallographic identification and functional characterization of phospholipids as ligands for the orphan nuclear receptor steroidogenic factor-1. *Mol Cell* (2005) 17(4):491–502. doi: 10.1016/j.molcel.2005.02.002

19. Krylova IN, Sablin EP, Moore J, Xu RX, Waitt GM, MacKay JA, et al. Structural analyses reveal phosphatidyl inositols as ligands for the Nr5 orphan receptors sf-1 and lrh-1. *Cell* (2005) 120(3):343–55. doi: 10.1016/j.cell.2005.01.024

20. Lewis AE, Rusten M, Hoivik EA, Vikse EL, Hansson ML, Wallberg AE, et al. Phosphorylation of steroidogenic factor 1 is mediated by cyclin-dependent kinase 7. *Mol Endocrinol* (2008) 22(1):91–104. doi: 10.1210/me.2006-0478

21. Wang W, Zhang C, Marimuthu A, Krupka HI, Tabrizizad M, Shelloe R, et al. The crystal structures of human steroidogenic factor-1 and liver receptor homologue-1. *Proc Natl Acad Sci U.S.A.* (2005) 102(21):7505–10. doi: 10.1073/pnas.0409482102

22. Whitby RJ, Dixon S, Maloney PR, Delerive P, Goodwin BJ, Parks DJ, et al. Identification of small molecule agonists of the orphan nuclear receptors liver receptor homolog-1 and steroidogenic factor-1. *J Med Chem* (2006) 49(23):6652–5. doi: 10.1021/jm060990k

23. Del Tredici AL, Andersen CB, Currier EA, Ohrmund SR, Fairbain LC, Lund BW, et al. Identification of the first synthetic steroidogenic factor 1 inverse agonists: Pharmacological modulation of steroidogenic enzymes. *Mol Pharmacol* (2008) 73(3):900–8. doi: 10.1124/mol.107.040089

24. Lee JM, Lee YK, Mamrosh JL, Busby SA, Griffin PR, Pathak MC, et al. A nuclear-Receptor-Dependent phosphatidylcholine pathway with antidiabetic effects. *Nature* (2011) 474(7352):506–10. doi: 10.1038/nature10111

25. Knower KC, Kelly S, Ludbrook LM, Bagheri-Fam S, Sim H, Bernard P, et al. Failure of Sox9 regulation in 46xy disorders of sex development with sry, Sox9 and Sf1 mutations. *PloS One* (2011) 6(3):e17751. doi: 10.1371/journal.pone.0017751

26. Van Durme J, Delgado J, Stricher F, Serrano L, Schymkowitz J, Rousseau F. A graphical interface for the foldx forcefield. *Bioinformatics* (2011) 27(12):1711–2. doi: 10.1093/bioinformatics/btr254

27. Porollo A, Meller J. Prediction-based fingerprints of protein-protein interactions. *Proteins* (2007) 66(3):630–45. doi: 10.1002/prot.21248

28. Tsuji T, Yoda T, Shirai T. Deciphering supramolecular structures with protein-protein interaction network modeling. *Sci Rep* (2015) 5:16341. doi: 10.1038/srep16341

29. Vihinen M. Guidelines for reporting and using prediction tools for genetic variation analysis. *Hum Mutat* (2013) 34(2):275–82. doi: 10.1002/humu.22253

30. Ioannidis NM, Rothstein JH, Pejaver V, Middha S, McDonnell SK, Baheti S, et al. Revel: An ensemble method for predicting the pathogenicity of rare missense variants. *Am J Hum Genet* (2016) 99(4):877–85. doi: 10.1016/j.ajhg.2016.08.016

31. Takasawa K, Ono M, Hijikata A, Matsubara Y, Katsumata N, Takagi M, et al. Two novel Hsd3b2 missense mutations with diverse residual enzymatic activities for Delta5-steroids. *Clin Endocrinol (Oxf)* (2014) 80(6):782–9. doi: 10.1111/cen.12394

32. Maatouk DM, DiNapoli L, Alvers A, Parker KL, Taketo MM, Capel B. Stabilization of beta-catenin in xy gonads causes Male-to-Female sex-reversal. *Hum Mol Genet* (2008) 17(19):2949–55. doi: 10.1093/hmg/ddn193

33. Schimmer BP, White PC. Minireview: Steroidogenic factor 1: Its roles in differentiation, development, and disease. *Mol Endocrinol* (2010) 24(7):1322–37. doi: 10.1210/me.2009-0519

34. Figueiredo BC, Cavalli LR, Pianovski MA, Lalli E, Sandrini R, Ribeiro RC, et al. Amplification of the steroidogenic factor 1 gene in childhood adrenocortical tumors. *J Clin Endocrinol Metab* (2005) 90(2):615–9. doi: 10.1210/jc.2004-0942

frontiers | Frontiers in Endocrinology

TYPE Original Research
PUBLISHED 20 January 2023
DOI 10.3389/fendo.2022.1045038

OPEN ACCESS

EDITED BY
Piero Ferolla,
Umbria Regional Cancer Network, Italy

REVIEWED BY
Roberta Modica,
University of Naples Federico II, Italy,
Simona Glasberg,
Hadassah Medical Center, Israel

*CORRESPONDENCE
Chiara Spadazzi
chiara.spadazzi@irst.emr.it

†These authors have contributed equally to this work and share first authorship

‡These authors have contributed equally to this work and share last authorship

SPECIALTY SECTION
This article was submitted to Cancer Endocrinology, a section of the journal Frontiers in Endocrinology

RECEIVED 15 September 2022
ACCEPTED 28 December 2022
PUBLISHED 20 January 2023

CITATION
Liverani C, Spadazzi C, Ibrahim T, Pieri F, Foca F, Calabrese C, De Vita A, Miserocchi G, Cocchi C, Vanni S, Ercolani G, Cavaliere D, Ranallo N, Chiadini E, Prisinzano G, Severi S, Sansovini M, Martinelli G, Bongiovanni A and Mercatali L (2023) HRAS overexpression predicts response to Lenvatinib treatment in gastroenteropancreatic neuroendocrine tumors. *Front. Endocrinol.* 13:1045038. doi: 10.3389/fendo.2022.1045038

HRAS overexpression predicts response to Lenvatinib treatment in gastroenteropancreatic neuroendocrine tumors

Chiara Liverani[1†], Chiara Spadazzi[1*†], Toni Ibrahim[2], Federica Pieri[3], Flavia Foca[4], Chiara Calabrese[1], Alessandro De Vita[1], Giacomo Miserocchi[1], Claudia Cocchi[1], Silvia Vanni[1], Giorgio Ercolani[5], Davide Cavaliere[5], Nicoletta Ranallo[6], Elisa Chiadini[1], Giovanna Prisinzano[1], Stefano Severi[7], Maddalena Sansovini[7], Giovanni Martinelli[8], Alberto Bongiovanni[6‡] and Laura Mercatali[1‡]

[1]Bioscience Laboratory, IRCCS Istituto Romagnolo per lo Studio dei Tumori (IRST) "Dino Amadori", Meldola, Italy, [2]Osteoncology, Bone and Soft Tissue Sarcomas and Innovative Therapies Unit, IRCCS Istituto Ortopedico Rizzoli, Bologna, Italy, [3]Pathology Unit, "Morgagni-Pierantoni" Hospital, Forlì, Italy, [4]Unit of Biostatistics and Clinical Trials, IRCCS Istituto Romagnolo per lo Studio dei Tumori (IRST) "Dino Amadori", Meldola, Italy, [5]General and Oncologic Surgery, "Morgagni-Pierantoni" Hospital, Forlì, Italy, [6]Osteoncology and Rare Tumors Center, IRCCS Istituto Romagnolo per lo Studio dei Tumori (IRST) "Dino Amadori", Meldola, Italy, [7]Unit of Nuclear Medicine, IRCCS Istituto Romagnolo per lo Studio dei Tumori (IRST) "Dino Amadori", Meldola, Italy, [8]Scientific Directorate, IRCCS Istituto Romagnolo per lo Studio dei Tumori (IRST) "Dino Amadori", Meldola, Italy

Introduction: Neuroendocrine neoplasms (NENs) are a rare group of tumors exceptionally heterogeneous, with clinical presentation ranging from well differentiated more indolent tumors to poorly differentiated very aggressive forms. Both are often diagnosed after the metastatic spread and require appropriate medical treatment. A high priority need in the management of this disease is the identification of effective therapeutic strategies for advanced and metastatic patients. The recent TALENT trial demonstrated the efficacy of lenvatinib, a multi-tyrosine kinase inhibitor, in patients with gastroenteropancreatic neuroendocrine tumors (GEP-NETs) with no other treatment indication. Further development of this drug in advanced NETs is warranted.

Methods: We investigated potential clinical and molecular determinants of lenvatinib response in human primary cultures derived from patients with GEP-NET of different grades and sites of origin. We correlated response to treatment with patient clinical characteristics, with the mutational status of 161-cancer associated genes and with the expression levels of MKI-related genes.

10.3389/fendo.2022.1045038

Results: Lenvatinib exerted a significant antitumor activity in primary GEP-NET cells, with median survival inhibitions similar or higher than those of standard frontline treatments. Of the 11 primary cultures analyzed in our case series, 6 were classified as responder showing a significant survival inhibition, and 5 as non-responder. We observed that the overexpression of HRAS in the original tumor tissue compared to the matched healthy tissue significantly correlated with responsiveness of primary cells to lenvatinib (p=.048). All 5 non-responder cultures showed normal HRAS expression, while of the 6 responder cultures, 4 had HRAS overexpression. Overexpression of HRAS was not associated with gene mutation. None of the other evaluated clinical variables (grade, Ki67, site of origin and syndromic disease) or molecular markers correlated with response.

Discussion: Lenvatinib appears to be a highly effective drug for the treatment of NETs. The evaluation of HRAS expression in the tumor tissue might improve patient selection and optimize therapeutic outcome.

KEYWORDS

nen, primary cultures, Lenvatinib efficacy, HRAS overexpression, predictive marker

1 Introduction

Neuroendocrine neoplams (NENs) are a rare group of tumors that arise in various anatomic locations (1). The most common sites of origin are the gastro-enteropancreatic (GEP) tract and the lung. NENs are classified according to their sites of origin. Gastroenteropancreatic (GEP)-NENs are divided into grade (G) 1 and G2, G3 neuroendocrine tumors (NETs) that have well-differentiated morphology and Ki-67 ≤2% for G1, 3-20% for G2 and >20% for G3, and neuroendocrine carcinomas (NECs) with poorly differentiated morphology and Ki-67 >20% (2, 3). The estimated annual incidence is 6.9 cases per 100,000 person-year and has increased more than 6-fold over the last 4 decades (4, 5). The prevalence of NETs is currently over 170,000 patients only in the United States and will continue to grow (6, 7). The disease is exceptionally heterogeneous, with clinical presentation ranging from well differentiated more indolent tumors to poorly differentiated very aggressive forms. Both are often diagnosed after the metastatic spread and require appropriate medical treatment (8). NENs are therefore a great public health problem. Unfortunately, few oncogenic mutations are known, limiting the availability of candidate targets for therapeutic intervention and biomarkers for patient stratification (9). Few drugs have been introduced in clinical practice and therapeutic options for systemic intervention are limited. Surgery is the best approach in patients with resectable tumor, while somatostatin analogues, peptide receptor radionuclide therapy (PRRT) and molecular targeted drugs such as sunitinib and everolimus are indicated in patients with advanced disease (10–13). Chemotherapy, in particular temozolomide and capecitabine, have shown to be effective in some subsets of patients with inoperable or metastatic GEP-NEN (14, 15).

Recently, Capdevila et al. reported the TALENT trial demonstrating the efficacy of lenvatinib in the treatment of advanced well differentiated GEP-NETs (16). Lenvatinib is a multi-tyrosine kinase inhibitor (MKI) targeting vascular endothelial growth factor receptors (VEGFR) 1-3, fibroblast growth factor receptors (FGFR) 1-4, platelet-derived growth factor receptor (PDGFR) α and the proto-oncogenes RET and KIT (17, 18). Lenvatinib represents a novel therapeutic opportunity for GEP-NET patients progressing from targeted therapies or somatostatin analogues with no other treatment indication (16). In the TALENT study, despite most of the patients requiring one or more dose reduction, the overall response rate (ORR) assessed centrally was 44.2% in patients with pancreatic NET and 16.4% in patients with gastrointestinal NET. This ORR is of note especially for patients with high and symptomatic tumor burden and it is the highest reported in a clinical trial with MKI (19, 20). However, the treatment approach of NEN patients lacks clinically validated tissue or blood biomarkers to identify patients who are likely to benefit from a specific therapy, improving efficacy and avoiding unnecessary side effects. The discovery of key molecular alterations that predict therapy response has dramatically changed the success rate of several targeted compounds. As an example, tyrosine kinase inhibitors (TKIs) targeting EGFR, initially tested in an unselected population, have been of limited usefulness until the identification of EGFR gene mutations (21). They now represent the

first-line therapy in the treatment of non-small cell lung cancer (NSCLC). Few studies report putative biomarkers of response to lenvatinib, but no conclusive data have been obtained. Lee et al. identified a combination of 5 serum cytokines that can predict patients with metastatic renal cell carcinoma that may benefit from second-line treatment with lenvatinib-plus-everolimus (22). Tahara et al. demonstrated that Angiopoietin 2 may be predictive of lenvatinib sensitivity in patients with thyroid cancer (23). In the era of precision medicine, evidence for a biomarker-based approach is crucially needed especially in patients with rare tumors.

The lack of reliable NEN models has represented a barrier for the identification of driver molecular alterations associated with disease pathogenesis, progression and responsiveness to anticancer agents (24). Few NEN cell lines are currently available and do not display a well-differentiated neuroendocrine phenotype (25). Moreover, the engraftment rate of NEN cells in murine models is less than 10% (26). The development of more efficient and informative preclinical models is urgently needed. To this aim, the use of patient-derived primary cultures enable the mapping of drug sensitivity and molecular profiles at individual level, representing a key technology for precision medicine (27, 28).

Here we established human primary cultures from GEP-NEN of different grades and sites of origin and assessed their sensitivity to lenvatinib in comparison with standard treatment agents for NEN patients. We characterized primary cultures to identify potential clinical and molecular markers with treatment predictive value.

2 Materials and methods

2.1 Case series

The study involved eleven patients with grade 1, grade 2 or grade 3 NETs who underwent surgical treatment at the Department of Surgical Oncology of the "Morgagni-Pierantoni" Hospital, Forlì, Italy. The protocol was approved by the Romagna Ethics Committee (CEROM) and performed according to Good Clinical Practice standards and the Declaration of Helsinki. Patients eligible for the study must have been adults (at least 18 years of age) of both sexes, undergoing surgery for NENs and must have provided written, informed consent. Included patients may have undergone or may be still in treatment, including chemotherapy (also neo-adjuvant settings), targeted therapy, radiotherapy, somatostatin analogue therapies and combination therapy.

2.2 Compounds

Lenvatinib mesilate (lenvatinib) were kindly provided by Eisai Co., Ltd. (Ibaraki, Japan). Everolimus was kindly provided by Novartis (NJ, USA). Temozolomide was purchased by Sigma-Aldrich (Sigma-Aldrich, Steinheim, Germany).

2.3 Establishment of primary cell culture

Patient-derived NEN cell cultures were isolated from surgical specimens. Prior to tissue processing, all specimens were analyzed by an expert pathologist who confirmed the presence of tumor cells in the surgical material. Tumor specimens were processed within 3 hours from resection. Samples were washed twice in sterile phosphate buffered saline (PBS) and sliced into 1-2 mm^3 pieces with a surgical scalpel. The obtained pieces were incubated in 2 mg/ml collagenase type I (Millipore Corporation, Billerica, MA, USA) at 37°C in stirring conditions for 30 min. Then, digestion was blocked by adding Dulbecco's modified Eagle's medium (DMEM) supplemented with 10% fetal bovine serum, 1% glutamine and 1% penicillin/streptomycin. The solution was filtered using 100-µm sterile filters (CellTrics, Partec, Münster, Germany). Cells were counted and seeded in monolayer cultures at a density of 80,000 cells/cm^2 and maintained in complete DMEM medium at 37°C in a 5% CO_2 atmosphere. All the experiments were conducted using low-passage primary cultures.

2.4 Drug testing

25,000 cells/well were seeded in 96-well plates. Cells were allowed to recover for 72 hours before treatment. The following concentrations were used on the basis of the peak plasma concentration of each tested compound obtained from pharmacokinetic clinical data: folfox 1 ug/ml oxaliplatin plus 100 ng/ml 5-fluorouracile (29), everolimus (eve) 0.1 ug/ml (30), temozolomide (tmz) 25 µM (31) and lenvatinib (lenva) 0.6 ug/ml (32). Drug efficacy was evaluated by MTT assay. Briefly, controls and treated samples were incubated with 0.5 mg/ml of MTT solution (Sigma Aldrich) in DMEM for 2 hours at 37°C. Cell viability was determined by reading the absorbance at 550 nm. Survival percentages were calculated as the average absorbance of treated cells over the absorbance of untreated controls.

2.5 Quantitative real-time reverse transcriptional-PCR (qRT-PCR)

Total mRNA was isolated using TRIzol Reagent (Invitrogen) and reverse-transcribed using the iScript cDNA Synthesis Kit (BioRad, Hercules, CA, USA) with the following incubation cycles: 25°C for 5 min, 42°C for 20 min, 47°C for 20 min, 50°C for 15 min and 5 min at 85°C. Real-Time PCR was performed on the 7500 Real-Time PCR System using the SYBR Select Master Mix and the Taqman Universal Master Mix (Applied

Biosystems, Foster City, CA, USA). Amplification was performed in a final volume of 20 µl containing 2x Gene expression master Mix (Applied Biosystem), 2 µl of cDNA in a total volume of 20 µl. The reaction mixtures were incubated for 2 min at 50°C, 10 min at 95°C followed by 40 PCR cycles at 95°C for 15 sec and 60°C for 1 min for overall markers. The amount of transcripts was normalized to the endogenous reference genes β-actin and HPRT and expressed as n-fold mRNA levels relative to a calibrator using a comparative threshold cycle (Ct) value method (ΔΔCt). The RNA extracted from untreated cells was used as the calibrator.

2.6 Focus Oncomine panel

We used an amplicon-based DNA/RNA NGS assay, known as Oncomine™ Comprehensive Assay v3 (OCAv3) (Thermo Fisher Scientific) covers 161 cancer-associated genes: 87 genes with hotspot mutations, 43 genes with focal CNV gains, 48 genes with full CDS for DEL mutations and 51 gene-fusion drivers. For all patients, 5 FFPE tumor sections of 5 µm were used for DNA and RNA extraction using the Maxwell RSC DNA and RNA FFPE Kit (Promega, Madison, WI, USA), following the manufacturer's protocol. DNA and RNA concentrations were determined by fluorometric quantitation using a Qubit 4.0 Fluorometer with Qubit DNA dsDNA HS Assay Kit and Qubit RNA HS Assay Kit (Thermo Fisher), as appropriate. Complementary DNA (cDNA) synthesis prior to library preparation for RNA panel was carried out using SuperScript™ IV VILO™ Master Mix (Thermo Fisher Scientific). Library preparation was performed using the Oncomine™ Comprehensive Assay v3 DNA/RNA Chef-Ready panel, designed for use with the Ion Chef™, following manufacturer's instructions, with 10 ng input DNA and RNA per sample. The libraries were loaded onto Ion Chef System (Thermo Fisher Scientific) for template preparation, using Ion 540™ Kit-Chef, and finally sequenced on the Ion S5 Plus platform (Thermo Fisher Scientific) using the Ion 540 Chips (Thermo Fisher Scientific). Primary analysis was carried out using a Torrent Suite Server™ (5.12.3) to perform initial quality control, including chip loading density, median read length and number of mapped reads. Afterwards, a second analysis was performed by Ion Reporter™ Software (5.16), hosting informatics tools for variants, filtering, and annotations. Variants were identified with VAF greater than or equal to 5% with coverage greater than 500X and clinically relevant. CNV algorithm in Ion Reporter is used with the following features: minimum % cellularity for accurate CNV calling is 50% and Median Absolute Pairwise Difference (MAPD) is <0.5. The RNA panel was able to identify 51 rearrangements. A fusion was classified as present with greater than 500,000 mapped reads, providing evidence for the fusion. The performance of the DNA/RNA panel was established, using Seraseq Lung & Brain CNV Mix, +6 copies and FFPE Fusion RNA Reference Material v4 (Seracare Life Sciences, Inc.).

2.7 Statistical analysis

Three independent replicates were performed for each experiment. Data are presented as mean ± standard deviation (SD) or mean ± standard error, as stated, with *n* indicating the number of replicates. Differences between groups were assessed by a two-tailed Student's t-test and accepted as significant at $p<.05$. Correlation of clinical and molecular variable with lenvatinib responsiveness was performed by Fisher's exact test and accepted as significant at $p<.05$.

3 Results

3.1 Descriptive characteristics

The main clinical and histological characteristics of the 11 patients analyzed in this study are shown in Table 1. Median follow up was 30 months (range 19-72). Nine patients (81.8%) were males and two (18.2%) were females. Median age at the time of diagnosis was 79 years (range 36-84). The site of the primary tumor was pancreas in four patients (36.4%), stomach in two patients (18.2%) and ileum in five patients (45.4%). Eight patients (72.7%)

TABLE 1 Clinicopathological characteristics.

	n (%)
Median follow up, months (range)	30 (19-72)
Age at diagnosis, years (range)	79 (36-84)
Gender	
Male	9 (81.8)
Female	2 (18.2)
Site of disease	
Pancreas	4 (36.4)
Stomach	2 (18.2)
Ileum	5 (45.4)
Grading	
G1	8 (72.7)
G2	2 (18.2)
G3	1 (9.1)
^{68}Ga-PET/CT Octreoscan	
Negative	0 (0.0)

(Continued)

10.3389/fendo.2022.1045038

TABLE 1 Continued

	n (%)
Positive	10 (90.9)
nd	1 (9.1)
^{18}F-FDG PET/CT	
Negative	0 (0.0)
Positive	3 (27.3)
nd	8 (72.7)
Metastatic disease	
Yes	2 (18.2)
No	9 (81.8)
Syndromic disease	
Yes	2 (18.2)
No	8 (72.7)
nd	1 (9.1)
Best response to firs line therapy	
PR	1 (9.1)
SD	2 (18.2)
nd	8 (72.7)

G, grade; ^{68}Ga, Gallium-68; nd, not determined: PR partial, response; SD, stable disease.

had grade (G) 1 well-differentiated NET, two patients (18.2%) had G2 well-differentiated NET and one patient (9.1%) had a G3 well-differentiated NET. Ten patients (90.9%) showed positive ^{68}Gallium-positron emission tomography/computerized tomography (^{68}Ga-PET/CT), while for one patient was not performed. Three patients (27.3%) showed positive ^{18}F-fluorodeoxyglucose (^{18}FDG)-PET/CT scan, while the ^{18}F-FDG PET/CT scan for the remaining patients was not performed. Two patients (18.2%) had a syndromic disease caused by hormonal hypersecretion. Only two patients (18.2%) developed metastatic disease. Three patients (27.3%) underwent first line therapy. One patient showed stable disease after receiving 3 subcutaneous administrations of lanreotide (120 mg every 28 days). One patient was treated with sandostatine (30 mg every 28 days) showing stable disease at the 3 months re-evaluation. One patient (G3 NET) was treated with folfox4 every 2 weeks (oxaliplatin 85 mg/m^2 and fluorouracil 400 mg/m^2 bolus on day 1, then fluouracil 600 mg/m^2 over 22 hours on days 1 and 2) showing a partial response after 7 cycles.

3.2 Establishment of NEN primary cultures

Primary NEN cells showed limited viable time after recovery from the tumor specimens. None of the isolated cultures was stable for more than 3 passages. For this reason, all treatments were performed within 1 week from isolation. Examples of primary NEN cell appearance are reported in Figure 1. All cells displayed an epithelioid morphology as confirmed by an expert pathologist. Net1 derived from an ileal G1 lesion and appeared as cells with very small dimensions with mixed shape. Net2 and Net5 derived from a G1 and a G2 pancreatic tumor, respectively. Net2 cells formed dense, large aggregates with varied morphology, some of them showing spheroid-like appearance; Net5 cells formed large disorganized aggregates. Net4 derived from a G1 pancreatic tumor and appeared as isolated cells mixed with fibroblasts. Net6 and Net7 derived from two G1 ileal tumors: Net6 formed large aggregates of rounded-shaped cells, while Net7 appeared as isolated cells mixed with fibroblasts. Net8 derived from a G3 gastric tumor and appeared as small aggregates of cells with rounded morphology over a fibroblast layer. Finally, Net11 derived from a G1 gastric tumor and appeared as small rounded cells forming aggregates with varied dimensions and spheroid-like morphology.

3.3 Efficacy of lenvatinib and conventional NEN therapies in primary cultures

We assessed the sensitivity of the eleven primary NEN cultures to lenvatinib. Efficacy was compared to that of fluoruracil plus oxapliplatin (folfox), temozolomide and everolimus which represent approved drugs for the treatment of NEN patients. Overall, lenvatinib exerted an antitumor activity in NET of ileal origin with a median survival inhibition of 25.6%. Also in gastric and pancreatic NET, lenvatinib showed good efficacy with a median survival inhibition of 11.0% and 11.6%, respectively (Figure 2A). Compared to other drugs, lenvatinib was the most effective treatment in ileal and gastric NETs, while in pancreatic NETs everolimus resulted to be the most active compound. Cluster heatmap of survival percentages in the primary cultures displayed response groups independent from the sites of origins (Figure 2B). Taking into consideration each primary culture, lenvatinib induced a significant inhibition of survival in all tested ileal cells (p=.0439 for Net1, p=.0050 for Net3, p<.001 for Net6, p=.0094 for Net7 and p<.001 for Net10) (Figure 3A). Folfox induced a significant inhibition of survival only in Net6 (p=.0297), everolimus exerted a significant activity in Net6 (p=.0045), Net7 (p=.0311) and Net 10 (p<.001), while temozolomide was effective only in Net3 (p=.0346) (Figure 3A). In primary pancreatic cells, lenvatinib induced a significant inhibition of survival in Net4 (p=.0433), while it was not significantly active in Net2, Net5 and Net9 (Figure 3B). Folfox was not effective in pancreatic cells, everolimus was effective in Net4 (p=.0187) and Net5 (p=.0358) but not in Net2, and Net9, temozolomide was effective only in Net5

10.3389/fendo.2022.1045038

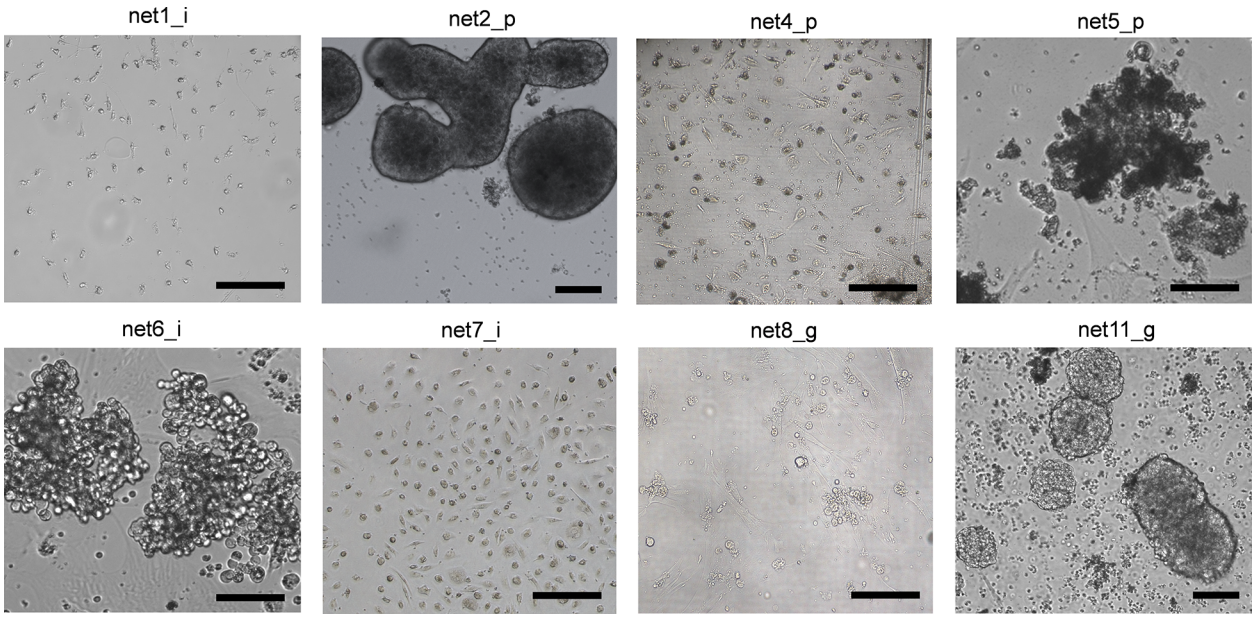

FIGURE 1
Human primary NEN cells showed varied morphology in monolayer culture. Bright field representative images of different primary NEN cells with ileal, pancreatic and gastric origins. Scale bar: 50 μm.

(p=.0354) (Figure 3B). In gastric primary cells lenvatinib was not significantly effective in any of the two primary cultures (Figure 3C). Net11 was not sensitive to any of the other tested drugs. In Net8 cells, folfox showed significant inhibition of cell survival (p=.0090). Everolimus was not effective in any of the two gastric primary cultures (Figure 3C). It is interesting to notice that for Net8, sensitivity of tumor cells to folfox was confirmed in the clinical setting. The patient was treated in neoadjuvant setting with folfox IV regimen for 12 cycles and showed a partial response (Table 1). Unfortunately, no other clinical data on treatment were available to match results with those obtained in primary cells, as most of the patients did not receive any first line therapy (Table 1).

3.4 Correlation of lenvatinib efficacy with clinical and molecular characteristics

Correlation of lenvatinib efficacy with patient clinical and molecular characteristics is reported in Table 2. Of the eleven primary cultures analyzed in our case series, six were classified as responder with a significant survival inhibition in treated cells compared to controls, and five as non-responder. We observed that the overexpression of HRAS in the tumor tissues compared to matched healthy tissues significantly correlated with responsiveness of primary NET cells to lenvatinib (p=.048) (Table 2 and Figure 4A). All five non-responder patients showed normal HRAS expression, while of the six responder patients, four showed HRAS overexpression and only one normal expression. For one responder patient HRAS was not determined. HRAS overexpression did not correlate with gene mutation. Tissue samples were subject to an NGS targeted sequencing assay for the detection of single nucleotide variants (SNVs), copy number variations (CNVs), gene fusions, and indels from 161 cancer driver genes. None of the analyzed primary tissues showed mutation in HRAS, and few molecular alterations were detected in the tumor tissues confirming the extremely low mutational burden of these tumors (Figure 4B). However, mutations in various genes related to TKs were detected in the tumor samples (JAK3, NRAS, NTRK2, NF1, SETD2) suggesting frequent alteration of TK pathways for neuroendocrine neoplasms.

Finally, none of the others analyzed markers and clinical variables (grade, Ki67, site of origin and syndromic disease) showed correlation with lenvatinib responsiveness (Table 2 and Supplementary Figure 1), although this result may depend on the small sample size.

4 Discussion

A high priority unmet need in the management of NEN patients is the improvement of the actual therapeutic landscape for patients with metastatic or locally-advanced disease. In the recent years, important scientific advances have been introduced for the treatment of NENs. However, predictive factors to select patients that would benefit from targeted treatments and to guide sequencing of systemic regimens are lacking (33). Advances have been limited by the lack of murine and human cell line models that

10.3389/fendo.2022.1045038

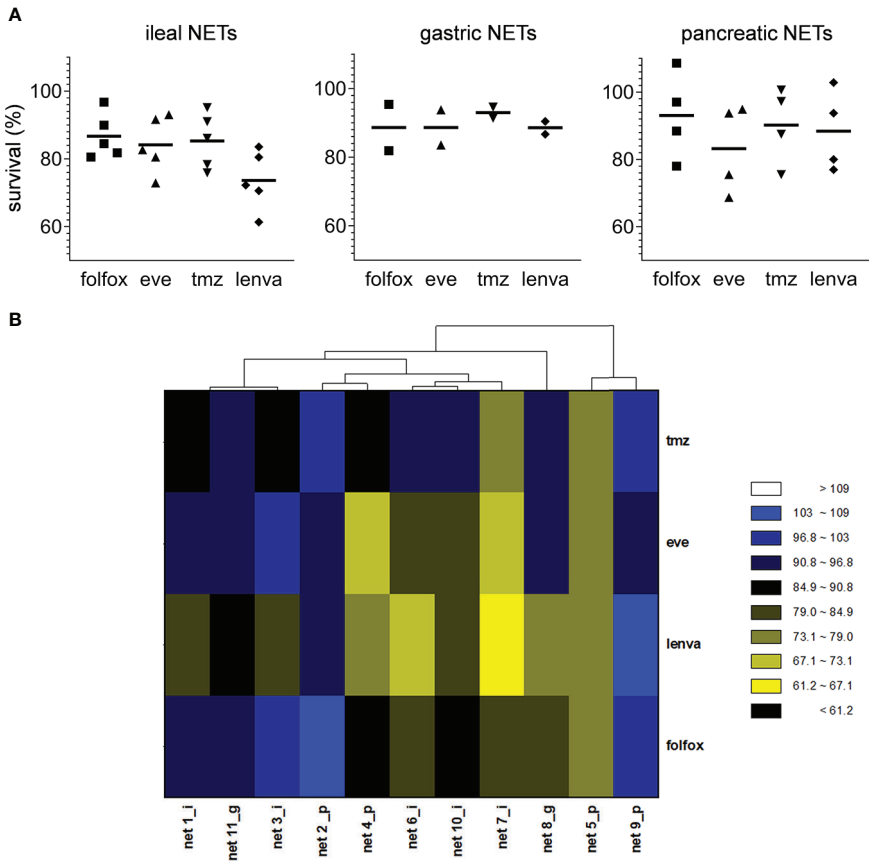

FIGURE 2
Effect of pharmacological treatments on cell viability in human primary NEN cultures. **(A)** Survival percentages values according to tumor site of origin in human primary NEN culture treated with folfox, everolimus (eve), temozolomide (tmz) and lenvatinib (lenva) compared to untreated controls. Data represent median value (line) and single values for each primary culture (*n*=1 per patient, 3 technical replicates). **(B)** Heatmap visualization comparing survival percentages for folfox, eve, tmz and lenva in human primary NEN cultures. Each column represents an individual primary culture. The dendrogram displays Pearson's clustering distance. The color code represents the scaled survival percentages for each drug.

do not accurately represent the well-differentiated and slow proliferative phenotypes of NETs and fail to reflect the inter-patient variability (34). Lenvatinib, a potent inhibitor of VEGF receptors (VEGFR1-3) and other pro-oncogenic receptor TKs, was recently tested in patients with G1 and G2 GEP-NETs showing encouraging results. Despite this, biomarkers to optimize the outcome of MKI treatment and avoid unnecessary side effects are still to be established (35). Here we evaluated the antitumor activity of lenvatinib in eleven primary GEP-NET cultures of different grade and sites of origin investigating clinical and molecular markers with potential predictive value. We observed that lenvatinib exerts a significant inhibition of cell growth in primary GEP-NET cells. No differences were found according to tumor site of origin. Compared to standard therapeutic drugs used in frontline treatment for NEN patients, lenvatinib resulted the most active compound in ileal and gastric primary cells, while in pancreatic NETs everolimus was the most effective drug. Of note, folfox was ineffective in the majority of primary cultures, confirming the scarce sensitivity of low grade neuroendocrine tumors to chemotherapy (14). We next demonstrated that overexpression of HRAS in the patient tumor tissue compared to matched healthy tissues significantly correlates with responsiveness of primary cells to lenvatinib. Of the six responder patients, four showed HRAS overexpression in the tumor tissue. The Ras-Raf-MEK-ERK pathway, downstream of TK receptors, is a key signaling pathway involved in tumorigenesis and angiogenesis of about a third of all human cancers, including NETs (36). The prevalence of HRAS overexpression and mutation in NET patients and its correlation with clinical outcomes have not been investigated. According to our evidence, HRAS overexpression can be found in about 40% of GEP-NET tumor tissues and might portend a higher sensitivity to lenvatinib treatment. Moreover, considering that Capdevila et al. propose lenvatinib to be effective in GEP-NET patients that progressed after treatment with targeted agents (16), it would be interesting to investigate the prevalence of HRAS overexpression in patients with resistance to upfront therapies.

10.3389/fendo.2022.1045038

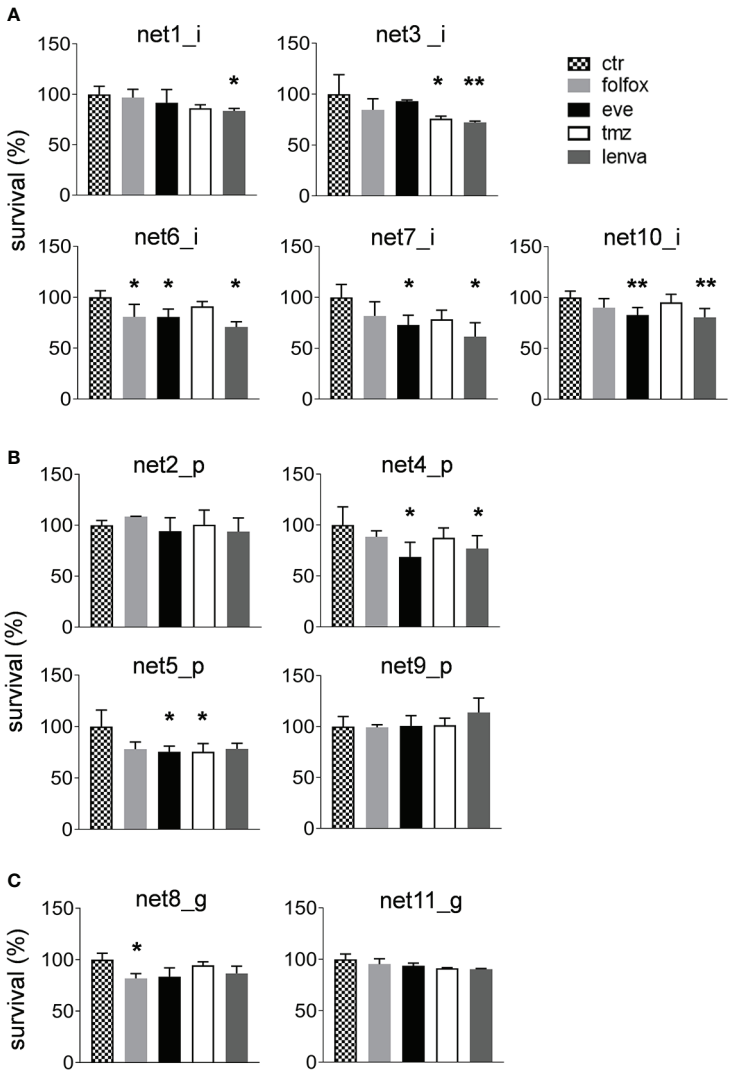

FIGURE 3
Sensitivity of primary NEN cells to standard upfront treatment or to lenvatinib. **(A)** Survival percentages of ileal primary NEN cultures (Net1, Net3, Net6, Net7, Net10) treated with folfox, eve, tmz and lenva compared to untreated controls. Data represent mean ± S.D. (n=3) *p<.05, two-tailed Student's t-test. **(B)** Survival percentages of pancreatic primary NEN cultures (Net2, Net4, Net5, Net9) treated with folfox, eve, tmz and lenva compared to untreated controls. Data represent mean ± S.D. (n=3) *p<.05, two-tailed Student's t-test. **(C)** Survival percentages of gastric primary NEN cultures (Net8, Net11) treated with folfox, eve, tmz and lenva compared to untreated controls. Data represent mean ± S.D. (n=3) *p<.05, **p<.001, two-tailed Student's t-test.

TABLE 2 Correlation of response to Lenvatinib with clinical and molecular data.

	Levatinib			*p*-value
	Non-responder (%)	Responder (%)	Total	
Overall	5 (45.5)	6 (54.5)	11	
Syndromic disease				
yes	4 (50.0)	4 (50.0)	8*	.467
no	0 (0.0)	2 (100.0)	2	

(Continued)

10.3389/fendo.2022.1045038

TABLE 2 Continued

	Levatinib			*p*-value
	Non-responder (%)	Responder (%)	Total	
Ki67				
≤2	2 (25.5)	6 (75.5)	8	.061
>2	3 (100.0)	0 (0.0)	3	
Grade				
1	2 (25.5)	6 (75.5)	8	
2	2 (100.0)	0 (0.0)	2	.061
3	1 (100.0)	0 (0.0)	1	
Site of origin				
G.I.	2 (28.6)	5 (71.4)	7	.242
pancreas	3 (75.5)	1 (25.5)	4	
HRAS overexpression				
no	5 (83.3)	1 (16.7)	6[†]	*.048*
yes	0 (0.0)	4 (100.0)	4	

*For 1 patient data on syndromes were not available.
[†]HRAS expression was not evaluable in 1 patient.
p-value <.05, Fisher's exact test.

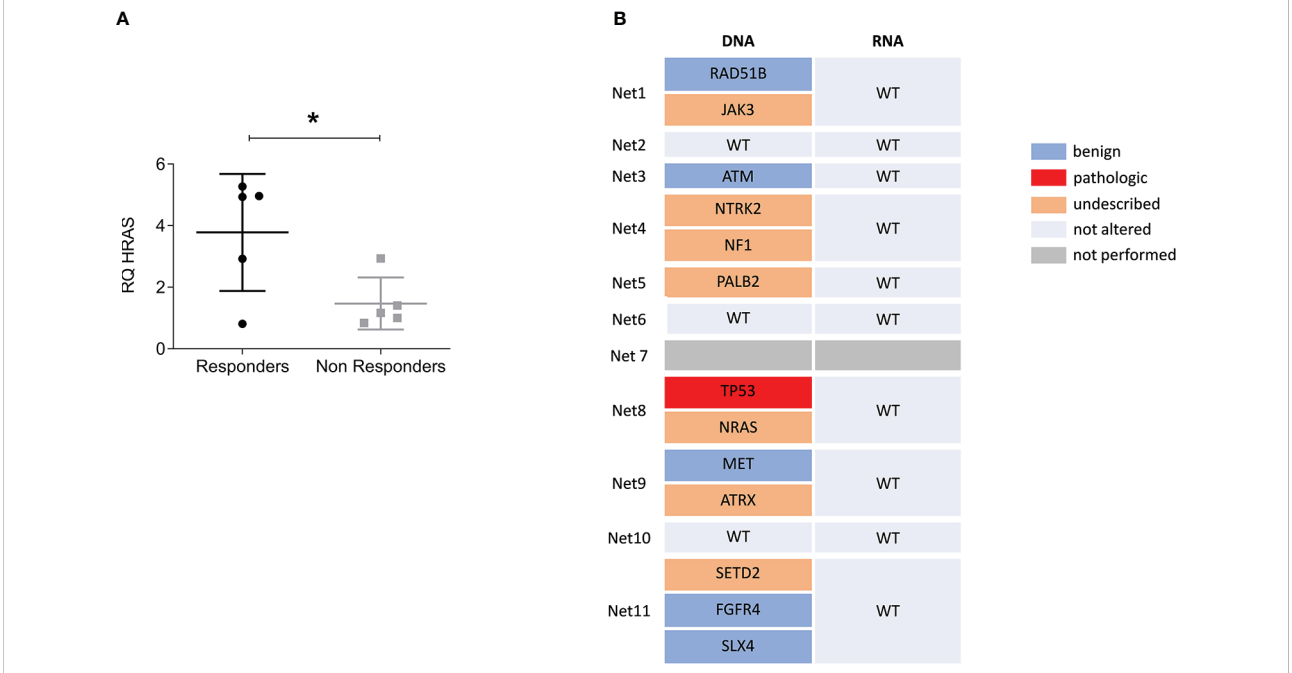

FIGURE 4
HRAS overexpression but not mutation predicts responsiveness to lenvatinib. **(A)** Relative expression levels of HRAS in tumor tissues over matched healthy tissues comparing responder versus non responder patients. Data represent mean ± S.D. (n=3) *p<.05, two-tailed Student's t-test. **(B)** Variant data from the Oncomine Focus Assay panel identified in the NEN patient cohort. The list of genes includes only those found to be altered. Variants were classified as benign, pathologic and of unknown significance. Wild type (WT) indicate that no alteration were found. For Net7 patient the assay was not performed.

Overexpression of HRAS was not correlated with gene mutation. None of the analyzed tumor samples resulted mutated for HRAS. A similar result emerged in the exploratory biomarker analysis of the phase III Study of (E7080) lenvatinib in differentiated cancer of the thyroid (SELECT trial) (23). Tahara et al. demonstrated that lenvatinib PFS benefit observed in patients with thyroid cancer was consistent in all analyzed subgroups regardless of the BRAF or RAS mutational status in the tumor tissues (23). From our sequencing analysis, we also confirmed that NENs are characterized by an extremely low tumor mutational burden (37). Interestingly, the mutations found in our case series consistently involve genes associated with TK pathways. Our study include a limited number of patients, thus a confirmatory analysis in a larger case series is needed to understand if NENs are enriched for alterations in TK genes. Results might uncover driver mutations that are currently lacking in this disease, and confirm data emerged in the TALENT study that reported the highest ORR ever in a clinical trial with a MKI.

In addition, data on lenvatinib mechanism of action in neuroendocrine cells are missing. Lenvatinib has shown antitumor activity against multiple tumor types, such as hepatocellular carcinoma (38), differentiated thyroid cancer (DTC) (39), anaplastic thyroid cancer (ATC) (40), medullary thyroid cancer (MTC) (41), gastric cancer (42), thymic carcinoma (43) and other solid tumors (44). In these tumors lenvatinib exerted diverse mechanisms of action linked to the block of cell proliferation through the targeting of proto-oncogenes RET and KIT and their pathways, and the inhibition of angiogenesis (17, 45–47). The relevance of tumor angiogenesis in NENs is well established. NENs are characterized by an extremely high vascularization, even in the low-grade forms, and strong expression of pro-angiogenic factors such as VEGF-A (48). Investigation into the antiangiogenic effects of lenvatinib and other TKIs in these tumors should be of great relevance.

5 Conclusions

In conclusion, lenvatinib effectively inhibits survival of GEP-NEN cells. The evaluation of HRAS expression in the tumor tissue might improve patient selection and optimize therapeutic outcome. Future efforts should focus on understanding the exact mechanism of action of lenvatinib and TKIs in these tumors.

Data availability statement

The dataset will be available upon request to the corresponding author, as they are part of genetic data obtained from analyses of patients.

Ethics statement

The studies involving human participants were reviewed and approved by Romagna Ethics Committee (CEROM). The patients/participants provided their written informed consent to participate in this study.

Author contributions

CL, CS, AB and LM designed the study. CL, CS, TI, FP, CCa, ADV, GMi, CCo, SV, GE, DC, NR, EC, GP, SS, MS, and GMa collected and analyzed all clinical and biological data. FF carried out the statistical analyses. CL, CS, AB and LM interpreted the data. CL and CS drafted the manuscript. LM and AB revised the manuscript for intellectual content. All authors contributed to the article and approved the submitted version.

Funding

This work was partly supported thanks to the contribution of Ricerca Corrente by the Italian Ministry of Health within the research line “Innovative therapies, phase I-III clinical trials and therapeutic strategy trials based on preclinical models, onco-immunological mechanisms and nanovectors”.

Conflict of interest

The authors declare that the research was conducted in the absence of any commercial or financial relationships that could be construed as a potential conflict of interest.

Publisher’s note

Supplementary material

The Supplementary Material for this article can be found online at: https://www.frontiersin.org/articles/10.3389/fendo.2022.1045038/full#supplementary-material

References

1. Modlin IM, Oberg K, Chung DC, Jensen RT, de Herder WW, Thakker RV, et al. Gastroenteropancreatic neuroendocrine tumours. *Lancet Oncol* (2008) 9 (1):61–72. doi: 10.1016/S1470-2045(07)70410-2

2. Klöppel G, Couvelard A, Hruban RH, Klimstra DS, Komminoth P, Osamura RY, et al. WHO classification of neoplasms of the neuroendocrine pancreas. In: Lloyd RV, Osamura RY, Klöppel G, Rosai J, editors. *WHO classification of tumours of endocrine organs*. Lyon: IARC Press (2017). p. 209–39.

3. Nagtegaal ID, Odze RD, Klimstra D, Paradis V, Rugge M, Schirmacher P, et al. The 2019 WHO classification of tumours of the digestive system. *Histopathology* (2020) 76(2):182–8. doi: 10.1111/his.13975

4. Dasari A, Shen C, Halperin D, Zhao B, Zhou S, Xu Y, et al. Trends in the incidence, prevalence, and survival outcomes in patients with neuroendocrine tumors in the united states. *JAMA Oncol* (2017) 3(10):1335–42. doi: 10.1001/jamaoncol.2017.0589

5. Das S, Dasari A. Epidemiology, incidence, and prevalence of neuroendocrine neoplasms: Are there global differences? *Curr Oncol Rep* (2021) 23(4):43. doi: 10.1007/s11912-021-01029-7

6. Chauhan A, Kohn E, Del Rivero J. Neuroendocrine tumors–less well known, often misunderstood, and rapidly growing in incidence. *JAMA Oncol* (2020) 6 (1):21–2. doi: 10.1001/jamaoncol.2019.4568

7. Cives M, Strosberg JR. Gastroenteropancreatic neuroendocrine tumors. *CA Cancer J Clin* (2018) 68(6):471–87. doi: 10.3322/caac.21493

8. Oronsky B, Ma PC, Morgensztern D, Carter CA. Nothing but NET: A review of neuroendocrine tumors and carcinomas. *Neoplasia* (2017) 19(12):991–1002. doi: 10.1016/j.neo.2017.09.002

9. Segelov E, Chan D, Lawrence B, Pavlakis N, Kennecke HF, Jackson C, et al. Identifying and prioritizing gaps in neuroendocrine tumor research: A modified Delphi process with patients and health care providers to set the research action plan for the newly formed commonwealth neuroendocrine tumor collaboration. *J Glob Oncol* (2016) 3(4):380–8. doi: 10.1200/JGO.2016.006916

10. Wang R, Zheng-Pywell R, Chen HA, Bibb JA, Chen H, Rose JB. Management of gastrointestinal neuroendocrine tumors. *Clin Med Insights Endocrinol Diabetes* (2019) 12:1179551419884058. doi: 10.1177/1179551419884058

11. Kwekkeboom DJ, Krenning EP. Peptide receptor radionuclide therapy in the treatment of neuroendocrine tumors. *Hematol Oncol Clin North Am* (2016) 30 (1):179–91. doi: 10.1016/j.hoc.2015.09.009

12. Uri I, Grozinsky-Glasberg S. Current treatment strategies for patients with advanced gastroenteropancreatic neuroendocrine tumors (GEP-NETs). *Clin Diabetes Endocrinol* (2018) 4:16. doi: 10.1186/s40842-018-0066-3

13. Herrera-Martínez AD, Hofland J, Hofland LJ, Brabander T, Eskens FALM, Gálvez Moreno MA, et al. Targeted systemic treatment of neuroendocrine tumors: Current options and future perspectives. *Drugs* (2019) 79(1):21–42. doi: 10.1007/s40265-018-1033-0

14. Bongiovanni A, Riva N, Ricci M, Liverani C, La Manna F, De Vita A, et al. First-line chemotherapy in patients with metastatic gastroenteropancreatic neuroendocrine carcinoma. *Onco Targets Ther* (2015) 8:3613–9. doi: 10.2147/OTT.S91971

15. Nigri G, Petrucciani N, Debs T, Mangogna LM, Crovetto A, Moschetta G, et al. Treatment options for PNET liver metastases: a systematic review. *World J Surg Oncol* (2018) 16(1):142. doi: 10.1186/s12957-018-1446-y

16. Capdevila J, Fazio N, Lopez C, Teulé A, Valle JW, Tafuto S, et al. Lenvatinib in patients with advanced grade 1/2 pancreatic and gastrointestinal neuroendocrine tumors: Results of the phase II TALENT trial (GETNE1509). *J Clin Oncol* (2021) 39 (20):2304–12. doi: 10.1200/JCO.20.03368

17. Tohyama O, Matsui J, Kodama K, Hata-Sugi N, Kimura T, Okamoto K, et al. Antitumor activity of lenvatinib (e7080): an angiogenesis inhibitor that targets multiple receptor tyrosine kinases in preclinical human thyroid cancer models. *J Thyroid Res* (2014) 2014:638747. doi: 10.1155/2014/638747

18. Matsuki M, Hoshi T, Yamamoto Y, Ikemori-Kawada M, Minoshima Y, Funahashi Y, et al. Lenvatinib inhibits angiogenesis and tumor fibroblast growth factor signaling pathways in human hepatocellular carcinoma models. *Cancer Med* (2018) 7(6):2641–53. doi: 10.1002/cam4.1517

19. Bongiovanni A, Liverani C, Recine F, Fausti V, Mercatali L, Vagheggini A, et al. Phase-II trials of pazopanib in metastatic neuroendocrine neoplasia (mNEN): A systematic review and meta-analysis. *Front Oncol* (2020) 10:414. doi: 10.3389/fonc.2020.00414

20. Xu J, Shen L, Zhou Z, Li J, Bai C, Chi Y, et al. Surufatinib in advanced extrapancreatic neuroendocrine tumours (SANET-ep): a randomised, double-blind, placebo-controlled, phase 3 study. *Lancet Oncol* (2020) 21(11):1500–12. doi: 10.1016/S1470-2045(20)30496-4

21. Lynch TJ, Bell DW, Sordella R, Gurubhagavatula S, Okimoto RA, Brannigan BW, et al. Activating mutations in the epidermal growth factor receptor underlying responsiveness of non-small-cell lung cancer to gefitinib. *N Engl J Med* (2004) 350 (21):2129–39. doi: 10.1056/NEJMoa040938

22. Lee CH, Motzer RJ, Glen H, Michaelson MD, Larkin J, Minoshima Y, et al. Correlative serum biomarker analyses in the phase 2 trial of lenvatinib-plus-everolimus in patients with metastatic renal cell carcinoma. *Br J Cancer* (2021) 124 (1):237–46. doi: 10.1038/s41416-020-01092-0

23. Tahara M, Schlumberger M, Elisei R, Habra MA, Kiyota N, Paschke R, et al. Exploratory analysis of biomarkers associated with clinical outcomes from the study of lenvatinib in differentiated cancer of the thyroid. *Eur J Cancer* (2017) 75:213–21. doi: 10.1016/j.ejca.2017.01.013

24. Kawasaki K, Fujii M, Sato T. Gastroenteropancreatic neuroendocrine neoplasms: genes, therapies and models. *Dis Model Mech* (2018) 11(2): dmm029595. doi: 10.1242/dmm.029595

25. Benten D, Behrang Y, Unrau L, Weissmann V, Wolters-Eisfeld G, Burdak-Rothkamm S, et al. Establishment of the first well-differentiated human pancreatic neuroendocrine tumor model. *Mol Cancer Res* (2018) 16(3):496–507. doi: 10.1158/1541-7786.MCR-17-0163

26. Kodack DP, Farago AF, Dastur A, Held MA, Dardaei L, Friboulet L, et al. Primary patient-derived cancer cells and their potential for personalized cancer patient care. *Cell Rep* (2017) 21(11):3298–309. doi: 10.1016/j.celrep.2017.11.051

27. van de Wetering M, Francies HE, Francis JM, Bounova G, Iorio F, Pronk A, et al. Prospective derivation of a living organoid biobank of colorectal cancer patients. *Cell* (2015) 161(4):933–45. doi: 10.1016/j.cell.2015.03.053

28. Pauli C, Hopkins BD, Prandi D, Shaw R, Fedrizzi T, Sboner A, et al. Personalized *In vitro* and *In vivo* cancer models to guide precision medicine. *Cancer Discovery* (2017) 7(5):462–77. doi: 10.1158/2159-8290.CD-16-1154

29. Siegel-Lakhai WS, Beijnen JH, Vervenne WL, Boot H, Keessen M, Versola M, et al. Phase I pharmacokinetic study of the safety and tolerability of lapatinib (GW572016) in combination with oxaliplatin/fluorouracil/leucovorin (FOLFOX4) in patients with solid tumors. *Clin Cancer Res* (2007) 13(15Pt1):4495–502. doi: 10.1158/1078-0432.CCR-07-0004

30. Kirchner GI, Meier-Wiedenbach I, Manns MP. Clinical pharmacokinetics of everolimus. *Clin Pharmacokinet* (2004) 43(2):83–95. doi: 10.2165/00003088-200443020-00002

31. Koumarianou A, Kaltsas G, Kulke MH, Oberg K, Strosberg JR, Spada F, et al. Temozolomide in advanced neuroendocrine neoplasms: Pharmacological and clinical aspects. *Neuroendocrinology* (2015) 101(4):274–88. doi: 10.1159/000430816

32. Dubbelman AC, Rosing H, Nijenhuis C, Huitema AD, Mergui-Roelvink M, Gupta A, et al. Pharmacokinetics and excretion of (14)C-lenvatinib in patients with advanced solid tumors or lymphomas. *Invest New Drugs* (2015) 33(1):233–40. doi: 10.1007/s10637-014-0181-7

33. Raj N, Fazio N, Strosberg J. Biology and systemic treatment of advanced gastroenteropancreatic neuroendocrine tumors. *Am Soc Clin Oncol Educ Book* (2018) 38:292–9. doi: 10.1200/EDBK_200893

34. April-Monn SL, Wiedmer T, Skowronska M, Maire R, Schiavo Lena M, Trippel M, et al. Three-dimensional primary cell culture: A novel preclinical model for pancreatic neuroendocrine tumors. *Neuroendocrinology* (2021) 111(3):273–87. doi: 10.1159/000507669

35. Yamauchi M, Ono A, Ishikawa A, Kodama K, Uchikawa S, Hatooka H, et al. Tumor fibroblast growth factor receptor 4 level predicts the efficacy of lenvatinib in patients with advanced hepatocellular carcinoma. *Clin Transl Gastroenterol* (2020) 11(5):e00179. doi: 10.14309/ctg.0000000000000179

36. Aristizabal Prada ET, Auernhammer CJ. Targeted therapy of gastroenteropancreatic neuroendocrine tumours: preclinical strategies and future targets. *Endocr Connect* (2018) 7(1):R1–R25. doi: 10.1530/EC-17-0286

37. Priestley P, Baber J, Lolkema MP, Steeghs N, de Bruijn E, Shale C, et al. Pan-cancer whole-genome analyses of metastatic solid tumours. *Nature* (2019) 575 (7781):210–6. doi: 10.1038/s41586-019-1689-y

38. Kudo M, Finn RS, Qin S, Han KH, Ikeda K, Piscaglia F, et al. Lenvatinib versus sorafenib in first-line treatment of patients with unresectable hepatocellular carcinoma: a randomised phase 3 non-inferiority trial. *Lancet* (2018) 391 (10126):1163–73. doi: 10.1016/S0140-6736(18)30207-1

39. Locati LD, Piovesan A, Durante C, Bregni M, Castagna MG, Zovato S, et al. Real-world efficacy and safety of lenvatinib: data from a compassionate use in the treatment of radioactive iodine-refractory differentiated thyroid cancer patients in Italy. *Eur J Cancer* (2019) 118:35–40. doi: 10.1016/j.ejca.2019.05.031

40. Fallahi P, Ruffilli I, Elia G, Ragusa F, Ulisse S, Baldini E, et al. Novel treatment options for anaplastic thyroid cancer. *Expert Rev Endocrinol Metab* (2017) 12(4):279–88. doi: 10.1080/17446651.2017.1340155

41. Schlumberger M, Jarzab B, Cabanillas ME, Robinson B, Pacini F, Ball DW, et al. A phase II trial of the multitargeted tyrosine kinase inhibitor lenvatinib (E7080) in advanced medullary thyroid cancer. *Clin Cancer Res* (2016) 22(1):44–53. doi: 10.1158/1078-0432.CCR-15-1127

42. Kawazoe A, Fukuoka S, Nakamura Y, Kuboki Y, Wakabayashi M, Nomura S, et al. Lenvatinib plus pembrolizumab in patients with advanced gastric cancer in the first-line or second-line setting (EPOC1706): an open-label, single-arm, phase 2 trial. *Lancet Oncol* (2020) 21(8):1057–65. doi: 10.1016/S1470-2045(20)30271-0

43. Sato J, Satouchi M, Itoh S, Okuma Y, Niho S, Mizugaki H, et al. Lenvatinib in patients with advanced or metastatic thymic carcinoma (REMORA): a multicentre, phase 2 trial. *Lancet Oncol* (2020) 21(6):843–50. doi: 10.1016/S1470-2045(20)30162-5

44. Taylor MH, Lee CH, Makker V, Rasco D, Dutcus CE, Wu J, et al. Phase IB/II trial of lenvatinib plus pembrolizumab in patients with advanced renal cell carcinoma, endometrial cancer, and other selected advanced solid tumors. *J Clin Oncol* (2020) 38(11):1154–63. doi: 10.1200/JCO.19.01598

45. Zhao Y, Zhang YN, Wang KT, Chen L. Lenvatinib for hepatocellular carcinoma: From preclinical mechanisms to anti-cancer therapy. *Biochim Biophys Acta Rev Cancer* (2020) 1874(1):188391. doi: 10.1016/j.bbcan.2020.188391

46. Ferrari SM, La Motta C, Elia G, Ragusa F, Ruffilli I, Quattrini L, et al. Antineoplastic effect of lenvatinib and vandetanib in primary anaplastic thyroid cancer cells obtained from biopsy or fine needle aspiration. *Front Endocrinol (Lausanne)* (2018) 9:764. doi: 10.3389/fendo.2018.00764

47. Shigesawa T, Maehara O, Suda G, Natsuizaka M, Kimura M, Shimazaki T, et al. Lenvatinib suppresses cancer stem-like cells in HCC by inhibiting FGFR1-3 signaling, but not FGFR4 signaling. *Carcinogenesis* (2021) 42(1):58–69. doi: 10.1093/carcin/bgaa049

48. Scoazec JY. Angiogenesis in neuroendocrine tumors: therapeutic applications. *Neuroendocrinology* (2013) 97(1):45–56. doi: 10.1159/000338371

10.3389/fendo.2022.1045038

Glossary

CDS	coding sequence
CNV	copy number variation
Ct	cycle threshold
DMEM	Dulbecco's modified Eagle's medium
FFPE	formalin-fixed paraffin-embedded
FGFR	fibroblast growth factor
receptors	
GEP	gastro-enteropancreatic
GEP-NET	gastro-enteropancreatic neuroendocrine tumor
MAPD	median absolute pairwise difference
MKI	multi-tyrosine kinase inhibitor
NEC	neuroendocrine carcinoma
NEN	neuroendocrine neoplasm
NET	neuroendocrine tumor
NSCLC	nonsmall cell lung cancer
ORR	overall response rate
PBS	phosphate buffered saline
PDGFR	platelet-derived growth factor receptor
PRC	polymerase chain reaction
PRRT	peptide receptor radionuclide therapy
SD	standard deviation
TKI	tyrosine kinase inhibitor
VAF	variant allele frequency;
VEGFR	vascular endothelial growth factor receptors.

frontiers | Frontiers in Endocrinology

TYPE Original Research
PUBLISHED 27 February 2023
DOI 10.3389/fendo.2023.1087442

OPEN ACCESS

EDITED BY
Radu Pîrlog,
Iuliu Haţieganu University of Medicine and Pharmacy, Romania

REVIEWED BY
Xiangtian Zhou,
Wenzhou Medical University, China
Biao Yan,
Fudan University, China

*CORRESPONDENCE
Dan Ji
gree1333@csu.edu.cn

†These authors have contributed equally to this work

SPECIALTY SECTION
This article was submitted to Cellular Endocrinology, a section of the journal Frontiers in Endocrinology

RECEIVED 02 November 2022
ACCEPTED 02 January 2023
PUBLISHED 27 February 2023

CITATION
You M, Rong R, Zeng Z, Fan C, Li H, Yang Q and Ji D (2023) Integrated analysis of long non-coding RNAs and mRNAs associated with glaucoma *in vitro*. *Front. Endocrinol.* 14:1087442. doi: 10.3389/fendo.2023.1087442

Integrated analysis of long non-coding RNAs and mRNAs associated with glaucoma *in vitro*

Mengling You[1,2,3†], Rong Rong[1,2,3†], Zhou Zeng[1,2,3†], Cong Fan[1,2,3], Haibo Li[1,2,3], Qian Yang[1,2,3] and Dan Ji[1,2,3*]

[1]Department of Ophthalmology, Xiangya Hospital, Central South University, Changsha, China, [2]Hunan Key Laboratory of Ophthalmology, Xiangya Hospital, Central South University, Changsha, China, [3]National Clinical Research Center for Geriatric Disorders, Xiangya Hospital, Central South University, Changsha, China

Introduction: In recent years, the biological functions and important roles of long non-coding RNAs (lncRNAs) have been widely reported in many diseases. Although glaucoma is the leading cause of blindness worldwide, the specific mechanisms of lncRNAs in the pathogenesis and progression of glaucoma remain unclear. Our research aims to elucidate the differentially expressed lncRNAs and mRNAs in glaucoma and to provide a basis for further exploration of the specific mechanism of action of lncRNAs in the progression of glaucoma.

Methods: We performed RNA sequencing on samples from a pressurized model of R28 cells and performed bioinformatics analyses on the sequencing results. The expression consistency of lncRNAs in clinical samples from patients with glaucoma or cataracts was detected using real-time quantitative polymerase chain reaction (RT-qPCR).

Results: RNA sequencing results showed that lncRNAs in cluster 5 were upregulated with increasing stress after typing all significantly altered lncRNAs using k-means in a cellular stress model. KEGG analysis indicated that they were associated with neurodegenerative diseases. Differentially expressed lncRNAs were verified by RT-qPCR, and the lncRNA expression levels of AC120246.2 and XLOC_006247 were significantly higher in the aqueous humor (AH) of patients with glaucoma than in those with cataracts. For LOC102551819, there was almost no expression in the AH and trabecular meshwork in patients with glaucoma but high expression was observed in the iris.

Conclusion: Our research proposes potential diagnostic or intervention targets for clinical applications as well as a theoretical basis for more in-depth research on the function of lncRNAs in glaucoma.

KEYWORDS

long non-coding RNA, mRNA, glaucoma, co-expression network, competitive endogenous RNA

1 Introduction

Glaucoma is a heterogeneous group of optic neuropathies characterized by the progressive loss of retinal ganglion cells (RGCs), thinning of the retinal nerve fiber layer, and vision loss (1). The pathogenesis of glaucoma is complex and diverse, involving pathologically high intraocular pressure (ph-IOP), microcirculation disorders, glutamate excitotoxicity, and immune abnormalities, which contribute to the primary causes of blindness worldwide (2–4). Currently, it is predicted that there will be 111.8 million patients with glaucoma aged 40–80 years worldwide by 2040 (5). Moreover, the early symptoms of glaucoma are mild and are often only found in the middle and late stages of the disease, which leads to delayed diagnosis. This puts significant pressure on social economy and public health. However, the pathogenic mechanisms underlying glaucoma are still not fully understood.

The continuous innovation in sequencing technology and development of genetic engineering has led to non-coding RNAs (ncRNAs) gradually receiving widespread attention. It is estimated that ncRNAs account for approximately 60% of the genetic material in the human genome (6). Additionally, more studies have revealed the diverse biological effects of ncRNAs in human developmental processes and diseases. Long non-coding RNAs (lncRNAs) are members of the ncRNA family and are characterized by a length greater than 200 nucleotides. The secondary structure of lncRNAs allows them to bind to certain proteins to facilitate chromatin remodeling and modification as well as the linear control of transcription factors. To date, various lncRNAs have been found to be differentially expressed in the aqueous humor, trabecular meshwork, iris and retinal cells, and venous blood of patients with glaucoma (7–9). However, the study of ncRNAs in glaucoma is still incomplete, and although their reported mechanism is mainly limited to competing endogenous RNA, it is generally thought that lncRNAs can bind related proteins or directly regulate mRNAs and encode short peptides to exert biological roles (10). Therefore, more in-depth exploration is required to understand how lncRNAs participate in both normal and pathogenic mechanisms.

We performed RNA sequencing on samples from a pressurized model of R28 cells (a retinal precursor cell line) that simulated the pathological process of acute high pressure in glaucoma. We also conducted a correlation analysis on the differentially expressed biological processes and signaling pathways to predict the network interaction of related lncRNA-miRNA-mRNA. We subsequently identified lncRNAs that showed significant changes in expression in clinical samples from glaucoma patients. In conclusion, our results provide novel targets for the clinical diagnosis and treatment of glaucoma and valuable information to support further in-depth studies of lncRNAs in glaucoma research.

2 Methods

2.1 R28 cell line cultivation

The R28 retinal cell line, an adherent retinal precursor cell line derived from the rat retina and is widely used in *in vitro* studies, was used in this study. It was provided by the Department of Anatomy and Neurobiology of Central South University (Changsha, China). R28 cells were cultured in Dulbecco's modified Eagle's medium (DMEM, Thermo Fisher Scientific, USA) with 10% fetal bovine serum (FBS, Thermo Fisher Scientific, USA), and 1% penicillin and streptomycin (NEST Biotechnology, Wuxi, China) at 37°C with an atmosphere containing 5% CO_2. Before model construction, R28 cells were assessed by mycoplasma detection (MD001, Yisemed, Shanghai, China).

2.2 Glaucoma cellular model construction

To prepare the polyacrylamide hydrogel, we followed two published protocols (11, 12). Young's moduli of the gels were measured using AFM. These moduli were 1.1, 2.5, 11.9, 34.4, and 50 kPa at bisacrylamide concentrations of 0.04%, 0.1%, 0.5%, 1.3%, and 2.08%, respectively. Rat R28 cells were seeded to confluency onto the gels.

2.3 Clinical sample collection

AH was obtained from patients with age-related cataract and primary angle-closure glaucoma (PACG). The iris and trabecular meshwork samples were collected from patients with POAG and PACG. All patients were operated on by the same experienced doctor in Xiangya Hospital (Changsha, China). Importantly, these patients did not have ocular surface disease, other optic nerve diseases, inflammatory diseases, or systemic diseases. The decision is taken by at least two clinicians with regard to the diagnosis of cataract and glaucoma (Table S1). This clinical portion of the study was approved by the Ethics Committee of Xiangya Hospital of Central South University, and written informed consent was obtained from all participating patients.

2.4 RNA-seq

Total RNA was extracted using the hot phenol method. The RNA was further purified with two phenol-chloroform treatments and then treated with RQ1 DNase (Promega, Madison, WI) to remove possible DNA contamination. The quality and quantity of the purified RNA were determined by measuring the absorbance at 260 nm/280 nm (A260/A280) using SmartSpec Plus (BioRad). The RNA integrity was further verified with 1.5% agarose gel electrophoresis.

For each sample, 2 μg total RNA were used for RNA-seq library preparation. Polyadenylated RNAs were purified and concentrated with oligo (dT) – conjugated magnetic beads (Invitrogen, Carlsbad, CA) before directional library preparation. The purified RNAs were then iron fragmented at 95°C followed by end repair and five adapter ligation. Reverse transcription was performed with an RT primer containing a three adapter sequences and a randomized hexamer. Complementary DNAs (cDNA) were purified, amplified, and stored at −80°C until sequencing.

2.5 Differentially expressed genes and lncRNA analysis

The raw paired-end reads were trimmed and qualitycontrolled with SeqPrep (https://github.com/jstjohn/SeqPrep) and Sickle (https://github.com/najoshi/sickle). The clean reads were aligned to a Rat genome DatabaseV6 using HISAT2 (V2.1.0) and using bowtie2 (V2.2.9). The mapped reads of each sample were assembled by StringTie (V1.3.3b) in a reference-based approach. Finally, assembled transcripts were annotated by Cuffcompare program from the Cufflflinks (V2.2.1). The R Bioconductor package edgeR (13) was used to select differentially expressed genes (DEGs). A false discovery rate < 0.05 and fold change >2 or < 0.5 were set as the cut-off criteria for identifying DEGs and lncRNAs.

2.6 GO and KEGG analyses

To identify functional categories of DEGs, gene ontology (GO) analysis was performed using KOBAS3.0 software (http://kobas.cbi.pku.edu.cn), and the Kyoto Encyclopedia of Genes and Genomes (KEGG) database was used for pathway analysis to identify the significant enrichment of different molecular pathways using KOBAS3.0 software (http://www.genome.jp/kegg). The hypergeometric test and Benjamini-Hochberg FDR controlling procedure were used to define the enrichment of each term.

2.7 Co-expression network construction

Based on the expression of each mRNA and DElncRNA, the Pearson's correlation coefficient (PCC) and P-value were obtained for each mRNA-DElncRNA pair. Then we filtered the result using a given threshold, with an absolute correlation coefficient of no less than 0.6 and P-value < 0.05. In addition to the positive correlation pairs, negative pairs with correlation coefficients less than 0 were also included. The filtered gene pairs were used to create the expression network. For each differentially expressed DElncRNA, we obtained the expressed genes from upstream and downstream regions within 10,000 bases. The genes were overlapped with co-expressed genes to obtain lncRNA targets. The co-expression network was illustrated using Cytoscape software (available online: https://cytoscape.org).

2.8 Competing endogenous RNA network construction

The lncRNAs and mRNAs were selected to predict miRNA targets using miRbase. Then, the miRNAs obtained from the predictions were screened with the miRanda and TargetScan programs. Afterwards, lncRNAs and mRNAs with miRNA recognition elements (MREs) for targeted miRNAs were predicted using RNA22. The competitive endogenous RNA (ceRNA) network was established and illustrated using Cytoscape software (14).

2.9 Quantitative real-time polymerase chain reaction (qRT–PCR)

Total RNA was extracted from the control and glaucoma patients by using TRIzol® Reagent (Invitrogen, Carlsbad, CA, United States). First-strand cDNA for quantitative real-time PCR (qRT-PCR) analysis was obtained from 1 μg total RNA using an oligo primer and the UEIris II RT-PCR System and a First-Strand cDNA Synthesis Kit (US Everbright Inc, R2028, Suzhou, China) according to the manufacturer's instructions. Real-time PCR was performed with a 2 × SYBR Green qPCR Master Mix (US Everbright Inc, S2014, Suzhou, China) using a 7500 FAST real-time PCR system (Applied Biosystems, Foster City, CA, United States). The expression of lncRNAs was calculated by the 2−ΔΔCt method. The forward and reverse primers for lncRNAs are shown in Supplementary Table S2.

2.10 Statistical analysis

Cluster3.0 and JavaTreeView were used to draw heat maps of gene and sample clusters. k-means were also used to cluster differently expressed model genes. Data are presented as mean ± standard deviation. All experiments were performed in triplicate. The statistical significance of differences between groups was calculated with the Student's t-test in GraphPad Prism 7 software (GraphPad Software, La Jolla, CA, USA). All statistical tests were two-tailed, and a P-value < 0.05 was considered statistically significant. P-values < 0.05, < 0.01, and < 0.001 are indicated by *, **, and ***, respectively.

3 Results

3.1 mRNA and lncRNA differential expression in glaucoma

lncRNAs and mRNAs possibly involved in the occurrence and development of glaucoma were identified by analyzing the lncRNA and mRNA expressed in the cellular stress model using RNA-seq. The expression of lncRNAs was divided into two types in the cell model. One type of lncRNA showed a gradual decrease in expression as the pressure increased, while the other type of lncRNA increased initially and then gradually decreased as the pressure increased. However, the overall trend observed was an increase in lncRNA and mRNA expression (Figures 1A, B).

3.2 GO and KEGG analysis of differentially expressed genes in glaucoma models

The expression analysis was used to examine the changes that occurred in cells between 50 and 1.1 kPa. GO analysis showed that in the cell model, 75 GO terms were significantly downregulated, and 30 GO terms were significantly upregulated and associated with biological processes. The top 10 GO terms that were significantly upregulated and downregulated are listed in Figures 2A–D, respectively. KEGG pathway analysis showed that 191 pathways in

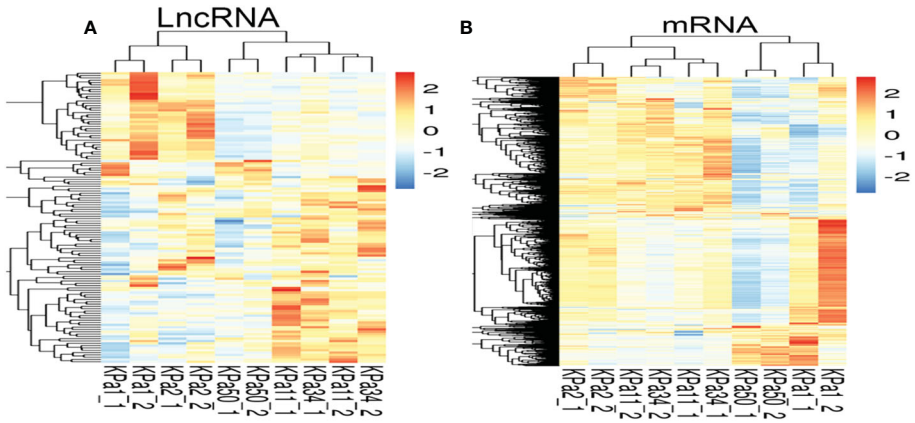

FIGURE 1
(A, B) Heat maps of mRNA and lncRNA(compare with 1 kpa). Each row represents one mRNA **(A)** or lncRNA **(B)**, and each column represents one different pressure value for the cell samples. Relative expression of mRNA or lncRNA is represented on a color scale. Red color indicates upregulation and blue indicates downregulation; 2, 0, -2, and 1.5, 0, -1.5 indicate fold changes in the corresponding spectrum.

the cell model were significantly downregulated, whereas 150 pathways were significantly upregulated. The top ten signaling pathways that were upregulated and downregulated are shown in Figures 2E–H, respectively. Signaling pathways related to axons were significantly downregulated in cell models, whereas signaling pathways related to various neurodegenerative diseases (such as Alzheimer's and Huntington's disease) were significantly upregulated. Additionally, genes related to these pathways were identified (Figures 2I, J).

3.3 Expression patterns of genes that respond to substrate stiffness cluster with functionally enriched pathways

Gene expression cluster analysis can be used to identify genes with similar expression patterns and functions. Therefore, we performed k-means cluster analysis on the DEG of lncRNAs in the cell model to identify genes with similar expression patterns (Figure 3A). We identified six main expression patterns (Figures 3B–G), that represented the gene responses to increased substrate stiffness. The expression characteristics of clusters 1 and 6 were similar, which illustrated that the expression levels gradually decreased with increasing pressure. The expression characteristics of clusters 3 and 5 were very similar, indicating that the expression levels gradually increased with increasing pressure, and this expression level was observed again at 50 kPa. Functional cluster analysis was performed on different gene clusters to obtain their respective enrichment functions. Clusters 1 and 6 were mainly enriched in pathways related to neuro-projection development, synaptic transmission, and glutamatergic pathways, whereas clusters 3 and 5 were mainly enriched in pathways related to apoptosis, oxidative stress, and ATP metabolism (Figures 3H–K). Clusters 2 and 4 had fewer genes and enriched functions. In the KEGG analysis, we focused on the enrichment of pathways related to neurodegenerative diseases in cluster 5, which is consistent with a previous report that glaucoma may be a neurodegenerative disease of the retina (Figures 3L–O) (15).

3.4 Construction of a lncRNA-mRNA co-expression network

The potential interaction between mRNA and lncRNAs was explored by establishing an lncRNA-mRNA co-expression network. We confirmed that 333 DElncRNAs were co-expressed with 1153 DEmRNAs (Pearson's correlation coefficient analysis > 0.99 or < -0.99). Some lncRNAs were selected with obvious and consistent expression changes from expression clusters 1, 3, 5, and 6, and constructed a simple lncRNA-mRNA network for further research (Figure 4).

3.5 Construction of a competing endogenous RNA network

A ceRNA network was constructed to reveal interactions between miRNAs, mRNAs, and lncRNAs. Among the four lncRNAs that we focused on, rho-miR-34a-5p, rho-miR-125a-5p, rho-miR-664-1-5p, rho-miR-330-5p, and rho-miR-29b-3p were enriched in this ceRNA network . These results indicate that these five miRNAs may play important roles in the regulation of glaucoma-related genes. Additionally, the ceRNA network diagram of the remaining lncRNAs showed a change in expression during glaucoma (Figure 5).

3.6 Candidate lncRNA screening and clinical sample verification

Clinically collected samples were used to verify the sequencing results. The lncRNA expression levels of AC120246.2 and XLOC_006247 in the AH of patients with glaucoma were significantly higher than those of patients without glaucoma

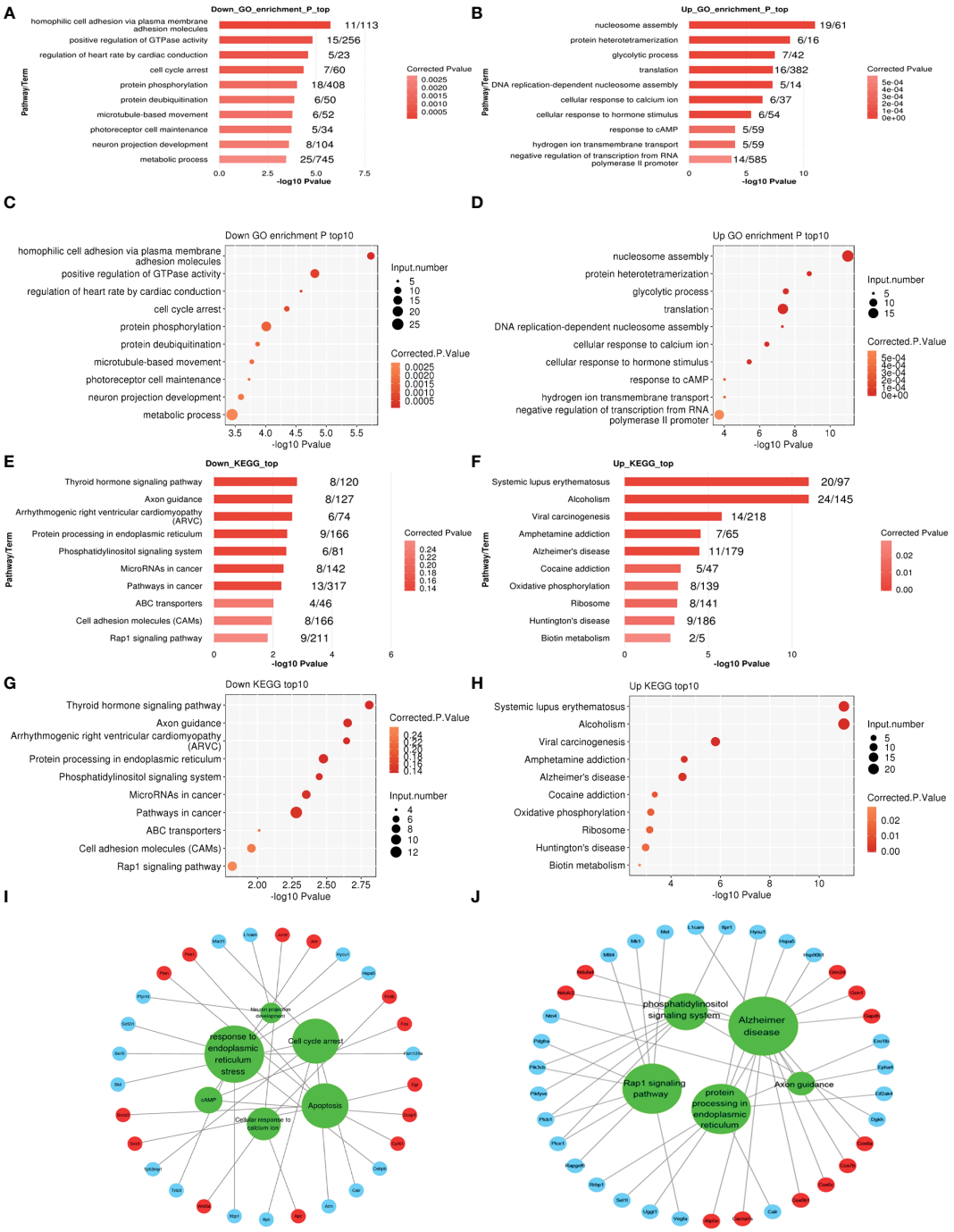

FIGURE 2
(A–D) The top ten enriched Gene Ontology (GO) biological process (BP), terms including down and upregulation (1 kPa vs. 50 kPa) in R28 cells. **(E–H)** The top ten enriched KEGG pathway terms associated with down and upregulation in R28 cells. **(I, J)** The interaction networks of all significantly enriched GO or KEGG and related genes in R28. The red circles are upregulated genes, and blue circles are downregulated genes linked to the GO or KEGG, indicated in the green circles.

(Figures 6A, B). LOC102551819 was observed to be specifically expressed in the iris. LOC102551819 expression was not detected in the AH and trabecular meshwork of patients with glaucoma. However, high expression was found in the iris tissue of patients with glaucoma, although no difference was observed between primary open-angle glaucoma and primary angle-closure glaucoma (Figure 6D). Rn60_13_0828.1 showed no significant differences in the test results from clinical samples (Figure 6C).

4 Discussion

The various biological effects and wide distribution of lncRNAs in the human body make them similar to other functional proteins. Currently, research on the specific mechanisms of lncRNAs in the pathogenesis of glaucoma is still in its infancy. The discovery of more meaningful lncRNAs in glaucoma is of great value for subsequent in-depth research. We performed RNA-seq on different samples from

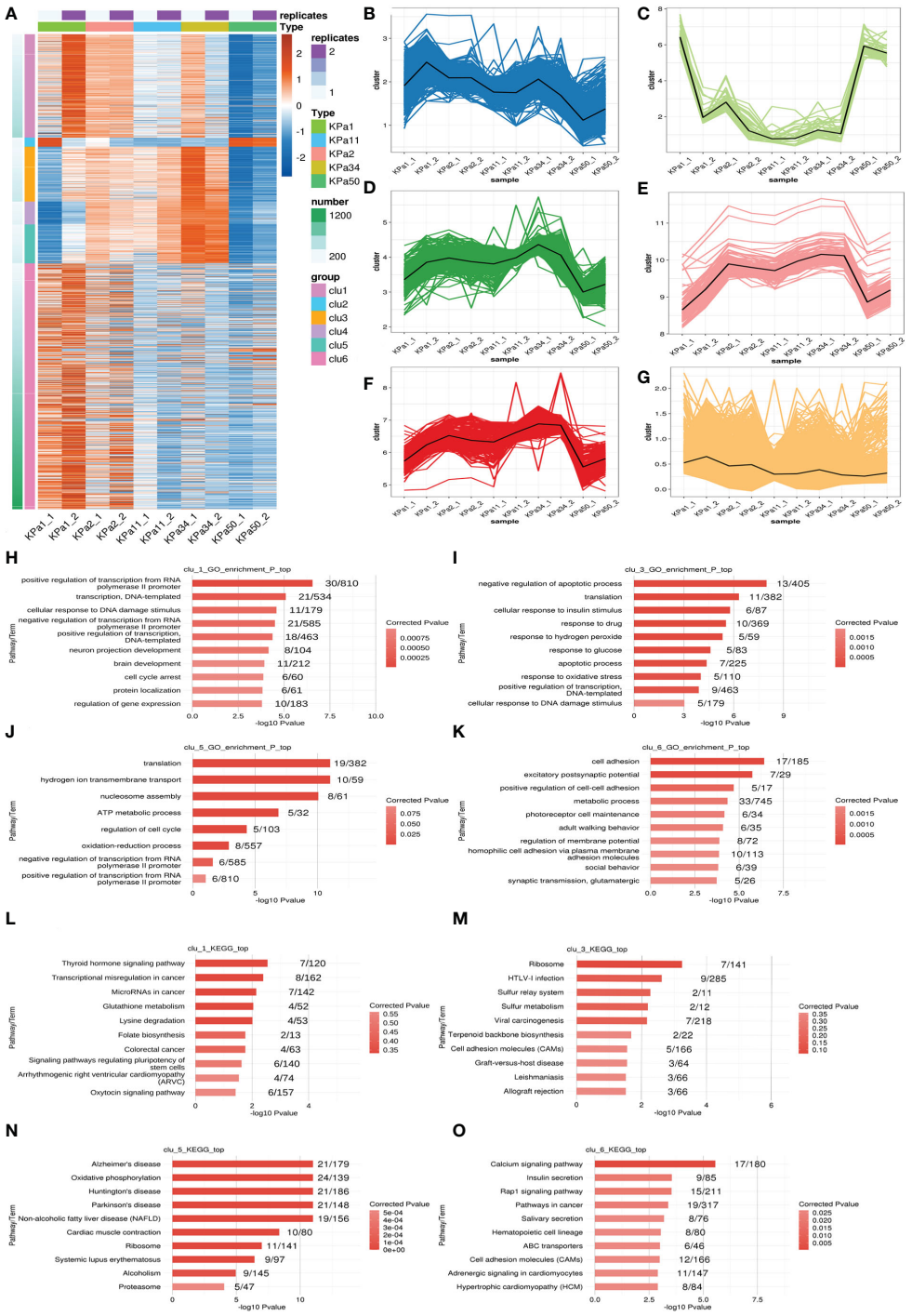

FIGURE 3
(A) k-means clustering of differentially expressed lncRNAs. **(B–G)** Genes are separated into 6 clusters, the black line represents the average expression value of all genes in each cluster. **(H–K)** Ten GO terms with significant differential expression identified from GO analysis of the biological processes represented in the different clusters. **(L–O)** The top ten KEGG pathways with significant expression differences in the identified clusters.

cell and mouse models and performed GO, KEGG, and k-means cluster analyses on the obtained results. We screened four of these lncRNAs with the closest expression, AC120246.2, XLOC_006247, Rn60_13_0828.1, and LOC102551819, and one previously reported lncRNA, AC120246.2, to perform RT-qPCR verification on clinical samples from patients with glaucoma and cataracts. Differential expression of these lncRNAs was observed between patients with glaucoma and patients without glaucoma, as well as between patients with POAG and patients with PACG, which may have potential applications in future clinical diagnosis and treatment. Previous reports have identified many DElncRNAs and DEmRNAs using RNA-seq based on the construction of a stress model in human trabecular meshwork cells (8, 11). The pathological progression of glaucoma is related to damage of Trabecular Meshwork (TM) cells regardless of the type of glaucoma; therefore, retinal cell damage and visual field loss will eventually occur. Our results are mainly based on

10.3389/fendo.2023.1087442

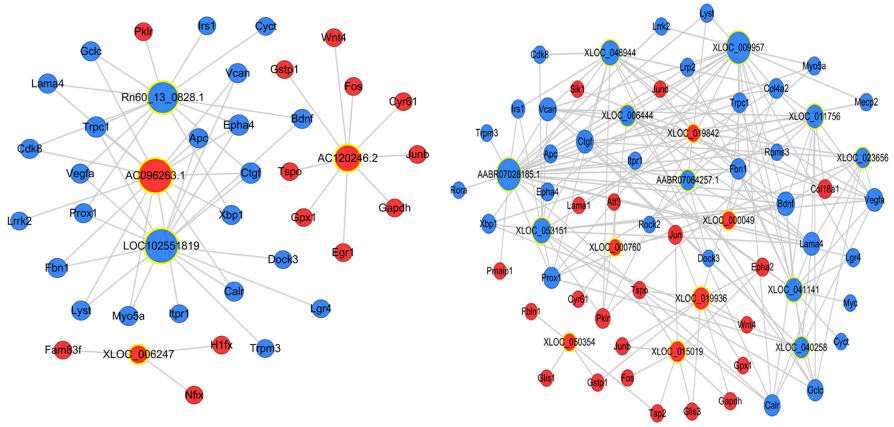

FIGURE 4
Construction of the lncRNA-mRNA co-expression network. A node with a yellow ring indicates lncRNA and a node without a yellow ring indicates mRNA. Upregulated lncRNAs and mRNAs are shown in red and downregulated lncRNAs and mRNAs are shown in blue.

data obtained from sequencing of retinal precursor cells. qRT-PCR verification of the clinical trabecular meshwork, iris, AH, and other tissue samples was also performed.

This study showed that there were many DElncRNAs and DEmRNAs in pressurized R28 cells. Moreover, GO and KEGG analyses identified cellular events, biological processes, and signaling pathways related to glaucoma development. GO analysis revealed several obvious changes in biological processes related to the pathology of glaucoma, including cellular response to calcium ions, neuron projection development, cAMP, response to endoplasmic reticulum stress, cell cycle arrest, and apoptosis. The typical related pathways or BP differences obtained by KEGG analysis in cells were the phosphatidylinositol signaling system, Alzheimer's disease, axon guidance, protein processing in the endoplasmic reticulum, and Rap1 signaling. The ECM-receptor interaction and PI3K-AKT, NF-κB, MAPK, and TNF signaling pathways were identified in mice. These associated pathways have been reported in many previous glaucomatous studies, most of which are related to RGC apoptosis (16, 17), trabecular meshwork dysfunction, and extracellular matrix proliferation (18). The co-expression results of the 21 lncRNAs and their corresponding mRNAs as an interaction network are displayed in the current study. Many of the genes associated with this network, such as *Jun*, *Jund*, *Apc*, *Xbp1*, *Fos*, and *Calr*, were consistent with the BP-related mRNAs. Among these, *Jun*, *Jund*, *Xbp1*, *Fos*, and *Calr* are associated with endoplasmic reticulum stress, astrocyte activation, and RGC apoptosis (19–22). *Apc* is related to human tenon fibroblast proliferation and can induce postoperative scarring of the glaucoma filter passage (23). It has been suggested that lncRNAs participate in biological processes related to glaucoma through direct or indirect interactions with these mRNAs.

lncRNAs function through multiple mechanisms, including the ceRNA hypothesis. This hypothesis states that lncRNAs, mRNA transcripts, and false gene transcripts can affect each other by competitively combining with MREs to influence post-transcriptional regulation (24). The ceRNA network links the functions of protein-coding mRNAs with non-coding RNAs such as miRNA, lncRNA, pseudogene RNA, and circular RNA. According to the ceRNA hypothesis, lncRNAs may act as miRNA "sponges" and compete with MREs, regulating miRNA-mediated biological processes (25, 26). We predicted miRNAs that interact with

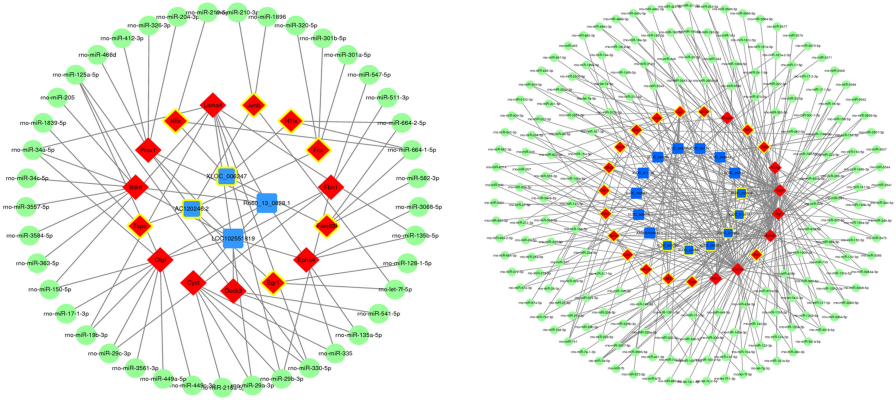

FIGURE 5
Construction of competitive endogenous RNA networks. Nodes with yellow circles indicate upregulated RNA, while nodes without yellow circles indicate downregulated RNA. lncRNA, mRNA, and miRNA are shown in blue, red, and green respectively.

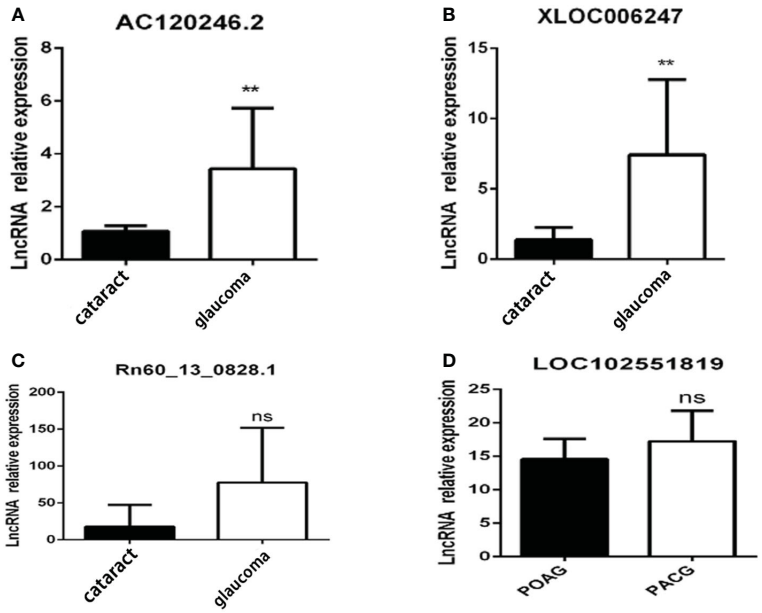

FIGURE 6
Candidate lncRNA expression in clinical patients. Candidate lncRNA expression in the aqueous humor **(A–C)** or iris **(D)** from patients with glaucoma (n=10) and patients with cataracts(n=5). **p < 0.01, ns p >0.05.

differentially expressed lncRNAs and mRNA in the course of glaucoma disease progression using ceRNA network constructions (Figure 5). The miRNAs rho-miR-34a-5p, rho-miR-125a-5p, rho-miR-664-1-5p, rho-miR-330-5p, and rho-miR-29b-3p were enriched in the ceRNA network, suggesting that they interacted with the largest number of DEmRNAs and DElncRNAs. Among them, rho-miR-34a-5p is a common miRNA with abnormal regulation in central nervous system diseases (27). Furthermore, rho-miR-125a-5p is related to ischemic stroke and neuronal differentiation (28, 29), and rho-miR-29b-3p targets genes such as *FOXO3a* and *TRAF5* in a cardiac ischemia-reperfusion model to protect cardiomyocytes from endotoxin-induced apoptosis and inflammation (30–32). Finally, rho-miR-330-5p and rho-miR-664-1-5p can also inhibit myocardial ischemia-reperfusion injury through targeted regulation (33, 34). The mechanism of ischemia reperfusion has also been shown to play a role in glaucoma pathogenesis (35). Recently, the hypothesis that glaucoma is a neurodegenerative disease has also gained scientific acceptance (36). Therefore, these miRNAs may play an important role in glaucoma pathogenesis, although the specific mechanism requires further investigation.

Aqueous humor, trabecular meshwork, and iris tissues were collected from patients with glaucoma and other types of patients and verified the lncRNA expression profiles. The expression of AC120246.2 and XLOC_ 006247 in the aqueous humor of patients with glaucoma increased significantly (Figure 6). The LOC102551819 lncRNA may be specifically expressed in the iris, as we did not detect its expression in the aqueous humor and trabecular meshwork of patients with glaucoma. Rn60_13_0828.1 showed no significant differences in the test results from clinical samples. The difference in expression of Rn60_13_0828.1 may be related to species differences or because the sample number of patients was insufficient; therefore, further investigation is needed to confirm these results.

In this study, we initially identified a few lncRNAs that may play a role in the pathogenesis of glaucoma, but did not delve into the mechanisms by which these lncRNAs are involved in the pathogenesis of glaucoma, which is an area that needs to be further explored in the future. lncRNAs are involved in the pathogenesis of glaucoma in three main ways, in addition to regulating the function of trabecular meshwork cells, participating in ECM and scar formation after glaucoma filtration surgery, and directly regulating RGC damage (37).It has been demonstrated that lncRNA may serve as a potential biomarker for primary open-angle glaucoma (38–40), and studies on the mechanism of lncRNA have mainly focused on the ceRNA mechanism. Several studies have demonstrated that lncRNA can regulate the loss of retinal ganglion cells (41–44), apoptosis of human trabecular meshwork cells and extracellular matrix deposition through the ceRNA mechanism (45–48). In the mechanistic studies of ceRNA or RBP, the current situation is that one lncRNA can target multiple molecules, and multiple lncRNAs can act on the same target. Therefore, when studying the disease development process at the molecular level, it should not be isolated to only one specific lncRNA, and targeting only this lncRNA may not achieve the desired therapeutic effect, and it may be necessary to use bioinformatics to network it and find the core lncRNA. However, lncRNAs act in a variety of ways. In addition to continuing to explore the role of lncRNAs in glaucoma through the ceRNA mechanism, the specific ways in which lncRNAs regulate glaucoma occurrence and development through other modalities should be more extensively explored in the future. Some studies have reported that some ncRNA can encode functional small proteins that are commonly referred to as small peptides (49, 50), highlighting the possibility that additional transcripts currently annotated as ncRNA encode proteins with important biological activity. This area is still unknown in glaucoma and also deserves to be studied and explored.

In conclusion, the expression profiles of lncRNA-mRNA associated with the pathogenesis of glaucoma was evaluated using RNA-seq and the underlying regulatory mechanism determined through bioinformatics analyses. We aimed to reveal the role of lncRNAs in glaucoma pathogenesis and our results may provide potential targets for the diagnosis and treatment of glaucoma. However, our study also has some limitations, such as the lack of functional studies on these DElncRNAs. Therefore, further research is needed to explore the role of these DElncRNAs in the pathogenesis of glaucoma.

Data availability statement

The data presented in the study are deposited in the Sequence Read Archive of NCBI repository, accession numberPRJNA919494.

Ethics statement

The studies involving human participants were reviewed and approved by Xiangya Hospital of Central South University. The patients/participants provided their written informed consent to participate in this study. The animal study was reviewed and approved by Xiangya Hospital of Central South University.

Author contributions

Conceptualization: DJ; Methodology: MY and CF; Formal analysis and investigation: RR, ZZ, HL, and QY; Writing- Original draft preparation, RR, MY, and ZZ; Writing- Reviewing and Editing: DJ. All authors contributed to the article and approved the submitted version.

Funding

This work was supported by the National key research and development program of China (2020YFC2008205, 2021YFA1101200 & 2021YFA1101202), the Key R & D plan of Hunan Province of China (No. 2020SK2076), National Natural Science Foundation of China (No. 82171058, 81974134, 81670858, 82271091) and Natural Science Foundation of Hunan Province (2021JJ31068).

Conflict of interest

The authors declare that the research was conducted in the absence of any commercial or financial relationships that could be construed as a potential conflict of interest.

Publisher's note

All claims expressed in this article are solely those of the authors and do not necessarily represent those of their affiliated organizations, or those of the publisher, the editors and the reviewers. Any product that may be evaluated in this article, or claim that may be made by its manufacturer, is not guaranteed or endorsed by the publisher.

Supplementary material

The Supplementary Material for this article can be found online at: https://www.frontiersin.org/articles/10.3389/fendo.2023.1087442/full#supplementary-material

References

1. Jonas JB, Aung T, Bourne RR, Bron AM, Ritch R, Panda-Jonas S. Glaucoma. *Lancet* (2017) 390:2183–93. doi: 10.1016/S0140-6736(17)31469-1

2. Chen CL, Bojikian KD, Wen JC, Zhang Q, Xin C, Mudumbai RC, et al. Peripapillary retinal nerve fiber layer vascular microcirculation in eyes with glaucoma and single-hemifield visual field loss. *JAMA Ophthalmol* (2017) 135:461–8. doi: 10.1001/jamaophthalmol.2017.0261

3. Schlüter A, Aksan B, Fioravanti R, Valente S, Mai A, Mauceri D. Histone deacetylases contribute to excitotoxicity-triggered degeneration of retinal ganglion cells in vivo. *Mol Neurobiol* (2019) 56:8018–34. doi: 10.1007/s12035-019-01658-x

4. Wei X, Cho KS, Thee EF, Jager MJ, Chen DF. Neuroinflammation and microglia in glaucoma: time for a paradigm shift. *J Neurosci Res* (2019) 97:70–6. doi: 10.1002/jnr.24256

5. Tham YC, Li X, Wong TY, Quigley HA, Aung T, Cheng CY. Global prevalence of glaucoma and projections of glaucoma burden through 2040: a systematic review and meta-analysis. *Ophthalmology* (2014) 121:2081–90. doi: 10.1016/j.ophtha.2014.05.013

6. Djebali S, Davis CA, Merkel A, Dobin A, Lassmann T, Mortazavi ,A, et al. Landscape of transcription in human cells. *Nature* (2012) 489:101–8. doi: 10.1038/nature11233

7. Xie L, Mao M, Wang C, Zhang L, Pan Z, Shi J, et al. Potential biomarkers for primary open-angle glaucoma identified by long noncoding RNA profiling in the aqueous humor. *Am J Pathol* (2019) 189:739–52. doi: 10.1016/j.ajpath.2018.12.011

8. Youngblood H, Cai J, Drewry MD, Helwa I, Hu E, Liu S, et al. Expression of mRNAs, miRNAs, and lncRNAs in human trabecular meshwork cells upon mechanical stretch. *Invest Ophthalmol Visual Sci* (2020) 61:2. doi: 10.1167/iovs.61.5.2

9. Zhou RR, Li HB, You QS, Rong R, You ML, Xiong K, et al. Silencing of GAS5 alleviates glaucoma in rat models by reducing retinal ganglion cell apoptosis. *Hum Gene Ther* (2019) 30:1505–19. doi: 10.1089/hum.2019.056

10. Peng WX, Koirala P, Mo YY. LncRNA-mediated regulation of cell signaling in cancer. *Oncogene* (2017) 36:5661–7. doi: 10.1038/onc.2017.184

11. Tie J, Chen D, Guo J, Liao S, Luo X, Zhang Y, et al. Transcriptome-wide study of the response of human trabecular meshwork cells to the substrate stiffness increase. *J Cell Biochem* (2020) 121:3112–23. doi: 10.1002/jcb.29578

12. Overby DR, Zhou EH, Vargas-Pinto R, Pedrigi RM, Fuchshofer R, Braakman ST, et al. Altered mechanobiology of schlemm's canal endothelial cells in glaucoma. *Proc Natl Acad Sci United States America* (2014) 111:13876–81. doi: 10.1073/pnas.1410602111

13. Robinson MD, McCarthy DJ, Smyth GK. edgeR: a bioconductor package for differential expression analysis of digital gene expression data. *Bioinformatics* (2010) 26:139–40. doi: 10.1093/bioinformatics/btp616

14. Chen HY, Chou HC, Chang SJ, Liao EC, Tsai YT, Wei YS, et al. Proteomic analysis of various rat ocular tissues after ischemia-reperfusion injury and possible relevance to acute glaucoma. *Int J Mol Sci* (2017) 18:334. doi: 10.3390/ijms18020334

15. Faiq MA, Wollstein G, Schuman JS, Chan KC. Cholinergic nervous system and glaucoma: From basic science to clinical applications. *Prog Retin Eye Res* (2019) 72:100767. doi: 10.1016/j.preteyeres.2019.06.003

16. Husain S, Ahmad A, Singh S, Peterseim C, Abdul Y, Nutaitis MJ. PI3K/Akt pathway: A role in δ-opioid receptor-mediated RGC neuroprotection. *Invest Ophthalmol Visual Sci* (2017) 58:6489–99. doi: 10.1167/iovs.16-20673

17. Zhang QL, Wang W, Jiang Y, Tuya A, Dongmei, Li LL, et al. GRGM-13 comprising 13 plant and animal products, inhibited oxidative stress induced apoptosis in retinal ganglion cells by inhibiting P2RX7/p38 MAPK signaling pathway. *Biomedicine Pharmacother = Biomedecine pharmacotherapie* (2018) 101:494–500. doi: 10.1016/j.biopha.2018.02.107

18. Kelley MJ, Rose AY, Song K, Chen Y, Bradley JM, Rookhuizen D, et al. Synergism of TNF and IL-1 in the induction of matrix metalloproteinase-3 in trabecular meshwork. *Invest Ophthalmol Visual Sci* (2007) 48:2634–43. doi: 10.1167/iovs.06-1445

19. Syc-Mazurek SB, Fernandes KA, Wilson MP, Shrager P, Libby RT. Together JUN and DDIT3 (CHOP) control retinal ganglion cell death after axonal injury. *Mol neurodegeneration* (2017) 12:71. doi: 10.1186/s13024-017-0214-8

20. Hashimoto K, Parker A, Malone P, Gabelt BT, Rasmussen C, Kaufman PS, et al. Long-term activation of c-fos and c-jun in optic nerve head astrocytes in experimental ocular hypertension in monkeys and after exposure to elevated pressure in vitro. *Brain Res* (2005) 1054:103–15. doi: 10.1016/j.brainres.2005.06.050

21. Lindsey JD, Duong-Polk KX, Hammond D, Leung CK, Weinreb RN. Protection of injured retinal ganglion cell dendrites and unfolded protein response resolution after long-term dietary resveratrol. *Neurobiol Aging* (2015) 36:1969–81. doi: 10.1016/j.neurobiolaging.2014.12.021

22. Yan X, Wu S, Liu Q, Li Y, Zhu W, Zhang J. Accumulation of Asn450Tyr mutant myocilin in ER promotes apoptosis of human trabecular meshwork cells. *Mol Vis* (2020) 26:563–73.

23. Eibl KH, Banas B, Kook D, Ohlmann AV, Priglinger S, Kampik A, et al. Alkylphosphocholines: a new therapeutic option in glaucoma filtration surgery. *Invest Ophthalmol Visual Sci* (2004) 45:2619–24. doi: 10.1167/iovs.03-1351

24. Wang Y, Zhang Y, Yang T, Zhao W, Wang N, Li P, et al. Long non-coding RNA MALAT1 for promoting metastasis and proliferation by acting as a ceRNA of miR-144-3p in osteosarcoma cells. *Oncotarget* (2017) 8:59417–34. doi: 10.18632/oncotarget.19727

25. Karreth FA, Pandolfi PP. ceRNA cross-talk in cancer: when ce-bling rivalries go awry. *Cancer Discovery* (2013) 3:1113–21. doi: 10.1158/2159-8290.CD-13-0202

26. Wu G-C, Hu Y, Guan S-Y, Ye D-Q, Pan H-F. Differential plasma expression profiles of long non-coding RNAs reveal potential biomarkers for systemic lupus erythematosus. *Biomolecules* (2019) 9:206. doi: 10.3390/biom9060206

27. van den Berg MMJ, Krauskopf J, Ramaekers JG, Kleinjans JCS, Prickaerts J, Briedé JJ. Circulating microRNAs as potential biomarkers for psychiatric and neurodegenerative disorders. *Prog Neurobiol* (2020) 185:101732. doi: 10.1016/j.pneurobio.2019.101732

28. Giorgi Silveira R, Perelló Ferrúa C, do Amaral CC, Fernandez Garcia T, de Souza KB, Nedel F. MicroRNAs expressed in neuronal differentiation and their associated pathways: Systematic review and bioinformatics analysis. *Brain Res Bull* (2020) 157:140–8. doi: 10.1016/j.brainresbull.2020.01.009

29. Rink C, Khanna S. MicroRNA in ischemic stroke etiology and pathology. *Physiol Genomics* (2011) 43:521–8. doi: 10.1152/physiolgenomics.00158.2010

30. Pei Y-H, Chen J, Wu X, He Y, Qin W, He S-Y, et al. LncRNA PEAMIR inhibits apoptosis and inflammatory response in PM2.5 exposure aggravated myocardial ischemia/reperfusion injury as a competing endogenous RNA of miR-29b-3p. *Nanotoxicology* (2020) 14:638–53. doi: 10.1080/17435390.2020.1731857

31. Li Z, Yi N, Chen R, Meng Y, Wang Y, Liu H, et al. miR-29b-3p protects cardiomyocytes against endotoxin-induced apoptosis and inflammatory response through targeting FOXO3A. *Cell Signal* (2020) 74:109716. doi: 10.1016/j.cellsig.2020.109716

32. Cai Y, Li Y. Upregulation of miR-29b-3p protects cardiomyocytes from hypoxia-induced apoptosis by targeting TRAF5. *Cell Mol Biol Lett* (2019) 24:27. doi: 10.1186/s11658-019-0151-3

33. Zuo W, Tian R, Chen Q, Wang L, Gu Q, Zhao H, et al. miR-330-5p inhibits NLRP3 inflammasome-mediated myocardial ischemia-reperfusion injury by targeting TIM3. *Cardiovasc Drugs Ther* (2021) 35:691–705. doi: 10.1007/s10557-020-07104-8

34. Zhu H-J, Han Z-Y, He S-F, Jin S-Y, Xu S-J, Fang X-D, et al. Specific MicroRNAs comparisons in hypoxia and morphine preconditioning against hypoxia-reoxygenation injury with and without heart failure. *Life Sci* (2017) 170:82–92. doi: 10.1016/j.lfs.2016.11.028

35. Minhas G, Sharma J, Khan N. Cellular stress response and immune signaling in retinal ischemia-reperfusion injury. *Front Immunol* (2016) 7:444. doi: 10.3389/fimmu.2016.00444

36. Tatton W, Chen D, Chalmers-Redman R, Wheeler L, Nixon R, Tatton N. Hypothesis for a common basis for neuroprotection in glaucoma and alzheimer's disease: anti-apoptosis by alpha-2-adrenergic receptor activation. *Surv Ophthalmol* (2003) 48:S25–37. doi: 10.1016/s0039-6257(03)00005-5

37. Rong R, Wang M, You M, Li H, Xia X, Ji D. Pathogenesis and prospects for therapeutic clinical application of noncoding RNAs in glaucoma: Systematic perspectives. *J Cell Physiol* (2021) 236:7097–116. doi: 10.1002/jcp.30347

38. Li H, Ye Z, Li Z. Identification of the potential biological target molecules related to primary open-angle glaucoma. *BMC Ophthalmol* (2022) 22:188. doi: 10.1186/s12886-022-02368-0

39. Wang L, Yu T, Zhang X, Cai X, Sun H. Network integration analysis and immune infiltration analysis reveal potential biomarkers for primary open-angle glaucoma. *Front Cell Dev Biol* (2021) 9:793638. doi: 10.3389/fcell.2021.793638

40. Yu S, Tam ALC, Campbell R, Renwick N. Emerging evidence of noncoding RNAs in bleb scarring after glaucoma filtration surgery. *Cells* (2022) 11:1301. doi: 10.3390/cells11081301

41. Xi X, Ma J, Chen Q, Wang X, Xia Y, Wen X, et al. Acteoside attenuates hydrogen peroxide-induced injury of retinal ganglion cells *via* the CASC2/miR-155/mTOR axis. *Ann Transl Med* (2022) 10:5. doi: 10.21037/atm-21-5630

42. Yang N, Yang J, He X, Zhang W, Xing Y. Construction and analysis of mRNA, lncRNA, and transcription factor regulatory networks after retinal ganglion cell injury. *Exp Eye Res* (2022) 215:108915. doi: 10.1016/j.exer.2021.108915

43. Yu Z, Wen Y, Jiang N, Li Z, Guan J, Zhang Y, et al. TNF-alpha stimulation enhances the neuroprotective effects of gingival MSCs derived exosomes in retinal ischemia-reperfusion injury *via* the MEG3/miR-21a-5p axis. *Biomaterials* (2022) 284:121484. doi: 10.1016/j.biomaterials.2022.121484

44. Zhang N, Cao W, He X, Xing Y, Yang N. Long non-coding RNAs in retinal ganglion cell apoptosis. *Cell Mol Neurobiol* (2022). doi: 10.1007/s10571-022-01210-x

45. Meng J, Yang X, Huang X, Li Q. Long non-coding RNA GAS5 knockdown attenuates H(2)O(2)-induced human trabecular meshwork cell apoptosis and promotes extracellular matrix deposition by suppressing miR-29b-3p and upregulating STAT3. *J Mol Neurosci* (2022) 72:516–26. doi: 10.1007/s12031-021-01926-3

46. Lv Y, Zhang Z, Xing X, Liu A. lncRNA TGFbeta2-AS1 promotes ECM production *via* TGF-beta2 in human trabecular meshwork cells. *Biochem Biophys Res Commun* (2020) 527:881–8. doi: 10.1016/j.bbrc.2020.05.003

47. Shen W, Huang B, He Y, Shi L, Yang J. Long non-coding RNA RP11-820 promotes extracellular matrix production via regulating miR-3178/MYOD1 in human trabecular meshwork cells. *FEBS J* (2020) 287:978–90. doi: 10.1111/febs.15058

48. Zhao J, Sun H, Zhang JM, Wang M, Du XJ, Zhang JL. Long non-coding RNA ANRIL down-regulates microRNA-7 to protect human trabecular meshwork cells in an experimental model for glaucoma. *Eur Rev Med Pharmacol Sci* (2019) 23:3173–82. doi: 10.26355/eurrev_201904_17675

49. Bazzini AA, Johnstone TG, Christiano R, Mackowiak SD, Obermayer B, Fleming ES, et al. Identification of small ORFs in vertebrates using ribosome footprinting and evolutionary conservation. *EMBO J* (2014) 33:981–93. doi: 10.1002/embj.201488411

50. Matsumoto A, Pasut A, Matsumoto M, Yamashita R, Fung J, Monteleone E, et al. mTORC1 and muscle regeneration are regulated by the LINC00961-encoded SPAR polypeptide. *Nature* (2017) 541:228–32. doi: 10.1038/nature21034

frontiers | Frontiers in Endocrinology

TYPE Original Research
PUBLISHED 07 March 2023
DOI 10.3389/fendo.2023.1066182

OPEN ACCESS

EDITED BY
Neil J Grimsey,
University of Georgia, United States

REVIEWED BY
Avinaash Vickram Maharaj,
Queen Mary University of London, United Kingdom
Mohammad Farhan,
Hamad Bin Khalifa University, Qatar
Muzamil Ahmad,
Indian Institute of Integrative Medicine (CSIR), India

*CORRESPONDENCE
Muzammil Ahmad Khan
MKhan12@sidra.org
Ammira Al-Shabeeb Akil
aakil@sidra.org

SPECIALTY SECTION
This article was submitted to Molecular and Structural Endocrinology, a section of the journal Frontiers in Endocrinology

RECEIVED 10 October 2022
ACCEPTED 23 January 2023
PUBLISHED 07 March 2023

CITATION
Ahmad S, Ali MZ, Abbasi SW, Abbas S, Ahmed I, Abbas S, Nawaz S, Ziab M, Ahmed I, Fakhro KA, Khan MA and Akil AA (2023) A GHRHR founder mutation causes isolated growth hormone deficiency type IV in a consanguineous Pakistani family. *Front. Endocrinol.* 14:1066182. doi: 10.3389/fendo.2023.1066182

A GHRHR founder mutation causes isolated growth hormone deficiency type IV in a consanguineous Pakistani family

Safeer Ahmad[1], Muhammad Zeeshan Ali[1], Sumra Wajid Abbasi[2], Safdar Abbas[1], Iftikhar Ahmed[1], Shakil Abbas[1], Shoaib Nawaz[3], Mubarak Ziab[4], Ikhlak Ahmed[4], Khalid A. Fakhro[3,5,6], Muzammil Ahmad Khan[1]* and Ammira Al-Shabeeb Akil[3,4]*

[1]Gomal Centre of Biochemistry and Biotechnology, Gomal University, D.I. Khan, Khyber Pakhtunkhwa, Pakistan, [2]Department of Biological Sciences, National University of Medical Sciences, Rawalpindi, Punjab, Pakistan, [3]Laboratory of Genomic Medicine-Precision Medicine Program, Sidra Medicine, Doha, Qatar, [4]Department of Human Genetics, Precision Medicine of Diabetes Prevention Program, Sidra Medicine, Doha, Qatar, [5]Department of Genetic Medicine, Weill Cornell Medical College-Doha, Doha, Qatar, [6]College of Health and Life Sciences, Hamad Bin Khalifa University, Doha, Qatar

Background: Isolated growth hormone deficiency (IGHD) is caused by a severe shortage or absence of growth hormone (GH), which results in aberrant growth and development. Patients with IGHD type IV (IGHD4) have a short stature, reduced serum GH levels, and delayed bone age.

Objectives: To identify the causative mutation of IGHD in a consanguineous family comprising four affected patients with IGHD4 (MIM#618157) and explore its functional impact *in silico*.

Methods: Clinical and radiological studies were performed to determine the phenotypic spectrum and hormonal profile of the disease, while whole-exome sequencing (WES) and Sanger sequencing were performed to identify the disease-causing mutation. *In-silico* studies involved protein structural modeling and docking, and molecular dynamic simulation analyses using computational tools. Finally, data from the Qatar Genome Program (QGP) were screened for the presence of the founder variant in the Qatari population.

Results: All affected individuals presented with a short stature without gross skeletal anomalies and significantly reduced serum GH levels. Genetic mapping revealed a homozygous nonsense mutation [NM_000823:c.G214T:p.(Glu72*)] in the third exon of the growth-hormone-releasing hormone receptor gene *GHRHR* (MIM#139191) that was segregated in all patients. The substituted amber codon (UAG) seems to truncate the protein by deleting the C-terminus GPCR domain, thus markedly disturbing the GHRHR receptor and its interaction with the growth hormone-releasing hormone.

Conclusion: These data support that a p.Glu72* founder mutation in *GHRHR* perturbs growth hormone signaling and causes IGHD type IV. *In-silico* and biochemical analyses support the pathogenic effect of this nonsense mutation, while our comprehensive phenotype and hormonal profiling has established the

genotype–phenotype correlation. Based on the current study, early detection of *GHRHR* may help in better therapeutic intervention.

KEYWORDS

isolated growth hormone deficiency (IGHD4), Pakistani family, whole-exome sequencing, GHRHR, modeling, docking and simulation

Introduction

Isolated growth hormone deficiency (IGHD) is a condition characterized by growth retardation and development failure in affected children as a result of reduced growth hormone (GH) levels. It is estimated that between 1:3,480 and 1:10,000 live births are affected by IGHD (1–4). There are four IGHD types, IGHD I–IV, differentiated by their clinical spectrum, inheritance pattern, and associated genetic factors. Two IGHD I subtypes, IGHD IA (MIM# 262400) and IGHD 1B (MIM# 612781), are caused by *GH1* (MIM# 139250) and *GHRHR* (MIM# 139191) gene defects, respectively. In addition, a mutation at 17q23.3 on *GH1* underlies both IGHD 1B (MIM# 617281) and IGHD II (MIM# 173100). IGHD III (MIM# 307200) is caused by a genetic defect in *BTK* (MIM# 300300) located on Xq22, and IGHD IV (MIM# 618157) is caused by a genetic defect in *GHRHR* (MIM# 139191) located on 7p14.3. IGHD IA and IV occur most frequently, while types II and III are rare (OMIM database, accessed on 20 August 2022).

Both IGHD types IA and IB are autosomal recessive conditions characterized by short stature. In type IA, there is an absence of serum GH, and those affected produce anti-GH antibodies after GH treatment (5, 6). In type IB, there are low (but detectable) serum GH levels and no evidence of antibody production after GH treatment (7). IGHD type II, however, is an autosomal dominant condition; as with type IB, low serum GH levels are detectable and no anti-GH antibodies are produced upon GH treatment (8). IGHD type III usually segregates in an X-linked manner and is often associated with agammaglobulinemia (9). IGHD type IV is a recessive condition characterized by early and severe growth failure. Those affected exhibit a reduced GH response to various provocation tests (e.g., tests for determining growth hormone level) and low insulin-like growth factor-I (IGF1) and IGF-binding protein-3 (IGFBP3) levels, but a good response to GH treatment. At the cellular level, we know that human GH binds to human growth receptor (GHR) molecules and induces signal transduction through receptor dimerization (10). When GHRH interacts with its corresponding transmembrane domains on somatotropic (GH-producing) cells, a G protein-mediated interaction with ion channels causes an increase in intracellular cAMP accumulation, which ultimately promotes GH release from secretory granules (10–12). Indeed, elevated cAMP causes protein kinase A to phosphorylate and activate CREB (13, 14), whose target genes include the pituitary-specific transcription factor *Pit-1* (also known as *GHF-1*) (15–17). Pit-1 is a prototypic POU domain protein that is required for the proper regulation of *GH* gene activity in somatotropic cells, thereby providing a pathway by which a GHRH signal can lead to increased pituitary GH synthesis. Somatostatin, an inhibitory peptide, is thought to interact with this same signaling pathway *via* G protein-mediated suppression of the cAMP pathway (18, 19). Indeed, the malfunctioning or underexpression of endogenous CREB protein in pituitary somatotropic cells causes somatotroph hypoplasia and dwarfism in mice (20). It is now clear that any disruption to this multistep GH signaling pathway can result in GH deficiency and ultimately lead to short stature and various other clinical problems.

Here, we analyzed a Pakistani family comprising four affected individuals with IGHD4. Whole-exome sequencing in this family revealed a nonsense mutation NM_000823:c.G214T:p.Glu72* in the third exon of *GHRHR*. The identified mutation presumably creates a premature terminator codon in the extracellular domain of the GHRHR and results in the synthesis of a truncated and non-functional receptor. *In-silico* findings and biochemical analysis support the pathogenic effect of the reported nonsense mutation.

Methods

Study design, declarations, and approvals

This study was approved by the Ethical Review Board of Gomal University, Dera Ismail Khan, Pakistan. Informed consent to perform genetic, molecular, and clinical analyses and to publish patient data and images was obtained from all study participants. The family was identified in Tehsil Paroa of District Dera Ismail Khan, Pakistan, through a local street-to-street survey. The genealogy was ascertained to assess the mode of disease inheritance and determine the level of consanguinity between the parents. Then, the blood samples were collected, and DNA was isolated using a GeneJET Genomic DNA purification kit (Thermo Fisher Scientific, USA, Cat# K0721), according to the manufacturer's instructions.

Whole-exome sequencing and data analysis

All the patients (V-4, V-10, V-11, V-12) were siblings and exhibited the same phenotype (Table 1). Therefore, due to the high probability of harboring common genetic variants, WES was performed on two randomly selected patients (V-4 and V-10). A sequencing library was constructed using an xGen Exome Research Panel v2.0 Kit (Integrated DNA Technologies, Coralville, IA, USA) and sequenced on a NovaSeq 6000 (Illumina, San Diego, CA, USA).

10.3389/fendo.2023.1066182

TABLE 1 Anthropometric, hormone level, and general phenotypic measurements in affected individuals with familial IGHD-associated dwarfism.

Patient ID	V-4	V-10	V-11	V-12
Sex	Female	Male	Male	Male
Age (years)	37	26	11	12
Height (cm)	114	119	121	127
Weight (kg)	20	26	24	26
Stature (with reference to the average normal population)[a]	−7.6 SD (short stature)	−8.0 SD (short stature)	−7.7 SD (short stature)	−6.9 SD (short stature)
Growth hormone level (ref: 2.0–5.0 ng/ml)	<0.05	<0.05	0.08	0.1
Digit development	Normal	Normal	Normal	Normal
Dentition	Delayed	Delayed	Delayed	Delayed
Puberty onset	Delayed	Delayed	Delayed	Delayed
Voice pitch[b]	High	High	High	High
Frontal bossing	No	No	No	No
Obesity	No	No	No	No
General physique	Normal	Normal	Normal	Normal
Polydactyly	No	No	No	No
Clinodactyly	No	No	No	Yes
Brachydactyly	No	No	No	No
Split hand-foot malformation	No	No	No	No
Abnormality of the axial skeleton	No	No	No	No
Abnormality of the appendicular skeleton	No	No	No	No
Structure of the jaw	Normal	Normal	Normal	Normal
Neurological findings	Normal	Normal	Normal	Normal

Ref, reference range.
[a]SimulConsult was used to determine the population-compared stature (URL: https://simulconsult.com/resources/).
[b]The assessment was based on the general observation of voice, i.e., it could either be a child-like or adult-like voice.

The base call files were converted to FASTQ files using bcl2fastq v2.20.0.422 (https://support.illumina.com/sequencing/sequencing_software/bcl2fastq-conversion-software.html). The sequence reads in the FASTQ files were aligned to the human reference genome (GRCh37/hg19) using BWA-mem 0.7.17 (arXiv:1303.3997v2 [q-bio.GN]) to generate BAM files. The BAM files were further processed for variant calling to generate VCF files using GATK v.3.8 (21). Finally, variant annotation and interpretation was performed using the EVIDENCE tool developed by "3billion" (South Korea) (22). To evaluate the authenticity of these predictions, variant annotation was carried out in parallel using wANNOVAR (https://wannovar.wglab.org/index.php) (23) and VariantStudio software (version 3.0) with the reference assembly "hg19." Variant prioritization was phenotype driven (i.e., based on the disease diagnosis), and previously reported genes were used as the training set (retrieved from the OMIM database, accessed on 20 August 2022). Primarily, the genes reported for IGHD were screened for the presence of possible candidate variants before the variant analysis was extended exome-wide to identify protein-disrupting mutations. For candidate variant prioritization, the analysis focused on filtering homozygous, missense and indel variants, and low-frequency and protein-encoding alleles. Finally, splice variants and untranslated region (UTR) variants were also investigated to exclude their possible involvement.

Preliminary computational screening

Before segregation analysis and 3D protein modeling, primary pathogenicity validation parameters were assessed. Initially, the biological significance of candidate variants was predicted using VarSome (24), which integrates multiple online pathogenicity prediction tools in a single platform. The gnomAD database (https://gnomad.broadinstitute.org/) was then consulted to assess the population allele frequency. To validate the clinical significance of identified candidate variants [as per ACMG guidelines (https://www.acmg.net/)], InterVar (25), VarSome (https://varsome.com/), and ClinVar databases (https://www.ncbi.nlm.nih.gov/clinvar/) were explored. Being a receptor protein, the integrity of transmembrane domains was assessed and visualized using TMHMM (https://services.healthtech.dtu.dk/service.php?TMHMM-2.0), Protter (https://wlab.ethz.ch/protter/start/), and Phobius (https://phobius.sbc.su.se/) prediction tools.

Segregation analysis

To validate the segregation of the candidate variant(s) with the disease phenotype, Sanger DNA sequencing was performed on DNA samples provided by all available family members: III-1, IV-1, V-4, V-6, and V-10. The Primer3web tool (version 4.1.0) (26) was used to design suitable primers, and the mutation analysis was performed using BioEdit software (version 7.1) (27, 28).

Biomedical analysis

To assess receptor functionality and GH deficiency, a clinical test for serum GH level was performed for two affected participants (V-10 and V-11). Blood samples (5 ml each) were collected from both the affected individuals under fasting conditions and referred to the CAP-certified (College of American Pathologists) laboratory at Aga Khan University Hospital, Karachi, Pakistan. X-ray images of the hands and feet were taken for all affected individuals to identify any limb abnormalities, e.g., bone degeneration (rheumatoid arthritis) and abnormal bone fusion (syndactyly).

In-silico functional assays

Computational 3D structural modeling, protein–protein interaction analyses, and molecular dynamic simulation analyses were performed to predict the pathogenic effects of the identified variant(s) on the structure and function of the protein.

Protein structure prediction

Structural modeling of normal and mutant GHRHR was performed using the I-TASSER tool (29) and SWISS-MODEL (30). After structure prediction, 3D models of the wild-type and mutant GHRHR were superimposed to detect gross structural anomalies.

Molecular docking

ClusPro (31) was used to investigate the GHRH–GHRHR interaction. Namely, protein–protein docking of wild-type and mutant GHRHR was performed with its close functional interactor, GHRH, which was identified through the STRING matching database (32). Molecular visualization was performed using Chimera 1.13.1 (33) and LigPlot+ (version 2.1) (34).

Molecular dynamics simulation

AMBER package (version 16) (35) was used for molecular dynamic (MD) simulations of GHRHR models (wild type and mutant) and their docked complexes (35). All models were solvated in a rectangular box (8.0 Å) in the presence of counter ions to neutralize the system. Prior to MD simulations, each system was separately minimized, heated, and equilibrated. While keeping the protein model fixed, the studied systems were minimized. After minimization, the systems were heated and equilibrated at 300 K for 100 ps with a constant volume. Once the systems were equilibrated, all restraints were removed under constant pressure before running further equilibration steps at 300 K. MD simulation trajectory files were saved at 0.5 ps intervals. The PTRAJ/CPPTRAJ module (36) was used to analyze the saved MD simulation trajectory files, and Xmgrace (37) was used for visualization. The root mean square deviation (RMSD) and root mean square fluctuation (RMSF) were analyzed with the CPPTRAJ module. The RMSD values of both the wild-type and mutant structures were calculated using the starting structure as a reference frame and the deviation of the coordinates of a given set of atoms in a time interval. The RMSF was calculated to measure the fluctuations of each residue from their mean positions.

Qatar Genome Program data analysis

The Qatar Genome Program (QGP) is a population-focused study that aims to generate a whole genome sequence for all participants in the Qatar Biobank (QBB) (38, 39). Qatar is a multicultural society where South Asian expats are considered to be one of the founder populations (40). The present study was conducted using information from ~15,000 QGP genomes that have been comprehensively phenotyped based on biomedical information deposited in the QBB. The whole genomes and phenotype data were investigated to determine the frequency of rs121918117 in the local Qatari population as well as their associated clinical phenotypes (including hormonal profiles and liver and kidney functions).

Results

Clinical findings of patients with IGHD type IV

A five-generation consanguineous Pakistani family affected by IGHD type IV was recruited through a local survey. The family consisted of five affected individuals, namely, four surviving patients [one female (V-4) and three male patients (V-10, V-11, V-12) aged 37, 26, 11, and 12 years (Figure 1A), respectively] and one who died of an unrelated cause. The parents were first cousins with no previous history of IGHD and were asymptomatic with normal height, stature, and physique. The disease had emerged only in the most recent generation, and none of their predecessors exhibited this phenotype. All the patients had been born at full term with a normal delivery and no pregnancy complications. Genealogical analysis indicated a pattern of autosomal recessive disease inheritance (Figure 1B).

We first collected anthropometric, hormone, and general clinical measurements from affected individuals with familial IGHD-associated dwarfism (Table 1). We saw that all the surviving patients were affected by severe growth retardation and short stature (i.e., dwarfism) (Figure 1A). This finding supported the low or negligible serum GH levels, indicating abnormal GHRHR function. Specifically, all patients measured −6.9 to −8.0 SD below the mean height for the relevant age group in the healthy population (https://simulconsult.com/resources). By comparison, all unaffected individuals from general population had an average height of ~5.5 feet. Digit curvature, namely, bilateral 4/5 clinodactyly, was observed in the hands of V-12; no other digit anomalies such as polydactyly or brachydactyly were observed. Moreover, no other gross anomalies were detected by X-ray analysis of the appendicular or axial skeleton.

10.3389/fendo.2023.1066182

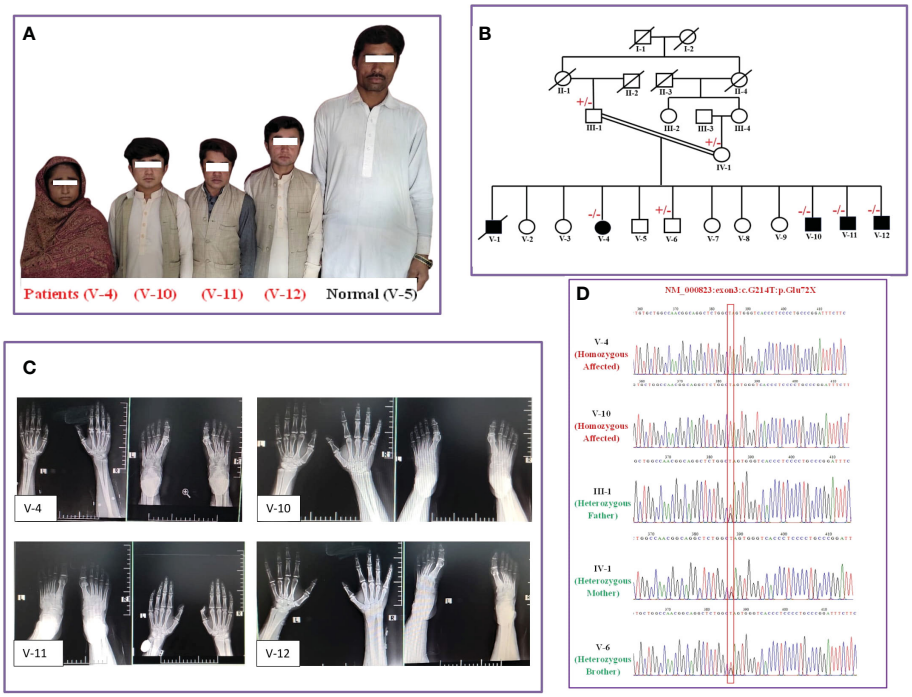

FIGURE 1
Genealogical analysis and clinical description of patients. **(A)** Photographs of normal (V-5) and affected individuals (V-4, V-10, V-11, V-12). **(B)** Genotype integrated family genealogy. **(C)** Radiographs of the hands and feet of affected patients. **(D)** Sequence chromatograms of affected patients (V-4 and V-10) and normal individuals, including the parents (III-1 and IV-1).

The body mass index (BMI) of all patients was in the normal range, and no one exhibited abdominal fat deposits. The head-to-body ratio was normal and non-indicative of micro- or macrocephaly; the thyroid gland examination was also normal. All patients exhibited a delay in the eruption of permanent dentition, yet the skull shape/size and jaw structure were normal in all patients, with no symptoms of hypoplastic maxilla. The radiological findings of the affected individuals revealed normally developed carpal/metacarpal and tarsal/metatarsal bones. There was no polydactyly, syndactyly, or brachydactyly of the hands or feet, thus suggesting normal digit development (Figure 1C).

The general clinical assessment of the patients did, however, indicate an underdevelopment of the body structure. All patients had a high-pitched voice. In medical examinations, no frontal bossing, depressed nasal bridge, or depressive behavior was observed. While fertility was not assessed in these patients, it was noted that all had reached puberty by 18 years of age (on average).

The findings of ophthalmologic, otorhinolaryngologic, neurologic, skeletal, and visceral organ examinations were normal. The patients had no current or previous history of diabetes, hypoglycemia, hypertension, cardiac problem, allergies (food or drug), dermal lesions, or autoimmune disorders.

Molecular analysis found founder mutation in GHRHR

Having comprehensively assessed the clinical phenotypes of all four affected patients, we next performed a WES analysis to determine the genetic basis of the disease. Here, we identified a recurrent homozygous nonsense mutation [NM_000823:c.G214T:p.(Glu72*); (rs121918117)] in the third exon of the *GHRHR* gene. Sanger sequencing confirmed the co-segregation of the identified mutation with the disease phenotype in all patients (Figure 1D). This variant was not found in the unaffected family members or in our in-house database comprising an ethnically matched control population. The minor allele frequency of this allele in gnomAD was 0.0001755, with no known homozygote. According to a database survey, the variant was reported in South Asian regions only and not found in any European, American, Ashkenazi Jews, or East Asian communities, thus indicating that the variant is Asian-specific (allele count 34). Indeed, the (p.Glu72*) nonsense mutation has previously been mapped in three South Asian families (Indian, Sri Lankan, and Pakistani), which suggests a founder effect of this mutation in IGHD.

The ClinVar, VarSome, and InterVar databases reported rs121918117 as a pathogenic variant. Indeed, the premature stop codon presumably truncates the protein by deleting the C-terminus GPCR transmembrane (TM) domains and, in part, the GPCR-2 extracellular domains. According to TM domain integrity prediction, the truncated protein is unable to anchor within the membrane due to loss of all the downstream TM domains, causing loss of receptor function (Figure 2). We thus speculate that the premature stop codon and early truncation of the protein product caused by the identified nonsense mutation (p.Glu72*) might activate the nonsense-mediated mRNA decay pathway, resulting in low GH production in affected patients.

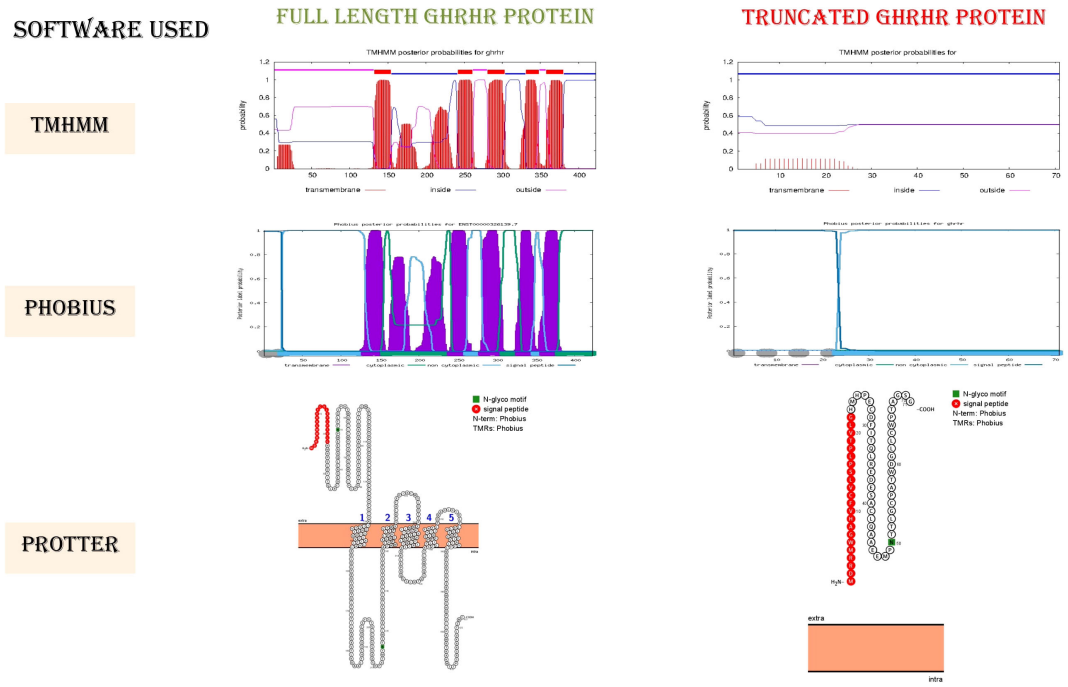

FIGURE 2
Membrane topology of GHRHR: images of the transmembrane topology of the GHRHR protein.

Protein structural analysis

Molecular modeling of wild-type and mutant GHRHR proteins and hormone-receptor docking

We next aimed to determine the structure and interaction studies. We first found that superimposition of the 3D models of both wild-type and mutant GHRHR was not possible (Figures 3A–C), confirming that the c.G214T: p.Glu72* nonsense mutation causes structural distortion of GHRHR due to protein truncation.

We next monitored the interactions between the wild-type and mutant GHRHR receptor proteins with GHRH. Compared with the full-length wild-type protein, the truncated GHRHR protein showed a different interaction pattern with respect to residue numbers, residue identity, and bonding category (Figures 3D, E). The wild-type receptor could interact with GHRH *via* 14 amino acid residues (Asp395, Lys130, Asp183, Ser124, Arg384, Asp190, Asp191, Lys329, Arg405, Lys417, Glu123, Gln381, Thr128, and Tyr125) and 27 bonding forces involving 23 H-bonds and four salt bridges. By contrast, the mutant receptor docked with GHRH *via* only six amino acids (Leu63, Cys64, Asp37, Arg4, Asp2, and Glu72) and eight hydrogen bonds. These findings suggest that the mutation protein binds more strongly with the interactor compared to the wild-type GHRHR.

Findings on molecular dynamic simulation analysis

Next, we evaluated the dynamic behavior of the wild-type and mutant GHRHR proteins and their interactions with GHRH by 100-ns MD simulation. We generated models of the wild-type–GHRHR–GHRH and mutant–GHRHR–GHRH complexes (Figures 3D, E, respectively). We determined the atomic positions of the modeled GHRHR protein structure and compared them with those of the mutant–GHRHR protein to examine the convergence and durability of the MD simulations. The trajectories of the MD simulations were analyzed in a multistep process to decode the backbone stability and residual flexibility. The RMSD was first calculated as a measure of the average distance between the backbone carbon alpha atoms in the overlay frames. The average distance between the backbone carbon alpha atoms of the overlay frames was then calculated, and the stability of the simulated C atoms of the protein was determined by plotting the modeled wild-type–GHRHR, mutant–GHRHR protein, wild-type–GHRHR–GHRH protein, and mutant–GHRHR–GHRH proteins as a function of time. We found evidence for a slightly greater deviation of the wild-type–GHRHR (RMSD mean 5.93364 Å, max. 8.2271 Å at 85,361 frames) than the mutant–GHRHR (RMSD mean 5.02231 Å, max. 7.2316 Å at 8,858 frames) (Figure 4, upper panel). In both the wild-type– and mutant–GHRHR, a constant displacement was observed in the first 25 ns of the MD simulation, indicating that the atoms were out of alignment and the structure was unstable. While the mutant–GHRHR showed minor fluctuations for the remaining simulation period, the wild-type–GHRHR–GHRH showed considerable deviations (RMSD mean 8.79908 Å, max. 8.79908 Å at 42,247 frames), indicating that the docked complex was stable after 60 ns (Figure 4, lower panel). By contrast, the RMSD plot for the mutant–GHRHR–GHRH revealed an unstable system that stabilized during the MD simulation and remained stable until the end. The plot showed considerable deviations (RMSD mean 6.73827 A, max. 8.7608 Å at 97,250 frames), indicating that the atoms were out of synchrony and the system was unstable. We also performed an RMSF analysis to assess the fluctuation of residues in the wild-type and mutant docked complexes. Here, the mutant structure showed much greater stability than the wild-type structure, which instead underwent marked fluctuations.

10.3389/fendo.2023.1066182

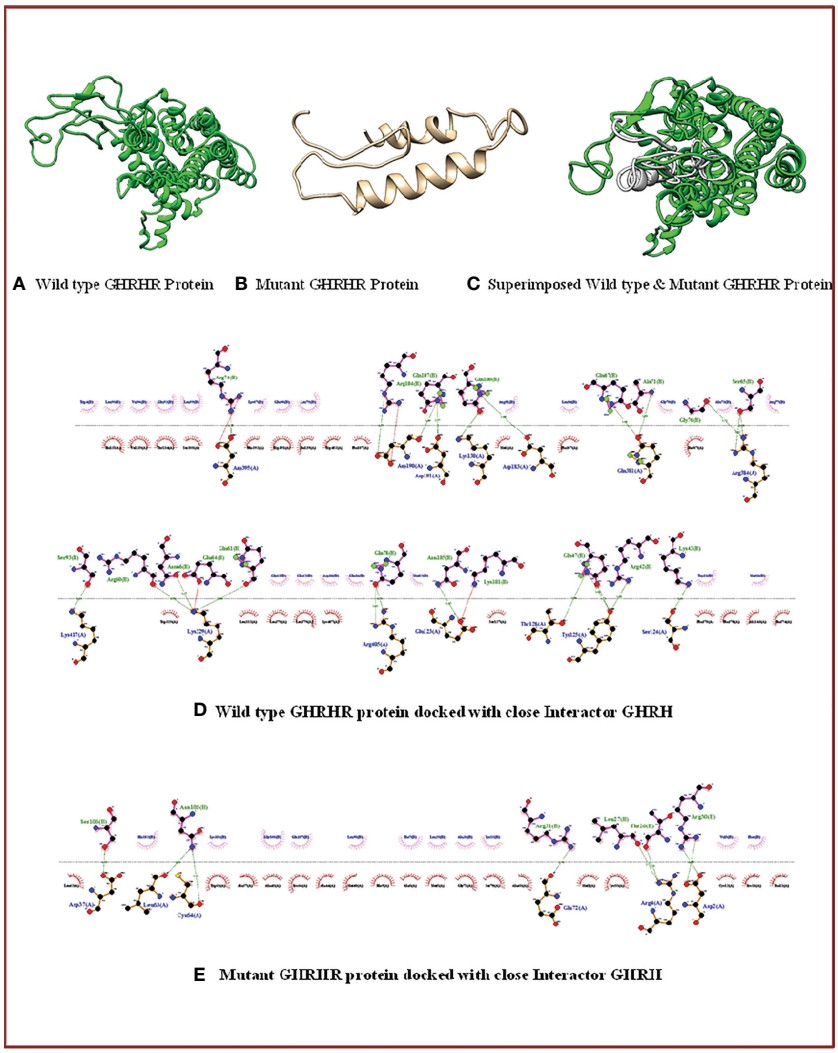

FIGURE 3
3D structure and docking properties of GHRHR: **(A–C)** Normal and mutant models of the GHRHR protein and their superimposed images. **(D, E)** Normal and mutant GHRHR proteins docked with a close interactor (GHRH).

Estimation of different binding free energies using MMGB/PBSA

We assessed the binding free energies of the wild-type and mutant GHRHR proteins complexed with GHRH. We calculated these based on the simulated trajectories using the MMGBSA and MMPBSA approaches. The net total energy for the wild-type–GHRHR–GHRH structure was −215.747, while that for the mutant–GHRHR–GHRH structure was −99.2622. In comparison to the MMGBSA approach, the MMPBSA net binding energy showed that the interaction energies of both systems were highly favorable and stable (Table 2).

QGP data outcomes

To determine the frequency of rs121918117 (GHRHR) in the population, we leveraged the QGP database and identified two heterozygous individuals (QGP1 and QGP2) with an alternate allele frequency of 0.00006817. Both QGP1 and QGP2 were clinically normal and asymptomatic although their seated height was slightly reduced compared to that of the average value of the QGP-cataloged individuals. In terms of standing height, QGP1 was in the normal range, while QGP2 had a short stature (−0.5 SD). All other available health indicators were in the good and excellent categories, with the exception that QGP2 was classified as obese and QGP1 had systolic/diastolic BP and pulse rates tending to 89/62 mmHg and 68 beats per minute.

Discussion

IGHD is an inherited condition of inadequate secretion of GH by the pituitary gland (41) that results in severe short stature (9). To date, 82 mutations in *GHRHR* have been identified in IGHD patients of multiple ethnicities. Of these mutations, six are nonsense, 12 are splice disrupting, 44 are missense, 16 are small indels, and four are

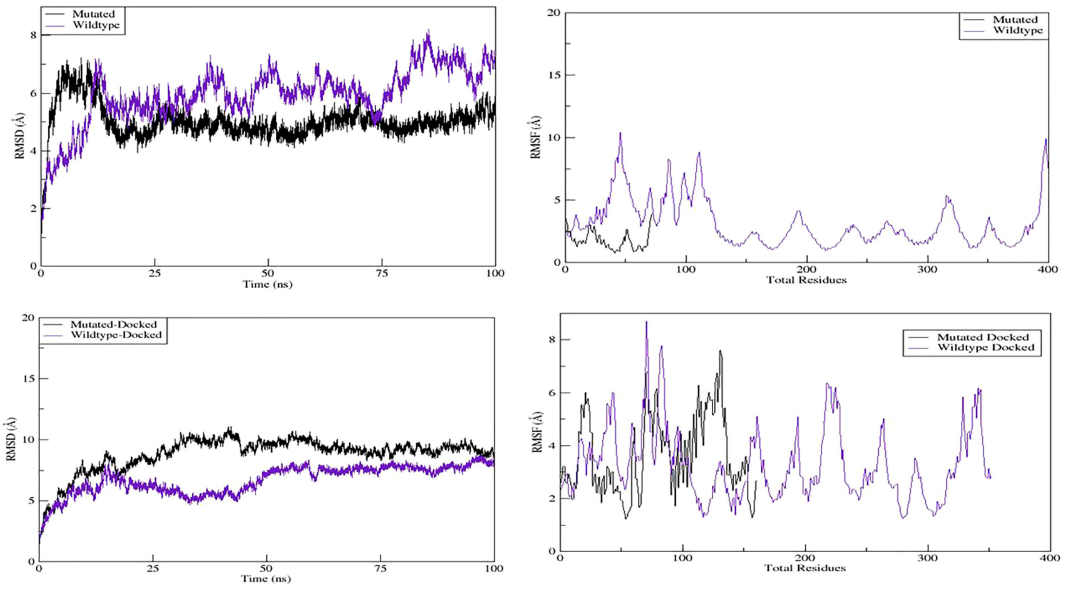

FIGURE 4
MD simulation properties: molecular dynamic simulation graphs of wild-type, mutant, and their docked complexes with GHRH.

TABLE 2 Calculation of binding free energies using MMGB/PBSA analysis.

	GB-normal	GB-mutant		PB-normal	PB-mutant
Complex					
Energy component	Average	Average	Energy component		Average
VDWAALS	−3,155.62	−1,061.13	VDWAALS	−3,155.62	−1,061.13
EEL	−28,758.908	−10,337.53	EEL	−28,758.91	−10,337.53
EGB	−6,074.956	−2,103.894	EPB	−5,976.96	−2,051.191
ESURF	203.5613	80.608	ENPOLAR	127.0985	52.8673
G gas	−31,914.528	−11,398.66	G gas	−31,914.53	−11,398.66
G solv	−5,871.3948	−2,023.286	G solv	−5,849.862	−1,998.324
TOTAL	−37,785.923	−13,421.94	TOTAL	−37,764.39	−13,396.98
Receptor					
VDWAALS	−2,325.1964	−330.9864	VDWAALS	−2,325.196	−330.9864
EEL	−21,591.286	−3,602.448	EEL	−21,591.29	−3,602.448
EGB	−5,949.3834	−1,480.209	EPB	−5,832.037	−1,438.954
ESURF	176.2588	38.5172	ENPOLAR	112.0205	25.7334
G gas	−23,916.482	−3,933.434	G gas	−23,916.48	−3,933.434
G solv	−5,773.1246	−1,441.692	G solv	−5,720.017	−1,413.22
TOTAL	−29,689.607	−5,375.127	TOTAL	−29,636.5	−5,346.655
Ligand					
VDWAALS	−555.6505	−603.0366	VDWAALS	−555.6505	−603.0366
EEL	−5,634.018	−5,790.622	EEL	−5,634.018	−5,790.622
EGB	−1,786.1916	−1,632.523	EPB	−1,767.252	−1,598.376
ESURF	65.4848	59.1637	ENPOLAR	44.7775	40.9695

(Continued)

TABLE 2 Continued

	GB-normal	GB-mutant		PB-normal	PB-mutant
G gas	−6,189.6685	−6,393.658	G gas	−6,189.669	−6,393.658
G solv	−1,720.7068	−1,573.359	G solv	−1,722.475	−1,557.407
TOTAL	−7,910.3753	−7,967.017	TOTAL	−7,912.143	−7,951.065
Differences (complex–receptor–ligand)					
VDWAALS	−274.7731	−127.1068	VDWAALS	−274.7731	−127.1068
EEL	−1,533.6038	−944.4587	EEL	−1,533.604	−944.4587
EGB	1,660.619	1,008.838	EPB	1,622.329	986.1388
ESURF	−38.1823	−17.0729	ENPOLAR	−29.6994	−13.8355
DELTA G gas	−1,808.3769	−1,071.566	DELTA G gas	−1,808.377	−1,071.566
DELTA G solv	1,622.4366	991.7649	DELTA G solv	1,592.63	972.3033
DELTA TOTAL	−185.9402	−79.8006	DELTA TOTAL	−215.747	−99.2622

TABLE 3 List of reported mutations in the *GHRHR* gene.

Missense/nonsense mutations					
S. no.	cDNA position	Amino acid position	Exon number	Phenotype	Reference
1	c.11G>A	p.R4Q	1	Growth hormone deficiency	(47)
2	c.10C>T	p.R4W	1	Isolated growth hormone deficiency	(48)
3	c.29T>G	p.V10G	1	Growth hormone deficiency	(49)
4	c.47C>T	p.P16L	1	Isolated growth hormone deficiency	(48)
5	c.97C>T	p.Q33X	2	Growth hormone deficiency	(50)
6	c.128C>T	p.Q43X	2	Growth hormone deficiency	(45)
7	c.164G>T	p.C55F	3	Isolated growth hormone deficiency	(51)
8	c.244G>A	p.A57T	3	Increased tumor sensitivity/isolated growth hormone deficiency	(52)
9	c.190T>G	p.C64G	3	Growth hormone deficiency	(53)
10	c.211G>T	p.G71C	3	Isolated growth hormone deficiency	(54)
11	265G>T 214G>T	p.E72X	3	Growth hormone deficiency	(55) (56) (57)
12	c.236C>T	p.P79L	3	Growth hormone deficiency	(47)
13	c.281G>T	p.R94L	4	Growth hormone deficiency	(57)
14	c.280C>T	p.R94W	4	Growth hormone deficiency	(58)
15	c.281G>A	p.R94Q	4	Isolated growth hormone deficiency	(48)
16	c.335G>A	p.C112Y	4	Isolated growth hormone deficiency	(59)
17	c.428T>C	p.V121D	4	Isolated growth hormone deficiency	(60)
18	c.407G>T	p.G136V	5	Isolated growth hormone deficiency	(43)
19	c.410A>T	p.H137L	5	Growth hormone deficiency	(61)
20	c.418T>C	p.S140P	5	Isolated growth hormone deficiency	(51)
21	c.431T>A	p.L144H	5	Growth hormone deficiency	(61)
22	c.458C>A	p.A153D	5	Pituitary	(62)

(Continued)

TABLE 3 Continued

Missense/nonsense mutations					
S. no.	cDNA position	Amino acid position	Exon number	Phenotype	Reference
23	c.481C>T	p.R161W	6	Growth hormone deficiency	(57)
24	c.537C>T	p.Y163Y	6	Isolated growth hormone deficiency	(60)
25	c.491T>C	p.V164A	6	Isolated growth hormone deficiency	(48)
26	c.495C>A	p.H165Q	6	Isolated growth hormone deficiency	(51)
27	c.507C>G	p.F169L	6	Isolated growth hormone deficiency	(48)
28	c.527C>T	p.A176V	6	Growth hormone deficiency	(63)
29	c.604T>C	p.C202R	7	Short stature	(64)
30	c.655C>A	p.A222E	7	Growth hormone deficiency	(61) (57)
31	c.728G>A	p.W243X	7	Isolated growth hormone deficiency	(48)
32	c.731G>A	p.W244X	7	Growth hormone deficiency	(65)
33	c.789C>T	p.L247L	7	Isolated growth hormone deficiency	(60)
34	c.758C>T	p.P253L	8	Isolated growth hormone deficiency	(59)
35	c.817A>G	p.T257A	8	Isolated growth hormone deficiency	(60)
36	c.776C>A	p.T259K	8	Isolated growth hormone deficiency	(48)
37	c.783G>A	p.V261V	8	Isolated growth hormone deficiency	(66)
38	c.838A>G	p.K264E	8	Isolated growth hormone deficiency	(60)
39	c.818G>C	p.W273S	9	Growth hormone deficiency	(57)
40	c.847T>C	p.W283R	9	Isolated growth hormone deficiency	(48)
41	c.998G>C	p.S317T	10	Isolated growth hormone deficiency	(60)
42	c.386A>G	p.K329E	11	Growth hormone deficiency	(45)
43	c.1037C>T	p.S330L	11	Isolated growth hormone deficiency	(60)
44	c.1071C>T	p.R357C	11	Growth hormone deficiency	(67)
45	c.1087G>C	p.G363R	12	Short stature	(64)
46	c.1102C>T	p.Q368X	11	Isolated growth hormone deficiency	(59)
47	c.1106G>T	p.G369V	12	Isolated growth hormone deficiency	(60)
48	c.1146G>A	p.E382E	12	Short stature	(46)
49	c.1160T>C	p.I387T	13	Isolated growth hormone deficiency	(48)
50	c.1265T>C	p.M422T	13	Major depressive disorder	(68)
Splice site mutations					
S. no.	Position	Intron number	Type	Phenotype	Reference
51	IVSI+1G>A	1	Splice donor	Growth hormone deficiency	(69)
52	IVS1+2T>G	1	Splice donor	Growth hormone deficiency	(70)
53	IVS2+3A>G	2	Splice donor	Isolated growth hormone deficiency	(43)
54	IVS3+1G>A	3	Splice donor	Growth hormone deficiency 1B	(45)
55	IVS7+1G>C	7	Splice donor	Growth hormone deficiency	(71)
56	IVS7−1G>A	7	Splice acceptor	Growth hormone deficiency	(72)
57	IVS8−30G>A	8	Splice acceptor	Isolated growth hormone deficiency	(66)

(Continued)

TABLE 3 Continued

Missense/nonsense mutations					
S. no.	cDNA position	Amino acid position	Exon number	Phenotype	Reference
58	IVS8+1G>A	8	Splice donor	Pituitary dwarfism	(73)
59	IVS12−1G>A	12	Splice acceptor	Growth hormone deficiency 1B	(46)
60	IVS12+2T>A	12	Splice donor	Growth hormone deficiency	(74)
61	IVS3161−1G>A	3	Splice acceptor	Isolated growth hormone deficiency	(48)
62	IVS2+27G>T	2	Splice donor	Isolated growth hormone deficiency	(66)
Insertion/deletion mutations					
S. no.	cDNA position	Amino acid	Exon number	Phenotype	Reference
63	c.340delG	p.V114Cfs*16	4	Isolated growth hormone deficiency	(44)
64	c. 1140-1144del	p.N380Kfs*5	13	Isolated growth hormone deficiency	(61)
65	c.1120_1123delATCC	p.I374Sfs*9	11	Growth hormone deficiency	(58)
66	c.4bp del	p.373	12	Isolated growth hormone deficiency	(75)
67	c.380insC	p.C112Lfs*9	4	Isolated growth hormone deficiency	(60)
68	c.920insC	V308Gfs*79	10	Isolated growth hormone deficiency	(66)
69	g.30999250_ 31006943delinsAGAGATCCA	–	5" UTR/exon 1	Isolated growth hormone deficiency	(76)
70	c.271dupG	p.A91Gfs*13	4	Isolated growth hormone deficiency	(48)
71	c.674_677delinsGC TGTTGGCAGAAG	p.V225 Gfs*165	7	Isolated growth hormone deficiency	(48)
72	c.465−91_1105−119del5291	p.R156 Afs*15	5	Isolated growth hormone deficiency	(48)
73	c.(?_−48)_(57 + 1_58−1)del	–	2	Isolated growth hormone deficiency	(48)
74	c.22_23insA	p.A8Dfs*22	1	Isolated growth hormone deficiency	(48)
75	c.1089_1093del	p.L364Ffs*21	11	Isolated growth hormone deficiency	(48)
76	c.597+153_883−273del	p.L201_V295del	7	Isolated growth hormone deficiency	(48)
77	c.-3166_58−2057del	–	Intron1	Isolated growth hormone deficiency	(77)
78	c.820_821ins	p.N274Afs*113	9	Congenital Hypopituitarism	(78)
Regulatory mutations					
S. no.	Position	Phenotype	Reference		
79	c.-261C>T	Breast cancer	(69)		
80	c.166T>C	Reduced promoter activity/short stature	(46)		
81	c.164T>C	Reduced promoter activity/short stature	(46)		
82	c.-124A>C	Growth hormone deficiency 1B	(45)		

regulatory mutations (42–46) (HGMD® Professional 2022.2, assessed on August 2022) (Table 3). Here, we have added to the portfolio of GHRHR mutations underlying IGHD after performing a WES analysis of a large, consanguineous Pakistani family comprising four individuals suffering from IGHD4.

Our WES and Sanger sequencing analysis revealed a nonsense *GHRHR* mutation [NM_000823:exon3:c.G214T:p.Glu72*] that segregated with the disease phenotype. This nonsense mutation results in the generation of a truncated protein devoid of the C-terminus membrane spanning TM domains. We speculate that this truncation triggers the nonsense-mediated decay of defective mRNA, which is the most likely reason for the loss of functional integrity of the GHRHR and hormonal signaling. Indeed, this phenomenon can be correlated with reduced or absent GH levels in patient serum and is consistent with the extremely reduced levels of serum GH in affected individuals observed in our hormone analysis.

In expression studies of truncated and chimeric epitope-linked GHRH receptors (i.e., GHRHR), DeAlmeida and Mayo (79) first identified the regions vital for the interaction of the receptor with GHRH. They investigated the fate of two truncated receptors; GHRH-delta-N, without the N-terminal domain (the region between the signal sequence and the first TM domain) and GHRH-delta-C, with trimmed downstream TM domains. In both experiments, they found diminished receptor–ligand interactions, showing that neither the N-terminus extracellular domain nor the membrane-spanning C-terminus domains were independently capable of interacting with GHRH. Instead, it was determined that although the N-terminal extracellular domain is necessary for ligand binding, the transmembrane domains and associated extracellular loop regions of the GHRHR are vital for the specific interaction with GHRH (79). The current findings also support this notion, wherein the C-terminal deletion mutation p.Glu72* also exhibits diminished interaction of GHRHR–GHRH as presented by the reduced level of growth hormones.

The p.Glu72* mutation detected in this study was previously identified by Wajnrajch et al. in an Indian family with profound GH deficiency (55), with the patient's phenotypes found to be similar to the "little mouse" harboring Ghrhr gene mutation(s). Furthermore, the human counterparts of the mutations in the "little mouse" model (especially Asp60Gly mutation in mouse being closest to human Glu72*), were associated with comparable phenotypic features in terms of stature and hormone level. The phenotypes of patients enrolled in our study showed considerable similarities with those reported by Wajnrajch et al.: all patients exhibited phenotypes as seen in the mouse model although they did not exhibit obesity or frontal bossing. Genetic studies, including our own, have shown that carriers of *GHRHR* mutations are asymptomatic and of normal height. In a clinical investigation of a cohort of 76 adults (aged 25–75 years) carrying a heterozygous *GHRHR* mutation, Pereira et al. (80) found no association between the GHRHR mutation and short stature. We also found that all the family members (including both wild-type and heterozygous carriers) were under 5 feet in height. However, the slightly reduced sitting height of individuals from the QGP cohort remains to be investigated.

The (p.Glu72*) nonsense mutation we identified here has also been mapped in three different South Asian families from Bombay (India), Delft (an island located between Sri Lanka and India), and Sindh (Pakistan). The relative geographic connection of these families indicates the possibility of a common origin. Wajnrajch et al. performed a microsatellite-based haplotype analysis to evaluate this hypothesis among these three apparently unconnected families from the Indian subcontinent harboring the common GHRHR mutation (p.Glu72*) (81). Their evolutionary analysis revealed that these families originated from a common ancestor between 1,350 and 2,700 years ago when the three traditionally and linguistically distinct families separated from their common ancestry (47). Our identification of the same p.Glu72* mutation in a Pakistani family increases the probability of its founder effect. Furthermore, since the family in our study originated from the southernmost part of Pakistan near the Sindh Province, our study also supports the possibility of Indo-Dravidian (or Indo-Aryan) migration (81).

Conclusions

In the current study, we identified a nonsense mutation (p.Glu72*) of GHRHR in a consanguineous Pakistani family affected by IGHD4. Biochemical analysis revealed extremely low GH levels, suggesting functional loss of the GHRHR. We confirmed the pathogenicity of this variant by *in-silico* analysis. To the best of our knowledge, this is the fourth report of a *GHRHR* mutation NM_000823:c.G214T:p.(Glu72*), and together with previous reports, our data provide further support for the founder effect of p.Glu72* in South Asian families. Our data will help to establish the genotype–phenotype correlation in IGHD type IV and, thus, will support molecular diagnosis in clinical practice. Evaluating *GHRHR* gene integrity is an important aspect of genetic evaluation in those of short stature, as early genetic diagnosis might support precision medicine treatment options. Indeed, successful treatment, i.e., hormonal therapy based on GHRHR detection, may help maintain a normal growth pattern and would subsequently enable affected patients to live a confident life in society and avoid any secondary implications of their disease, such as delayed puberty, fertility, and physique.

Data availability statement

The datasets presented in this study can be found in online repositories. The names of the repository/repositories and accession number(s) can be found in the article/supplementary material.

Ethics statement

This medico-genetic study was approved by the Institutional Ethical Review Board of Gomal University D.I. Khan (IRB# 04/ERB/GU), KPK, Pakistan. Informed consent was obtained from all study participants and their parents/guardians. The patients/participants provided their written informed consent to participate in this study. Written informed consent was obtained from the individual(s) for the publication of any potentially identifiable images or data included in this article.

Author contributions

SA, MA, IAhma, and ShA assisted with the patient recruitment, conducted the experiments, and performed the data analysis. SWA performed the bioinformatic analysis. IAhme, SN, and MZ performed the sequence data analysis. MK, AAA, and KF conceptualized and supervised the study, obtained funding to support the study, and drafted the manuscript. All authors contributed to and approved the final version of this manuscript.

Funding

This study was supported by Sidra Medicine, through funding number 20.6545-632157 (provided to AAA, Sidra Medicine, Doha, Qatar).

Acknowledgments

We are grateful to all patients and family members for participating in this study. The authors also thank 3billion, South Korea, for their generous help in performing the whole-exome sequencing. 3billion was not involved in the study design, analysis, interpretation of data, the writing of this article or the decision to submit it for publication.

Conflict of interest

The authors declare that the research was conducted in the absence of any commercial or financial relationships that could be construed as a potential conflict of interest.

Publisher's note

References

1. Lacey K, Parkin J. Causes of short stature: A community study of children in Newcastle upon Tyne. *Lancet* (1974) 303(7846):42–5. doi: 10.1016/S0140-6736(74)93041-4

2. Vimpani GV. Short stature in Scottish schoolchildren: A community study with special emphasis on the prevalence of severe growth hormone deficiency. In: *Annexe thesis digitisation project 2016 block 4* (1977). Available at: https://era.ed.ac.uk/handle/1842/17702?show=full.

3. Rona R, Tanner J. Aetiology of idiopathic growth hormone deficiency in England and Wales. *Arch Dis Childhood* (1977) 52(3):197–208. doi: 10.1136/adc.52.3.197

4. Lindsay R, Feldkamp M, Harris D, Robertson J, Rallison M. Utah Growth study: Growth standards and the prevalence of growth hormone deficiency. *J Pediatr* (1994) 125 (1):29–35. doi: 10.1016/S0022-3476(94)70117-2

5. Cogan JD, Phillips JA3rd. Gh1 gene deletions and ighd type 1a. *Pediatr Endocrinol Rev* (2006) 3:480–8.

6. Laron Z, Kelijman M, Pertzelan A, Keret R, Shoffner J, Parks J. Human growth hormone gene deletion without antibody formation or growth arrest during treatment–a new disease entity? *Israel J Med Sci* (1985) 21(12):999–1006.

7. Baumann G. Genetic characterization of growth hormone deficiency and resistance. *Am J Pharmacogenomics* (2002) 2(2):93–111. doi: 10.2165/00129785-200202020-00003

8. Wit JM, Oostdijk W, Losekoot M, van Duyvenvoorde HA, Ruivenkamp CA, Kant SG. Mechanisms in endocrinology: Novel genetic causes of short stature. *Eur J Endocrinol* (2016) 174(4):R145–R73. doi: 10.1530/EJE-15-0937

9. Rimoin D, Phillips IIIJ. Genetic disorders of the pituitary gland. *Principles Pract Med Genet* (1997) 3:1331–64.

10. Lin C, Lin S-C, Chang C-P, Rosenfeld MG. Pit-1-Dependent expression of the receptor for growth hormone releasing factor mediates pituitary cell growth. *Nature* (1992) 360(6406):765–8. doi: 10.1038/360765a0

11. Mayo KE. Molecular cloning and expression of a pituitary-specific receptor for growth hormone-releasing hormone. *Mol Endocrinol* (1992) 6(10):1734–44.

12. Gaylinn BD, Harrison JK, Zysk JR, Lyons C, Lynch K, Thorner M. Molecular cloning and expression of a human anterior pituitary receptor for growth hormone-releasing hormone. *Mol Endocrinol* (1993) 7(1):77–84.

13. Gonzalez GA, Montminy MR. Cyclic amp stimulates somatostatin gene transcription by phosphorylation of creb at serine 133. *Cell* (1989) 59(4):675–80. doi: 10.1016/0092-8674(89)90013-5

14. Sheng M, Thompson MA, Greenberg ME. Creb: A Ca2+-regulated transcription factor phosphorylated by calmodulin-dependent kinases. *Science* (1991) 252(5011):1427–30. doi: 10.1126/science.1646483

15. Bodner M, Castriilo J-L, Theill LE, Deerinck T, Ellisman M, Karin M. The pituitary-specific transcription factor ghf-1 is a homeobox-containing protein. *Cell* (1988) 55(3):505–18. doi: 10.1016/0092-8674(88)90037-2

16. Ingraham HA, Chen R, Mangalam HJ, Elsholtz HP, Flynn SE, Lin CR, et al. A tissue-specific transcription factor containing a homeodomain specifies a pituitary phenotype. *Cell* (1988) 55(3):519–29. doi: 10.1016/0092-8674(88)90038-4

17. McCormick A, Brady H, Theill LE, Karin M. Regulation of the pituitary-specific homeobox gene Ghf1 by cell-autonomous and environmental cues. *Nature* (1990) 345 (6278):829–32. doi: 10.1038/345829a0

18. Tallent M, Reisine T. Gi alpha 1 selectively couples somatostatin receptors to adenylyl cyclase in pituitary-derived att-20 cells. *Mol Pharmacol* (1992) 41(3):452–5.

19. Bell GI, Reisine T. Molecular biology of somatostatin receptors. *Trends Neurosci* (1993) 16(1):34–8. doi: 10.1016/0166-2236(93)90050-V

20. Struthers RS, Vale WW, Arias C, Sawchenko PE, Montminy MR. Somatotroph hypoplasia and dwarfism in transgenic mice expressing a non-phosphorylatable creb mutant. *Nature* (1991) 350(6319):622–4. doi: 10.1038/350622a0

21. McKenna A, Hanna M, Banks E, Sivachenko A, Cibulskis K, Kernytsky A, et al. The genome analysis toolkit: A mapreduce framework for analyzing next-generation DNA sequencing data. *Genome Res* (2010) 20(9):1297–303. doi: 10.1101/gr.107524.110

22. Seo GH, Kim T, Choi IH, Park J, Lee J, Kim S, et al. Diagnostic yield and clinical utility of whole exome sequencing using an automated variant prioritization system, evidence. *Clin Genet* (2020) 98(6):562–70. doi: 10.1111/cge.13848

23. Wang K, Li M, Hakonarson H. Annovar: Functional annotation of genetic variants from high-throughput sequencing data. *Nucleic Acids Res* (2010) 38(16):e164–e. doi: 10.1093/nar/gkq603

24. Kopanos C, Tsiolkas V, Kouris A, Chapple CE, Aguilera MA, Meyer R, et al. Varsome: The human genomic variant search engine. *Bioinformatics* (2019) 35(11):1978. doi: 10.1093/bioinformatics/bty897

25. Li Q, Wang K. Intervar: Clinical interpretation of genetic variants by the 2015 acmg-amp guidelines. *Am J Hum Genet* (2017) 100(2):267–80. doi: 10.1016/j.ajhg.2017.01.004

26. Untergasser A, Cutcutache I, Koressaar T, Ye J, Faircloth BC, Remm M, et al. Primer3–new capabilities and interfaces. *Nucleic Acids Res* (2012) 40(15):e115–e. doi: 10.1093/nar/gks596

27. Sanger F, Nicklen S, Coulson AR. DNA Sequencing with chain-terminating inhibitors. *Proc Natl Acad Sci* (1977) 74(12):5463–7. doi: 10.1073/pnas.74.12.5463

28. Kent WJ, Sugnet CW, Furey TS, Roskin KM, Pringle TH, Zahler AM, et al. The human genome browser at ucsc. *Genome Res* (2002) 12(6):996–1006. doi: 10.1101/gr.229102

29. Yang J, Zhang Y. I-Tasser server: New development for protein structure and function predictions. *Nucleic Acids Res* (2015) 43(W1):W174–W81. doi: 10.1093/nar/gkv342

30. Bienert S, Waterhouse A, de Beer TA, Tauriello G, Studer G, Bordoli L, et al. The Swiss-model repository–new features and functionality. *Nucleic Acids Res* (2017) 45(D1): D313–D9. doi: 10.1093/nar/gkw1132

31. Kozakov D, Hall DR, Xia B, Porter KA, Padhorny D, Yueh C, et al. The cluspro web server for protein–protein docking. *Nat Protoc* (2017) 12(2):255–78. doi: 10.1038/nprot.2016.169

32. Szklarczyk D, Gable AL, Lyon D, Junge A, Wyder S, Huerta-Cepas J, et al. String V11: Protein–protein association networks with increased coverage, supporting functional discovery in genome-wide experimental datasets. *Nucleic Acids Res* (2019) 47(D1):D607–D13. doi: 10.1093/nar/gky1131

33. Pettersen EF, Goddard TD, Huang CC, Couch GS, Greenblatt DM, Meng EC, et al. Ucsf chimera–a visualization system for exploratory research and analysis. *J Comput Chem* (2004) 25(13):1605–12. doi: 10.1002/jcc.20084

34. Laskowski RA, Swindells MB. "LigPlot+: Multiple Ligand–Protein Interaction Diagrams for Drug Discovery". *J Chem Inform Modeling* (2011) 51(10):2778–86.

35. Pearlman DA, Case DA, Caldwell JW, Ross WS, Cheatham TEIII, DeBolt S, et al. Amber, a package of computer programs for applying molecular mechanics, normal mode analysis, molecular dynamics and free energy calculations to simulate the structural and energetic properties of molecules. *Comput Phys Commun* (1995) 91(1-3):1–41. doi: 10.1016/0010-4655(95)00041-D

36. Roe DR, Cheatham TEIII. Ptraj and cpptraj: Software for processing and analysis of molecular dynamics trajectory data. *J Chem Theory Comput* (2013) 9(7):3084–95. doi: 10.1021/ct400341p

37. Turner P. *Xmgrace, version 5.1. 19* Vol. 2. . Beaverton, OR: Center for Coastal and Land-Margin Research, Oregon Graduate Institute of Science and Technology (2005).

38. Mbarek H, Devadoss Gandhi G, Selvaraj S, Al-Muftah W, Badji R, Al-Sarraj Y, et al. Qatar Genome: Insights on genomics from the middle East. *Hum Mutat* (2022) 43 (4):499–510. doi: 10.1002/humu.24336

39. Al Kuwari H, Al Thani A, Al Marri A, Al Kaabi A, Abderrahim H, Afifi N, et al. The Qatar biobank: Background and methods. *BMC Public Health* (2015) 15(1):1–9. doi: 10.1186/s12889-015-2522-7

40. Fakhro KA, Staudt MR, Ramstetter MD, Robay A, Malek JA, Badii R, et al. The Qatar genome: A population-specific tool for precision medicine in the middle East. *Hum Genome Variation* (2016) 3(1):1–7. doi: 10.1038/hgv.2016.16

41. Hernández LM, Lee PD, Camacho-Hübner C. Isolated growth hormone deficiency. *Pituitary* (2007) 10(4):351–7. doi: 10.1007/s11102-007-0073-3

42. Corazzini V, Salvatori R. Molecular and clinical aspects of ghrh receptor mutations. *Hormone Resistance Hypersensitivity* (2013) 24:106–17. doi: 10.1159/000342575

43. Soneda A, Adachi M, Muroya K, Asakura Y, Takagi M, Hasegawa T, et al. Novel compound heterozygous mutations of the growth hormone-releasing hormone receptor gene in a case of isolated growth hormone deficiency. *Growth Hormone IGF Res* (2013) 23(4):89–97. doi: 10.1016/j.ghir.2013.03.003

44. Shohreh R, Sherafat-Kazemzadeh R, Jee YH, Blitz A, Salvatori R. A novel frame shift mutation in the ghrh receptor gene in familial isolated gh deficiency: Early occurrence of anterior pituitary hypoplasia. *J Clin Endocrinol Metab* (2011) 96(10):2982–6. doi: 10.1210/jc.2011-1031

45. Salvatori R, Fan X, Mullis PE, Haile A, Levine MA. Decreased expression of the ghrh receptor gene due to a mutation in a pit-1 binding site. *Mol Endocrinol* (2002) 16(3):450–8. doi: 10.1210/mend.16.3.0785

46. Inoue H, Kangawa N, Kinouchi A, Sakamoto Y, Kimura C, Horikawa R, et al. Identification and functional analysis of novel human growth hormone–releasing hormone receptor (Ghrhr) gene mutations in Japanese subjects with short stature. *Clin Endocrinol* (2011) 74(2):223–33. doi: 10.1111/j.1365-2265.2010.03911.x

47. Gregory LC, Alatzoglou KS, McCabe MJ, Hindmarsh PC, Saldanha JW, Romano N, et al. Partial loss of function of the ghrh receptor leads to mild growth hormone deficiency. *J Clin Endocrinol Metab* (2016) 101(10):3608–15. doi: 10.1210/jc.2016-2254

48. Cohen E, Belkacem S, Fedala S, Collot N, Khallouf E, Dastot F, et al. Contribution of functionally assessed ghrhr mutations to idiopathic isolated growth hormone deficiency in patients without Gh1 mutations. *Hum Mutat* (2019) 40(11):2033–43. doi: 10.1002/humu.23847

49. Lessi M, Giordano M, Paracchini R, Petri A, Federico G, Wasniewska M, et al. Molecular analysis of the growth hormone releasing hormone receptor (Ghrh-r) gene in isolated growth hormone deficiency: Identification of a likely etiological mutation in the signal peptide. *Int J Disability Hum Dev* (2001) 2(4):215–28. doi: 10.1515/IJDHD.2001.2.4.215

50. Galli-Tsinopoulou A, Kotanidou EP, Kleisarchaki AN, Kauli R, Laron Z. A novel variant c. 97c> T of the growth hormone releasing hormone receptor gene causes isolated growth hormone deficiency type ib. *J Clin Res Pediatr Endocrinol* (2018) 10(3):284.

51. Kale S, Gada JV, Jadhav S, Lila AR, Sarathi V, Budyal S, et al. Genetic spectrum and predictors of mutations in four known genes in Asian Indian patients with growth hormone deficiency and orthotopic posterior pituitary: An emphasis on regional genetic diversity. *Pituitary* (2020) 23(6):701–15. doi: 10.1007/s11102-020-01078-4

52. Adams EF, Symowski H, Buchfelder M, Poyner DR. A polymorphism in the growth hormone (Gh)-releasing hormone (Ghrh) receptor gene is associated with elevated response to ghrh by human pituitary somatotrophinomas in vitro. *Biochem Biophys Res Commun* (2000) 275(1):33–6. doi: 10.1006/bbrc.2000.3247

53. Demirbilek H, Tahir S, Baran RT, Sherif M, Shah P, Ozbek MN, et al. Familial isolated growth hormone deficiency due to a novel homozygous missense mutation in the growth hormone releasing hormone receptor gene: Clinical presentation with hypoglycemia. *J Clin Endocrinol Metab* (2014) 99(12):E2730–E4. doi: 10.1210/jc.2014-2696

54. Sundralingam T, Tennekoon KH, de Silva S, De Silva S, Hewage AS. Pathogenic and likely pathogenic genetic alterations and polymorphisms in growth hormone gene (Gh1) and growth hormone releasing hormone receptor gene (Ghrhr) in a cohort of isolated growth hormone deficient (Ighd) children in Sri Lanka. *Growth Horm IGF Res* (2017) 36:22–9. doi: 10.1016/j.ghir.2017.08.006

55. Wajnrajch MP, Gertner JM, Harbison MD, Chua SC, Leibel RL. Nonsense mutation in the human growth hormone-releasing hormone receptor causes growth failure analogous to the little (Lit) mouse. *Nat Genet* (1996) 12(1):88–90. doi: 10.1038/ng0196-88

56. Netchine I, Talon P, Dastot F, Vitaux F, Goossens M, Amselem S. Extensive phenotypic analysis of a family with growth hormone (Gh) deficiency caused by a mutation in the gh-releasing hormone receptor gene. *J Clin Endocrinol Metab* (1998) 83(2):432–6.

57. Alatzoglou KS, Turton JP, Kelberman D, Clayton PE, Mehta A, Buchanan C, et al. Expanding the spectrum of mutations in Gh1 and ghrhr: Genetic screening in a Large cohort of patients with congenital isolated growth hormone deficiency. *J Clin Endocrinol Metab* (2009) 94(9):3191–9. doi: 10.1210/jc.2008-2783

58. Cho SY, Ki C-S, Park H-D, Kim S, Sohn YB, Maeng S, et al. Genetic investigation of patients with undetectable peaks of growth hormone after two provocation tests. *Clin Endocrinol* (2012) 78:316–20. doi: 10.1111/j.1365-2265.2012.04514.x

59. Blum WF, Klammt J, Amselem S, Pfäffle HM, Legendre M, Sobrier M-L, et al. Screening a Large pediatric cohort with gh deficiency for mutations in genes regulating pituitary development and gh secretion: Frequencies, phenotypes and growth outcomes. *EBioMedicine* (2018) 36:390–400. doi: 10.1016/j.ebiom.2018.09.026

60. Arman A, Dündar BN, Çetinkaya E, Erzaim N, Büyükgebiz A. Novel growth hormone-releasing hormone receptor gene mutations in Turkish children with isolated growth hormone deficiency. *J Clin Res Pediatr Endocrinol* (2014) 6(4):202. doi: 10.4274/jcrpe.1518

61. Salvatori R, Fan X, Phillips JAIII, Espigares-Martin R, Martin de Lara I, Freeman KL, et al. Three new mutations in the gene for the growth hormone (Gh)-releasing hormone receptor in familial isolated gh deficiency type ib. *J Clin Endocrinol Metab* (2001) 86(1):273–9.

62. Abouelhoda M, Sobahy T, El-Kalioby M, Patel N, Shamseldin H, Monies D, et al. Clinical genomics can facilitate countrywide estimation of autosomal recessive disease burden. *Genet Med* (2016) 18(12):1244–9. doi: 10.1038/gim.2016.37

63. Carakushansky M, Whatmore AJ, Clayton PE, Shalet SM, Gleeson HK, Price DA, et al. A new missense mutation in the growth hormone-releasing hormone receptor gene in familial isolated gh deficiency. *Eur J Endocrinol* (2003) 148(1):25–30. doi: 10.1530/eje.0.1480025

64. Hattori A, Katoh-Fukui Y, Nakamura A, Matsubara K, Kamimaki T, Tanaka H, et al. Next generation sequencing-based mutation screening of 86 patients with idiopathic short stature. *Endocrine J* (2017) 64(10):947–54. doi: 10.1507/endocrj.EJ17-0150

65. Yu C, Xie B, Zhao Z, Zhao S, Liu L, Cheng X, et al. Whole exome sequencing uncovered the genetic architecture of growth hormone deficiency patients. *Front Endocrinol* (2021) 12:711991. doi: 10.3389/fendo.2021.711991

66. Birla S, Khadgawat R, Jyotsna VP, Jain V, Garg M, Bhalla AS, et al. Identification of novel ghrhr and Gh1 mutations in patients with isolated growth hormone deficiency. *Growth Hormone IGF Res* (2016) 29:50–6. doi: 10.1016/j.ghir.2016.04.001

67. Haskin O, Lazar L, Jaber L, Salvatori R, Alba M, Kornreich L, et al. A new mutation in the growth hormone-releasing hormone receptor gene in two Israeli Arab families. *J Endocrinological Invest* (2006) 29(2):122–30. doi: 10.1007/BF03344084

68. Wong M-L, Dong C, Andreev V, Arcos-Burgos M, Licinio J. Prediction of susceptibility to major depression by a model of interactions of multiple functional genetic variants and environmental factors. *Mol Psychiatry* (2012) 17(6):624–33. doi: 10.1038/mp.2012.13

69. Salvatori R, Hayashida C, Aguiar-Oliveira MH, Phillips JAIII, Souza AH, Gondo R, et al. Familial dwarfism due to a novel mutation of the growth hormone-releasing hormone receptor gene. *J Clin Endocrinol Metab* (1999) 84(3):917–23. doi: 10.1210/jc.84.3.917

70. Hilal L, Hajaji Y, Vie-Luton M-P, Ajaltouni Z, Benazzouz B, Chana M, et al. Unusual phenotypic features in a patient with a novel splice mutation in the ghrhr gene. *Mol Med* (2008) 14(5):286–92. doi: 10.2119/2007-00128.Hilal

71. Roelfsema F, Biermasz NR, Veldman RG, Veldhuis JD, Froülich M, Stokvis-Brantsma W, et al. Growth hormone (Gh) secretion in patients with an inactivating defect of the gh-releasing hormone (Ghrh) receptor is pulsatile: Evidence for a role for non-ghrh inputs into the generation of gh pulses. *J Clin Endocrinol Metab* (2001) 86(6):2459–64. doi: 10.1210/jcem.86.6.7536

72. Marui S, Trarbach EB, Boguszewski MC, França MM, Jorge AA, Inoue H, et al. Gh-releasing hormone receptor gene: A novel splice-disrupting mutation and study of founder effects. *Hormone Res Paediatrics* (2012) 78(3):165–72. doi: 10.1159/000342760

73. Wang Q, Diao Y, Xu Z, Li X, Luo XP, Xu H, et al. Identification of a novel splicing mutation in the growth hormone (Gh)-releasing hormone receptor gene in a Chinese family with pituitary dwarfism. *Mol Cell Endocrinol* (2009) 313(1-2):50–6. doi: 10.1016/j.mce.2009.08.021

74. Alba M, Hall CM, Whatmore AJ, Clayton PE, Price DA, Salvatori R. Variability in anterior pituitary size within members of a family with gh deficiency due to a new splice mutation in the ghrh receptor gene. *Clin Endocrinol* (2004) 60(4):470–5. doi: 10.1111/j.1365-2265.2004.02003.x

75. Horikawa R. Isolated gh deficiency due to inactivating mutation of ghrh receptor. *Nihon Rinsho Japanese J Clin Med* (2002) 60(2):297–305.

76. Kale S, Budyal S, Kasaliwal R, Shivane V, Raghavan V, Lila A, et al. A novel gross indel in the growth hormone releasing hormone receptor gene of Indian ighd patients. *Growth Hormone IGF Res* (2014) 24(6):227–32. doi: 10.1016/j.ghir.2014.07.003

77. Sundralingam T, Tennekoon KH, de Silva S, De Silva S, Hewage S, Ranasinghe R. Novel gross deletion at the ghrhr gene locus possibly mediated by alu specific microhomology identified in a Sri Lankan patient with isolated growth hormone deficiency. *Growth Hormone IGF Res* (2018) 42:94–101. doi: 10.1016/j.ghir.2018.10.005

78. Nakaguma M, Correa FA, Santana LS, Benedetti AF, Perez RV, Huayllas MK, et al. Genetic diagnosis of congenital hypopituitarism by a target gene panel: Novel pathogenic variants in Gli2, Otx2 and ghrhr. *Endocrine Connections* (2019) 8(5):590–5. doi: 10.1530/EC-19-0085

79. DeAlmeida VI, Mayo KE. Identification of binding domains of the growth hormone-releasing hormone receptor by analysis of mutant and chimeric receptor proteins. *Mol Endocrinol* (1998) 12(5):750–65. doi: 10.1210/mend.12.5.0102

80. Pereira RM, Aguiar-Oliveira MH, Sagazio A, Oliveira CR, Oliveira FT, Campos VC, et al. Heterozygosity for a mutation in the growth hormone-releasing hormone receptor gene does not influence adult stature, but affects body composition. *J Clin Endocrinol Metab* (2007) 92(6):2353–7. doi: 10.1210/jc.2007-0092

81. Wajnrajch MP, Gertner JM, Sokoloff AS, Ten I, Harbison MD, Netchine I, et al. Haplotype analysis of the growth hormone releasing hormone receptor locus in three apparently unrelated kindreds from the Indian subcontinent with the identical mutation in the ghrh receptor. *Am J Med Genet Part A* (2003) 120(1):77–83. doi: 10.1002/ajmg.a.10209

frontiers | Frontiers in Endocrinology

TYPE Original Research
PUBLISHED 14 April 2023
DOI 10.3389/fendo.2023.1170461

OPEN ACCESS

EDITED BY
Clemens Fürnsinn,
Medical University of Vienna, Austria

REVIEWED BY
David Hill,
Lawson Health Research Institute, Canada
Ewa Gurgul-Convey,
Hannover Medical School, Germany

*CORRESPONDENCE
Feyza Engin
fengin@wisc.edu

†These authors have contributed equally to this work

SPECIALTY SECTION
This article was submitted to Diabetes: Molecular Mechanisms, a section of the journal Frontiers in Endocrinology

RECEIVED 20 February 2023
ACCEPTED 31 March 2023
PUBLISHED 14 April 2023

CITATION
Hurley LD, Lee H, Wade G, Simcox J and Engin F (2023) *Ormdl3* regulation of specific ceramides is dispensable for mouse β-cell function and glucose homeostasis under obesogenic conditions. *Front. Endocrinol.* 14:1170461. doi: 10.3389/fendo.2023.1170461

Ormdl3 regulation of specific ceramides is dispensable for mouse β-cell function and glucose homeostasis under obesogenic conditions

Liam D. Hurley[1†], Hugo Lee[1†], Gina Wade[2], Judith Simcox[2] and Feyza Engin[1,3,4*]

[1]Department of Biomolecular Chemistry, School of Medicine and Public Health, University of Wisconsin-Madison, Madison, WI, United States, [2]Department of Biochemistry, College of Agricultural and Life Sciences, University of Wisconsin-Madison, Madison, WI, United States, [3]Division of Endocrinology, Diabetes & Metabolism, Department of Medicine, School of Medicine and Public Health, University of Wisconsin-Madison, Madison, WI, United States, [4]Department of Cell and Regenerative Biology, School of Medicine and Public Health, University of Wisconsin-Madison, Madison, WI, United States

Chronic elevation of sphingolipids contributes to β-cell failure. ORMDL3 has been identified as a key regulator of sphingolipid homeostasis, however, its function in pancreatic β-cell pathophysiology remains unclear. Here, we generated a mouse model lacking *Ormdl3* within pancreatic β-cells (*Ormdl3*$^{\beta-/-}$). We show that loss of β-cell *Ormdl3* does not alter glucose tolerance, insulin sensitivity, insulin secretion, islet morphology, or cellular ceramide levels on standard chow diet. When challenged with a high fat diet, while *Ormdl3*$^{\beta-/-}$ mice did not exhibit any alteration in metabolic parameters or islet architecture, lipidomics analysis revealed significantly higher levels of very long chain ceramides in their islets. Taken together, our results reveal that loss of *Ormdl3* alone is not sufficient to impinge upon β-cell function or whole-body glucose and insulin homeostasis, however, β-cell-specific loss of *Ormdl3* does significantly alter levels of specific sphingolipid species in islets upon high fat feeding.

KEYWORDS

islet, knockout mouse, lipid, lipidomics, high fat diet, Ormdl3, beta cell

1 Introduction

In obesity, chronically elevated levels of circulating free fatty acids contribute to the *de novo* production of cellular lipids, including sphingolipids. Left unchecked, elevated sphingolipid production can lead to the accumulation of sphingolipid species such as ceramide within the cell (1, 2). In pancreatic β-cells, obesity-directed sphingolipid

accumulation contributes to β-cell dysfunction through induction of apoptotic, inflammatory, and cellular stress (1, 3, 4).

Orosomucoid-like proteins (ORMDLs) are an ER-resident protein family that inhibits serine palmitoyltransferase (SPT), the rate limiting enzyme in *de novo* sphingolipid biosynthesis (5–7). ORMDL3 is one of three isoforms of this protein family, and genome-wide association studies (GWAS) have identified *Ormdl3* as an obesity-related gene whose expression negatively correlates with body mass index (8). While this suggests that ORMDL3 plays a role in obesity, the role of ORMDL3 in β-cell physiology and pathology remains unknown.

In the current study, we designed a β-cell-specific *Ormdl3* knockout mouse and investigated the consequences of its loss of function under non-stressed (chow or low fat diet) and high fat diet (HFD) challenged conditions. Our results showed that *Ormdl3* is dispensable for β-cell function regardless of diet. Indeed, β-cell loss of *Ormdl3* did not alter fasting blood glucose, body weight, islet morphology, glucose tolerance, insulin sensitivity, or insulin secretion. Lipidomics of isolated islets identified significantly elevated levels of very long chain ceramides in HFD challenged knockout animals. Taken together, our results suggest that *Ormdl3* is not required for β-cell function and survival under physiological or surplus nutrition conditions.

2 Results

2.1 Chow-fed *Ormdl3*$^{\beta-/-}$ mice do not exhibit altered β-cell function or glucose homeostasis

To examine the function of ORMDL3 in β-cells, we generated β-cell specific *Ormdl3* knockout mice (KO; *Ormdl3*$^{\beta-/-}$) by mating mice harboring floxed (exons 2-4) *Ormdl3* (*Ormdl*$^{fl/fl}$) with mice expressing Cre recombinase under the control of the *Ins1* promotor (Ins1tm1.1 Cre) (9). To determine the efficiency of deletion, we performed qPCR analysis in pancreatic islets isolated from 7-week-old *Ormdl3*$^{\beta-/-}$ mice and found approximately 80% reduction in *Ormdl3* mRNA levels (Figure 1A). We also investigated the expression of *Ormdl1* and *Ormdl2* in these islets and found no significant differences in gene expression level relative to wild type (Wt) mice, suggesting that the deletion of *Ormdl3* in β-cells did not trigger compensation by either *Ormd1* or *Ormdl2* at the mRNA level (Figure 1A).

Next, we monitored chow-fed male and female Wt, *Ormdl3*$^{fl/fl}$, and Cre mice (as control conditions) as well as *Ormdl*$^{\beta+/-}$ (β-cell *Ormdl3* heterozygous knockout; Het), and KO mice starting from 5 weeks of age for 27 weeks (Figure 1B). During this 27-week period, we measured fasting blood glucose and body weights weekly. We observed a trend towards elevation of blood glucose levels only in male KO mice when compared to Cre control mice (Figures 1C, D) while body weight remained comparable between knockout and Cre control mice (Figures 1E, F).

To determine if *Ormdl3* ablation would result in impairment of β-cell insulin secretion, we performed fast-refeed experiments in male mice at 12 weeks of age and analyzed serum C-peptide and proinsulin levels (Figure 1G). Knockout mice did not exhibit altered levels of C-peptide in the *ad libitum* basal condition, after six hours of fasting, or during the refeed condition. Proinsulin levels were also unchanged during the refeed condition (Figure 1H). The ratio of proinsulin to C-peptide during the refeed condition (Figure 1I) was unaffected. Taken together, these data suggest that loss of *Ormdl3* in β-cells does not significantly alter insulin secretion.

Next, we examined if the loss of β-cell *Ormdl3* would result in aberrant glucose homeostasis. We performed glucose and insulin tolerance tests in both male and female mice. Our results showed that there were no significant alterations in glucose tolerance in male and female mice at 13 (Figures 1J-M) or 31 weeks of age (Figures 1N-Q). We also measured insulin tolerance in 31-week-old male (Figures 1R, S) and female mice (Figures 1T, U) and found no change in insulin sensitivity between KO mice and controls (Wt, Het, and Cre). These results suggest that *Ormdl3* deletion in β-cells does not impair whole-body insulin sensitivity or glucose metabolism.

To determine the impact of loss of *Ormdl3* on islet morphology and composition, we stained pancreatic sections from male 34-week-old KO, het, and control (Wt and Cre) mice either with hematoxylin and eosin (H&E) or co-stained sections with insulin and glucagon. Our analysis did not reveal any changes in gross morphology with H&E staining (Figure 1V), alterations in islet architecture, or α:β cell ratio in *Ormdl3*-deficient mice (Figures 1W, X). Lastly, we examined β-cell mass in insulin-stained sections and did not find a significant change in KO mice as compared to control (Figure 1Y). Collectively, our data suggest that under chow-fed conditions, *Ormdl3* deletion is dispensable for β-cell function and glucose homeostasis.

2.2 High fat diet feeding in *Ormdl3*$^{\beta-/-}$ mice does not impact β-cell function or glucose homeostasis

Our initial results revealed that deletion of *Ormdl3* in the β-cells of mice fed chow diet did not contribute to β-cell dysfunction or impair glucose homeostasis. The ORMDL proteins are known to inhibit serine palmitoyltransferase, the enzyme responsible for the condensation of palmitoyl-CoA and serine into 3-ketosphinganine (10). Since this condensation reaction requires palmitic acid-derived palmitoyl-CoA, we reasoned that low levels of palmitic acid present in chow diet may not lead to sufficient accumulation of sphingolipids underlying β-cell dysfunction. Therefore, we decided to nutritionally challenge these mice with HFD, a model of diet induced obesity. To this end, we placed male mice on HFD or control low fat diet (LFD) starting at 6 weeks of age for 24 weeks (Figure 2A) and measured fasting blood glucose levels and body weights weekly. We did not observe any significant changes in fasting blood glucose levels in the LFD-fed Wt, Het, Cre, or KO animals (Figure 2B). When challenged with a HFD, there were also no changes observed in fasting blood glucose levels (Figure 2C). Additionally, besides the expected weight gain resulting from high fat diet, there was no significant difference in body weights (Figure 2D) or food consumption (Figures 2E, F) between Wt, Het, Cre, or KO mice on either diet.

10.3389/fendo.2023.1170461

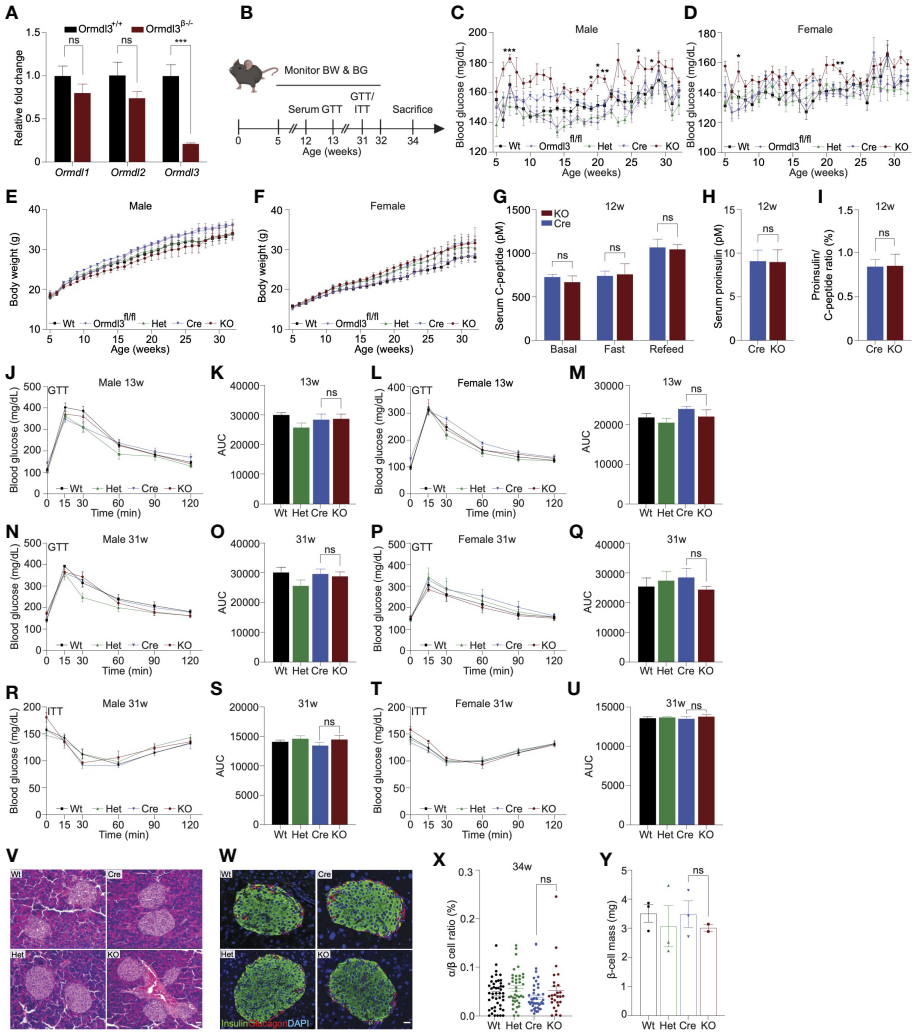

FIGURE 1
Chow-fed *Ormdl3*$^{\beta-/-}$ mice do not exhibit altered β-cell function or glucose homeostasis. **(A)** Fold change gene expression of *Ormdl* isoforms in isolated islets of 7-week-old wild-type (Wt) and knockout (KO; *Ormdl3*$^{\beta-/-}$) mice (n=3/group; Student's t-test). **(B)** Schematic representation of mouse monitoring. **(C)** Weekly blood glucose measurements in Wt, *Ormdl3*$^{fl/fl}$, Cre, Heterozygous (Het; *Ormdl*$^{\beta+/-}$), and KO male (n=5-8/group) and **(D)** female (n=7-8/group) mice (Two-way ANOVA with Tukey's *post-hoc* test; stars indicate significant differences between Cre and KO groups). **(E)** Weekly body weight measurements in Wt, *Ormdl3*$^{fl/fl}$, Cre, Het, and KO male (n=5-8/group) and **(F)** female (n=7-8/group) mice (Two-way ANOVA with Tukey's *post-hoc* test). **(G-I)** ELISAs on serum samples from 12-week-old Cre and KO mice (Student's t-test). **(G)** ELISA for C-peptide before/after a 6 hour fast and after 1 hour refeeding (n=5-6/group). **(H)** ELISA for proinsulin after 1 hour refeeding (n=5-6/group). **(I)** Ratio of proinsulin/C-peptide after 1 hour refeeding (n=5-6/group). **(J-Q)** Glucose tolerance and area under the curve (AUC) calculations for male and female Wt, Het, CO, and KO mice. **(J)** Glucose tolerance and **(K)** total area under the curve (AUC) of 13-week-old male mice (n=5-6/group; Two- and one-way ANOVA with Tukey's *post-hoc* test, respectively). **(L)** Glucose tolerance and **(M)** total AUC of 13-week-old female mice (n=5-6/group; Two- and one-way ANOVA with Tukey's *post-hoc* test, respectively). **(N)** Glucose tolerance and **(O)** total AUC of 31-week-old male mice (n=5-6/group; Two- and one-way ANOVA with Tukey's *post-hoc* test, respectively). **(P)** Glucose tolerance and **(Q)** total AUC of 31-week-old female mice (n=4/group; Two- and one-way ANOVA with Tukey's *post-hoc* test, respectively). **(R-U)** Insulin tolerance and AUC calculations for 31-week-old male and female Wt, Het, Cre, and KO mice **(R)** Insulin tolerance and **(S)** total AUC of male mice (n=5-6/group; Two- and one-way ANOVA with Tukey's *post-hoc* test, respectively). **(T)** Insulin tolerance and **(U)** total AUC of female (n=4/group; Two- and one-way ANOVA with Tukey's *post-hoc* test, respectively). **(V)** Representative images of hematoxylin and eosin staining of 34-week-old male Wt, Cre, Het, and KO mice. **(W)** Co-staining for insulin and glucagon in pancreatic sections from 34-week-old male Wt, Cre, Het, and KO mice. **(X)** Ratio of α:β cells in co-stained insulin and glucagon sections (n=3/group; One-way ANOVA with Tukey's *post-hoc* test). **(Y)** β-cell mass in insulin-stained sections (n=2-3/group; One-way ANOVA with Tukey's *post-hoc* test). Data are presented as means ± SEM. One- and two-way ANOVA with Tukey's *post-hoc* test (*p<0.05, **p<0.01, ***p<0.001, ****p<0.0001) and Student's t-test (***p<.001) are applied where indicated. BW, body weight; BG, blood glucose; GTT, glucose tolerance test; ITT, insulin tolerance test; Wt, wild type; Ormdl3$^{fl/fl}$, Ormdl3 floxed mouse not expressing cre recombinase; Het, Ormdl3$^{\beta+/-}$ heterozygous knockout; Cre, mouse expressing Ins1$^{tm1.1(cre)Thor/J}$ with wild type Ormdl3 alleles; KO, Ormdl3$^{\beta-/-}$ homozygous knockout; AUC, area under the curve; DAPI, 4′,6-diamidino-2-phenylindole; w, weeks; ns, not significant; ANOVA, analysis of variance. Scale bars are 20 μm.

We next examined glucose and insulin tolerance throughout the course of the study. Our results indicated that KO mice did not display any significant difference in glucose tolerance compared to Cre mice following 6 (Figures 2G-J) or 24 weeks of LFD or HFD feeding (Figures 2K-N). In addition, we did not observe any significant effects of *Ormdl3* deletion on insulin tolerance following 11 (Figures 2O-R) and 23 weeks of LFD or HFD feeding (Figures 2S-V).

10.3389/fendo.2023.1170461

To investigate islet morphology, we performed H&E staining of pancreatic sections on LFD and HFD-fed control (Cre) and knockout mice that had been on diet for 24 weeks (Figure 2W). Further, insulin and glucagon immunofluorescence co-staining showed no significant alterations in islet morphology or composition between HFD- or LFD-fed Cre and KO mice (Figure 2X).

Next, we asked whether loss of *Ormdl3* would result in changes to lean and fat mass using Dual-energy X-ray absorptiometry (DEXA) assessment of Cre and KO mice. Following 24 weeks of LFD or HFD feeding, there were no significant changes in lean or fat mass in mice on either diet (Figures 2Y, Z). Taken together, our results suggest that *Ormdl3* deletion does not impinge upon β-cell function and is dispensable for glucose and insulin homeostasis even under obesogenic conditions.

2.3 Lipidomics analysis reveals significant upregulation of very long chain ceramide species in islets of high fat diet-fed *Ormdl3*$^{\beta-/-}$ mice

Given the inhibitory role of ORMDL proteins in SPT-mediated sphingolipid catabolism (Figure 3A), we hypothesized that the levels of sphingolipid species downstream of SPT could be altered. To test this, we performed targeted lipidomic analysis (Figure 3A; stars indicate species measured) in isolated islets of chow-fed, LFD-fed, and HFD-fed Cre and *Ormdl3*$^{\beta-/-}$ mice. We first examined fold change between 10-week-old chow-fed *Ormdl3*$^{\beta-/-}$ and Cre mice, but we did not observe any significantly upregulated or downregulated ceramides species between groups (Figure 3B). We next analyzed the levels of ceramides from LFD-fed or HFD-challenged *Ormdl3*$^{\beta-/-}$ mice after 24 weeks of feeding. Initial fold change comparison between LFD-fed *Ormdl3*$^{\beta-/-}$ and Cre mice revealed upregulation and downregulation of d18:1/24:1 and d18:2/24:0 ceramides, respectively (Figure 3C). However, fold change comparison between HFD counterparts revealed striking upregulation of islet long chain ceramide species d18:1/16:0 as well as very long chain ceramide species d18:1/24:1, d18:1/24:0, d18:1/22:0, d18:0/24:0, m18:1/22:0, and d18:1/26:1 as compared to Cre control mice (Figure 3D). There were no significant differences between total very long chain ceramide species (C22-26) in chow-fed (Figure 3E) and LFD-fed (Figure 3F) KO mice as compared to control. Interestingly, levels of total very long chain ceramides species were increased in HFD-fed KO mice compared to Cre mice (Figure 3G). Furthermore, analysis of individual sphingolipid species confirms these changes are indeed observed between HFD-fed *Ormdl3*$^{\beta-/-}$ mice as compared to Cre control mice (Figures 3H-N). Taken together, our results suggest that while loss of β-cell *Ormdl3* alone does not impinge upon systemic metabolism or β-cell function in nutritionally unstressed conditions, deletion of *Ormdl3* results in a significant increase in very long chain ceramide species in obesity.

3 Discussion

ORMDL3 has been implicated in a variety of disorders including asthma, inflammatory bowel disease, and obesity (8, 11–13). Recently, it was reported that a whole-body knockout of *Ormdl3* when challenged with cold exposure or HFD exhibit impaired regulation of brown adipose tissue thermogenesis, white adipose tissue browning, and insulin resistance (14). Yet the contribution of β-cells to this phenotype remained unknown. We previously showed that islets from overweight/obese human donors displayed significant downregulation of *ORMDL3* expression compared with islets from lean donors (15). In contrast, *Ormdl3* was substantially upregulated in the islets of leptin-deficient obese (*ob/ob*) mice compared with lean mice (15). *Ormdl3* knockdown in a murine β-cell line induced expression of pro-apoptotic markers suggesting a role for *Ormdl3* in β-cell apoptosis (15). In this study, we found that genetic ablation of *Ormdl3* did not affect glucose metabolism, insulin sensitivity, insulin secretion, or islet architecture. However, despite seemingly unaltered β-cell health and function, targeted lipidomic determination of ceramide levels revealed increases in very long chain ceramides (C22-C26) and long chain C16 ceramide when *Ormdl3*$^{\beta-/-}$ mice were fed HFD. While our results suggest that β-cell expression of *Ormdl3* is dispensable for normal islet function and glycemic control, they also suggest that ORMDL3 regulates sphingolipid levels in the β-cell.

Ormdl3 ablation has generated conflicting reports on SPT regulation and sphingolipid metabolism (16, 17). For instance, sphingolipid levels were found to be unchanged in transgenic *Ormdl3* overexpression and whole-body *Ormdl3* KO mice, and this observation was recapitulated in HEK cells (17). However, many studies report some effect of *Ormdl3* overexpression or deletion on systemic sphingolipid levels with minor changes to rodent health measures (14, 18, 19). For example, while absence of *Ormdl3* has been associated with increased levels of sphingolipids within the brain, *Ormdl3* knockout mice appeared metabolically healthy and similar to control mice (19). Our results are in line with these reports demonstrating increased ceramide levels following *Ormdl3* ablation.

Our findings revealed that β-cell loss of *Ormdl3* during obesity leads to increased generation of islet very long chain ceramide species, hinting at a potential regulatory axis in which ORMDL3 contributes to control of this sphingolipid class. In mammals, CERS2 catalyzes the N-acylation of the sphingoid base with very long chain fatty acyl-CoAs during *de novo* sphingolipid production to produce very long chain ceramides species (C22-26) (20, 21). Additionally, reports suggest that the ratio of very long chain:long chain ceramides is important for proper cellular function (20, 22). For instance, in BALB/c primary mouse hepatocytes overexpressing *Cers2*, the ratio of very long chain:long chain ceramides was increased, but despite the increase in overall ceramide abundance, insulin signal transduction was improved while markers of ER stress and gluconeogenesis were reduced (22). In addition, a recent report proposes an obesity-independent CERS2-dependent lipid

10.3389/fendo.2023.1170461

signature of imbalanced very long chain:long chain ceramides as contributing to β-cell failure through impaired proinsulin processing (23). Our findings suggest that very long chain ceramide species may be neither beneficial nor deleterious within the β-cell. However, future work including feeding with a ketogenic diet containing a higher fat content could be performed to determine the optimal abundance and ratio of very long acyl chain-containing lipids for normal β-cell health. Additionally,

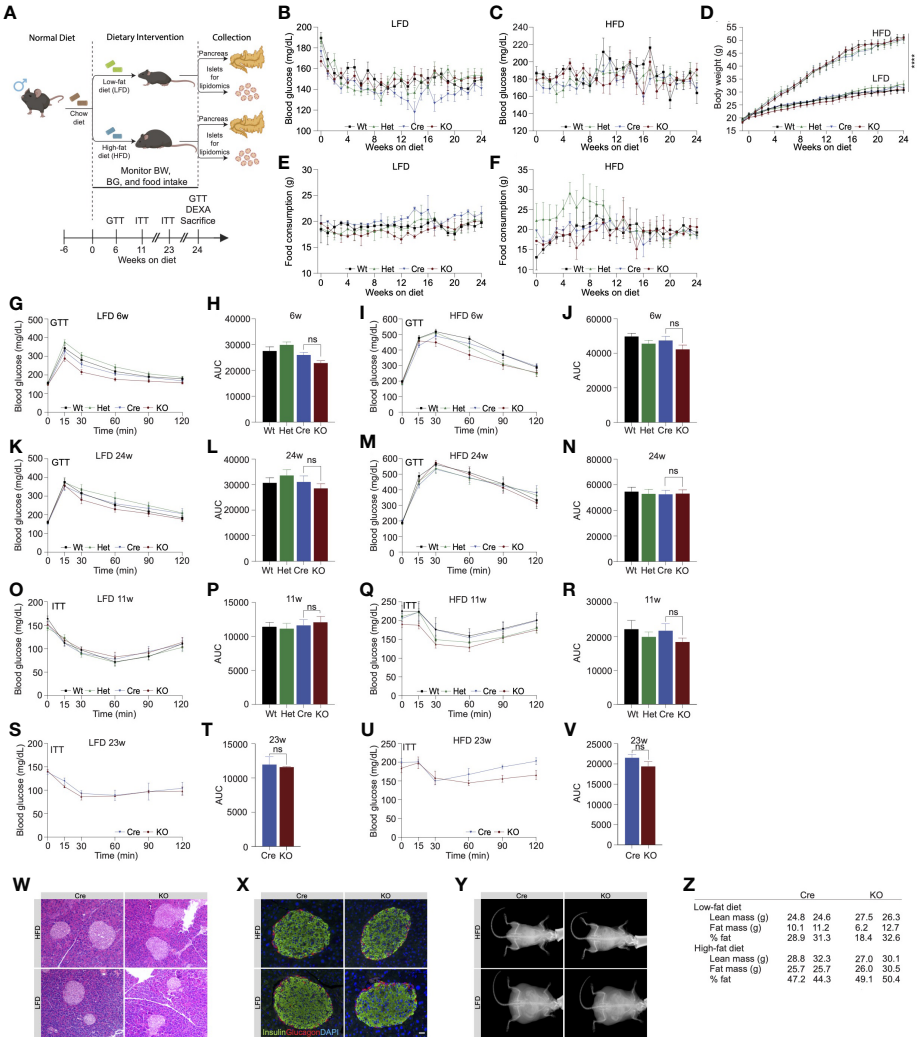

FIGURE 2
High fat diet feeding in *Ormdl3*$^{\beta-/-}$ mice does not impact β-cell function or glucose homeostasis. **(A)** Schematic representation of mouse monitoring and study design. **(B)** Weekly fasting blood glucose assessment of Wt, Het, Cre, and KO mice under LFD and **(C)** HFD conditions (n=9/group; two-way ANOVA with Tukey's *post-hoc* test). **(D)** Weekly body weight measurements in LFD and HFD-fed Wt, Het, Cre, and KO mice (n=9/group; Two-way ANOVA with Tukey's *post-hoc* test). **(E)** Weekly food consumption in Wt, Het, Cre, and KO LFD and **(F)** HFD-fed mice (grams of food eaten/mouse/week; Two-way ANOVA with Tukey's *post-hoc* test). **(G-N)** Glucose tolerance and area under the curve (AUC) calculations for LFD and HFD-fed male Wt, Het, Cre, and KO mice. **(G)** Glucose tolerance and **(H)** total AUC of 6-weeks-on-diet LFD-fed mice (n=9/group; Two- and one-way ANOVA with Tukey's *post-hoc* test, respectively). **(I)** Glucose tolerance and **(J)** total AUC of 6-weeks-on-diet HFD-fed mice (n=9/group; Two- and one-way ANOVA with Tukey's *post-hoc* test, respectively). **(K)** Glucose tolerance and **(L)** total AUC of 24-weeks-on-diet LFD-fed mice (n=9/group; Two- and one-way ANOVA with Tukey's *post-hoc* test, respectively). **(M)** Glucose tolerance and **(N)** total AUC of 24-weeks-on-diet HFD-fed mice (n=9/group; Two- and one-way ANOVA with Tukey's *post-hoc* test, respectively). **(O-V)** Insulin tolerance and AUC calculations for LFD and HFD-fed male Wt, Het, Cre, and KO mice. **(O)** Insulin tolerance and **(P)** total AUC of 11-weeks-on-diet LFD-fed mice (n=9/group; Two- and one-way ANOVA with Tukey's *post-hoc* test, respectively). **(Q)** Insulin tolerance and **(R)** total AUC of 11-weeks-on-diet HFD-fed mice (n=9/group; Two- and one-way ANOVA with Tukey's *post-hoc* test, respectively). **(S)** Insulin tolerance and **(T)** total AUC of 23-weeks-on-diet LFD-fed mice (n=9/group; Two- and one-way ANOVA with Tukey's *post-hoc* test, respectively). **(U)** Insulin tolerance and **(V)** total AUC of 23-weeks-on-diet HFD-fed mice (n=9/group; Two- and one-way ANOVA with Tukey's *post-hoc* test, respectively). **(W)** Representative images of H&E staining of 24-weeks-on-diet male LFD and HFD-fed Cre and KO mice. **(X)** Representative images from co-staining for insulin and glucagon in pancreatic sections from 24-weeks-on-diet LFD and HFD-fed male Cre and KO mice. **(Y)** Representative images of DEXA assessment in 24-weeks-on-diet LFD and HFD-fed male Cre and KO mice. **(Z)** Table of DEXA assessment of lean mass and fat mass (n=2/group). Data are presented as means ± SEM. One- and two-way ANOVA with Tukey's *post-hoc* test (****p<0.0001) are applied where indicated. BW, body weight; BG, blood glucose; GTT, glucose tolerance test; ITT, insulin tolerance test; DEXA, dual-energy x-ray absorptiometry; Wt, wild type; Het, Ormdl3$^{\beta+/-}$ heterozygous knockout; Cre, mouse expressing Ins1$^{tm1.1(cre)Thor/J}$ with wild type Ormdl3 alleles; KO, Ormdl3$^{\beta-/-}$ homozygous knockout; LFD, low fat diet; HFD, high fat diet; AUC, area under the curve; DAPI, 4′,6-diamidino-2-phenylindole; w, weeks; ns, not significant; ANOVA, analysis of variance. Scale bars are 20 μm.

10.3389/fendo.2023.1170461

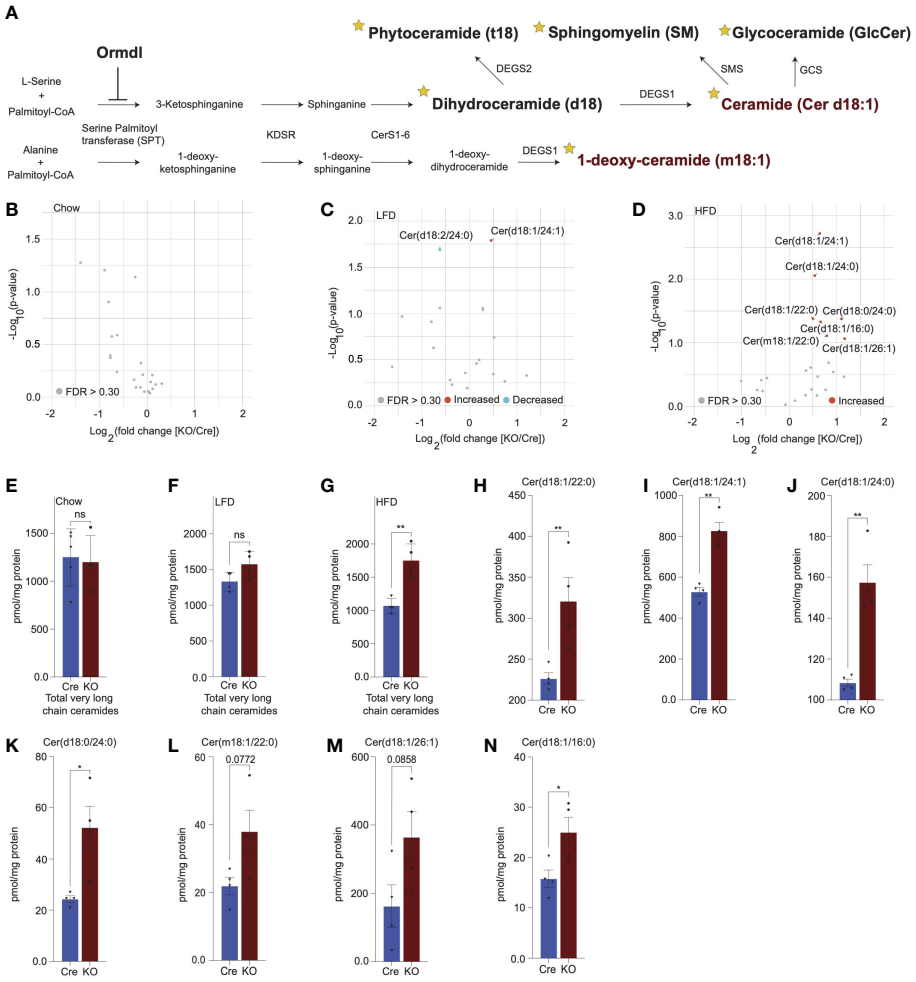

FIGURE 3
Lipidomics analysis reveals significant upregulation of very long chain ceramide species in islets of high fat diet-fed *Ormdl3*$^{\beta-/-}$ mice. **(A)** Schematic illustration of *de novo* sphingolipid biosynthetic pathway (stars denote lipid classes measured). **(B)** Volcano plot of fold change in lipid species between 10-week-old chow-fed Cre and KO mice. **(C)** Volcano plot of fold change in lipid species between LFD-fed Cre and KO mice after 24-weeks-on-diet (30 weeks of age). **(D)** Volcano plot of fold change in lipid species between HFD-fed Cre and KO mice after 24-weeks-on-diet (30 weeks of age). **(E-G)** pmol total very long chain ceramide species (C22-26) normalized to total protein content (mg) in (Welch's t-test) **(E)** 10-week-old chow-fed Cre (n=5) and KO (n=4) mice. **(F)** LFD-fed Cre (n=4) and KO (n=4) after 24-weeks-on-diet (30 weeks of age). **(G)** HFD-fed Cre (n=4) and KO (n=4) mice after 24-weeks-on-diet (30 weeks of age). **(H-N)** pmol ceramide species for HFD-fed mice normalized to total protein content (mg) for (Welch's t-test) **(H)** Cer(d18:1/22:0), **(I)** Cer(d18:1/24:1), **(J)** Cer(d18:1/24:0), **(K)** Cer(d18:0/24:0), **(L)** Cer(m18:1/22:0), **(M)** Cer(d18:1/26:1), and **(N)** Cer(d18:1/16:0). Data are presented as means ± SEM. Unpaired t-test with Welch correction (*p<0.05, **p<0.01) is applied where indicated. KDSR, 3-keto-dihydrosphingosine reductase; CerS1-6, Ceramide synthase 1-6; DEGS1, Δ4-dihydroceramide desaturase 1; DEGS2, Δ4-dihydroceramide desaturase 2; GCS, glycoceramide synthase; SMS, sphingomyelin synthase. FDR, false discovery rate; FDR q >.3, grey dots; FDR q <.3, red dots represent upregulated species and blue dots represent downregulated species; Cre, mouse expressing Ins1$^{tm1.1(cre)Thor/J}$ with wild type Ormdl3 alleles; KO, Ormdl3$^{\beta-/-}$ homozygous knockout; ns, not significant.

while the 60% HFD model used in this study simulates rapid weight gain, we cannot rule out that the impact of β-cell *Ormdl*3-deficiency may be more pronounced after a longer dietary intervention period, in aged mice, or upon feeding with other diets that can impair lipid metabolism such as high fat/sucrose/fructose western diet.

Taken together, our results suggest that β-cell ORMDL3 regulates sphingolipid production but does not alter metabolic health. While we did not observe a distinct role for ORMDL3 in β-cell health and glucose homeostasis, our results and others suggest that ORMDL3 contributes to the regulation of very long chain sphingolipid generation (14).

4 Materials and methods

4.1 Animals

The animal care and experimental procedures were carried out in accordance with the recommendations of the National Institutes of Health Guide for the Care and Use of Laboratory Animals. The protocol (#M005064-R01-A02 by F.E. for mice) was approved by the University of Wisconsin-Madison Institutional Animal Care and Use Committee. Mice were bred and maintained under specific pathogen-free conditions at University of Wisconsin-Madison

under approved protocols and were housed at 20–24°C on a 12 h light/12 h dark cycle. Animals were observed daily for health status, any mice that met IACUC criteria for euthanasia were immediately euthanized.

4.2 Generation of β-cell specific *Ormdl3* knockout mice

β-cell specific *Ormdl3* knockout mice (*Ormdl3*$^{\beta-/-}$) were generated by Cyagen Biosciences on C57BL/6N background. Briefly, a targeting vector containing mouse *Ormdl3* was generated, containing LoxP sites surrounding exons 2-4 of the *Ormdl3* gene and a Neo selection cassette flanked by Frt motifs. This construct was then electroporated into embryonic stem cells (ESC) of C57BL/6N background, and the resulting cells were then screened for homologous recombination. The ESCs were then validated, and neo-excision was achieved *in vitro* by electroporation with an Flp-O expression plasmid. The resulting neo-excised ESC clones were then screened for successful deletion by PCR and injected into blastocysts isolated from pregnant B6 albino B6(Cg)-Tyr^{c-2J}/J females. This resulted in generation of *Ormdl*$^{fl/fl}$ mice on C57BL/6N background. We then bred these mice with commercially available mice expressing a Cre construct expressed under the control of the insulin promotor (B6(Cg)-Ins1$^{tm1.1(cre)Thor/J}$) to delete *Ormdl3* specifically from β-cells.

4.3 Diets, feeding regimen, and weekly measurements

Chow, low fat diet, and high fat diet (Envigo 2919, Research Diets D12450J, and Research diets D12492, respectively) fed animals had *ad libitum* access to food and water unless otherwise specified. Mice that were fed a 60% high fat diet (Research Diets D12492) and 10% low fat diet (Research Diets D12492) began feeding on diet at 6 weeks of age and extending for a period of 24 weeks. Experiments on chow fed mice were performed on male and female mice between 5 and 34 weeks of age. Experiments on low-fat diet and high-fat diet fed mice were performed on male mice between 5 and 30 weeks of age. Weekly assessment of blood glucose and body weights was done after 6 hours of fasting. Blood glucose was analyzed by glucometer (Contour Next EZ 9628) after tail snip.

4.4 Histology

Pancreata from mice were fixed with 10% zinc formalin overnight and paraffin embedded. 5-µm sections of the pancreata were generated, and staining was performed after blocking with 5% normal goat serum with anti-Insulin (Linco) and anti-Glucagon (Cell Signaling) antibodies using established protocols. Antigen retrieval was prepared by using citrate buffer pH 6.0. After staining, slides were mounted with antifade mounting medium containing 4,6-diamidino-2-phenylindole (DAPI) (Vector Laboratories). Immunofluorescent images of pancreatic sections were obtained using a Nikon Storm/Tirf/Epifluorescence. Images used for β-cell mass calculations were obtained with an EVOS FL Auto imaging system. The images of hematoxylin and eosin (H&E)-stained pancreatic sections were obtained using an AmScope light microscope. For analysis of β-cell mass and α:β cell ratio, the images were analyzed by using the Nikon Elements Advanced Research software program.

4.5 Islet isolation

Islets were isolated using the standard collagenase/protease digestion method as previously described (15, 24). Briefly, the pancreatic duct was cannulated and distended with 4°C collagenase/protease solution using Collagenase P (Sigma-Aldrich, USA) in 1x Hank's balanced salt solution and 0.02% bovine serum albumin. The protease reaction was stopped using RPMI 1640 with 10% fetal bovine serum. Islets were separated from the exocrine tissue using Histopaque-1077 (Sigma-Aldrich, USA). Hand-picked islets were spun briefly at 1000 rpm for 1 minute before snap freezing in liquid nitrogen and storage at -80°C.

4.6 C-peptide and proinsulin ELISA

For measurement of serum C-peptide and proinsulin, blood was collected from mice *via* tail snip. Whole blood was then spun at 9000 rpm for 7 minutes and serum was collected and stored at -80° C. Frozen serum was thawed and measured by ELISA for proinsulin (Mercodia, 10-1232-01) and C-peptide (Alpco 80-CPTMS-E01). Samples were analyzed in duplicate.

4.7 Glucose and insulin tolerance tests

Glucose tolerance tests were performed on wild-type, heterozygous, knockout, and Cre control mice on chow, low fat, and high fat diets after a 6-hour morning fast. Blood glucose levels were measured at 0, 15, 30, 60, 90, and 120 minutes after an intraperitoneal administration of glucose at dose of 2g/kg body weight or insulin at dose of .75 U/kg body weight. Blood glucose measurements were measured using a glucometer (Contour Next EZ 9628). Blood glucose readings above the limit of detection were input as 600 mg/dL.

4.8 RT-qPCR

Total RNA was extracted from *Ormdl3*$^{\beta+/+}$ and *Ormdl3*$^{\beta-/-}$ mouse islets using TRIzol reagent (Invitrogen) according to manufacturer's instructions. cDNAs were synthesized from extracted RNA by using Superscript III First Strand RT-PCR kit (Invitrogen). Real-time quantitative PCR amplifications were

Gene	Forward primer	Reverse primer
Ormdl1	ACAGTGAGGTAAACCCCAATACT	GCAAAAACACATACATCCCCAGA
Ormdl2	CACAGCGAAGTAAACCCCAAC	AGGGTCCAGACAACAGGAATG
Ormdl3	CCAACCTTATCCACAACCTGG	GACCCCGTAGTCCATCTGC
Actb	TCTTGGGTATGGAATCCTGTGGCA	TCTCCTTCTGCATCCTGTCAGCAA

performed on CFX96 Touch Real-time PCR detection system (Bio-Rad). β-Actin was used as internal control for the quantity of the cDNAs in real time PCR assays.

4.9 DEXA measurement

DEXA assessment of lean and fat mass was performed in 24-week-old low fat and high fat diet fed male mice. Mice were anesthetized with isoflurane before determination of body composition using a Faxitron Ultrafoucus in DXA mode. All measurements of body composition were performed in the University of Wisconsin – Madison Small Animal Imaging Facility Core.

4.10 Lipid extraction

70-90 isolated pancreatic islets were homogenized in 215 µL MeOH with internal standard using a Qiagen TissueLyzer II (9244420) for 4x40s cycles using chilled (4°C) blocks. 750 µL MTBE was added followed by 250 µL water. Samples were mixed by inversion and phase separation was carried out by centrifugation at 4°C for 10 min at 16,000 *g*. The top organic phase was transferred to a new 1.5 mL tube and extracts were dried in a SpeedVac. Samples were resuspended in 50:50 ACN/MeOH. A processed blank was prepared in the same way without internal standards added. Samples were stored at -20°C for 1 week before analysis.

4.11 LC-MS parameters

LC-MS analysis was performed on an Agilent 1290 Infinity II UHPLC system coupled to an Agilent 6495C triple quadrupole MS. Lipid extracts were separated on an Acquity BEH C18 column (Waters 186009453; 1.7 µm 2.1 × 100 mm) with a VanGuard BEH C18 precolumn (Waters 18003975) maintained at 60°C. Samples were held at 4°C in a multisampler prior to analysis. Sphingolipids were detected with multiple reaction monitoring (MRM) in positive ion mode. The gas temperature was 210°C with flow of 11 l/min and the sheath gas temperature was 400°C with a flow of 12 l/min. The nebulizer pressure was 30 psi, the capillary voltage was set at 4000 V, and the nozzle voltage at 500 V. High pressure RF was 190 and low-pressure RF was 120. Sample injection volume was 10 µL and the injection order was randomized. The chromatography gradient consisted of mobile phase A containing 60:40 ACN/H_2O in 10 mM ammonium formate and 0.1% formic acid and mobile phase B containing 90:9:1 IPA/ACN/H_2O in 10 mM ammonium formate and 0.1% formic acid at a flow rate of 0.500 mL/min. The gradient began with 30% B, increasing to 60% over 1.8 min, then increasing to 80% until 7 min, and 99% until 7.14 min held until 10 minutes.

Collision energies, retention times, and scanning windows were optimized based on standards and pooled plasma lipid extracts. Sphingolipid class MRM transitions from are found in Supplementary Table 1. Retention times for sphingolipids without standards were adjusted using a standard of similar acyl chain length and full scan analysis with a matching chromatography gradient.

4.12 Data processing

Quantification was performed in the Agilent MassHunter Workstation. Volcano plots and bar graphs were made using the ggpubr package in R version 4.1.2. Data were normalized to protein content as measured by BCA assay (Thermo Scientific 23225) on the pellet in the aqueous phase following lipid extraction. Data is considered "semi-quantitative" because standards were not available for all compounds detected.

Data availability statement

The raw data supporting the conclusions of this article will be made available by the authors, without undue reservation.

Ethics statement

The animal study was reviewed and approved by The University of Wisconsin-Madison School of Medicine and Public Health Institutional Animal Care and Use Committee.

Author contributions

LH and HL designed and performed the *in vitro* and *in vivo* experiments, analyzed the data, and prepared the figures. LH wrote the manuscript. GW performed lipidomics analysis and prepared the figures. JS interpreted lipidomics data. FE conceived, supervised and supported the project, designed experiments, interpreted results and wrote the manuscript. All authors contributed to the article and approved the submitted version.

Funding

HL was supported by the NIH National Research Service Award T32 GM007215 and a University of Wisconsin Stem Cell and Regenerative Medicine Center Graduate Fellowship. JS is supported by grants from the Juvenile Diabetes Research Foundation (JDRF201309442), the Glenn Foundation for Medical Research (GFMR) and American Federation for Aging Research (AFAR) (22068), the National Institutes of Health (R01DK133479), and the University of Wisconsin-Madison College of Agricultural and Life Science's Hatch Grant (WIS04000). FE is supported by grants from the National Institutes of Health (DK130919 and DK128136), the Juvenile Diabetes Research Foundation (3-SRA-2023-1315-S-B), Greater Milwaukee Foundation, and startup funds from the University of Wisconsin-Madison.

Acknowledgments

We thank Dr. William Holland for providing the protocol and guidance on islet lipidomic studies.

Conflict of interest

The authors declare that the research was conducted in the absence of any commercial or financial relationships that could be construed as a potential conflict of interest.

Publisher's note

All claims expressed in this article are solely those of the authors and do not necessarily represent those of their affiliated organizations, or those of the publisher, the editors and the reviewers. Any product that may be evaluated in this article, or claim that may be made by its manufacturer, is not guaranteed or endorsed by the publisher.

Supplementary material

The Supplementary Material for this article can be found online at: https://www.frontiersin.org/articles/10.3389/fendo.2023.1170461/full#supplementary-material

References

1. Holland WL, Summers SA. Sphingolipids, insulin resistance, and metabolic disease: new insights from *in vivo* manipulation of sphingolipid metabolism. *Endocrine Rev* (2008) 29(4):381–402. doi: 10.1210/er.2007-0025

2. Summers SA. Ceramides in insulin resistance and lipotoxicity. *Prog Lipid Res* (2006) 45(1):42–72. doi: 10.1016/j.plipres.2005.11.002

3. Ye R, Onodera T, Scherer PE. Lipotoxicity and Beta; cell maintenance in obesity and type 2 diabetes. *J Endocrine Soc* (2019) 3(3):617–31. doi: 10.1210/js.2018-00372

4. Ertunc ME, Hotamisligil GS. Lipid signaling and lipotoxicity in metaflammation: indications for metabolic disease pathogenesis and treatment. *J Lipid Res* (2016) 57 (12):2099–114. doi: 10.1194/jlr.R066514

5. Davis D, Kannan M, Wattenberg B. Orm/Ormdl proteins: gate guardians and master regulators. *Adv Biol Regul* (2018) 70:3–18. doi: 10.1016/j.jbior.2018.08.002

6. Breslow DK, Collins SR, Bodenmiller B, Aebersold R, Simons K, Shevchenko A, et al. Orm family proteins mediate sphingolipid homeostasis. *Nature* (2010) 463 (7284):1048–53. doi: 10.1038/nature08787

7. Siow DL, Wattenberg BW. Mammalian ormdl proteins mediate the feedback response in ceramide biosynthesis. *J Biol Chem* (2012) 287(48):40198–204. doi: 10.1074/jbc.C112.404012

8. Pan DZ, Garske KM, Alvarez M, Bhagat YV, Boocock J, Nikkola E, et al. Integration of human adipocyte chromosomal interactions with adipose gene expression prioritizes obesity-related genes from gwas. *Nat Commun* (2018) 9 (1):1512. doi: 10.1038/s41467-018-03554-9

9. Thorens B, Tarussio D, Maestro MA, Rovira M, Heikkila E, Ferrer J. Ins1(Cre) knock-in mice for beta cell-specific gene recombination. *Diabetologia* (2015) 58 (3):558–65. doi: 10.1007/s00125-014-3468-5

10. Hanada K. Serine palmitoyltransferase, a key enzyme of sphingolipid metabolism. *Biochim Biophys Acta* (2003) 1632(1-3):16–30. doi: 10.1016/s1388-1981(03)00059-3

11. Moffatt MF, Gut IG, Demenais F, Strachan DP, Bouzigon E, Heath S, et al. A Large-scale, consortium-based genomewide association study of asthma. *N Engl J Med* (2010) 363(13):1211–21. doi: 10.1056/NEJMoa0906312

12. Moffatt MF, Kabesch M, Liang L, Dixon AL, Strachan D, Heath S, et al. Genetic variants regulating Ormdl3 expression contribute to the risk of childhood asthma. *Nature* (2007) 448(7152):470–3. doi: 10.1038/nature06014

13. McGovern DP, Gardet A, Torkvist L, Goyette P, Essers J, Taylor KD, et al. Genome-wide association identifies multiple ulcerative colitis susceptibility loci. *Nat Genet* (2010) 42(4):332–7. doi: 10.1038/ng.549

14. Song Y, Zan W, Qin L, Han S, Ye L, Wang M, et al. Ablation of Ormdl3 impairs adipose tissue thermogenesis and insulin sensitivity by increasing ceramide generation. *Mol Metab* (2022) 56:101423. doi: 10.1016/j.molmet.2021.101423

15. Lee H, Fenske RJ, Akcan T, Domask E, Davis DB, Kimple ME, et al. Differential expression of ormdl genes in the islets of mice and humans with obesity. *iScience* (2020) 23(7):101324. doi: 10.1016/j.isci.2020.101324

16. Li S, Xie T, Liu P, Wang L, Gong X. Structural insights into the assembly and substrate selectivity of human spt-Ormdl3 complex. *Nat Struct Mol Biol* (2021) 28 (3):249–57. doi: 10.1038/s41594-020-00553-7

17. Zhakupova A, Debeuf N, Krols M, Toussaint W, Vanhoutte L, Alecu I, et al. Ormdl3 expression levels have no influence on the activity of serine palmitoyltransferase. *FASEB J* (2016) 30(12):4289–300. doi: 10.1096/fj.201600639R

18. Debeuf N, Zhakupova A, Steiner R, Van Gassen S, Deswarte K, Fayazpour F, et al. The Ormdl3 asthma susceptibility gene regulates systemic ceramide levels without altering key asthma features in mice. *J Allergy Clin Immunol* (2019) 144(6):1648–59 e9. doi: 10.1016/j.jaci.2019.06.041

19. Clarke BA, Majumder S, Zhu H, Lee YT, Kono M, Li C, et al. The ormdl genes regulate the sphingolipid synthesis pathway to ensure proper myelination and neurologic function in mice. *Elife* (2019) 8:e51067. doi: 10.7554/eLife.51067

20. Raichur S. Ceramide synthases are attractive drug targets for treating metabolic diseases. *Front Endocrinol (Lausanne)* (2020) 11:483. doi: 10.3389/fendo.2020.00483

21. Garic D, De Sanctis JB, Shah J, Dumut DC, Radzioch D. Biochemistry of very-Long-Chain and long-chain ceramides in cystic fibrosis and other diseases: the importance of side chain. *Prog Lipid Res* (2019) 74:130–44. doi: 10.1016/j.plipres.2019.03.001

22. Montgomery MK, Brown SH, Lim XY, Fiveash CE, Osborne B, Bentley NL, et al. Regulation of glucose homeostasis and insulin action by ceramide acyl-chain length: a beneficial role for very long-chain sphingolipid species. *Biochim Biophys Acta* (2016) 1861(11):1828–39. doi: 10.1016/j.bbalip.2016.08.016

23. Griess K, Rieck M, Muller N, Karsai G, Hartwig S, Pelligra A, et al. Sphingolipid subtypes differentially control proinsulin processing and systemic glucose homeostasis. *Nat Cell Biol* (2023) 25(1):20–9. doi: 10.1038/s41556-022-01027-2

24. Lee H, Engin F. Preparing highly viable single-cell suspensions from mouse pancreatic islets for single-cell rna sequencing. *STAR Protoc* (2020) 1(3):100144. doi: 10.1016/j.xpro.2020.100144

frontiers | Frontiers in Endocrinology

TYPE Mini Review
PUBLISHED 08 May 2023
DOI 10.3389/fendo.2023.1180211

OPEN ACCESS

EDITED BY
Ernestina Marianna De Francesco,
University of Catania, Italy

REVIEWED BY
Guido Zavatta,
University of Bologna, Italy

*CORRESPONDENCE
Angeliki Chorti
angeliki.g.chorti@gmail.com

RECEIVED 05 March 2023
ACCEPTED 07 April 2023
PUBLISHED 08 May 2023

CITATION
Chorti A, Cheva A, Chatzikyriakidou A, Achilla C, Boulogeorgou K, Despoina K, Milias S, Zarampoukas T and Papavramidis T (2023) Sporadic parathyroid adenoma: an updated review of molecular genetics. *Front. Endocrinol.* 14:1180211. doi: 10.3389/fendo.2023.1180211

Sporadic parathyroid adenoma: an updated review of molecular genetics

Angeliki Chorti[1]*, Angeliki Cheva[2], Anthoula Chatzikyriakidou[3], Charoula Achilla[3], Kassiani Boulogeorgou[2], Krokou Despoina[1], Stefanos Milias[4], Thomas Zarampoukas[5] and Theodossis Papavramidis[1,4]

[1]1st Propedeutic Department of Surgery, AHEPA University Hospital of Thessaloniki, Aristotle University of Thessaloniki, Thessaloniki, Greece, [2]Laboratory of Pathology, Faculty of Medicine, School of Health Sciences, Aristotle University, Thessaloniki, Greece, [3]Laboratory of Medical Biology - Genetics, Faculty of Medicine, School of Health Sciences, Aristotle University, Thessaloniki, Greece, [4]Minimal Invasive Endocrine Surgery Department, Kyanos Stavros, Euromedica, Thessaloniki, Greece, [5]Laboratory of Pathology, Interbalkan Medical Center, Thessaloniki, Greece

Introduction: Primary HPT (PHPT) is a common disorder, affecting approximately 1% of the general population. Parathyroid adenomas emerge as non-familial sporadic in 90% of cases. The aim of this review is to give a detailed update of molecular genetics of sporadic parathyroid adenoma reported in international literature.

Methods: A bibliographic research was conducted in PubMed, Google Scholar, and Scopus.

Results: Seventy-eight articles were included in our review. CaSR, MEN1, CCND1/PRAD, CDKI, angiogenic factors like VEGF, FGF, TGFβ, and IGF1, and apoptotic factors are important genes in parathyroid adenomas pathogenesis that have been established by several studies. A huge list of proteins is differently expressed in parathyroid adenomas measured by Western Blotting, MALDI/TOF, MS spectrometry, and immunohistochemistry. These proteins take part in several cell processes such as cell metabolism, cytoskeleton structural stability, cell oxidative stress regulation, cell death, transcription, translation, cell connection, and cell signaling transmission, while they can be found over- or underexpressed in abnormal tissues.

Conclusion: This review gives a detailed analysis of all reported data on genomics and proteomics of parathyroid adenoma. Further studies should be applied on understanding parathyroid adenoma pathogenesis and introducing new biomarkers for early detection of primary hyperparathyroidism.

KEYWORDS

parathyroid adenoma, parathyroid genomis, parathyroid proteomics, parathyroid adenoma tumorigenesis, parathyroid pathogenesis

1 Introduction

Hyperparathyroidism (HPT) is defined as the hypersecretion of parathormone and it is classified as primary, secondary, and tertiary. Primary HPT (PHPT) is a common disorder, affecting approximately 1% of the general population. It is more frequent in women, with a women-to-men ratio of 3–4:1. PHPT results from a single parathyroid adenoma in 80%–85% of cases, multi-gland hyperplasia in 15%, and cancer in 1%. In the majority of cases, PHPT remains asymptomatic and is diagnosed incidentally during routine blood examination. In cases of symptomatic disease, musculoskeletal, urinary, gastrointestinal, neural, and cardiovascular systems are affected. Surgical treatment is the only curative treatment and is indicated in cases of symptomatic disease and in asymptomatic if at least one of these conditions is fulfilled: (a) age <50 years old; (b) serum Ca >1 mg/dl (>0.25 mmol/L); (c) T-score below -2.5 in one of the following bone regions: lumbar spine, total hip, femoral neck, or 1/3 distal radius bone or detection of asymptomatic vertebral fracture by any imaging method; (d) creatinine clearance <60 cc/min; (e) 24-h urine calcium >300 mg/d (<10 mmol/d) together with increased risk of kidney stones based on biochemical stone risk analysis, presence of asymptomatic nephrolithiasis, or nephrocalcinosis detected by imaging methods (1–4).

Parathyroid adenomas emerge as non-familial sporadic in 90% of cases or scarcely as familial- either as a manifestation of a syndrome such as the various forms of the MEN syndrome and the HPT- jaw tumor syndrome or as a non-syndromic hereditary form of PHPT, such as FIHPT, FHH, and NS-HPT (5).

The aim of this review is to give a detailed update of molecular genetics of sporadic parathyroid adenoma reported in international literature.

2 Methods

A bibliographic research was performed using PubMed, Google Scholar, and Scopus. The search terms employed were “genetic pathways AND sporadic parathyroid adenoma” and “molecular genetics AND sporadic parathyroid adenoma “. An ethical approval is not required because this study is a review of the existing international literature.

3 Review

A total of 199 were found under the term “genetic pathways AND sporadic parathyroid adenoma”, from which only 43 were relevant, whereas 159 articles were found under the term “molecular genetics AND sporadic parathyroid adenoma “, from which 65 were relevant. Duplicate results were excluded (30 articles). At last, 78 articles were included in our systematic review.

The first genetic studies on the pathogenesis of sporadic parathyroid adenoma were conducted in 1990, and until now a large amount of genes are associated with adenoma development. These genes are mainly regulators of cell cycle, growth factors, apoptosis factors, death receptors, and signal transduction molecules. A great variety of genetic mutations, especially somatic ones, have been observed such as base insertions, deletions, and substitutions (6, 7). Table 1 shows genetic alterations in parathyroid adenoma pathogenesis.

3.1 Genomics

Alteration in CaSR (calcium sensing receptor) signaling pathway, regulating parathormone (PTH) secretion, has been identified. CaSR protein is a plasma membrane G-protein and acts as a receptor on chief parathyroid cell surface. It binds serum calcium and activates the signaling pathway, which includes the phospholipase Cβ and the protein kinase C, resulting in suppression of PTH secretion. In addition, vitamin D receptors are proliferated, binding 1.25 dihydroxivitamin D and also suppressing PTH secretion. CaSR gene, located in chromosome 33q13.3–21, spans about 103 kb and has eight exons. Exons 2–7 encode a CASR protein of 1,078 amino acids (8). It is an oncosuppressor as when suppressed, cell growth is enhanced (9, 10). CaSR gene plays an important role in parathyroid adenoma development, as only a single genetic mutations has been identified, which is not confirmed by other studies (11). In Arnold et al. studies in rats, CaSR, VDR, and RET gene evolvement in parathyroid adenoma has not been confirmed, although these are involved in hereditary disease and play significant role in parathyroid gland biological processes (12).

MEN1 gene, which plays an important role in hereditary disease, is an oncosuppressor gene, located in chromosome 11q13 and aims menin protein through Wnt/β-catenin signaling pathway (5, 10, 13). Menin acts as transcription regulator factor (12). In sporadic disease, somatic mutations in both alleles are required, which occur in 20.2%. Somatic mutations include deletions, loss, insertions, transposition, and loss of heterozygosity. Loss of heterozygosity occurs in 30.5% (11). Loss of 11q, 1p, 6q, 9p, 11p, 13q, and 15q and insertion of 7, 16p, and 19p are involved in MEN1 dysregulation. Loss of one MEN1 allele is found in 25%–40% of parathyroid adenomas, together with inactivating mutations of other alleles, which is an early event as it is identified in cases of small adenomas with mild hypercalcemia (14). MEN1 gene mutations are responsible for 15%–20% of parathyroid adenoma development (12).

CCND1/PRAD1 gene is a proto-oncogene, located in 11q13 chromosome, nearby another gene that regulates PTH secretion, and is translated to cyclin D1 protein. Cyclin D1 is a regulator factor of G1-S cell cycle phase and binds to CDK4 and CDK6 which belongs to the same family (11, 13). CCND1 gene aims the primer of PTH gene (12). Its involvement in parathyroid adenoma development is 20%–40%, whereas mutation that occurs in 8% DNA translocation is a type of mutation which occurs in 8% and leads to over expression of cyclin D1 (11, 12, 14). Overexpression of cyclin D1 has been correlated to enhancement of parathyroid cell proliferation and PTH oversecretion (12).

Mutations in CDKI genes (cyclin D1 inhibitors) are involved in CCND1 gene regulation. CDKN1B, CDKN1A, CDKN2B, and CDKN2C germline mutations have been recorded (5). Germline

10.3389/fendo.2023.1180211

TABLE 1 Proteins expressed in Parathyroid Adenomas.

PTH	CHD3	AINX	MAP3K1
QCR1	CLSPN	GSTO1	MAP3K13
ATPA	STAG2	PURA	MAP3K5
ECHM	COL14A1	IF4A3	PRDX2
FUMH	MSH6	AL1A1	PIK3CA
ATP5H	DNM2	SERA	ATP12A
CH60	DTNBP1	ANXA2	PCDHB12
IDH3A	TOPORS	AMPL	RALGAPA1
ETFA	EPHA2	IDHC	RAPGEF2
HNRNPAB	EIF3C	GBB2	RASEF
MDH2	CASR	ANXA4	RASGRF1
SODM	FGFR4	ERP29	PTPRK
ODPB	FGD6	RUVB1	PLA2R1
GPDM	KAT6A	PGM1	SLC20A2
ATPB	LAMC1	LMNA	SMC1B
CAPG	LRRC7	AGRN	SMARCC2
PRDX6	PPFIA1	TECTA	TBX2
ENOA	LRP8	APP	TNS1
GSTP1	KDM2A	AKNA	SUPT5H
TPIS	MPDU1	ABCA3	TAF3
TGM2	MADD	BRCA1	PROS1
UCHL1	MAP2	CAMSAP3	SLC30A8
K2C8	MAST1	CP	VDAC1
K1C19	MAPK8	COX5A	NUFIP1
KMT5A	UBE2N	UQCRC1	KRBOX4
NPIPA7	HNRNPA2B1	BMP2K	HSP90B1
SLTM	RPSA	MED12	HSPD1
S100A11	CALM1	LUC7L	PRDX3
PA2G4	ANXA5	TCHP	PRDX1
PARK7	MAPK1	GOLGA8Q	FGG
BSPRY	DEGS1	CCDC174	GAPDH
YWHAZ	TMBIM6	ZNF674	APOA1
CCT5	SSBP3	CTTNBP2	S100A13
SNORA74A	FZD6	ARIH2	KRT4
DPYD	ATP6AP2	GOLGA8O	EZR
ALG5	PIGG	PPM1B	PVALB
ZNF552	UBAP1	ZNF605	ALB
NBEAL1	ST13	COPS7B	TF
OGN	YTHDC2	ZNF33A	SPDYE16
CALR	CPE	NPM	PITPNB

(Continued)

TABLE 1 Continued

PRDX2	MED26	ACO2	ZNF394
BCL2L10	FSD1	TUFM	RAB7B
DNAJC2	VMP1	MPP11	PHB
ATP5H	NRBF2		

mutations are rare in sporadic parathyroid adenomas without familiar history. Somatic mutations on CDKNB1 gene, encoding p27kit1 protein, have been found after DNA sequencing in 86 patients. These mutations include alterations in both alleles or loss of heterozygosity and are rare (1%) (11). The result of these mutations is p27kit1 downregulation or destabilization (15). CDKN2A, CDKN2B, and RASSF1A gene expression is lower in parathyroid adenomas compared to normal tissue, caused by hypermethylation of genes' primers in pathological tissue (16, 17). One single somatic mutation related to parathyroid adenoma has been recorded in CDKN2C gene (11).

Duan et al. found mutations related to parathyroid adenoma development in 5% of ZFX gene aiming cyclin D1, in 2%–5% of CTNNB1 gene, encoding β-catenin, in 1% of EZH2 gene, accelerating β-catenin and <1% of POT1 which is a genome stabilizer (10).

EZH2 gene encodes histone methylase H3K27 and a rare mutation (p. Y641N) has been correlated to parathyroid adenoma development (14). Gene oncogenesis mechanism has not been yet clarified, while EZH2 overexpression is supposed to be related to downregulation of oncogenes or oncosuppressors. Furthermore, EZH2 interacts with β-catenin, menin, and Wnt signaling pathway suppressors (11). EZH2 represses growth-suppressive Axin2 and negatively regulates β-catenin (14).

ZFX gene encodes a transcription factor related to cell renewal maintenance. Somatic mutations have been identified in 4.6% in abnormal parathyroid tissue, while gene oncogenesis mechanism remains unclear (11).

Wnt/β-catenin/CTNNB1 signaling pathway is enrolled in tumorigenesis, but its role in parathyroid adenoma has not been yet elucidated. β-catenin is the first molecule in Wnt pathway. The Costa-Guda et al. study in 97 patients with sporadic parathyroid adenoma for mutations in exon 3 on CTNNB1 gene was negative for novel mutations except for S37A mutation which is already known from previous studies (18). S37A mutation in exon 3 of CTNNB1 gene has been detected in 7.3% of sporadic adenomas and is related to β-catenin, while its functional role has been verified by immunohistochemical examination, in which β-catenin was found overexpressed in abnormal tissue (19). Furthermore, another somatic mutation S33C in exon 3 of CTNBB1 gene has been detected by Guarnieri et al. after gene sequencing, whereas cyclin D1 and β-catenin expression has not been found altered in immunohistochemical examination (20). Starker et al. restudied somatic mutations in exon 3 and resulted that these mutations are rarely detected in parathyroid adenoma (0.68% for S33C), while in an immunohistochemical study β-catenin was found elevated in mutated cells (21). Other factors related to both Wnt signaling pathway and parathyroid adenoma pathogenesis are the following: (a) LRP5 gene, which is associated with β-catenin destruction complex and is found in 86% in parathyroid adenomas, (b) APC gene, methylated in parathyroid adenomas and (c) RASSF1A gene, which is hypermethylated and underexpressed in parathyroid adenomas in 71% (11, 14). APC gene mutations were detected in the Park et al. Next-generation sequencing study (22).

Erb/ηer-1/EGFR gene is associated with other endocrine disorders or tumors such as breast cancer. DNA from 33 patients with PHPT was assessed using real-time PCR concluding in one amplification of ErbB-1/Her-1/EGFR gene, two deletions of ErbB-2/Her-2 gene, and six deletions of ErbB-4/Her-4 gene, which was reasonably selected as the most appropriate for further investigation (23).

SMAD3 gene is located in chromosome 15 and encodes a TGF-β pathway molecule that binds to menin. Due to this association with menin, SMAD3 mutations leading to abnormal development of parathyroid chief cells were carefully investigated. Indeed, loss of heterozygosity was detected in 24% of parathyroid adenomas, but SMAD3 cannot be characterized as oncosuppressor gene as clonal mutations were not found (24).

CYP27B1 gene was analyzed for mutations correlated to parathyroid adenoma, as this gene encodes 25-hydroxy-vitamin D-1α-hydroxylase, a P450 mitochondrial enzyme, which converts 25-hydroxy-vitamin D to 1.25-dihydroxy-vitamin D, the functional form. No mutations were detected in the CYP27B1 gene, so its role in parathyroid adenoma pathogenesis was not confirmed (25).

Genetic alterations were detected on chromosome 9 in 10/14 patients with parathyroid adenoma in the Garcia et al. study. These alterations include insertions in 9p22-24 and 9q34, in Xq26 (in 6/14 patients), and in 4q21-28 and 8p22-23 (in 4/14 patients). Deletions were found in chromosomes 11 and 20 (20q12-13) in 2/14 cases (26).

Furthermore, mutations in the ASXL3 gene, two somatic mutations in CDC73 parafibromin gene (Y54X), and one somatic mutation in the EZH2 gene were detected in a Chinese population study. In this study, whole genome sequencing was applied in 22 blood samples from patients with sporadic parathyroid adenoma (27).

A germline mutation (deletion) in CDC73/HRPT2 gene was verified in 35% of patients with sporadic parathyroid adenoma by real-time PCR. This gene is involved in Hyperparathyroidism-jaw tumor, so it is recommended as a possible oncogene in sporadic parathyroid adenoma cases (28). CDC73/HRPT2 gene is rarely involved in sporadic disease, while its mutant allele, caused by germline mutations, is detected in cystic and large adenomas and in recurrent cases (11). Germline mutation in the GCM2 gene was found in patients with sporadic disease threefold more frequent compared to the control group, concluding that patients with this

mutation have predisposition in parathyroid adenoma development (29). The GCM2 or GCMB gene encodes an important transcription factor for parathyroid adenomas, while familiar absence causes hypoparathyroidism. Mutations in adenoma cases have been detected as Y282D in predisposed allele, V382M, and Y394S. Oncogenesis mechanism has not been found yet (11). GCM2 was verified to be part of parathyroid adenoma pathogenesis in a next-generation sequencing study by Park et al. (22).

By comparative genomic hybridization (CGH) application, genome from 53 parathyroid adenomas was analyzed, and both insertions in 16p and 19p genes and deletions in 11p and 11q genes were detected. These findings introduce new oncogenes and oncosuppressor genes involved in parathyroid adenoma pathogenesis (30).

By PCR, macroarray, protein, and mRNA expression techniques, additional genes in parathyroid adenoma tissues were inserted in an involved gene list: APOLLON, BCL2, CK19, CK18, CHROMOGRANIN-A, BAX, PARATHORMONE, ATM,MDM2, CK8, CYCLIN D1, SYNAPTOPHYSIN, FLIP και TRAIL (31). Epigenetic alterations have been found in APC, SFRP1 SFRP2, SFRP4, WT1, RIZ1, HIC1, c-Met, and MYC και CDH1 genes (10, 32).

In a review by Westin et al. in 2016, β-catenin is an essential part of molecular pathways in parathyroid adenoma pathogenesis. MEN1, HRPT2, EZH2, RASSF1A, HIC1, WT1, APC, SFRP1, SFRP2, SFRP4, SFRP5, and LRP5 genes are related to β-catenin by promoting or inhibiting its production. Wnt/β-catenin genetic pathway is suggested as the main pathway in sporadic parathyroid adenoma development, although further studies is required to verify its role (14).

Further molecular pathways involved in parathyroid adenoma pathogenesis include angiogenic factors. VEGF, FGF, TGFβ, and IGF1 factors were found to be correlated with parathyroid adenoma. VEGF has a pre-angiogenic action and takes part in cell proliferation. FGF factor is increased in adenomas, as it regulates cell cycle and cell development. TGFβ is also increased in adenomas, related to several cell processes. IGF1 is involved in cell proliferation and stands for the main mediatory factor in PTH anabolic role on bones (33).

Apoptosis factors also seem to be associated with parathyroid adenomas. These molecular pathways include anti-apoptotic and apoptotic agents, of which action is altered in adenoma development. TRAIL protein is bound to DR4 and DR5 death receptors and has an anti-cancer role; although TRAIL protein can create complexes with caspase-8 and FADD, leading to opposite action. TRAIL protein is highly expressed in parathyroid adenomas. FAS protein is a death receptor participating in DISC (death inducing signaling complex) formation and its production is elevated in adenomas. BCL2 gene promotes caspase activation and mitochondrial external membrane permeability and was found decreased in adenomas. MDM2, negative regulator of p53, is elevated in adenomas and acts as oncogene (33).

Lu et al. in 2018 studied genetic factors involved in parathyroid adenoma pathogenesis applying immunohistochemistry, real-time PCR, and spectrometry in both histological types of parathyroid adenomas (oxyphil and chief cell adenomas). CaSR, VDR, PTH, MEN1, FGFR1, CNND1, CDKN1B, GCM2, CYP27B1, CYP24A1, PTHLH, and NDUFA13 expression has no statistical significant difference between two groups. VDR and PTH gene expression in parathyroid adenomas ranges from very low to high compared to normal tissue where PTH and VDR are highly expressed (34).

Although several genes have been detected in sporadic parathyroid adenoma, genetic testing in sporadic disease is not recommended, as the majority of mutations is somatic and is developed after disease progression (13). On the other hand, calcium sensing receptor has been proposed as imaging agent for parathyroid detection (35).

3.2 Proteomics

In international literature, studies of proteomic analysis of parathyroid adenoma tissues have been reported. Proteins differently expressed in the abnormal tissues have been measured by Western Blotting, MALDI/TOF, MS spectrometry, and immunohistochemistry. There are a vast number of proteins which expression is modified in parathyroid adenomas. Except for the quantitative measurement of these proteins, studies also focus on their functional role and their localization in cells, in order that genetic pathways related to these proteins are detected. Table 2 shows the large list of proteins associated with parathyroid adenoma.

The functional role of proteins usually is translated as parts of cell metabolism, cytoskeleton structural stability, cell oxidative stress regulation, cell death, transcription, translation, cell connection, and cell signaling transmission (34, 36–39). Arya et al. detected 206 proteins in parathyroid adenomas with different expression, from which 39 were cytoplasmatic proteins, 48 were attached to cytoplasmatic membrane, 49 were macromolecular complexes, 38 were part of a cellular organelles, 21 were related to cell connection, and 10 have extracellular localization. In particular, from those related to cellular organelles, 19 were found in the cellular nucleus, 9 in the cytoskeleton, 5 in the cytoplasm, 3 in the mitochondria, and 2 in the cytoplasmatic membrane. In terms of their functional role, 37.8% had catalytic function on enzymes, 32% were related to cellular connection, while other functions included cellular processes, metabolism, development, localization, regulation, and stimuli response (36). Same results had also Varshney et al. study, which concluded that 33% of proteins were related to cell regulation, 27% to cell death, 27% to transcription, 13% to cell cycle, and 7% to cell signaling transmission. Furthermore, in this study 11 proteins were detected to be differently expressed in parathyroid adenoma cells compared to normal tissue (37).

In sporadic parathyroid adenomas, localization of several proteins is in the cytoplasm, as Akpinar et al. reported (39). Different proteins are expressed in oxyphil cell adenomas in comparison with chief cell adenomas. Lu et al. reported 199 proteins that are differently expressed between two types of parathyroid adenomas. Compared to normal tissue, 83 proteins seem to have modified expression in chief cell adenomas and 44

10.3389/fendo.2023.1180211

TABLE 2 Genomics of parathyroid adenoma development.

Gene	Genetic pathway	Intra- or Extracellular pathway
CaSR	Phospholipase C	Intracellular
MEN1	Wnt/β-catenin	Intracellular
CCND1/PRAD1	Cyclin D1	Intracellular
CDKI	Cyclin D1	Intracellular
ZFX	Cyclin D1	Unknown
CTNNB1	Wnt/β-catenin	Intracellular
EZH2	Wnt/β-catenin	Unknown
POT1	Unknown	Unknown
LRP5	Wnt/β-catenin	Intracellular
APC	Wnt/β-catenin	Unknown
RASSF1A	Wnt/β-catenin	Unknown
Erb/ηer-1/EGFR	Unknown	Unknown
SMAD3	TGF-β	Intracellular
ASXL3	Unknown	Unknown
CDC73/HRPT2	Unknown	Unknown
GCM2	Unknown	Intracellular
APOLLON	Unknown	Unknown
BCL2	Apoptosis	Intracellular
CK19	Unknown	Unknown
CK18	Unknown	Unknown
CHROMOGRANIN A	Unknown	Unknown
BAX	Unknown	Unknown
PTH	Unknown	Unknown
ATM	Unknown	Unknown
MDM2	Apoptosis	Intracellular
CK8	Unknown	Unknown
SYNAPTOPHYSIN	Unknown	Unknown
FLIP	Unknown	Unknown
TRAIL	apoptosis	Extracellular
SFRP1 and SFRP2 and SFRP4	Wnt/β-catenin	Unknown
WT1	Wnt/β-catenin	Unknown
RIZ1	Unknown	Unknown
HIC1	Wnt/β-catenin	Unknown
c-MET	Unknown	Unknown
MYC	Unknown	Unknown
CDH1	Unknown	Unknown
VEGF	VEGF	Intracellular
FGF	VEGF	Intracellular
TGFβ	VEGF	Intracellular

(Continued)

TABLE 2 Continued

Gene	Genetic pathway	Intra- or Extracellular pathway
IGF1	VEGF	Intracellular
FAS	Apoptosis/ DISC	Extracellular
VDR	Wnt/β-catenin (?)	Intracellular
CYP27B1 and CYP24A1	Unknown	Unknown
NDUFA13	Unknown	Unknown

proteins in oxyphil cell adenomas (34). Chief cells can be transformed to oxyphil cells during puberty and are recognized by intense appearance of mitochondria in them. In the Akpinar et al. study, several mitochondrial proteins were detected in hyperplastic cells, which can be explained by the cell transformation model described above (39).

ANXA-2, ATP5H, and LMNA are examples of proteins detected in parathyroid adenomas, fact that has been verified by three different studies (37, 39, 40). These three proteins are bound to ubiquitin C, the main molecule of their function (39). Calcium-binding proteins are involved in phospholipase C signaling pathway (PLC) and are overexpressed in parathyroid adenomas (36). Additionally, MAPK, Ras, and IP signaling pathways seem to be related to parathyroid adenomas pathogenesis, as several proteins-parts of these pathways have modified expression in parathyroid adenomas (36). Increased intracellular calcium activates mitochondrial function and oncogenetic and oncosuppressive processes are modified, so it may play an important role in oncogenesis. Chromatic regulatory proteins seem to be underexpressed in adenomas, while mitochondrial proteins are increased (36).

VDAC1, ANXA5, ANXA2, and S100-A11 proteins are increased in parathyroid adenomas. VDAC1 is involved in the mitochondrial molecule release process that intensifies apoptosis, and its overexpression in adenomas is found to cause PTH release to peripheral circulation. Annexin role in oncogenesis is under intense investigation. ANXA-5 is found to be related to apoptotic processes, while ANXA-2 enhances tumor metastasis by reinforcing cell detachment and translocation.

COX-5A, PARK-7, PRDX-3, HSP90, HSP60, and CCT5 proteins are also found overexpressed in parathyroid adenomas. These proteins are involved in early cell response to oxidative stress, fact that characterizes adenomas which have intense cell proliferation and neoangiogenesis. BSPRY protein, related to calcium receptors, is underexpressed in parathyroid adenomas, leading to decreased inhibitory role on calcium receptors. Its role remains unclear (40). Prolactin receptor (PRLr) has been found increased in parathyroid adenoma cell surface, fact that implies prolactin role in parathormone regulation and adenoma pathogenesis (41). Vitamin D receptor (VDR) has been found decreased in parathyroid adenomas tissue, which is verified by genomic analysis as previously mentioned (37).

Donaldio et al., in their proteomic analysis, used paraffin embed parathyroid adenoma tissues which were reconstituted with formalin solution. Ten from 20 proteins detected in their study were found in these tissues, which is of great importance for future studies on specially processed adenoma samples in order that new biomarkers are discovered (38).

4 Conclusion

This review gives a detailed analysis of all reported data on genomics and proteomics of parathyroid adenoma. Different signaling pathways are involved in adenoma development. Wnt/β-catenin, MAPK, Ras, IP, TGF-β, and PLC have already been established, including many genes and proteins with different functional roles. Further studies should be applied on understanding parathyroid adenoma pathogenesis and introducing new biomarkers for early histological biomarkers to predict recurrence in other parathyroid glands.

Author contributions

ACho, TP, AChe, ACha: Conceptualization. ACha, CA, KB: Data curation. ACho, AChe, ACha: Formal analysis. SM, TZ, ACho, CA, KB, KD: Investigation. ACho: Methodology. TP, AChe, ACha: Supervision. TP: Validation. ACho: Writing - original draft. TP, AChe, ACha: Writing - review and editing. All authors contributed to the article and approved the submitted version.

Conflict of interest

The authors declare that the research was conducted in the absence of any commercial or financial relationships that could be construed as a potential conflict of interest.

Publisher's note

References

1. Bilezikian JP, Khan AA, Silverberg SJ, Fuleihan GE, Marcocci C, Minisola S, et al. Evaluation and management of primary hyperparathyroidism: summary statement and guidelines from the fifth international workshop. *J Bone Mineral Res* (2022) 37 (11):2293–314. doi: 10.1002/jbmr.4677

2. Erickson LA, Mete O, Juhlin CC, Perren A, Gill AJ. Overview of the 2022 WHO classification of parathyroid tumors. *Endocrine Pathol* (2022) 33(1):64–89. doi: 10.1007/s12022-022-09709-1

3. Zavatta G, Clarke BL. Normocalcemic hyperparathyroidism: a heterogeneous disorder often misdiagnosed? *JBMR plus* (2020) 4(8):e10391. doi: 10.1002/jbm4.10391

4. Cusano NE. Cetani f normocalcemic primary hyperparathyroidism. *Arch Endocrinol Metab* (2022) 66(5):666–77. doi: 10.20945/2359-3997000000556

5. Cetani F, Pardi E, Banti C, Collecchi P, Viacava P, Borsari S, et al. Beta-catenin activation is not involved in sporadic parathyroid carcinomas and adenomas. *Endocrine-related Cancer* (2010) 17(1):1–6. doi: 10.1677/ERC-09-0147

6. Segiet O, Deska M, Michalski M, Gawrychowski J, Wojnicz R. Molecular profiling in primary hyperparathyroidism. *Head Neck* (2014) 37(2):299–307. doi: 10.1002/hed.23656

7. Marini F, Giusti F, Iantomasi T, Brandi ML. Parathyroid tumors: molecular signatures. *Int J Mol Sci* (2021) 22(20):11206. doi: 10.3390/ijms222011206

8. Hendy GN, Cole DE. Genetic defects associated with familial and sporadic hyperparathyroidism. *Front hormone Res* (2013) 41. doi: 10.1159/000345675

9. Diez-Fraile A, Lammens T, Benoit Y. D'Herde K the calcium-sensing receptor as a regulator of cellular fate in normal and pathological conditions. *Curr Mol Med* (2013) 13(2):282–95. doi: 10.2174/156652413804810763

10. Duan K, Gomez Hernandez K. Mete O clinicopathological correlates of hyperparathyroidism. *J Clin Pathol* (2015) 68(10):771–87. doi: 10.1136/jclinpath-2015-203186

11. Brewer K, Costa-Guda J, Arnold A. Molecular genetic insights into sporadic primary hyperparathyroidism. *Endocrine-related Cancer* (2019) 26(2):R53–72. doi: 10.1530/ERC-18-0304

12. Arnold A. Major molecular genetic drivers in sporadic primary hyperparathyroidism. *Trans Am Clin Climatol Assoc* (2016) 127:235–44.

13. Marini F, Cianferotti L, Giusti F, Brandi M. Molecular genetics in primary hyperparathyroidism: the role of genetic tests in differential diagnosis, disease prevention strategy, and therapeutic planning. a 2017 update. *Clin Cases Miner Bone Metab* (2017) 14(1):60–70. doi: 10.11138/ccmbm/2017.14.1.060

14. Westin G. Molecular genetics and epigenetics of nonfamilial (sporadic) parathyroid tumours. *J Internal Med* (2016) 280(6):551–8. doi: 10.1111/joim.12458

15. Costa-Guda J, Marinoni I, Molatore S, Pellegata NS, Arnold A. Somatic mutation and germline sequence abnormalities in CDKN1B, encoding p27Kip1, in sporadic parathyroid adenomas. *J Clin Endocrinol Metab* (2011) 96(4):E701–706. doi: 10.1210/jc.2010-1338

16. Arya AK, Bhadada SK, Singh P, Sachdeva N, Saikia UN, Dahiya D, et al. Promoter hypermethylation inactivates CDKN2A, CDKN2B and RASSF1A genes in sporadic parathyroid adenomas. *Sci Rep* (2017) 7(1):3123. doi: 10.1038/s41598-017-03143-8

17. Arya AK, Singh P, Saikia UN, Sachdeva N, Dahiya D, Behera A, et al. Dysregulated mitogen-activated protein kinase pathway mediated cell cycle disruption in sporadic parathyroid tumors. *J Endocrinological Invest* (2020) 43 (2):247–53. doi: 10.1007/s40618-019-01098-3

18. Costa-Guda J, Arnold A. Absence of stabilizing mutations of beta-catenin encoded by CTNNB1 exon 3 in a large series of sporadic parathyroid adenomas. *J Clin Endocrinol Metab* (2007) 92(4):1564–6. doi: 10.1210/jc.2006-2554

19. Björklund P, Akerström G, Westin G. An LRP5 receptor with internal deletion in hyperparathyroid tumors with implications for deregulated WNT/beta-catenin signaling. *PloS Med* (2007) 4(11):e328. doi: 10.1371/journal.pmed.0040328

20. Guarnieri V, Baorda F, Battista C, Bisceglia M, Balsamo T, Gruppioni E, et al. A rare S33C mutation of CTNNB1 encoding beta-catenin in a parathyroid adenoma found in an Italian primary hyperparathyroid cohort. *Endocrine* (2012) 41(1):152–5. doi: 10.1007/s12020-011-9558-y

21. Starker LF, Fonseca AL, Akerström G, Björklund P, Westin G, Carling T. Evidence of a stabilizing mutation of beta-catenin encoded by CTNNB1 exon 3 in a large series of sporadic parathyroid adenomas. *Endocrine* (2012) 42(3):612–5. doi: 10.1007/s12020-012-9690-3

22. Park HS, Lee YH, Hong N, Won D, Rhee Y. Germline mutations related to primary hyperparathyroidism identified by next-generation sequencing. *Front Endocrinol* (2022) 13:853171. doi: 10.3389/fendo.2022.853171

23. Bednarz N, Błaut K, Sworczak K, Oseka T, Bielawski K. The profile of ErbB/Her family genes copy number assessed by real-time PCR in parathyroid adenoma and hyperplasia associated with sporadic primary hyperparathyroidism. *Acta Biochim Pol* (2009) 56(1):83–8. doi: 10.18388/abp.2009_2519

24. Shattuck TM, Costa J, Bernstein M, Jensen RT, Chung DC, Arnold A. Mutational analysis of Smad3, a candidate tumor suppressor implicated in TGF-beta and menin pathways, in parathyroid adenomas and enteropancreatic endocrine tumors. *J Clin Endocrinol Metab* (2002) 87(8):3911–4. doi: 10.1210/jcem.87.8.8707

25. Lauter K, Arnold A. Analysis of CYP27B1, encoding 25-hydroxyvitamin d-1alpha-hydroxylase, as a candidate tumor suppressor gene in primary and severe secondary/tertiary hyperparathyroidism. *J Bone Mineral Res* (2009) 24(1):102–4. doi: 10.1359/jbmr.080903

26. Garcia JL, Tardio JC, Gutierrez NC, Gonzalez MB, Polo JR, Hernandez JM, et al. Chromosomal imbalances identified by comparative genomic hybridization in sporadic parathyroid adenomas. *Eur J Endocrinol* (2002) 146(2):209–13. doi: 10.1530/eje.0.1460209

27. Wei Z, Sun B, Wang ZP, He JW, Fu WZ, Fan YB, et al. Whole-exome sequencing identifies novel recurrent somatic mutations in sporadic parathyroid adenomas. *Endocrinology* (2018) 159(8):3061–8. doi: 10.1210/en.2018-00246

28. Bricaire L, Odou MF, Cardot-Bauters C, Delemer B, North MO, Salenave S, et al. Frequent large germline HRPT2 deletions in a French national cohort of patients with primary hyperparathyroidism. *J Clin Endocrinol Metab* (2013) 98(2):E403–408. doi: 10.1210/jc.2012-2789

29. Riccardi A, Aspir T, Shen L, Kuo CL, Brown TC, Korah R, et al. Analysis of activating GCM2 sequence variants in sporadic parathyroid adenomas. *J Clin Endocrinol Metab* (2019) 104(6):1948–52. doi: 10.1210/jc.2018-02517

30. Palanisamy N, Imanishi Y, Rao P, Tahara H, Chaganti R, Arnold A. Novel chromosomal abnormalities identified by comparative genomic hybridization in parathyroid adenomas. *J Clin Endocrinol Metab* (1998) 83(5):1766–70. doi: 10.1210/jc.83.5.1766

31. Arvai K, Nagy K, Barti-Juhasz H, Petak I, Krenacs T, Micsik T, et al. Molecular profiling of parathyroid hyperplasia, adenoma and carcinoma. *Pathol Oncol Res POR* (2012) 18(3):607–14. doi: 10.1007/s12253-011-9483-7

32. Sadowski SM, Pusztaszeri M, Brulhart-Meynet MC, Petrenko V, De Vito C, Sobel J, et al. Identification of differential transcriptional patterns in primary and secondary hyperparathyroidism. *J Clin Endocrinol Metab* (2018) 103(6):2189–98. doi: 10.1210/jc.2017-02506

33. Mizamtsidi M, Nastos C, Mastorakos G, Dina R, Vassiliou I, Gazouli M, et al. Diagnosis, management, histology and genetics of sporadic primary hyperparathyroidism: old knowledge with new tricks. *Endocrine Connections* (2018) 7(2):R56–68. doi: 10.1530/EC-17-0283

34. Lu M, Kjellin H, Fotouhi O, Lee L, Nilsson IL, Haglund F, et al. Molecular profiles of oxyphilic and chief cell parathyroid adenoma. *Mol Cell Endocrinol* (2018) 470:84–95. doi: 10.1016/j.mce.2017.10.001

35. Yusof AM, Kothandaraman S, Zhang X, Saji M, Ringel MD, Tweedle MF, et al. Development of a calcium-sensing receptor molecular imaging agent. *Surgery* (2013) 154(6):1378–84. doi: 10.1016/j.surg.2013.06.044

36. Arya AK, Bhadada SK, Singh P, Dahiya D, Kaur G, Sharma S, et al. Quantitative proteomics analysis of sporadic parathyroid adenoma tissue samples. *J Endocrinological Invest* (2019) 42(5):577–90. doi: 10.1007/s40618-018-0958-1

37. Varshney S, Bhadada SK, Saikia UN, Sachdeva N, Behera A, Arya AK, et al. Simultaneous expression analysis of vitamin d receptor, calcium-sensing receptor, cyclin D1, and PTH in symptomatic primary hyperparathyroidism in Asian indians. *Eur J Endocrinol* (2013) 169(1):109–16. doi: 10.1530/EJE-13-0085

38. Donadio E, Giusti L, Cetani F, Da Valle Y, Ciregia F, Giannaccini G, et al. Evaluation of formalin-fixed paraffin-embedded tissues in the proteomic analysis of parathyroid glands. *Proteome Sci* (2011) 9(1):29. doi: 10.1186/1477-5956-9-29

39. Akpinar G, Kasap M, Canturk NZ, Zulfigarova M, Islek EE, Guler SA, et al. Proteomics analysis of tissue samples reveals changes in mitochondrial protein levels in parathyroid hyperplasia over adenoma. *Cancer Genomics Proteomics* (2017) 14(3):197–211. doi: 10.21873/cgp.20031

40. Giusti L, Cetani F, Ciregia F, Da Valle Y, Donadio E, Giannaccini G, et al. A proteomic approach to study parathyroid glands. *Mol Biosyst* (2011) 7(3):687–99. doi: 10.1039/C0MB00191K

41. Haglund F, Lu M, Vukojevic V, Nilsson IL, Andreasson A, Džabić M, et al. Prolactin receptor in primary hyperparathyroidism–expression, functionality and clinical correlations. *PloS One* (2012) 7(5):e36448. doi: 10.1371/journal.pone.0036448

frontiers | Frontiers in Endocrinology

TYPE Original Research
PUBLISHED 12 May 2023
DOI 10.3389/fendo.2023.1105602

OPEN ACCESS

EDITED BY
Julian Lui,
Eunice Kennedy Shriver National Institute of Child Health and Human Development (NIH), United States

REVIEWED BY
Michael M. Chau,
Cedars Sinai Medical Center, United States
Jeffrey Baron,
National Institutes of Health (NIH), United States

*CORRESPONDENCE
Leonardo Guasti
l.guasti@qmul.ac.uk

†These authors have contributed equally to this work

RECEIVED 22 November 2022
ACCEPTED 28 March 2023
PUBLISHED 12 May 2023

CITATION
Mistry JN, Silvennoinen S, Zaman F, Sävendahl L, Mariniello K, Hall C, Howard SR, Dunkel L, Sankilampi U and Guasti L (2023) The crosstalk between FGF21 and GH leads to weakened GH receptor signaling and IGF1 expression and is associated with growth failure in very preterm infants. *Front. Endocrinol.* 14:1105602. doi: 10.3389/fendo.2023.1105602

The crosstalk between FGF21 and GH leads to weakened GH receptor signaling and IGF1 expression and is associated with growth failure in very preterm infants

Jayna N. Mistry[1†], Sanna Silvennoinen[2†], Farasat Zaman[3], Lars Sävendahl[3], Katia Mariniello[1], Charlotte Hall[1], Sasha R. Howard[1], Leo Dunkel[1†], Ulla Sankilampi[2†] and Leonardo Guasti[1*†]

[1]Centre for Endocrinology, William Harvey Research Institute, Barts and the London Faculty of Medicine and Dentistry, Queen Mary University of London, London, United Kingdom, [2]Department of Pediatrics, Kuopio University Hospital and University of Eastern Finland, Kuopio, Finland, [3]Department of Women's and Children's Health, Karolinska Institutet and Karolinska University, Solna, Sweden

Background: Fibroblast growth factor 21 (FGF21) is an essential metabolic regulator that adapts to changes in nutritional status. Severe childhood undernutrition induces elevated FGF21 levels, contributing to growth hormone (GH) resistance and subsequent linear growth attenuation potentially through a direct action on chondrocytes.

Methods: In this study, we assessed expression of the components of both GH and FGF21 pathways in rare and unique human growth plates obtained from children. Moreover, we investigated the mechanistic interplay of FGF21 on GH receptor (GHR) signaling in a heterologous system.

Results: Chronic FGF21 exposure increased GH-induced GHR turnover and SOCS2 expression, leading to the inhibition of STAT5 phosphorylation and IGF-1 expression. The clinical significance of FGF21 signaling through GH receptors was tested in nutritionally driven growth failure seen in very preterm (VPT) infants right after birth. VPT infants display an immediate linear growth failure after birth followed by growth catch-up. Consistent with the *in vitro* model data, we show that circulating FGF21 levels were elevated during deflection in linear growth compared to catch-up growth and were inversely correlated with the length velocity and circulating IGF1 levels.

Conclusions: This study further supports a central role of FGF21 in GH resistance and linear growth failure and suggests a direct action on the growth plate.

KEYWORDS

GH signaling, GH resistance, FGF21, growth plate, preterm infants

1 Introduction

Fibroblast growth factor 21 (FGF21), a member of the FGF19 subfamily of FGFs, is a key regulator in the metabolic adaptations to fasting, inducing gluconeogenesis, fatty acid oxidation and ketogenesis (1–3). FGF21 lacks the heparin binding domain allowing it to diffuse away from its tissue of synthesis and function as an endocrine factor (4, 5). FGF21 signals *via* FGFR1 isoform IIIC with the assistance of co-receptor β-Klotho (4, 6). Recent studies have identified a novel role of FGF21 as a potential candidate in developing GH resistance and growth failure with underlying chronic conditions (7, 8). Infants born very pre-term (VPT) (< 32 weeks) in intensive care are susceptible to undernutrition, causing poor linear growth and/or weight gain (9, 10). We previously highlighted a significant inverse association between serum FGF21 levels during the first 5 weeks of life and growth in length, but not for weight. In addition, we showed that FGF21 inhibits GH-induced pSTAT5 activity and *IGF-1* expression whilst stimulating *SOCS2* levels in human primary chondrocytes/chondroblasts established from ribs (1). Similarly, other studies showed serum FGF21 levels to be negatively associated with linear growth (11, 12), further emphasizing an inverse correlation with growth rates in infancy.

This study aimed to provide insight into the mechanistic interplay of FGF21 on GH receptor (GHR) and downstream signaling events involving the JAK/STAT cascade, directly linked with linear growth. Furthermore, the association between FGF21 levels and growth attenuation was evaluated to assess FGF21 levels during linear growth deflection and catch-up growth in a large cohort of VPT infants.

2 Materials and methods

2.1 Patients

A total of 64 VPT infants born before 32 gestational weeks (41 males, 64.1%) were recruited during the first week of life in the PreBaby study on metabolism and growth at the Kuopio University Hospital neonatal intensive care unit. The infants showed typical morbidity associated with prematurity (Table 1). However, they all survived until discharge. VPT infants were monitored regularly for their weight and recumbent length from birth (in-patient) to final growth follow-up (out-patient) at the mean age of 119.8 postmenstrual (PM) weeks (corresponding to around 18 months from the term-equivalent age of 40 PM weeks). The growth data were converted into Standard Deviation Score (SDS) using the contemporary population-based references (14).

Peripheral venous or arterial samples were obtained at the age of 1, 3, 5, 7 and 9 weeks (in-patient) and at two follow-up visits after discharge (out-patient). Serum samples were prepared by centrifugation after blood collection, separated into aliquots and stored at -80˚C until analyzed.

Serum FGF21 concentrations were measured by human FGF21 ELISA kit (BioVendor, detection range 30 to 1920 pg/ml) using the manufacturer's instruction. Serum IGF-1 concentration was measured by human IGF-1 ELISA kit (Mediagnost GmbH, detection range 2 to 50 ng/ml).

The growth pattern of VPT infants was evaluated during two distinct growth phases; 1) period of steady decrease in length/weight SDS (Growth deflection) and 2) period of steady increase in length/weight SDS (catch-up growth) differentiated by the point of nadir (the lowest point of length/weight SDS). The sampling of hormonal levels (FGF21 and IGF-1) was evaluated at the obtained timepoints, separated by the point of nadir to reflect the mean hormonal levels during growth deflection and catch-up growth.

2.2 Cells

HEK-293 were grown in DMEM high-glucose (4500mg/L, GIBCO) supplemented with 10% fetal-bovine serum (FBS, GIBCO) and 1% penicillin/streptomycin (P/S, Sigma) at 37°C in a humidified incubator with 5% CO_2. Cells stably expressing GHR (HEK-293 hGHR) were generated by transfecting pCMV6-AC-Myc-DDK human GHR plasmid (Origene) into HEK-293 cells. Neomycin (500µg/ml; Sigma) was used as a positive selection marker.

2.3 PCR and quantitative RT-PCR

RNA extraction from human rib cartilage has been previously described (1). RNA from cells was obtained using RNeasy Mini Kit. 1µg of RNA was used to generate cDNAs: 1µg of random hexamers (New England Biolabs) was added to RNA samples to make a total volume of 15µl with Rnase/Dnase free water. The preparation was incubated at 70°C for 5 minutes for RNA denaturation (Veriti 96 well thermos cycler, Applied Biosystems). A master-mix made of 2µl of (10x) Moloney Murine Leukemia virus (M-MLV) reaction buffer (New England Biolabs), 1µl (10mM) deoxyribonucleotide triphosphate (dNTPs) (New England Biolabs), 1µl M-MLV RT (New England Biolabs) and 1µl Ribonuclease inhibitor (RNAsin) (New England Biolabs) was prepared per reaction sample. 5µl was added to the RNA sample following the initial incubation stage. Samples were further incubated at 25°C for 10 minutes, 42°C for 90 minutes and 70°C for 15 minutes for 1 cycle. cDNA was stored at -20°C.

PCR to detect *GHR*, *FGF21*, *FGFR1*, isoform *–IIIC*, *β-KLOTHO* and *GAPDH* was performed in a GS1 thermocycler (G-storm). Each reaction was prepared using 0.15µl (5U/µl) *Taq* polymerase (New England Biolabs), 2.5µl (10x) Standard *Taq* buffer (New England Biolabs), 0.5µl (200µM) of each dNTP, 1µl cDNA, 0.5µl (0.5µM) of specific primers and 20.35µl RNase/DNase free water.

Quantitative RT-PCR (RT-qPCR) reactions were prepared using 1µl of cDNA (~25ng), 0.5µl of each specific primer (0.5µM), 3µl dH_2O and 5µl of SYBR green (QIAGEN) in Mx3000 thermocycler (Stratagene). Data was evaluated using MxPro software (Stratagene).

GAPDH was used as a house-keeping gene in PCR and RT-qPCR. Primers and cycle/amplification conditions are reported in Supplementary Tables 1, 2.

10.3389/fendo.2023.1105602

TABLE 1 Clinical characteristics of the 64 VPT infants (41 males, 64.1%).

Multiple gestation (twins) n/%	27/42.2	
Bronchopulmonary dysplasia n/%	12/18.8	
Sepsis n/%	12/18.8	
Necrotizing enterocolitis n/%	2/3.1	
Severe (grade III-IV) IVH n/%	2/3.1	
Retinopathy of prematurity n/%	4/6.3	
	Mean	Range
At birth		
Gestational age, week	28.5	23.4 – 31.9
Weight, kg	1.14	500 – 1880
Weight, SD[a]	-0.49	-3.76 – 2.36
Length, cm	36.78	29.0 – 44.0
Length, SD[a]	-0.41	-4.70 – 4.10
At nadir		
Postmenstrual age for weight, week	33.6	28.0 – 40.0
Weight, kg	1.57	660 – 2630
Weight, SD[a]	-2.60	-4.88 – -0.49
Postmenstrual age for length, week	34.3	29.6 – 40.4
Length, cm	40.83	32.4 – 50.0
Length, SD[a]	-2.74	-6.05 – -0.43
Final growth follow-up visit		
Postmenstrual age, week	119.8	36.9 – 184.6
Weight, kg	10.45	2.81 – 15.60
Weight, SD[b]	-0.83	-4.49 – 1.87
Length, cm	80.72	46.80 – 98.20
Length, SD[b]	-0.70	-4.51 – 1.40

[a]Birth weight and length and weight and length at nadir were converted to SDS using the population-based birth size reference (13).
[b]Weight and length at the final growth follow-up visit were converted to SDS using the contemporary population based growth reference (13).

The relative cycle threshold method (15) was used for the normalization and quantification of RT-qPCR data. Data are expressed as fold change relative to *GAPDH*.

10x cell ranger raw data (matrix, features and barcodes) was downloaded for P19 control mice from GEO Accession viewer (GSE162033). Data was imported to R (v. 4.2.2) using Seurat (v4.3.0).

Cells were filtered so that those with unique feature counts over 6000 or less than 200 and those with >10% mitochondrial counts were removed.

2.4 Single cell sequencing analysis

10x cell ranger raw data (matrix, features and barcodes) was downloaded for postnatal day 19 mice from GEO Accession viewer (GSE162033) (16). Data was imported to R (v. 4.2.2) using Seurat (v4.3.0). Cells were filtered so that those with unique feature counts over 6000 or less than 200 and those with >10% mitochondrial counts were removed. The global-scaling normalization technique "LogNormalize" was used to normalize the UMI count matrix. Seurat package "ScaleData" function was used to remove the unwanted sources of variation. The dimensionality of the dataset was determined using Seurat packages JackStraw and ElbowPlot. PC15 was decided the correct cut off to use going forward. Clusters were identified using 'Find Neighbours' and 'FindClusters' function. RunUMAP was used to create the UMAPs.

To annotate the clusters, differentially expressed features were identified by looking at the markers differing between clusters using the function "FindAllMarkers". Plots were generated using Seurat functions, FeaturePlot and ggplot2.

2.5 Cell treatments

To assess glycosylation, HEK-293 hGHR cells (3 x 10^5 cells per well in 6-well plates) were grown to reach ~90% confluency. Media

was discarded and cells were washed with PBS before cell lysis with 20mM sodium phosphate (Sigma) pH 7.5, 0.1% sodium dodecyl sulfate (Sigma), 0.75% Nonidet P-40 (Sigma), 50mM β-mercaptoethanol (Sigma) and protease tablet inhibitor cocktail (Sigma), for 20 minutes in ice. Cells were then centrifuged at 13,000rpm for 10 minutes at 4°C, and the supernatant was collected. 20µl of cell lysate was treated, with or without N-glycosidase F (New England Biolabs) overnight at 37°C. The enzymatic reaction was stopped by 2x Laemmli buffer (Sigma) and processed for Western blotting.

To assess GH and FGF21 responsiveness, HEK-293 hGHR cells (3 x 10^5 cells per well in 6-well plates) were grown to reach 80% confluency. Cells were serum starved overnight and treated in the absence or presence of Cycloheximide (CHX) (100µg/ml; Sigma), recombinant GH (0.5µg/ml; Life Technologies) or recombinant FGF21 (5µg/ml; VWR) for 1 – 8 hours and then processed for GHR expression using Western blotting.

HEK-293 hGHR cells were grown at 3 x 10^5 cells per well in 6-well plates. The following day, cells were serum starved and treated with or without recombinant FGF21 (5µg/ml) overnight before being challenged with recombinant GH (0.5µg/ml) for 10 and 30 minutes for the assessment of pSTAT5(Ty694) by Western blotting or 8 and 16 hours for the evaluation of *SOCS2* and *IGF-1* mRNA expression *via* RT-qPCR.

2.6 Cell proliferation

96-well plates were coated with 100µl per well of collagen (collagen I, Rat tail (1µl; GIBCO), acetic acid (0.67µl; Fisher Scientific), 50µl dH_2O) for 1 hour at 23°C. Collagen was aspirated and wells were washed twice with PBS and air-dried for 2 hours. HEK-293 hGHR cells were plated at 5 x 10^3 cells per well and grown to reach 50% confluency before being serum starved in the absence or presence of recombinant FGF21 (5µg/ml) overnight. Cells were then challenged with recombinant GH (0.5µg/ml) for 96 hours. Media was removed and cells were treated with 100µl cell-counting reagent kit-8 (10:100 dilution in serum free media; Sigma) incubated at 37°C for 1 hour. The absorbance was measured at 450nm with a Microplate Reader (Bio-Rad)

2.7 Immunohistochemistry and RNAScope

Human liver paraffin sections were obtained from Generon. Human growth plate biopsies were obtained from pediatric patients undergoing epiphyseal surgery to arrest longitudinal bone growth due to constitutional tall stature or leg length difference and cultured *ex-vivo* as previously described (17). Sections were then incubated at 60°C for 40 minutes, deparaffinized in xylene (twice for 10 minutes), and then hydrated in graded alcohol (ethanol) baths; 99% ethanol (twice for 5 minutes), 95% ethanol (10 minutes), 70% ethanol (5 minutes) and dH_2O (10 minutes). Antigen retrieval was performed in citric acid (0.01M) and sodium citrate (0.1M) in dH_2O at 80°C for 20 minutes. After, sections were washed with PBS twice and with PBS 0.01% Tween followed by incubation with 3% goat serum for 1 hour and overnight incubation with primary antibodies at 4°C (Supplementary Table 3). Sections were washed in PBS 0.01% Tween (five times), followed by incubation with secondary antibody; goat anti-rabbit IgG (Vector Laboratories) or goat anti-mouse IgG (Santa-Cruz Biotechnology) at 1:200 dilution in 1% BSA in PBS for 1 hour at 23°C. After washing in PBS 0.01% Tween for 20 minutes, peroxidase activity was detected under a microscope using DAB-kit (Vector Laboratories). The reaction was stopped by rinsing the section with dH_2O and counterstained with Alcian blue. Dehydration of sections was performed in graded alcohol baths; dH_2O, 70% ethanol, 95% ethanol, 99% ethanol and xylene each for 5 minutes and mounted with Pertex (Histolab products AB).

Human liver sections were processed for human FGF21 RNAScope (Supplementary Table 5) using the 2.5 HD Assay-BROWN Kit (ACD) according to the manufacturer's instructions.

2.8 Immunoprecipitation

HEK-293 hGHR cells (1 x 10^5 cells per/ml in T75cm^2 flasks) were grown to reach 70% confluency. Cells were serum starved in the absence or presence of recombinant FGF21 (5µg/ml) overnight before being challenged with recombinant GH (0.5µg/ml) for 16 hours. Cells were lysed in 1ml RIPA buffer (Sigma) supplemented with protease inhibitor cocktail (Sigma) and kept on ice for 20 minutes following centrifugation at 13,000rpm for 10 minutes. Supernatant was collected and reacted with protein A/G plus agarose beads (30µl; Santa-Cruz Biotechnology) on a rotor at 4°C for 1 hour. Samples were centrifuged at 2500rpm for 5 minutes and the sample was transferred to a new Eppendorf tube followed by antibody incubation; normal rabbit IgG or anti-GHR B-10 on a rotor at 4°C overnight. 30µl of protein A/G plus agarose beads were added to each sample and placed on a rotor at 4°C for 2 hours. The samples were centrifuged at 2500rpm for 5 minutes and the supernatant was discarded. The cell pellet was washed with RIPA buffer and twice with PBS centrifuging at 2500rpm for 5 minutes between washes. 80µl of 2X Laemmli buffer was added, and the sample boiled at 95°C for 5 minutes followed by centrifugation at 13,300rpm for 1 minute and transferred to a new Eppendorf tube and processed for Western blotting.

2.9 Western blotting

Cell lysates obtained from HEK-293 hGHR cells were size-separated on a 10% SDS gel, against the PageRuler, Plus Prestained protein ladder (ThermoFisher Scientific) and blotted onto a nitrocellulose membrane (GE Health care Life sciences). Membranes were incubated with blocking buffer, 5% non-fat dry milk (Asda) in PBS containing 0.1% Tween-20 for 1 hour at 23°C followed by incubation with primary antibody (Supplementary Table 4) prepared in blocking buffer overnight at 4°C.

Membranes were washed with PBS 0.1% Tween-20 (three times, 15-minute intervals) and then incubated with secondary antibody with goat anti-mouse IRDye680/800 and goat anti-rabbit

IRDye680/800, dilution 1:10,000 (LI-COR). Immunoblots were scanned using the Odyssey Infrared Imaging System (LI-COR)

2.10 Study approval

This study was approved by the Ethics Committee of the Pohjois-Savo Health Care District, Finland. Informed consent was obtained from both parents of all study participants.

The local ethical committee, (Karolinska Institutet Research Ethics Committee North at the Karolinska University Hospital, Stockholm, Sweden) approved the collection of human growth plate biopsies. Informed consent was obtained from each subject and their parents, which was also documented in the original hospital records.

2.11 Statistical analyses

Clinical data evaluation was performed in SPSS software (version 24.0). FGF21 and IGF-1 serum concentrations were not normally distributed when tested using the Kolmogorov-Smirnov test and therefore the values were first log transformed to achieve normality of residuals. Log transformed FGF21/IGF-1 levels at weeks 1, 3, 5, 7 and 9 postnatally (in-patient) and weeks 1 and 2 (out-patient) after birth were separated individually for each patient and averaged to reflect mean levels during growth deflection and catch-up growth. Statistical tests to evaluate hormonal levels during deflection and catch-up growth included bivariate correlation and paried *t*-test analysis.

In vitro data were evaluated by One-way ANOVA, Dunnett's *post hoc* test, Two-way ANOVA, Bonferroni post *t*-test or Non-linear regression one phase decay using GraphPad Software version 5. Each experiment was performed a minimum of 3 times. Data are expressed as mean ± standard error of the mean (SEM). Statistical significance was defined as p values <0.05.

3 Results

3.1 GHR, FGF21 and FGF21 receptor complex are expressed in the human growth plate

Previous data, including *ex-vivo* cultures of human chondroblasts with a pre-hypertrophic/proliferative phenotype (1) and *in vivo* animal studies (2) alluded that FGF21 could act directly at the level of growth plate; however, whether components of the FGF21 pathway are expressed in the growth plate is not known. Immunohistochemical analysis showed that expression of GHR, FGF21, FGFR1 and β-Klotho was highly localized in the proliferative and pre-hypertrophic zones (Figures 1A–F; Supplementary Figure 1), suggestive of a potential functional crosstalk between GH and FGF21 pathways in these cells, regulating longitudinal growth. In contrasts with immunohistochemistry, analysis of single cell sequencing datasets of mouse growth plates (18) indicated extremely low counts of *Fgf21* compared to *GhR* or *Fgfr1*, suggesting either differences in expression between mice and humans or a potential cross-reactivity of anti-FGF21 antibody in the human growth plate samples. *GhR* or *Fgfr1* were enriched in clusters enriched with chondrocyte lineage progenitors and growth plate chondrocytes, albeit proliferative and pre-hypertrophic zones could not be safely identified in the single cell clusters (Supplementary Figure 2).

3.2 Development of an *in vitro* model to investigate GH/FGF21 crosstalk

We next aimed at further assessing the functional crosstalk between FGF21 and GH pathways by establishing a GH- and FGF21-responsive *in vitro* model. HEK-293 cells stably expressing human GHR (HEK-293hGHR) displayed multiple GHR bands in Western Blot experiments, representing both ER-resident and plasmamembrane/mature GHR (Figures 2A, B), as described by others (12). Heterologous GHR was functional as recombinant human GH induced rapid STAT5 phosphorylation and increased negative regulator SOCS2 expression (Figure 2C). HEK-293hGHR endogenously expressed FGF21 receptor complex; *FGFR1*, isoform *FGFR1-IIIC* and *β-KLOTHO*, indicating their potential responsiveness to FGF21 (Figure 2D). HEK-293hGHR also expressed *FGF21*, although at significant lower levels compared to human liver; interestingly, GH had no effect on the endogenous expression of *FGF21* suggesting that FGF21 induced GH-resistance may partially be driven by chronic hepatic FGF21 levels (Figure 2E).

3.3 FGF21 enhances GH-mediated GHR turnover

GH action depends on the availability of GHR on the cell surface and its baseline turnover can be accelerated by GH itself *via* proteolysis and ligand-induced endocytosis (19). We tested the hypothesis that FGF21 might affect the amount of GHR on the cell surface by modulating GHR turnover. HEK-293hGHR were treated with cycloheximide (CHX) to block protein translation, and mature GHR protein levels were assessed over a period of 8 hours by Western Blot. CHX treated cells challenged with GH resulted in a significant reduction in GHR half-life at 1 hour (p<0.0001), 2 hours (p<0.0001) and 3 hours (p=0.136) compared to CHX treated cells only (Figure 3A, left panel). The rate of mature GHR degradation was significantly reduced in CHX + GH treated cells compared to CHX treated only from 1.355 to 0.7741 hours (p=0.0007) (Figure 3A, right panel). This is in keeping with data reported by other investigators (19). No significant differences were detected in mature GHR half-life when cells were treated with CHX + FGF21 compared to CHX treatment alone. Interestingly, a greater shift and rapid reduction of GHR half-life was observed when cells were concomitantly treated with FGF21 and GH with the expression of mature GHR almost abolished by 5 to 8 hours (Figure 3A). This difference in mature GHR expression was most significant at the 1-hour time-point (p=0.0003) (Figure 3A, right panel). The rate of mature GHR degradation was significantly reduced in FGF21 + GH, treated cells compared to GH

10.3389/fendo.2023.1105602

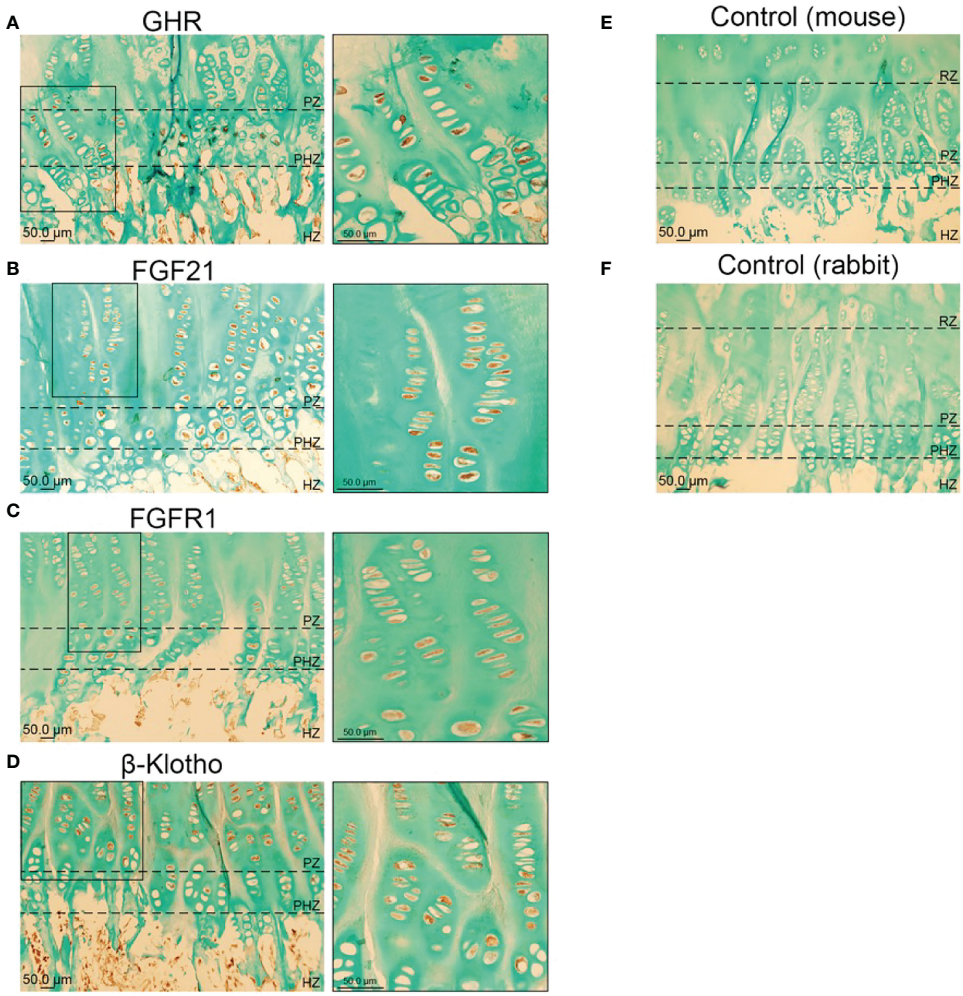

FIGURE 1
Immunohistochemical localization of GHR **(A)**, FGF21 **(B)**, FGFR1 **(C)** and β-KLOTHO **(D)** in male human growth plate tissue (tibia) in late puberty; mean age 12.3 years (*n*=6). Negative control: Human growth plate tissue incubated with secondary antibody, goat anti-mouse **(E)** and goat anti-rabbit **(F)**, (*n*=6).

alone, from 0.7741 to 0.4518 hours (p=0.0015) (Figure 3A, right panel). These results suggest that FGF21 enhances GH-mediated GHR turnover and degradation *in vitro*.

We next investigated whether FGF21 could affect GHR-mediated signal transduction. FGF21 inhibited GH-induced STAT5 phosphorylation at 10 and 30 minutes compared to GH treatment alone (Figure 3B). This also led to a reduction in *IGF-1* mRNA expression at both the timepoints analyzed (8 and 16 hours) compared to GH treatment alone (Figure 3C). Furthermore, treatment with FGF21 and GH significantly inhibited cell proliferation compared to GH treatment alone (Figure 3D).

SOCS2 affects GHR function either *via* binding to phosphorylated tyrosine residues on GHR, blocking downstream signaling events, or by regulating cellular GHR levels by facilitating GHR ubiquitination and proteasomal dependent degradation (20, 21). In HEK-293hGHR, FGF21 was able to potentiate GH-induced upregulation of *SOCS2* expression (Figure 4A), however, chronic FGF21 had no effect on GH-induced ubiquitination of GHR (Figures 4B–D). Taken together, these results suggest that FGF21 increased GH-mediated GHR degradation resulting in attenuation of downstream signaling (pSTAT5), culminating in a reduction of *IGF1* expression. This mechanism could be mediated by FGF21-dependent upregulation of SOCS2, leading to GHR degradation.

3.4 Linear growth trends in VPT infants and FGF21 levels

VPT infants displayed a relatively uniform growth pattern, consisting of a poor linear growth rate immediately after birth, as evident by a rapid decrease in the mean length/weight SDS (growth deflection). This was followed by a period of catch-up growth, observed by an increase in the mean length/weight SDS after nadir (lowest point of length/weight SDS) (Figure 5A). At nadir the average length SDS was -2.74 SDS, which was seen at an average age of 34.3 PM weeks. The average weight SDS at nadir was -2.60 SDS, which was seen at an average age of 33.6 PM weeks. The magnitude of deflection (ΔSDS for length from birth to nadir) was

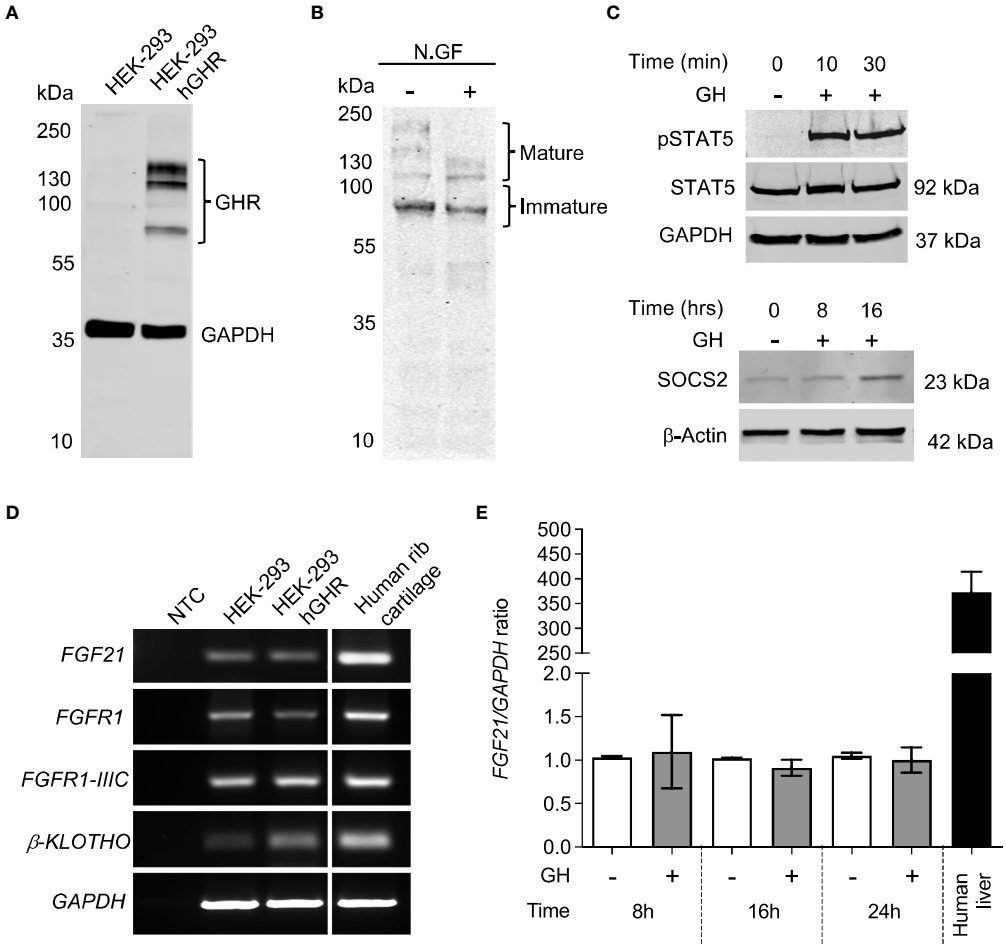

FIGURE 2
HEK-293 exogenously expressing GHR are responsive to GH. **(A)** Western blot analysis of GHR expression in HEK-293 (control) and HEK-293hGHR with GHR antibody. The molecular weight (kDa) of protein standard is reported on the left. **(B)** Protein extracts obtained from HEK-293 hGHR cells were incubated with or without N-glycosidase F (N.GF) and immunoblotted with GHR antibody. The band at ~140 kDa represent the glycosylated mature GHR while the lower m.w. bands represent immature GHR in the ER and Golgi. **(C)** (upper panel) HEK-293hGHR cells were serum starved overnight and incubated with or without recombinant human GH (0.5µg/ml) for 10 or 30 minutes. Whole cell lysates were subjected to western blot analysis of STAT5 (92kDa) and pSTAT5(Tyr694) protein expression; (lower panel) HEK-293hGHR cells were serum starved overnight and challenged with recombinant human GH (0.5µg/ml) for 8 and 16 hours. Whole cell lysates were subjected to western blot analysis of SOCS2 (23kDa) protein expression. **(D)** PCR analysis of *FGF21, FGFR1, isoform -IIIC, β-KLOTHO*, and *GAPDH* in HEK-293 and HEK-293hGHR stable line cells; negative controls (NTC) were PCR samples where cDNA was omitted. Human rib cartilage was used as a positive control. **(E)** HEK-293 hGHR cells were serum starved overnight and challenged with GH (0.5 µg/ml) for 8, 16 and 24 hours before analysis of endogenous *FGF21* expression by RT-qPCR. All values are relative to untreated cells at 8 hours. n=3 applies to all panels.

significantly negatively correlated with total catch-up growth (ΔSDS for length from nadir to final growth follow-up) (r= -0.25, p= 0.045) (Figure 5B), such that infants who experienced a greater decline in SDS during the deflection stage exhibited a greater SDS increase during the catch-up phase. Evaluation of length SDS (assessed at the age of 1, 3, 5, 7 and 9 weeks during hospitalization) in comparison to catch-up growth at two follow-up visits after discharge (out-patient) demonstrated that VPT with a greater degree of growth deflection were more susceptible to a more negative short-term Δ in length SDS, whilst faster catch-up growth was reflective of a more positive short-term Δ in length (r= 0.35, p< 0.001) (Figure 5C).

Individual serum FGF21 and IGF-1 levels were evaluated at weeks 1, 3, 5, 7 and 9 (in-patient) and at two follow-up visits after discharge (out-patient) to assess the correlation between hormonal levels with time interval (weeks) to the length SDS nadir. A weak but significant negative correlation was observed between LogFGF21 levels and time interval (weeks) to the length SDS nadir (r = -0.17, p=0.002) (Figure 6A). Thus, FGF21 levels were higher during deflection (mean = 483.35 pg/ml, *SD* = 581.32) than during catch-up (mean = 223.04 pg/ml, *SD* = 211.50; p<0.001) (Figure 6B). This correlation was not seen without logarithmic correction of FGF21 concentrations (Supplementary Figures 4A, C). Inversely, there was positive correlation between IGF-1 levels and time interval (weeks) to the length SDS nadir (r = 0.15, p=0.009) (Figure 6C and Supplementary Figures 3B, D), and consistently, IGF-1 levels were higher during catch-up (mean 5.63ng/ml, *SD* = 5.46) than during deflection (mean 7.82ng/ml, *SD* = 7.13; p=0.044) (Figure 6D).

10.3389/fendo.2023.1105602

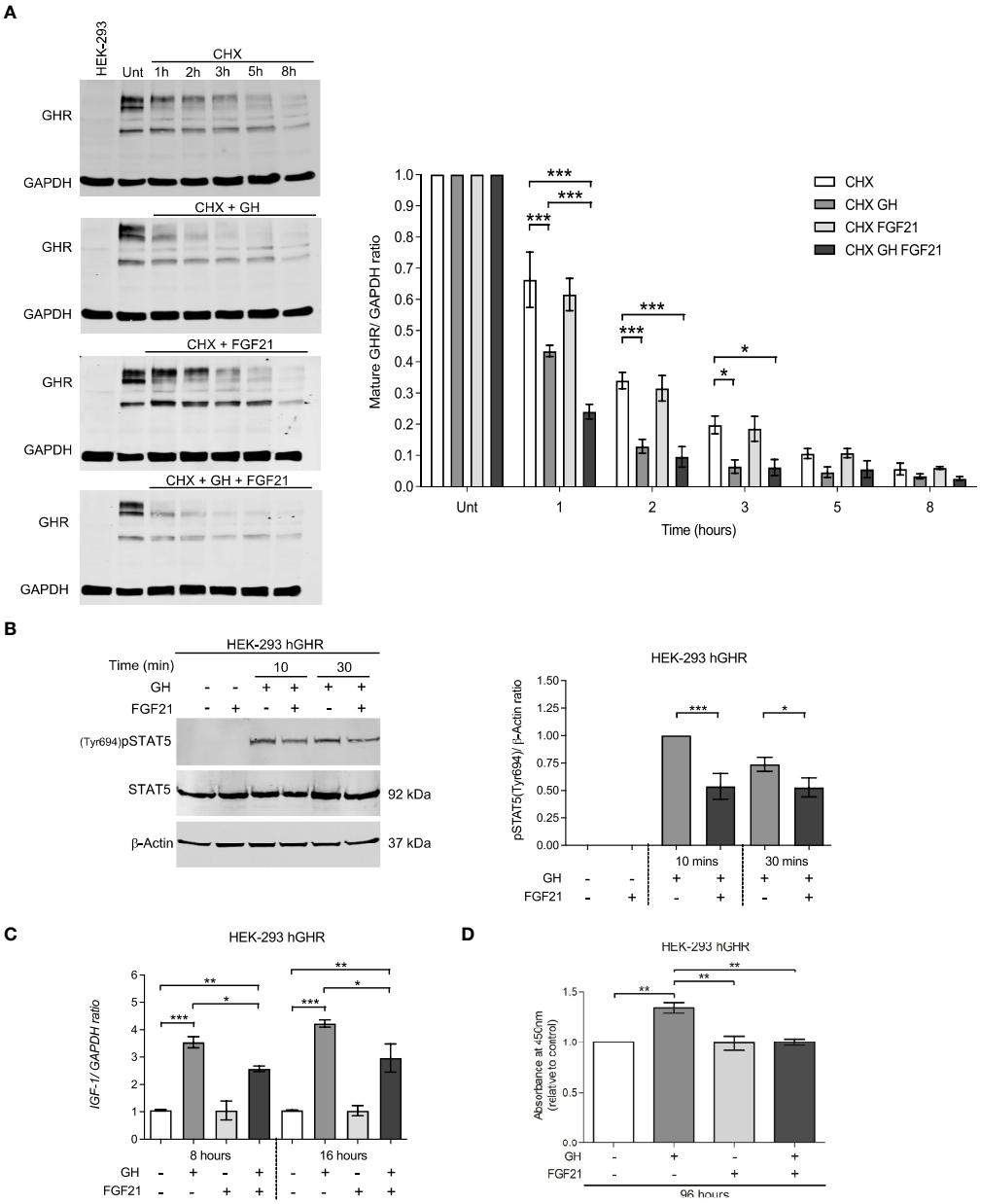

FIGURE 3
FGF21 decrease GHR half-life and inhibits downstream GHR signaling events. **(A)** HEK-293hGHR cells were serum starved overnight and incubated in the absence or presence of CHX (100 µg/ml), GH (0.5 µg/ml) or FGF21 (5 µg/ml) at the indicated timepoints up to 8 hours before analysis of GHR by Western blot; Unt: Untreated at 0 hours; HEK-293, non-transfected cells. The right panel indicates the ratio of mature GHR *vs.* untreated. 0 hours normalized to housekeeping GAPDH. (right bottom panel) Quantification of the rate (hours) of mature GHR half-life, expressed as % of time at 0 hours, *n*=4. **(B)** HEK-293hGHR cells were serum starved and treated in the absence or presence of FGF21 (5 µg/ml) overnight and then challenged with GH (0.5 µg/ml) for 10 to 30 minutes before analysis of pSTAT5(Tyr694) by Western blot (left panel). The right panel indicates the ratio of pSTAT5(Tyr694) *vs.* total protein, normalized to GH treatment alone at 10 minutes, *n*=5. **(C)** HEK-293hGHR cells were serum starved with or without FGF21 (5 µg/ml) overnight and then challenged with GH (0.5 µg/ml) for 8 or 16 hours before analysis of *IGF-1* expression by RT-qPCR, *n*=3. **(D)** HEK-293hGHR cells were serum starved with or without FGF21 (5 µg/ml) overnight and then challenged with GH (0.5 µg/ml) for 96 hours before analysis of cell proliferation, *n*=3. *p<0.05; **p<0.01; ***p<0.001.

4 Discussion

The clinical evaluation on VPT infants undertaken in this study has broadened our understanding of the role of elevated circulating FGF21 levels in the development of GH resistance and subsequent poor linear growth outcomes. It is well described that premature birth poses long-term health risks, particularly associated with growth failure which is further magnified by underlying chronic conditions i.e., undernutrition (9, 10, 22–25). However, the molecular signals leading to GH insensitivity remain ill-defined.

Recruitment of VPT infants as part of a clinical evaluation has thus offered an applicable model to investigate the unknown mechanisms associated with childhood growth failure. Our cohort of VPT infants showed a uniform growth trend demonstrated by an

10.3389/fendo.2023.1105602

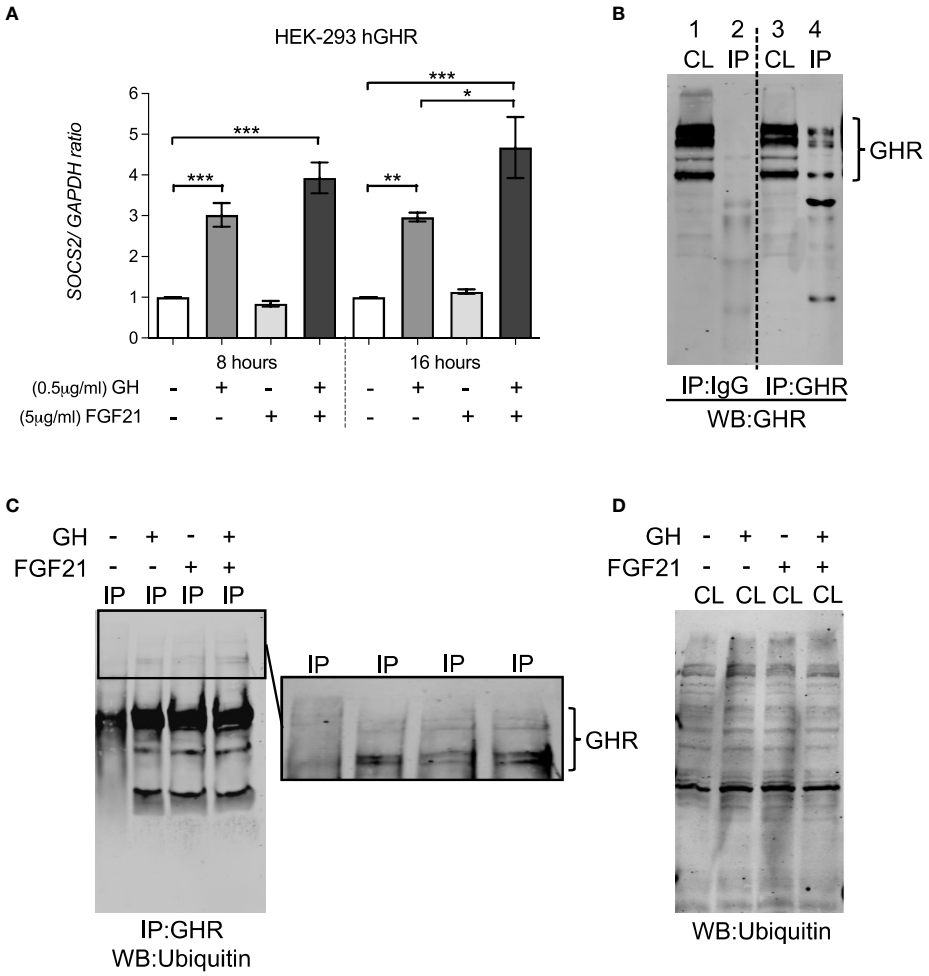

FIGURE 4
FGF21 increased GH-induced *SOCS2* expression but had no effect on the ubiquitination of GHR. **(A)** HEK-293hGHR cells were serum starved in the absence or presence of FGF21 (5 µg/ml) overnight and then challenged with GH (0.5 µg/ml) for 8 or 16 hours before analysis of *SOCS2* by RT-PCR (left panel) **(B)** Anti GHR can immunoprecipitate GHR in HEK-293hGHR cells: cells were immunoprecipitation with antiGHR antibodies or control IgG. Cell lysates and immunoprecipitated were developed with antiGHR antibodies CL, cell lysate; IP, immunoprecipitated sample; HC, heavy chain IgG; LC, light chain IgG. Negative control; IgG. **(C)** Western blot of GHR ubiquitination in immunoprecipitated samples after treatment with GH with or without FGF21. **(D)** Western blot of ubiquitin in whole cell lysates (n=3). *p<0.05; **p<0.01; ***p<0.001.

immediate growth deficit after birth, followed by catch-up growth after the point of nadir. This unique linear growth pattern in preterm infants has been widely reported across some clinical studies (26, 27). Interestingly, an independent evaluation of deflection and catch-up growth revealed an upregulation in FGF21 levels during deflection compared to catch-up growth, which was inversely correlated with IGF-1 levels. This offers evidence to suggest that upregulation in FGF21 levels as seen during growth deflection may lead to growth failure in VPT infants potentially *via* mechanisms of GH resistance evaluated in our *in vitro* observations. The period of catch-up growth appears to be marked by the opposite – alleviation of FGF21 mediated GH resistance.

The potential functional cross talk between GH and FGF21 signaling was studied in the human growth plate and in a cell model responsive to both hormones. GHR and FGF21/FGF21 receptor complexes were both expressed in chondrocytes of the proliferative and pre-hypertrophic zone; their expression in the resting zone should be investigated in biopsies contain an intact resting zone, which was not possible in our samples. The proliferative, pre-hypertrophic and hypertrophic growth plate zones play an essential role in chondrocyte proliferation and maturation where GHR signaling occurs to promote longitudinal bone growth (28–30). The inability to reliably detect endogenous GHR with antibodies in many experimental settings prompted us to generate a line heterologously expressing a detectable GHR. We showed that HEK-293hGHR responded to recombinant GH whilst endogenously expressing the FGF21 receptor complex. This allowed us to assess, for the first time, the effects of recombinant GH and FGF21 on the turnover of GHR and the activity of GHR-activated pathways such as pSTAT5, SOCS2, IGF1 expression and GHR ubiquitination. Growth plates (Figure 1), rib cartilage and HEK-293hGHR (Figure 2) expressed FGF21 suggesting a potential paracrine/autocrine mechanism of action; despite this, the amount of FGF21 expressed in the HEK-293hGHR was significantly lower

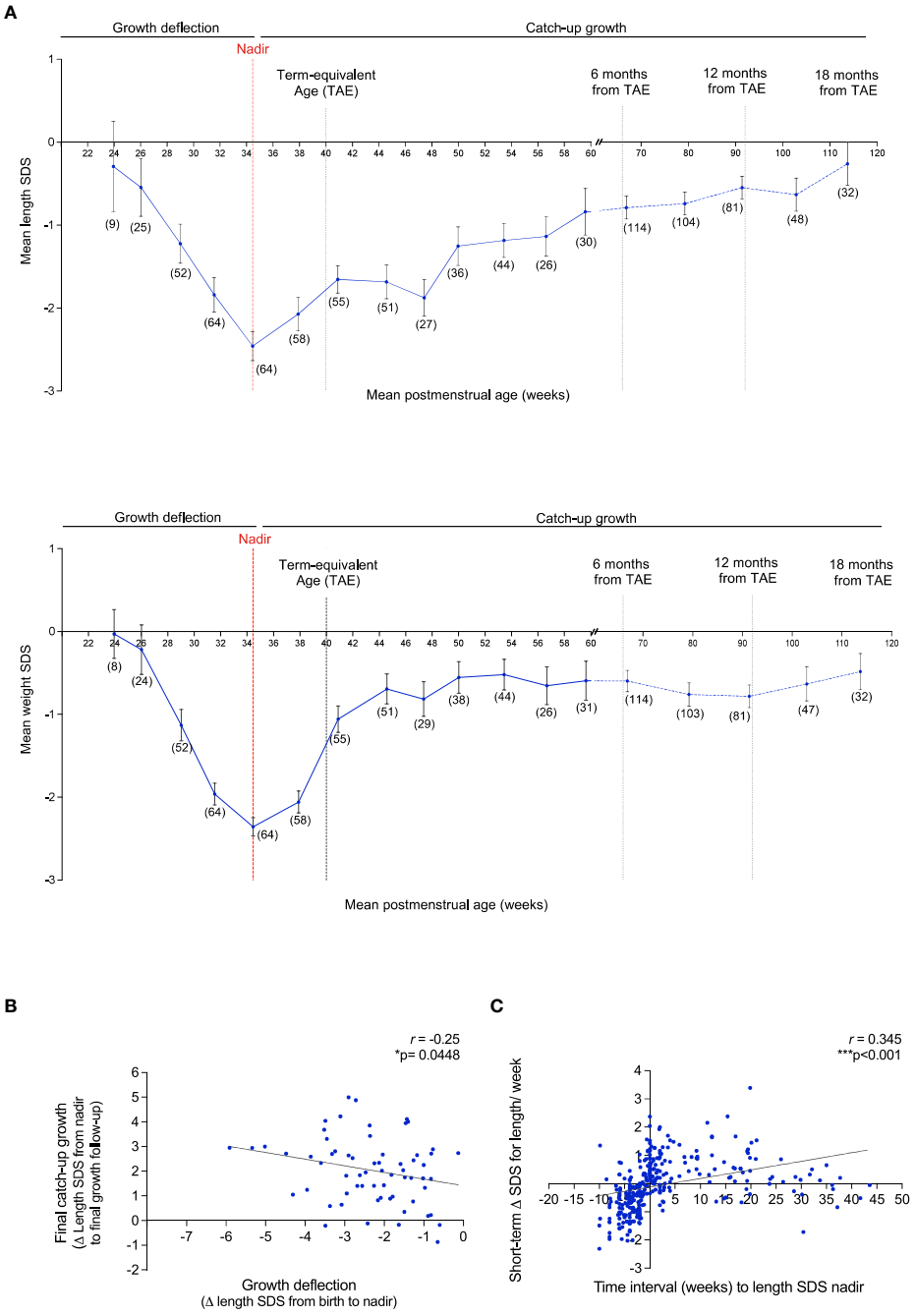

FIGURE 5
Growth pattern of VPT infants born <32 gestational weeks display an immediate postnatal growth failure in length and weight followed by a catch-up growth after nadir. **(A)**: Mean length SDS (top panel) and weight SDS (bottom panel) at the average of 3 week intervals from birth to 61 postmenstrual (PM) weeks (corresponding to 4 months of corrected age from the term-equivalent age of 40 PM weeks), and at 12 week intervals thereafter, until 119.8 PM weeks (corresponding to 18 months of corrected age). Observations per a sub-group at certain PM age (weeks) is reported as *n*=(x). Error bars represent the mean ± SEM. Nadir: Lowest length/weight SDS score. **(B)**: Association of the magnitude of growth deflection (ΔSDS for length from birth to nadir) and total catch-up growth (ΔSDS for length from nadir to final growth follow-up). **(C)**: Assessment of ΔSDS for length/ week (length assessed at the age of 1, 3, 5, 7 and 9 weeks during hospitalization) and time interval (weeks) to the length SDS nadir. 511 Pearson's R correlation (r) and p values were obtained from Bivariate correlation analyses.

compared to the liver. Moreover, GH had no effect on the endogenous expression of FGF21 and can therefore be excluded as a potential co-factor in regulating FGF21 levels.

Intriguingly, chronic FGF21 was seen to increase GH-induced GHR turnover. This may be due to a functional interaction between the GH and FGF21 pathways with unknown molecular events linking the two. The action of FGF21 on GHR degradation/ internalization led to the abrogation of GHR signaling events. This was demonstrated through the rapid reduction in signaling components including STAT5 phosphorylation and IGF-1

10.3389/fendo.2023.1105602

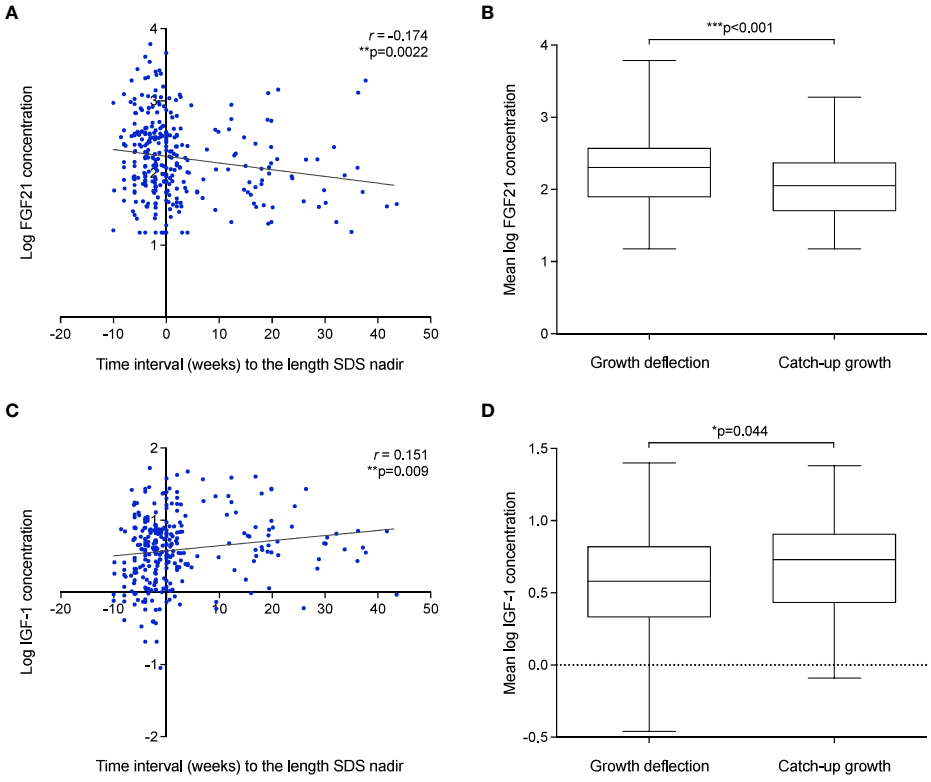

FIGURE 6
Growth failure after birth in VPT infants is associated with elevated FGF21 and low IGF-1 levels. **(A–D)**: The association of FGF21 **(A)** and IGF-1 **(C)** concentration and time interval (weeks) to the length SDS nadir. Pearson's R correlation (*r*) and *p* values were obtained from Bivariate correlation analyses. Assessment of mean FGF21 **(B)** and IGF-1 **(D)** concentration during deflection and catch-up growth phase. *p* values were obtained from Paired *t*-test analysis.

expression. Thus, the inhibitory effect of chronic FGF21 levels on early (pSTAT5) and late (IGF-1) downstream events of the GHR signaling cascade, reveals FGF21s' ability to develop GH resistance, highlighting its role in linear growth attenuation.

A second independent action of chronic FGF21 was confirmed on GH-induced SOCS2 upregulation. We speculate that an increase in the negative feedback regulator SOCS2, acts as an additive effect on the role of chronic FGF21 in GH-induced GHR degradation by further prohibiting the activation of GHR signaling to induce a state of GH resistance. It is well described that SOCS2 exerts its actions *via* two main mechanisms. 1) *via* binding to phosphorylated tyrosines on GHR resulting in blocking the association of positive signaling regulators (JAK2 and STAT5b activation), 2) *via* regulating cellular GHR levels by direct ubiquitination in a proteasomal dependent manner (21, 31). Interestingly, FGF21 did not increase GH-induced ubiquitination of cell surface GHR, despite our observations of FGF21s' actions on increased GHR turnover/degradation and SOCS2 expression. An inability to detect subtle albeit biologically relevant changes in ubiquitination in the western blot setting may explain why FGF21 was not seen to induce GHR ubiquitination. Further investigation is required to explore alternative mechanisms of GHR ubiquitination potentiated by chronic FGF21 e.g. *via* ubiquitin independent proteasomal degradation.

Overall, a thorough evaluation of the mechanistic role of chronic FGF21 on GHR signaling has provided further insights into the direct actions of FGF21 in the development of GH resistance. These findings suggest two main mechanisms of FGF21 in GH insensitivity and subsequent growth failure. 1) Chronic FGF21 increases GHR turnover, reducing the activation of GH-induced STAT5 phosphorylation and IGF-1 expression. 2) Chronic FGF21 upregulates GH-induced SOCS2 expression, suppressing GHR activation and downstream signaling events. As we employed a suitable, but inherently imperfect *in vitro* model, appropriate validation in either *ex vivo* primary cultures of growth plate/organoids or *in vivo* models would be needed to fully substantiate the proposed mechanisms.

The clinical evaluation of growth trends in VPT infants further provided evidence to suggest that elevated FGF21 levels as seen during growth deflection may drive GH insensitivity and stunted growth. The regulation of FGF21 expression associated with GH resistance, however, warrants further experimental evaluation. Several recent investigations describe the interplay of macronutrient (carbohydrates, fatty acids, and proteins) availability on the endogenous expression of hepatic and circulating FGF21 levels (32–34). Our data did not distinguish whether the observed declines in FGF21 and increase in IGF-1 are driven by the change in

nutritional state or by increasing age. We did not have access to detailed nutritional data for this cohort; assessment of the nutritional intake in another cohort of VPT infants may highlight a potential co-factor associated with upregulating FGF21 expression.

This study has opened new avenues for an opportunity to consider more tailored treatment strategies in children with debilitating chronic conditions. Novel treatment approaches will aid to enhance therapeutic management, having a significant cost saving effect for failed GH treatment in the healthcare system. Ultimately, advancement in clinical outcomes associated with GH resistance will improve the overall quality of life of infants in both the short and long-term.

Data availability statement

The raw data supporting the conclusions of this article will be made available by the authors, without undue reservation.

Ethics statement

The studies involving human participants were reviewed and approved by Pohjois-Savo Health Care District, Finland. Written informed consent to participate in this study was provided by the participants' legal guardian/next of kin.

Author contributions

LG, LD, US, and SH: conception and design of the study, supervision, acquisition of data, analysis and interpretation of data, writing the article, and approval of final version. JM and SS: conception and design of the study, performed experiments, analysis and interpretation of data, and writing the article. FZ and LS: acquisition of data, analysis and interpretation of data. KM: performed RNAScope experiments. CH: performed single cell sequencing analysis. All authors contributed to the article and approved the submitted version.

Funding

JM, LG, and LD were funded by Merck Serono Grant for Growth Innovation 2014. LG is funded by the BBSRC (BB/V007246/1). US was funded by Kuopion Yliopistollinen Sairaala (US; 2017-2018), and Päivikki ja Sakari Sohlbergin Säätiö (US; 2017). LS was funded by the Swedish Research Council, Stockholm City Council, European Society for Paediatric Endocrinology, The Masonic Barnhuset Foundation in Stockholm, Sällskapet Barnavård, Märta och Gunnar V. Philipsons Stiftelse. FZ was funded by the Swedish Childhood Cancer Foundation, Åke Wibergs Stiftelse. SH is funded by the Wellcome Trust (222049/Z/20/Z) and Barts charity (MGU0552).

Conflict of interest

Author FZ is in the editorial board of Frontiers for Endocrinology.

The remaining authors declare that the research was conducted in the absence of any commercial or financial relationships that could be construed as a potential conflict of interest.

Publisher's note

Supplementary material

The Supplementary Material for this article can be found online at: https://www.frontiersin.org/articles/10.3389/fendo.2023.1105602/full#supplementary-material

References

1. Guasti L, Silvennoinen S, Bulstrode NW, Ferretti P, Sankilampi U, Dunkel L. Elevated FGF21 leads to attenuated postnatal linear growth in preterm infants through GH resistance in chondrocytes. *J Clin Endocrinol Metab* (2014) 99(11):E2198–206. doi: 10.1210/jc.2014-1566

2. Kubicky RA, Wu S, Kharitonenkov A, De Luca F. Role of fibroblast growth factor 21 (FGF21) in undernutrition-related attenuation of growth in mice. *Endocrinology* (2012) 153(5):2287–95. doi: 10.1210/en.2011-1909

3. Wu S, Levenson A, Kharitonenkov A, De Luca F. Fibroblast growth factor 21 (FGF21) inhibits chondrocyte function and growth hormone action directly at the growth plate. *J Biol Chem* (2012) 287(31):26060–7. doi: 10.1074/jbc.M112.343707

4. Cuevas-Ramos D, Aguilar-Salinas CA, Gomez-Perez FJ. Metabolic actions of fibroblast growth factor 21. *Curr Opin Pediatr* (2012) 24(4):523–9. doi: 10.1097/MOP.0b013e3283557d22

5. Kilkenny DM, Rocheleau JV. The FGF21 receptor signaling complex: Klothobeta, FGFR1c, and other regulatory interactions. *Vitam Horm* (2016) 101:17–58. doi: 10.1016/bs.vh.2016.02.008

6. Ornitz DM, Itoh N. The fibroblast growth factor signaling pathway. *Wiley Interdiscip Rev Dev Biol* (2015) 4(3):215–66. doi: 10.1002/wdev.176

7. Grunwald T, De Luca F. Role of fibroblast growth factor 21 (FGF21) in the regulation of statural growth. *Curr Pediatr Rev* (2015) 11(2):98–105. doi: 10.2174/1573396311666150702105152

8. Sun H, Sherrier M, Li H. Skeletal muscle and bone - emerging targets of fibroblast growth factor-21. *Front Physiol* (2021) 12:625287. doi: 10.3389/fphys.2021.625287

9. Cole TJ, Statnikov Y, Santhakumaran S, Pan H, Modi N, Neonatal Data Analysis U, et al. Birth weight and longitudinal growth in infants born below 32 weeks' gestation: a UK population study. *Arch Dis Child Fetal Neonatal Ed* (2014) 99(1):F34–40. doi: 10.1136/archdischild-2012-303536

10. Hollanders JJ, van der Pal SM, van Dommelen P, Rotteveel J, Finken MJJ. Growth pattern and final height of very preterm vs. very low birth weight infants. *Pediatr Res* (2017) 82(2):317–23. doi: 10.1038/pr.2017.63

11. Mericq V, De Luca F, Hernandez MI, Pena V, Rossel K, Garcia M, et al. Serum fibroblast growth factor 21 levels are inversely associated with growth rates in infancy. *Horm Res Paediatr* (2014) 82(5):324–31. doi: 10.1159/000367922

12. Arndt MB, Richardson BA, Mahfuz M, Ahmed T, Haque R, Gazi MA, et al. Plasma fibroblast growth factor 21 is associated with subsequent growth in a cohort of

underweight children in Bangladesh. *Curr Dev Nutr* (2019) 3(5):nzz024. doi: 10.1093/cdn/nzz024

13. Sankilampi U, Hannila ML, Saari A, Gissler M, Dunkel L. New population-based references for birth weight, length, and head circumference in singletons and twins from 23 to 43 gestation weeks. *Ann Med* (2013) 45(5-6):446–54. doi: 10.3109/07853890.2013.803739

14. Saari A, Sankilampi U, Hannila ML, Kiviniemi V, Kesseli K, Dunkel L. New Finnish growth references for children and adolescents aged 0 to 20 years: Length/height-for-age, weight-for-length/height, and body mass index-for-age. *Ann Med* (2011) 43(3):235–48. doi: 10.3109/07853890.2010.515603

15. Livak KJ, Schmittgen TD. Analysis of relative gene expression data using real-time quantitative PCR and the 2(-delta delta C(T)) method. *Methods* (2001) 25(4):402–8. doi: 10.1006/meth.2001.1262

16. Hawkes CP, Oni OA, Dempsey EM, Ryan CA. Potential hazard of the neopuff T-piece resuscitator in the absence of flow limitation. *Arch Dis Child Fetal Neonatal Ed* (2009) 94(6):F461–3. doi: 10.1136/adc.2008.155945

17. Zaman F, Chrysis D, Huntjens K, Chagin A, Takigawa M, Fadeel B, et al. Dexamethasone differentially regulates bcl-2 family proteins in human proliferative chondrocytes: role of pro-apoptotic bid. *Toxicol Lett* (2014) 224(2):196–200. doi: 10.1016/j.toxlet.2013.10.020

18. Haseeb A, Kc R, Angelozzi M, de Charleroy C, Rux D, Tower RJ, et al. SOX9 keeps growth plates and articular cartilage healthy by inhibiting chondrocyte dedifferentiation/osteoblastic redifferentiation. *Proc Natl Acad Sci U S A* (2021) 118 (8). doi: 10.1073/pnas.2019152118

19. van Kerkhof P, Smeets M, Strous GJ. The ubiquitin-proteasome pathway regulates the availability of the GH receptor. *Endocrinology* (2002) 143(4):1243–52. doi: 10.1210/endo.143.4.8755

20. Bullock AN, Debreczeni JE, Edwards AM, Sundstrom M, Knapp S. Crystal structure of the SOCS2-elongin c-elongin b complex defines a prototypical SOCS box ubiquitin ligase. *Proc Natl Acad Sci U S A* (2006) 103(20):7637–42. doi: 10.1073/pnas.0601638103

21. Vesterlund M, Zadjali F, Persson T, Nielsen ML, Kessler BM, Norstedt G, et al. The SOCS2 ubiquitin ligase complex regulates growth hormone receptor levels. *PLoS One* (2011) 6(9):e25358. doi: 10.1371/journal.pone.0025358

22. Hiltunen H, Loyttyniemi E, Isolauri E, Rautava S. Early nutrition and growth until the corrected age of 2 years in extremely preterm infants. *Neonatology* (2018) 113 (2):100–7. doi: 10.1159/000480633

23. Niklasson A, Engstrom E, Hard AL, Wikland KA, Hellstrom A. Growth in very preterm children: a longitudinal study. *Pediatr Res* (2003) 54(6):899–905. doi: 10.1203/01.PDR.0000091287.38691.EF

24. Villar J, Giuliani F, Bhutta ZA, Bertino E, Ohuma EO, Ismail LC, et al. Postnatal growth standards for preterm infants: the preterm postnatal follow-up study of the INTERGROWTH-21(st) project. *Lancet Glob Health* (2015) 3(11):e681–91. doi: 10.1016/S2214-109X(15)00163-1

25. Blake RA, Park S, Baltazar P, Ayaso EB, Monterde DB, Acosta LP, et al. LBW and SGA impact longitudinal growth and nutritional status of Filipino infants. *PLoS One* (2016) 11(7):e0159461. doi: 10.1371/journal.pone.0159461

26. Euser AM, de Wit CC, Finken MJ, Rijken M, Wit JM. Growth of preterm born children. *Horm Res* (2008) 70(6):319–28. doi: 10.1159/000161862

27. Knops NB, Sneeuw KC, Brand R, Hille ET, den Ouden AL, Wit JM, et al. Catch-up growth up to ten years of age in children born very preterm or with very low birth weight. *BMC Pediatr* (2005) 5:26. doi: 10.1186/1471-2431-5-26

28. Abad V, Meyers JL, Weise M, Gafni RI, Barnes KM, Nilsson O, et al. The role of the resting zone in growth plate chondrogenesis. *Endocrinology* (2002) 143(5):1851–7. doi: 10.1210/endo.143.5.8776

29. van der Eerden BC, Karperien M, Wit JM. Systemic and local regulation of the growth plate. *Endocr Rev* (2003) 24(6):782–801. doi: 10.1210/er.2002-0033

30. Brito I, Gil-Pena H, Molinos I, Loredo V, Henriques-Coelho T, Caldas-Afonso A, et al. Growth cartilage expression of growth hormone/insulin-like growth factor I axis in spontaneous and growth hormone induced catch-up growth. *Growth Horm IGF Res* (2012) 22(3-4):129–33. doi: 10.1016/j.ghir.2012.04.004

31. Greenhalgh CJ, Rico-Bautista E, Lorentzon M, Thaus AL, Morgan PO, Willson TA, et al. SOCS2 negatively regulates growth hormone action *in vitro* and in vivo. *J Clin Invest* (2005) 115(2):397–406. doi: 10.1172/JCI22710

32. Erickson A, Moreau R. The regulation of FGF21 gene expression by metabolic factors and nutrients. *Horm Mol Biol Clin Investig* (2016). doi: 10.1515/hmbci-2016-0016

33. Perez-Marti A, Sandoval V, Marrero PF, Haro D, Relat J. Nutritional regulation of fibroblast growth factor 21: from macronutrients to bioactive dietary compounds. *Horm Mol Biol Clin Investig* (2016) 30(1). doi: 10.1515/hmbci-2016-0034

34. Solon-Biet SM, Cogger VC, Pulpitel T, Heblinski M, Wahl D, McMahon AC, et al. Defining the nutritional and metabolic context of FGF21 using the geometric framework. *Cell Metab* (2016) 24(4):555–65. doi: 10.1016/j.cmet.2016.09.001

Frontiers in Endocrinology

Explores the endocrine system to find new therapies for key health issues

The second most-cited endocrinology and metabolism journal, which advances our understanding of the endocrine system. It uncovers new therapies for prevalent health issues such as obesity, diabetes, reproduction, and aging.

Discover the latest Research Topics

See more →

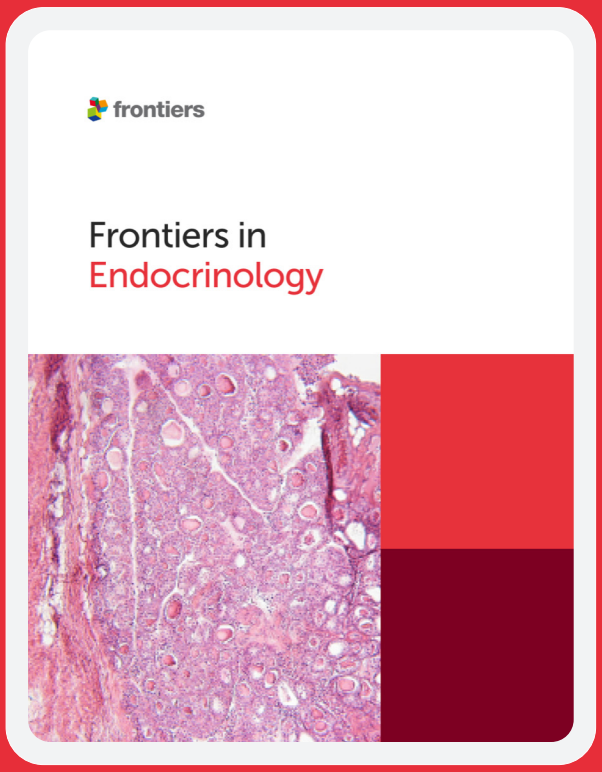

Frontiers

Avenue du Tribunal-Fédéral 34
1005 Lausanne, Switzerland
frontiersin.org

Contact us

+41 (0)21 510 17 00
frontiersin.org/about/contact